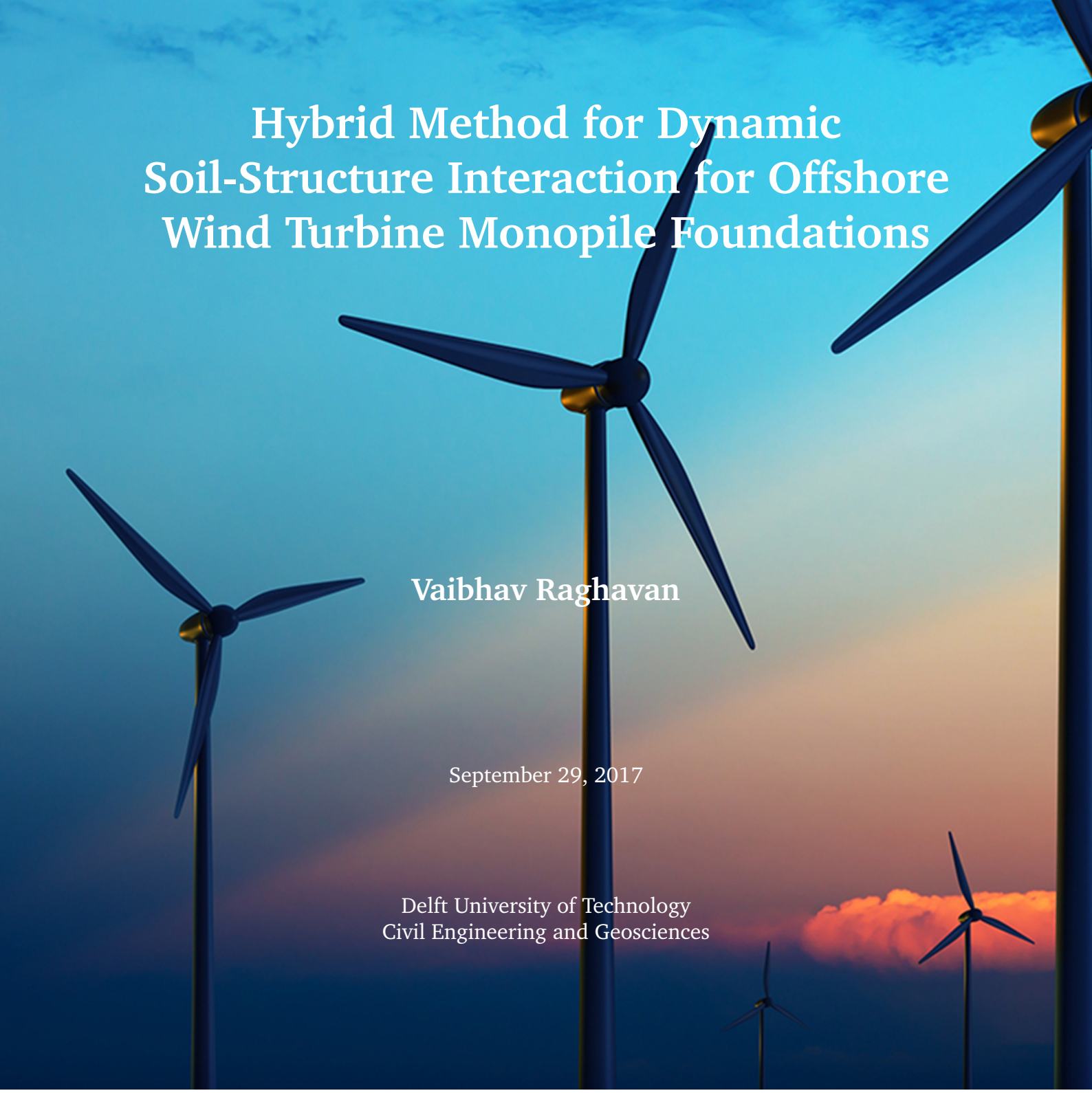

Hybrid Method for Dynamic Soil-Structure Interaction for Offshore Wind Turbine Monopile Foundations

Vaibhav Raghavan

September 29, 2017

Delft University of Technology
Civil Engineering and Geosciences

SIEMENS Gamesa
RENEWABLE ENERGY

TU Delft

Hybrid Method for Dynamic Soil-Structure Interaction for Offshore Wind Turbine Monopile Foundations

Master of Science Thesis

Author: Vaibhav Raghavan

Committee:

Ir. F.W. Renting	TU Delft
Dr. Ir. K.N. van Dalen	TU Delft
Prof. Dr. Ir. A.V. Metrikine	TU Delft - Chairman
Ir. J. Bongers	Siemens Gamesa Renewable Energy
Ir. C.E. de Winter	Siemens Gamesa Renewable Energy

September 29, 2017

SIEMENS Gamesa RENEWABLE ENERGY

TU Delft

Abstract

The Offshore wind industry is constantly expanding and one of the key cost drivers is the offshore wind turbine support structure. The foundation accounts for up to 35 % of the total installation cost of the wind turbine [6]. The monopile foundations are the most commonly used support structure with diameters up to 6m and Embedded length/depth (L/D)<7. Proper modeling of the soil-structure interaction (SSI) is important for safe and efficient design. With the introduction of large diameter rigid monopile foundations, the applicability of the current design standard is in question.

The current industry standard model for SSI for laterally loaded monopiles is the Winkler foundation model. In this model, the soil is idealized as a row of one dimensional discrete springs spanning along the beam. The stiffness of these springs is obtained using empirically derived $p-y$ curves, which gives the relation between the soil-pressure (p) and deflection (y). The $p-y$ method describes the construction of the $p-y$ curves for any arbitrary set of soil parameters. This method has been applied in the oil and gas industry and is based on field tests conducted on slender piles with diameter 2m.

Various studies on the applicability of the model have shown to give erroneous results for large diameter monopiles. Since the soil is idealized as a row of discrete (local) springs, it neglects the continuous (non-local) nature of soil. Additionally, monopiles with L/D <7 exhibit a more rigid behavior and hence industry standard assumptions for laterally loaded piles with respect to vertical tangent criteria and 'zero-toe-kick' do not hold on.

A plane strain semi-analytical model is developed which considers the continuous (non-local) nature of soil as well as the soil below the pile toe/tip, which could be significant to the dynamic behavior of the monopile foundations. In this approach, the pile is modeled as an elastic rectangular plate which is discretized using modified Euler-bernoulli beam elements. and the soil is modeled as an elastic continuum waveguide. The two entities are combined via the discretized interface. Assuming wave motion in soil, semi-analytical solutions satisfying homogeneous and inhomogeneous boundary conditions are obtained for the waveguide, which are used to derive the frequency dependent soil stiffness matrices at the interface. These are then coupled to the plate.

For the current study, the L/D ratio of the plate is restricted to the flexible regime, due to the availability of a comparable reference solution in this regime. It is shown that, with L/D ratio of 12.5 already, the dynamic behavior of the plate is sensitive to the soil below the tip. Therefore, with smaller L/D ratios, it is expected that the tip will have a significant influence on the dynamic behavior of the pile.

Acknowledgements

For almost a year, I had the privilege of being associated with this project at Siemens Gamesa Renewable Energy. I feel very fortunate for the opportunity and am grateful for all the help I received during the course of this thesis.

First and foremost, thank you Karel, for your complete support and encouragement throughout the project. You encouraged me to look for the physical meanings and always gave critical insights. I value the long discussions we had on the theory of wave propagation and the basic dynamic principles involved. To my team of daily supervisors, Frank, Corine and Jeroen, for the hours of discussion, guidance and amazing support throughout the project. You all helped me stay, on track, and see the big picture, the final goal. Andrei, thank you for making time and always digging straight to the critical points, which helped me gain a deeper understanding of the subject. To my fellow students and colleagues at Siemens, thank you for creating a fun-filled and intellectual environment to work in. I value all the hours of Fuzbal, and can definitely say that my game has improved. I hope to take the knowledge gained on to the field, haha!.

Finally, to mom, dad and my sister Rohini, thank you for always believing in me and giving the confidence to overcome all challenges not only through this project, but the entire course of the MSc.

Vaibhav Raghavan
Delft, September 2017

Nomenclature

Latin symbols

a	Radius of circular plate	m
b	Shift parameter	-
c_p	Compressional wave speed	ms^{-1}
c_s	Shear wave speed	ms^{-1}
D	Diameter	m
D_b	Bending stiffness of plate	Nm
E	Young's modulus	Nm^{-2}
G	Shear modulus	Nm^{-2}
H	Domain depth	m
h	Homogeneous	–
I	Moment of Inertia	m^4
i	Inhomogeneous	–
K	Stiffness matrix	Nm^{-2}
k_0	Initial stiffness	Nm^{-2}
k_{pz}	Vertical compressional wavenumber	m^{-1}
k_p	Compressional wavenumber	m^{-1}
k_{sz}	Vertical shear wavenumber	m^{-1}
k_s	Shear wavenumber	m^{-1}
k_x	Horizontal wavenumber	m^{-1}
L	Embedded length	m
M	Bending moment	Nm
M_b	Mass matrix of plate	kg
p	Soil pressure	Nm^{-1}
Q	Compliance matrix	m^2N^{-1}

R	Radius of plate element	m
$\tilde{s}$	Dimensional variable s	-
s	Dimensionless variable s	-
s_{ij}	Matrix S component ij	-
s	Vector s	-
T	Time	s
u	Displacement	m
V	Shear force	N
W	Plate displacement	m
x	Horizontal coordinate	m
y	Spring displacement	m
z	Vertical coordinate	m
ϵ	Relative difference	–
ϕ	Plate rotation	–

Greek symbols

β	Roots of the Euler Bernoulli beam dispersion equation	–
δ	Kronecker delta	–
ϵ	Strain	–
γ	Shear Strain	–
λ	Lame's first constant	Nm^{-2}
μ	Shear modulus/Lame's second constant	Nm^{-2}
ν	Poisson's ratio	–
ω	Circular frequency	$rads^{-1}$
ϕ	Elastic Dilational potential	m^2s^{-1}
ψ	Elastic Rotational potential	m^2s^{-1}
ρ	Density	kgm^{-3}
σ	Stress	Nm^{-2}
τ	Shear Stress	Nm^{-2}

Abbreviations

avg	average

mod	modified
ANSYS	Analysis of systems
API	American Petroleum Institute
DISSTINCT	Dynamic Interaction between Soil and Structure, Tools and Investigation using Numerical Calculations and Testing
DNV-GL	Det Norske Veritas Germanischer Lloyd
LCOE	Levelized cost of energy
SH	Shear horizontal wave
SSI	Soil-structure interaction
SV	Shear vertical wave

Contents

List of Figures

List of Tables

Chapter 1

Introduction

We currently rely on coal, oil and gas for almost 70 % of our energy needs [9]. The continuous use of these sources has given rise to greenhouse gas emissions, which are directly affecting our environment, climate change being the most prominent effect. Hence, a shift to more sustainable ways of power generation is requirement for the future.

One of the most promising ways of sustainable electricity generation is wind power. The wind power industry has evolved over the past thirty-five years transitioning from small scale manufacturing centered in Denmark in 1979 to a billion-dollar industry now spread across the world. Although the development in this field has been significant, cost is still one parameter that can be reduced, for which new and innovative ideas are constantly required and need to be developed.

1.1 Offshore Wind Energy

One of the most promising fields within Wind energy is Offshore wind energy. Europe is the world leader in offshore wind power, with the first Offshore wind farm being installed in Denmark in 1991 [29]. As of 2013, offshore wind power contributed to 16 % of the total wind power capacity across Europe. Projections for 2020 show an estimate of 40 GW in European waters, providing 4 % of Europe's demand for electricity [31].

OWT Support Structures

Various support structures are used/proposed for Offshore Wind turbines. The most commonly used are monopiles, due to the ease in design and fabrication. As of 2016, 88% of the total support structures used for Offshore wind turbines are monopiles [18]. These were initially designed for water depths up to 25m. For depths from 25-45 m, jacket structures are generally used. However now with the introduction of XL monopiles, these can be used for water depths up to 40m. Other support structures include Gravity based structures, tripod structures, tripile structures etc. These are shown in Figure 1.1.

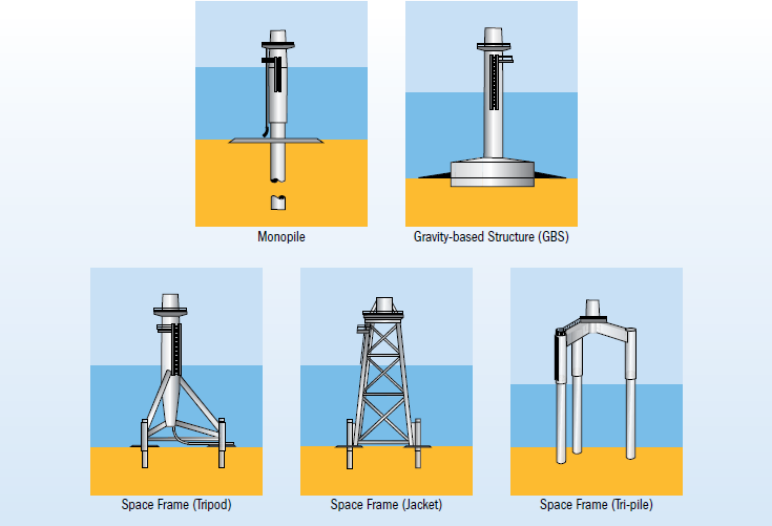

Figure 1.1: ***Typical Offshore foundations [14]***

1.2 Dynamic behavior of soil

Soil has a complex behavior under dynamic loading. Various properties of soil that are responsible for this include density, isotropy and porosity. The stress-strain relations form the basis for describing the static and dynamic behavior of soil and these relations depend on the strain range. For Offshore monopile structures, the cyclic strain level in the subsoil is in the elastic range [12], and hence a linear elastic constitutive model could suffice for modelling soil. The characteristic of an elastic material is in its ability to return to its original state once the static or dynamic load has been removed, meaning there is no permanent deformation in the material.

1.3 Soil-Structure interaction(SSI)

As the Offshore wind turbine industry is expanding, the design of the support structure is becoming more critical. The foundation accounts for up to 35 % of the total installation cost of the wind turbine [6]. Given the large number of turbines that are produced and the profits being marginal, this is significant. Furthermore, the turbines now are becoming larger, hence the diameter of the monopile foundations used is also increasing. The foundation transfers the load from the structure to the soil, hence the soil-structure interaction is an important part of its design.

The DISSTINCT (Dynamic Interaction between Soil and Structure, Tools and Investigation using Numerical Calculations and Testing) project was started at Siemens, focusing on two key areas - 1. Methods for determining the stiffness and damping parameters for the soil and 2. Accurate models for the Soil-Pile interaction mechanism. These play a crucial role in the dynamic behavior of Offshore wind turbines. An accurate estimation of stiffness and damping properties of soil is currently lacking, which leads to higher Levelized cost of energy (LCOE). With more precise methodologies, this could be reduced.

Various models exist which describe Soil-Structure interaction (SSI). For Offshore monopile foundations, the model should be able to describe the static and dynamic lateral load-deflection relations. The monopile in most models is idealised as a beam with Euler-Bernoulli beam model and the Timoshenko beam models being the most well-known models. With regard

to modelling the soil, two approaches currently exist - The Winkler foundation and Elastic foundation.

- Winkler foundation model disregards the continuous nature of the soil medium and the reaction from the soil to the pile is modelled as discrete springs. The reaction of a point along the pile is directly related to the deflection at that point.
- In the elastic foundation model, the soil is assumed to be an ideal elastic continuum.

(a) ***Winkler foundation***

(b) ***Elastic foundation***

Figure 1.2: ***Differentiating the soil behavior in Winkler and Elastic foundation models [33]***

These models are explained in greater detail in the following sections.

1.4 Winkler Foundation

The Winkler foundation model characterizes the soil as a series of independent linearly elastic springs, so that the deformation is localized to the points where the loading exists. In this method, a non-linear p-y curve is used whose properties depend on the set of soil parameters. This is also referred to as the subgrade reaction model.

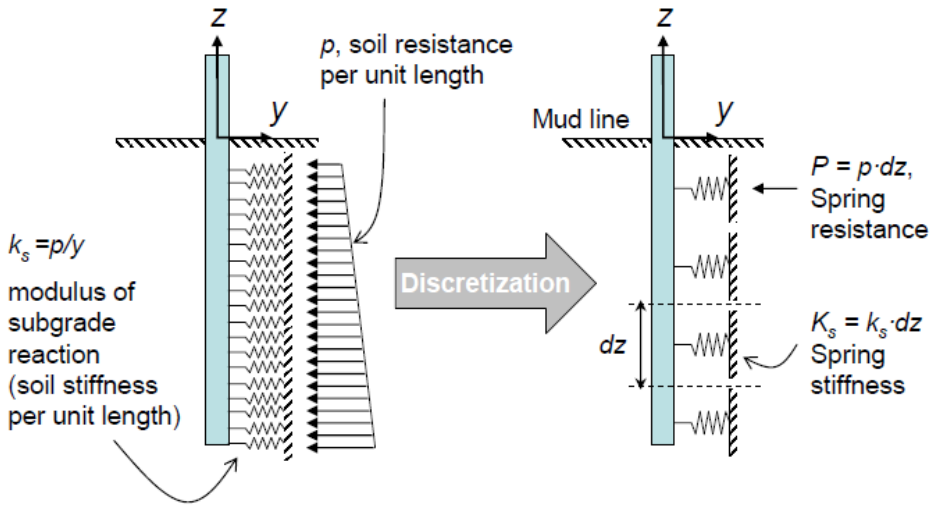

Figure 1.3: ***Discretized beam on Winkler foundation model[33]***

According to the Winkler hypothesis, the subgrade reaction p at a certain point in the soil at depth z is proportional to the displacement y at the same point given by:

$$p(y, z) = k_s(z) * y(z)$$

When modelling linearly elastic springs, the proportionality constant k_s is referred to as the modulus of subgrade reaction, and has units in terms of stiffness per unit length. Since discrete springs are modelled along the beam, there exists a spring spacing. The spring resistance is hence obtained by multiplying the soil resistance and stiffness by this spring spacing. The current standards assume a linear relation of the horizontal subgrade modulus over depth. The spring modulus of the Winkler foundation in most cases, is dependent on the size of the foundation, however when the laterally loaded pile is modelled as a one-dimensional problem, the subgrade modulus k_s is assumed to be independent of the width of the pile, which is in close relation with the elastic foundation model.

1.4.1 Estimating the Winkler foundation stiffness - p-y method

The p-y curves give the load-deflection behavior for the distributed springs in the Winkler model. These were originally developed for slender foundations used for the oil and gas industry and were based on field tests in uniform soil with piles with a diameter of less than 1m and embedded lengths of up to 20m [28]. Analysis of laterally loaded piles for offshore structures is performed using the solution to the relations shown in Equation 1.1.

$$\begin{aligned} E_p I_p \frac{d^4 y}{dx^4} &= p \\ p &= -E_s y \end{aligned} \tag{1.1}$$

Here y is the deflection of the pile, x is the coordinate along the length of the pile, $E_p I_p$ is the flexural stiffness of the pile, p is the soil resistance and E_s is soil stiffness. By knowing the pile goemetry ,boundary conditions and the soil resistance p (which can be obtained as a function of y), the above equations can be solved. The curves representing the relation between p and y are the p-y curves.

The initial slope of the p-y curves is equal the initial stiffness k_0. The linearized stiffness is used in the Winkler model when doing modal analysis. Depending on the type of soil and its characteristics, the assumed initial stiffness values vary. For example, in case of sand, the initial stiffness depends on the angle of friction according to

$$k_0 = k * z$$

where k is the material property depending on the angle of internal friction ϕ. For clays, the initial slope in the $p - y$ curves is infinity, hence standards such as those given by Det Norske Veritas Germanischer Lloyd(DNV-GL) propose some relations for the initial stiffness. These can be found in [13].

1.4.2 Drawbacks of the Winkler Foundation

The Winkler foundation model is the most commonly used soil model in the industry. The guidelines provided by the American Petroleum Institute (API) and DNV are currently based on the field tests carried out on 1m diameter piles with embedded lengths of up to 20 m. Given that wind turbines are now growing in size, the monopile foundations are also increasing in length and diameter. The question then is if these guidelines are still applicable for such large diameter (up to 6m) monopiles. Some limitations of the Winkler foundation are -

- **Lack of continuity** - The real soil is continuous to some extent, since displacements at any given point will be influenced by the forces in the surrounding points. Furthermore, the soil has no mass in the Winkler foundation, hence the true nature of how the soil behaves cannot be accurately captured with this model.

- **Dependency of k_s on depth** - Different estimation methods for obtaining stiffness parameter k_s are used in the p-y method with regard to depth dependency. For sands, a linear relation exists between the stiffness parameter and the depth. For clayey soil, empirical relationships are derived based on field tests. However, in a 3D finite element study conducted by Lesny et.al. [22] on considering scale effects for lateral load response of large diameter monopiles, they concluded that the p-y method over predicts the response for larger depths, which could result in insufficient pile length design. This is attributed to the assumed linear relation between k_s and depth z.

- **Flexible vs Rigid pile** - The p-y curves were originally developed based on field tests carried out on piles, whose slenderness ratio (Embedded length/Depth) L/D was close to 35, meaning these were highly flexible. However most monopiles installed today have L/D in the range of 3 to 7, where their behavior is much stiffer. This is shown in Figure 1.4 . The assumptions made in the standards with respect to the vertical tangent criteria and the 'zero-toe-kick' requirement give large and hardly realistic embedded length estimations [21].

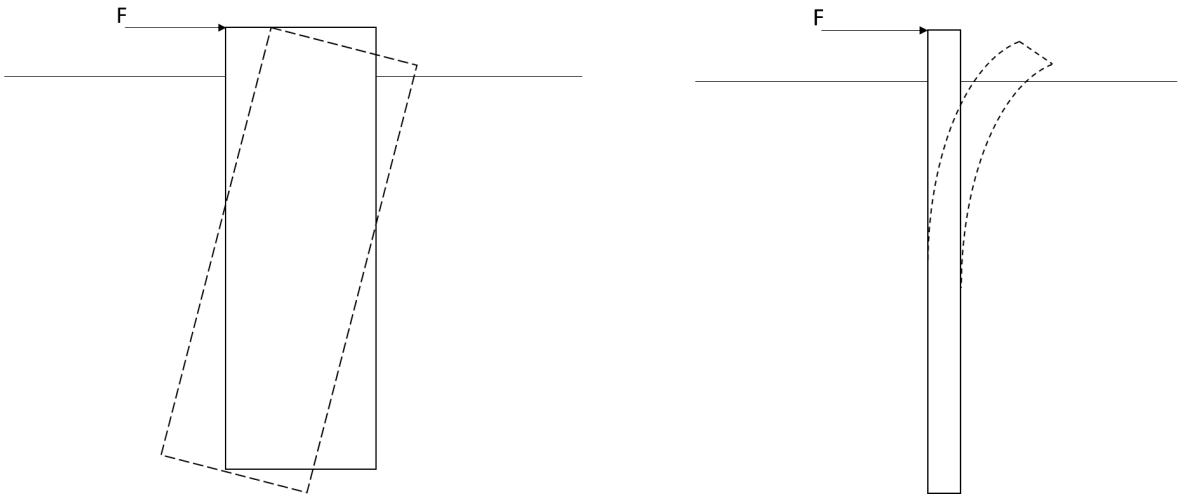

(a) ***Rigid pile*** **(b)** ***Flexible pile***

Figure 1.4: ***Rigid vs Flexible pile***

1.5 Elastic foundation

In the Elastic foundation model, the continuous nature of the soil is considered. The soil is modelled as an elastic continuum, which is based on the three-dimensional theory of elasticity. The detailed description of the theory as well as the governing equations is given in Chapter 2, since the elastic continuum model is used as the basis for modelling soil in this thesis. The main model parameters required include the Young's Modulus (E) and the Poisson's ratio (ν). Although the approach to obtain these parameters for practical problems is significant, this section gives a brief description of the solution techniques currently employed to solve SSI problems with this soil model and their advantages and drawbacks.

1.5.1 Analytical solution

The analytical solution is the exact solution to the problem. Wherever possible and feasible, this solution technique is definitely preferable. One example of this is the solution of a rigid circular plate on resting on the surface of an elastic half space. The solution, although

simplified is comparable to the lateral pile soil interaction problem, where a distributed load acts over an area on the surface of a half space. This is shown in Figure 1.5

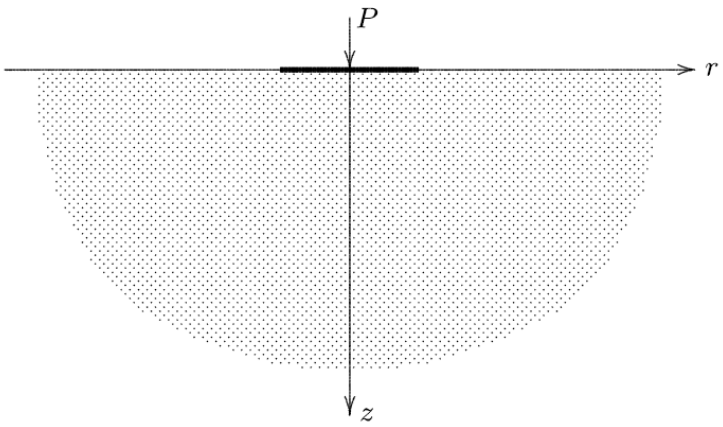

Figure 1.5: ***Rigid circular plate on an elastic half space [32]***

The problem is solved using boundary conditions at the top. The obtained solution is given as

$$\begin{aligned} \sigma_{zz} &= \frac{P}{2\pi a(a^2 - r^2)^{0.5}} \quad 0 < r < a, z = 0 \\ &= 0 \qquad\qquad\qquad\qquad r > a, z = 0 \end{aligned} \tag{1.2}$$

where P is the total force applied on the plate and a is the radius of the plate. There are many analytical solutions available for a wide range of problems, and these can be found in [32]. It is well known that the analytical solutions are applicable only for structures with simple geometries, and linear and uniform soil media, hence limiting its applicability.

1.5.2 Finite Element Method (FEM)

Solutions to complex problems can be hard to find analytically, however using simplified techniques such as discretization of the continuous media using finite element methods can be a good alternative. Finite element method is a numerical solution technique to obtain solutions for partial differential equations by reducing the order of the differential equations.

Constitutive models are used in this method to approximate soil behavior. Due to the complex behavior of soil, most constitutive models employed are empirical in nature. The parameters required are approximated using laboratory tests such as the tri-axial test. Finite element softwares such as ANSYS and PLAXIS are quite widely used for modelling SSI.

With regard to the FE method, one of the most important parameters is the mesh size. The finer the mesh, the better is the accuracy of the solution, and the more is the computational power required. With wave propagation problems for systems with finite or semi-infinite extension, FE methods require a large scale mesh which gives the near field response as well as far fields represented by artificial boundaries. In numerical wave propagation problems, artificial boundaries can introduce spurious reflections. A special artificial boundary condition known as the non-reflecting viscous boundary layer developed by Lysmer and Kuhlemeyer [20] is capable of absorbing wave energy. This is however is limited to transmitting plane and cylindrical waves,and therefore must be located far away from the sources[16]. As a result

the mesh size required is higher, which results in the requirement of more computational power.

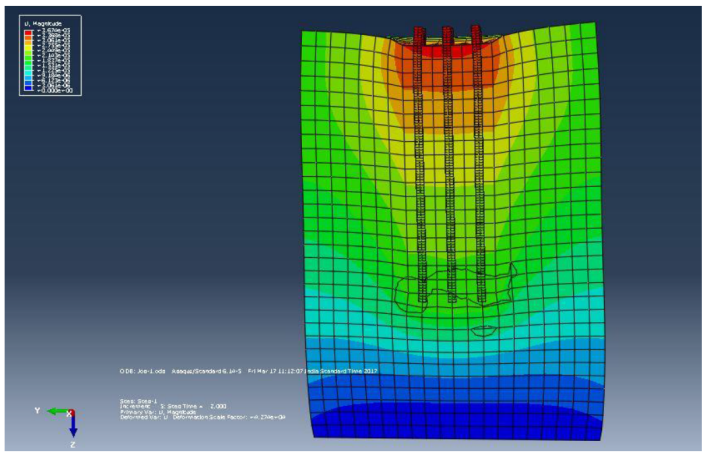

Figure 1.6: ***Deflection behavior of a pile group in Abaqus [5]***

Constitutive models for soil have been developed considering the incorporation of elasto-plasticity, visco-elaticity, elasto-visco-plasticity and linear elasticity. a few models most commonly used in practice are the Mohr Coloumb (Elasto-perfect plastic) model and CAM-Clay (Elasto-hardening plasticity) model.

1.5.3 Boundary Element Method (BEM)

With the BEM, the level of complexity to obtain the solution can be further reduced as compared to FEM. In this method, the pile-soil interface is discretized into small elements, and a fundamental, analytical solution is used to obtain the response of a point in the soil mass due to the application of a point load at another point in the soil mass. The solutions thus obtained are imposed at the center of each element. For pile-soil interaction problems, Mindlin's solution is often used as the fundamental solution. When used for a semi-infinite half space, Sommerfield's radiation condition is inherently satisfied. Figure 1.7 shows the essence of BEM.

The advantage of this method is it retains the advantages of FEM along with incorporating the continuity of soil in its solutions. Furthermore, since the discretization is now limited to the interface, the computational effort required could be significantly reduced. However, since a fundamental analytical solution is required, it could be limited in its application.

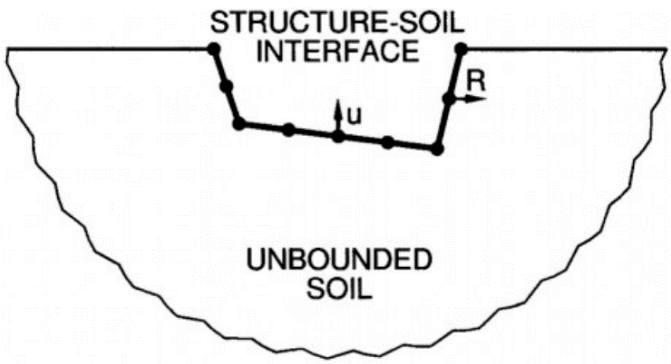

Figure 1.7: ***Essence of BEM [34]***

1.6 Motivation

The monopile foundations currently used for wind turbines are large diameter monopiles (up to 6m), with L/D ratio between 3 and 7. The Winkler foundation combined with the p-y curve method gives highly erroneous estimations for the pile-soil behavior and these can be attributed to the following reasons

- The p-y curves were originally derived from field tests carried out on small diameter slender piles.
- Due to the stiffer behavior of the monopile, the assumptions in standards with respect to the vertical tangent criteria and 'zero-toe-kick' are no longer applicable.
- The continuous nature of soil is neglected.

Hence, a new approach to model SSI for monopile foundations is required which would consider the continuous (non-local) nature of soil as well consider the soil below the tip, that could have a significant influence on the dynamic behavior of the monopile.

1.7 Thesis objective and tasks

The main objective of the thesis then follows as

"*Develop a soil-pile interaction model considering the non-local nature of soil and interaction of the pile tip with soil*"

An elastic constitutive model is sufficient for modelling the soil around the monopile. Employing FE methods to obtain the solution for this problem with reduced complexity (since inclusion of effects of plasticity, hardening are currently neglected in the soil) could lead to large computational effort.

An alternative modelling approach is hence introduced where the monopile is modelled using Finite elements, and the soil is modelled as an elastic waveguide. An elastic waveguide is an elastic halfspace with a definite boundary along one direction. The two entities are then combined via the discretized interface. Since two different solution techniques are combined into one method, the term **'Hybrid'** is introduced. The model is a 2D plane strain model.

The approach is similar to the BEM in terms of the application of a discretized interface between the pile and soil, however differs from BEM on the requirement of an analytical solution for the point load acting at points on the discretized interface.

The proposed soil-pile interaction model contains four domains. Domain 1,3 and 4 are the soil domains and Domain 2 is the pile domain. Domain 1 and 3 can be differentiated based on the direction of propogation of waves along the horizontal direction. Domain 4 is the tip domain introduced below the tip of the pile. To develop a steady understanding of the approach, the model is developed in a step-wise manner. The thesis contains three main parts

1. **Hybrid solution for the pile-soil system with a single domain of soil** - The pile-soil interaction model with a single domain of soil is analyzed. In this case, the pile is assumed to be clamped at the bottom. This is compared with a reference solution.

2. **Waveguide with a cavity subjected to excitation in the cavity surface** - The tip domain is introduced. Considering homogeneous and inhomogeneous boundary conditions, semi-analytical solutions are derived for excitation imposed on the boundary of all domains.

3. **Hybrid solution for the pile-soil system with a plate embedded in an elastic waveguide** - The pile is introduced into the caviy in the elastic waveguide. The pile-soil interaction model with a three domains of soil is analyzed. This is compared with the reference solution

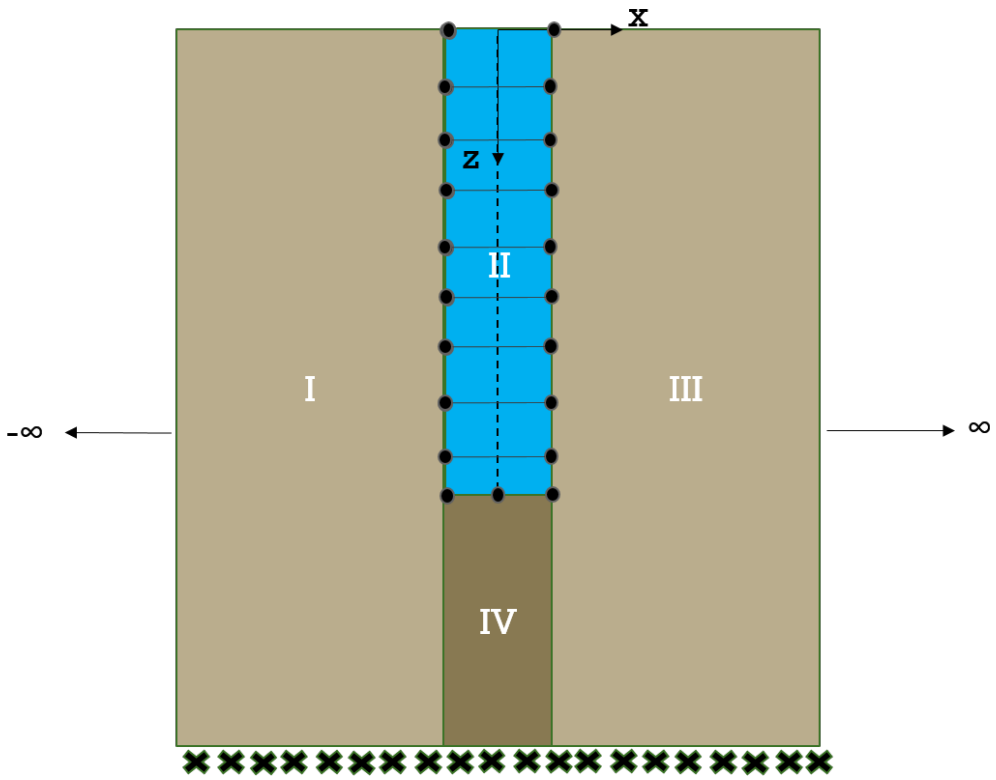

Figure 1.8: ***Proposed Pile-soil model***

1.8 Thesis outline

Chapter 2 gives an theory and derivations for modelling soil as an elastic continuum. These relations form the basis for the proposed soil - pile interaction model.

Chapter 3 introduces the pile-soil interaction model considering a single domain of soil (Domain 3). The frequency dependent soil stiffness matrix obtained at the interface is combined with the mass and stiffness matrices of the FE pile giving the dynamic stiffness matrix of the system. These are compared with the reference solution.

Chapter 4 describe the problem of a waveguide with a cavity subjected to an excitation in the cavity boundary. The chapter explains the derivation of the stress and displacement solutions for the problem including the tip domain which are used to obtain the stiffness matrices for each domain to be used for the pile-soil interaction problem.

Chapter 5 explains the pile-soil interaction problem for the pile embedded in the waveguide. Convergence studies with varying number of segments across Domains 1 and 3 as well as Domain 4 interface are done. These are compared with the reference solution.

Chapter 6 summarizes the important conclusions of the thesis and gives recommendations for future research.

Appendix A gives a detailed description of the benchmark solution, which is used as a comparison for the model. The remaining appendices give a mathematical background for some of the solution methods adopted, and results from the convergence studies performed for the plate-soil system.

1.9 Scope

The soil domain is modelled as a linearly elastic material, with constant properties across the entire waveguide. Furthermore, material damping within the soil as well as the pile are currently neglected. In reality, the soil domain would be inhomogeneous in nature as the density would be expected to increase with depth from the surface. Hence the current model is fairly simplified.

The model developed is compared with a reference solution, which is explained in detail in Appendix A. The L/D ratio used for the pile to validate the model range from 12.5 to 25, meaning the pile is highly flexible. This was done since the reference solution was obtained for this range of L/D. This model could be extended to smaller L/D ratios since there is no direct dependency observed in the background theory and derivation on this ratio. Furthermore, both solutions have not been validated with experimental results.

The soil stiffness matrices obtained through the model are frequency dependent which is more realistic as compared to the p-y curve method, since the behavior of soil would depend of the frequency of the force imposed on the surface.

The model developed is essentially a problem of a rectangular cavity in an elastic waveguide, where Somerfield's radiation condition is used as a boundary condition along the horizontal direction. Hence the soil model can further be used as a boundary condition for SSI problems, where non-linearities is introduced in soil surrounding the structure. This is shown in Figure 1.9.

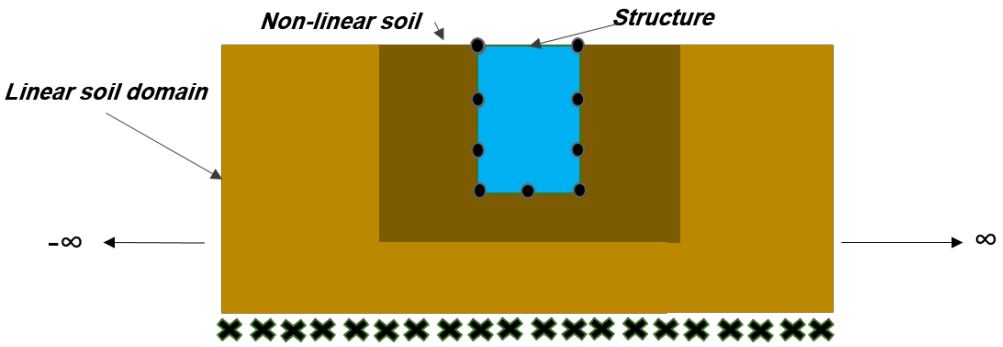

Figure 1.9: ***Soil model as a Boundary condition***

Stiffness matrices for the various domains surrounding the FE structure can be extracted from the model. Since these are independent from the structure, coupling with more complex geometries as well as different type of finite elements is possible.

Chapter 2

Soil as an Elastic Waveguide

Among the constitutive models for elastic soil medium introduced in the previous chapter, the elastic continuum soil model is the main emphasis of this thesis. This chapter provides the theoretical background and derivation of the elastodynamic equation for stress wave propagation which is used to obtain the characteristic wavenumbers and eigen modes.

2.1 Theoretical background

The soil is modelled as a linear isotropic elastic solid. In general there four main types of waves that propagate through soil with this property[26] [4] [10]. There are two body waves - P-waves and S-waves and two surface waves - Rayleigh waves and Love waves. P-waves, also referred to as longitudinal waves are associated with longitudinal particle motion, where the soil undergoes local compression and elongation when the wave passes. S-waves or Shear waves are associated with particle motion perpendicular to the direction of motion of the wave, resulting in shear stresses. The S waves can in turn be decomposed into horizontal and vertically polarized components referred to as SH and SV waves.

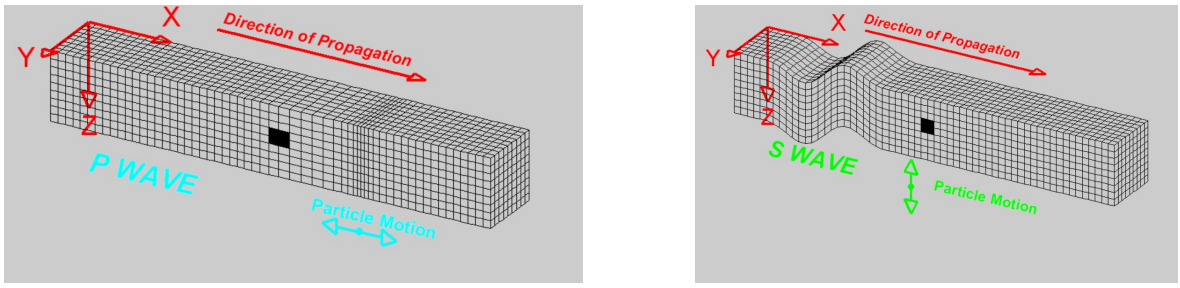

(a) ***P-wave*** **(b)** ***S-wave***

Figure 2.1: ***Body waves***

Rayleigh waves are combinations of SV and P-waves interacting at the surface, resulting in elliptical particle motion. Love waves result from the interaction of SH waves and P-waves and results in the ground moving side-to-side. Additionally, two more types of waves exist - Scholte waves and Stoneley waves whose particle motion is similar to Rayleigh waves. Scholte waves exist between a fluid-soil interface whereas Stoneley waves exist at the interface between two solids. Only P and S-waves are considered in this thesis since we primarily deal with soil behavior within the soil body and not at the surface.

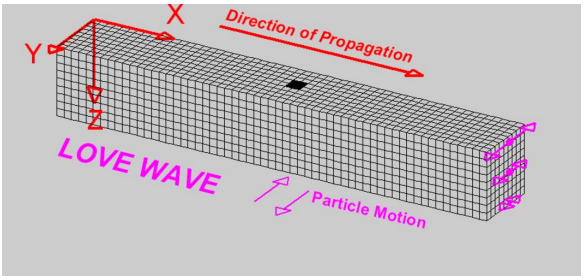

(a) *Love Wave*

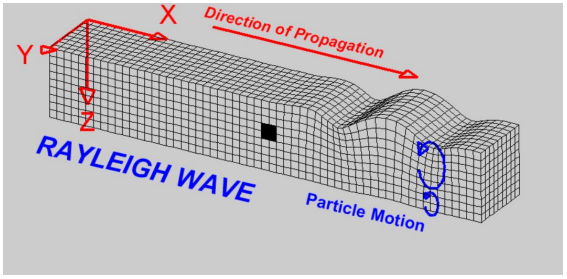

(b) *Rayleigh Wave*

Figure 2.2: *Surface waves*

2.2 Deriving the Equation of motion of the soil

The soil is to be modeled as an elastic continuum and the governing equation of motion of the soil system is based on classical physical laws such as the Newton's second law of motion.

The derivation of the equation of motion of the soil consists of three relations in three dimensions namely the kinematic, constitutive and equilibrium relations, which are combined together to obtain a single equation of motion governing the soil. For brevity, the Einstein index notation is used. The kinematic equation describes the relationship between the strains and displacements. The constitutive equation relates the stresses and the strains. The equilibrium equation (Newton's second law) relates the internal stresses to the external forces acting on the soil.

2.2.1 Kinematic equation

As a direct implication of the notion of a continuum, the deformation of the medium can be expressed in terms of the gradients of the displacement vector [2]. Within the linearized theory, the deformation can be described in the form of the strain ϵ, with components

$$\epsilon_{ij} = \frac{1}{2}(u_{i,j} + u_{j,i}) \tag{2.1}$$

In 3 dimensions, all strain components form a second order tensor. This tensor is symmetric with 6 independent strain components. The "," seen in Equation 2.1 denotes the derivative of the particular quantity with respect to the direction that follows it.

2.2.2 Constitutive equation

In general, the stiffness depends on the strain level. We assume small strains (see section 1.2) in soil, therefore the stiffness could be assumed to be constant and the material linear elastic. Furthermore, the material is assumed to be homogeneous, and isotropic meaning the properties are the same in all directions. Using Hooke's law, the normal stresses and normal strains can then be related as

$$\begin{bmatrix} \epsilon_{xx} \\ \epsilon_{yy} \\ \epsilon_{xy} \end{bmatrix} = \frac{1}{E} \begin{bmatrix} 1 & -\nu & -\nu \\ -\nu & 1 & -\nu \\ -\nu & -\nu & 1 \end{bmatrix} \begin{bmatrix} \sigma_{xx} \\ \sigma_{yy} \\ \sigma_{xy} \end{bmatrix} \tag{2.2}$$

Here, E is the Young's Modulus, ν is the Poisson's ratio, which is the ratio of the transverse strain to the longitudinal strain. For a linear elastic, isotropic material, the Poisson's ratio can range from -1.0 to 0.5 with the requirement of a positive Young's modulus, Shear

modulus and Bulk modulus [17]. A perfectly incompressible material(infinitely stiff) at small strains will have a poisson's ratio of 0.5. Generally for most materials, the poisson's ratio ranges between 0.0 and 0.5. E and ν are defined as

$$E = \frac{Stress}{Strain} = \frac{\sigma}{\epsilon} \tag{2.3}$$

$$\nu = \frac{Transversestrain}{Longitudinalstrain} = -\frac{\epsilon_{tr}}{\epsilon_{lo}} \tag{2.4}$$

The negative sign in Equation 2.4 implies that expansion in one direction will cause compression in the other two directions. Inverting Equation 2.2 gives the relation of the normal stress to the normal strain given by

$$\begin{bmatrix} \sigma_{xx} \\ \sigma_{yy} \\ \sigma_{xy} \end{bmatrix} = \begin{bmatrix} \lambda + 2\mu & \lambda & \lambda \\ \lambda & \lambda + 2\mu & \lambda \\ \lambda & \lambda & \lambda + 2\mu \end{bmatrix} \begin{bmatrix} \epsilon_{xx} \\ \epsilon_{yy} \\ \epsilon_{xy} \end{bmatrix} \tag{2.5}$$

where λ and μ are called Lame's constants, which are functions of Young's modulus and Poisson's ratio as -

$$\lambda = \frac{\nu E}{(1-2\nu)(1+\nu)} \tag{2.6}$$

$$\mu = \frac{E}{2(1+\nu)} \tag{2.7}$$

μ is referred to as the Shear modulus and is also denoted by G in geotechnical terms.

The shear stresses for a isotropic linear elastic medium can be related to the shear strain as follows -

$$\sigma_{ij} = \tau_{ij} = \mu\gamma_{ij} = 2\mu\epsilon_{ij} \tag{2.8}$$

where $i \neq j$. This implies -

$$\begin{bmatrix} \sigma_{xy} \\ \sigma_{yz} \\ \sigma_{xz} \end{bmatrix} = \begin{bmatrix} 2\mu & 0 & 0 \\ 0 & 2\mu & 0 \\ 0 & 0 & 2\mu \end{bmatrix} \begin{bmatrix} \epsilon_{xy} \\ \epsilon_{yz} \\ \epsilon_{xz} \end{bmatrix} \tag{2.9}$$

Combining the equations for the normal stresses and the shear stresses (Equation 2.5 and Equation 2.9), we get a general relation between the stresses and strains given by -

$$\sigma_{ij} = \lambda\epsilon_{kk}\delta_{ij} + 2\mu\epsilon_{ij} \tag{2.10}$$

where δ_{ij} is the Kronecker delta.

2.2.3 Equilibrium equation

For obtaining the equilibrium equation, we apply Newton's second law of motion for a control volume as shown in Figure 2.3

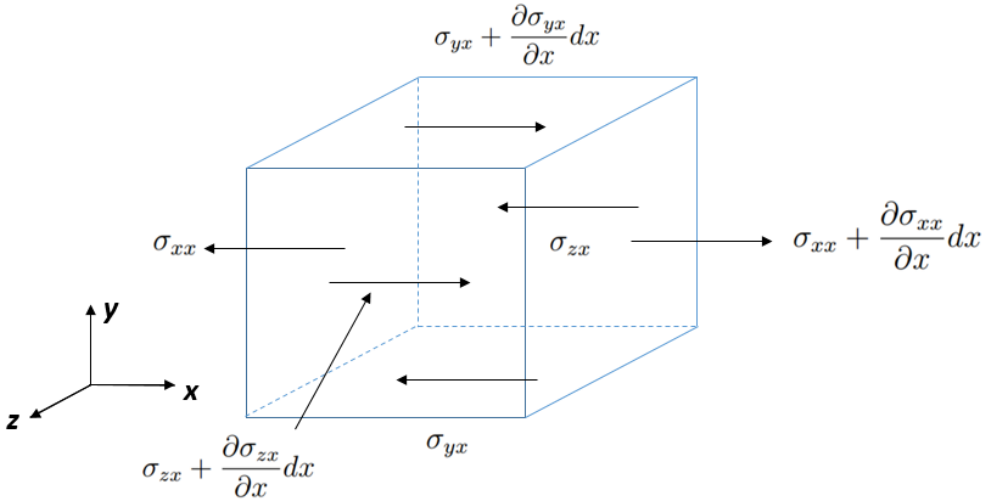

Figure 2.3: ***Control volume - Stresses in the x-direction***

Considering equilibrium in the x direction, with the inclusion of the inertia term, we obtain -

$$\rho \Delta x \Delta y \Delta z \frac{\partial^2 u}{\partial t^2} = \frac{\partial \sigma_{xx}}{\partial x} \Delta x \Delta y \Delta z + \frac{\partial \sigma_{yx}}{\partial x} \Delta x \Delta y \Delta z + \frac{\partial \sigma_{zx}}{\partial x} \Delta x \Delta y \Delta z \tag{2.11}$$

This can be reduced to

$$\rho \frac{\partial^2 u}{\partial t^2} = \frac{\partial \sigma_{xx}}{\partial x} + \frac{\partial \sigma_{yx}}{\partial x} + \frac{\partial \sigma_{zx}}{\partial x} \tag{2.12}$$

In Einstein notation, this can be written as -

$$\rho \frac{\partial^2 u_i}{\partial t^2} = \sigma_{ji,j} \tag{2.13}$$

Here i and j take the values from 1 to 3 since the equation is defined for a 3D solid.

2.2.4 Elastic equation of motion

By combining Equation 2.1 and Equation 2.10, we obtain

$$\sigma_{ij} = \lambda u_{k,k} + \mu(u_{i,j} + u_{j,i}) \tag{2.14}$$

This when substituted into Equation 2.13 gives

$$\rho \frac{\partial^2 u_i}{\partial t^2} = (\lambda + \mu) u_{j,ij} + \mu u_{i,jj} \tag{2.15}$$

In vector notation, this can be written as

$$\rho \partial_t^2 u = (\lambda + \mu) \nabla (\nabla . u) + \mu \nabla^2 u + f_{ex} \tag{2.16}$$

where f_{ex}, the external force acting on the solid is taken for the obtaining the final equation.

2.2.5 Dimensional equation of motion of the soil

'~' is used to indicate that the quantities are dimensional. This means that the quantities have an assigned unit. The dimensional equation of soil is hence given as

$$\rho_s \partial_t^2 \tilde{u} = (\lambda + \mu) \tilde{\nabla} (\tilde{\nabla} . \tilde{u}) + \mu \tilde{\nabla}^2 \tilde{u} \tag{2.17}$$

$\tilde{u}$ is the displacement vector, ρ_s is the density, λ and μ are the lame's constants. $\lambda = K_b - \frac{2}{3}\mu$ with K_b as the bulk modulus[3].

2.3 Making soil equation dimensionless

The Equation 2.17 is made dimensionless by using the waveguide depth H, time parameter T, resulting in

$$u_i = \frac{\tilde{u}_i}{H} \qquad x_i = \frac{\tilde{x}_i}{H} \qquad t = \frac{\tilde{t}}{T} \tag{2.18}$$

Furthermore, the dimensionless derivatives can be calculated as

$$\partial_{\tilde{t}} = \frac{1}{T}\partial_t \qquad \partial^2_{\tilde{t}} = \frac{1}{T^2}\partial^2_t \qquad \partial_{\tilde{x}_i} = \frac{1}{H}\partial_{x_i} \qquad \partial^2_{\tilde{x}_i} = \frac{1}{H}\partial^2_{x_i} \tag{2.19}$$

Substituting these quantities and their dimensionless derivatives in Equation 2.18 and Equation 2.19 into Equation 2.17, the dimensionless governing equation can be written as

$$\partial^2_t u = \frac{(\lambda + 2\mu)T^2}{\rho_s H^2}\nabla(\nabla \cdot u) - \frac{\mu T^2}{\rho_s H^2}\nabla \times \nabla \times u \tag{2.20}$$

This can be obtained using the identity

$$\nabla(\nabla \cdot u) - \nabla^2 u = \nabla \times (\nabla \times u) \tag{2.21}$$

To find an expression for the time scale T used for the normalization, we set the coefficient of the second term on RHS of Equation 2.20 to 1. Thus, we obtain -

$$T = \frac{H}{c_s} \tag{2.22}$$

where c_s is the shear wave speed. The shear wave speed c_s and the compressional wave speed c_p are given as

$$c_s = \sqrt{\frac{\mu}{\rho_s}} \qquad c_p = \sqrt{\frac{\lambda + 2\mu}{\rho_s}} \tag{2.23}$$

Equation 2.20 can then be written as

$$\partial^2_t u = \frac{c_p^2}{c_s^2}\nabla(\nabla \cdot u) - \nabla \times \nabla \times u = v^2\nabla(\nabla \cdot u) - \nabla \times \nabla \times u \tag{2.24}$$

where $v = \frac{c_p}{c_s}$ is the ratio of the velocities. The dimensionless stress-strain relation is given by

$$\begin{aligned} \sigma_{ij} &= \frac{\tilde{\sigma}_{ij}}{\mu} = \frac{\lambda}{\mu}\epsilon_{kk}\delta_{ij} + 2\epsilon_{ij} \\ &= \frac{(\lambda + 2\mu - 2\mu)\rho_s}{\mu\rho_s}\epsilon_{kk}\delta_{ij} + 2\epsilon_{ij} \\ &= (v^2 - 2)\epsilon_{kk}\delta_{ij} + 2\epsilon_{ij} \end{aligned} \tag{2.25}$$

2.4 Helmholtz decomposition for displacement of soil

We can use the Helmholtz decomposition [3] to decouple the elastic wave equations into a scalar potential ϕ and a vector potential ψ, hence separating the displacement into a rotation free part and a divergence free part. This can be represented as

$$\mathbf{u} = \nabla\phi + \nabla \times \boldsymbol{\psi} = \mathbf{u_p} + \mathbf{u_s} \tag{2.26}$$

where $\nabla \times \mathbf{u_p} = 0$ and $\nabla \cdot \mathbf{u_s} = 0$. When we consider a 2D plane, there is only one axis of rotation, perpendicular to the 2D plane. Hence, the vector field ψ will be a scalar field associated with the y-direction in this case. Substituting Equation 2.26 in the equation of motion given by Equation 2.24, we get -

$$\partial_t^2(\nabla\phi + \nabla \times \boldsymbol{\psi}) = v^2\nabla(\nabla \cdot (\nabla\phi + \nabla \times \boldsymbol{\psi})) - \nabla \times \nabla \times (\nabla\phi + \nabla \times \boldsymbol{\psi}) \tag{2.27}$$

This can be written as

$$\partial_t^2\phi + \nabla \times \partial_t^2\boldsymbol{\psi} = v^2\nabla\nabla^2\phi + \nabla \times \nabla^2\boldsymbol{\psi} \tag{2.28}$$

using the following vector identities

$$\begin{aligned} \nabla \cdot (\nabla \times \boldsymbol{\psi}) &= 0 \\ \nabla \cdot \nabla &= \nabla^2 \\ \nabla^2(\nabla\phi) &= \nabla(\nabla^2\phi) \\ \nabla^2(\nabla \times \boldsymbol{\psi}) &= \nabla \times (\nabla^2\boldsymbol{\psi}) \end{aligned} \tag{2.29}$$

To satisfy the Equation 2.28, the potentials must satisfy the following individual relations

$$\begin{aligned} \nabla(\partial_t^2\phi - v^2\nabla^2\phi) &= 0 \\ \nabla \times (\partial_t^2\psi - \nabla^2\psi) &= 0 \end{aligned} \tag{2.30}$$

In the steady state regime, the solutions to the above equations are assumed as

$$\begin{aligned} \phi(x, z, t) &= \phi_1(x, z)e^{i\omega t} \\ \psi(x, z, t) &= \psi_1(x, z)e^{i\omega t} \end{aligned} \tag{2.31}$$

Here, ω is the dimensionless angular frequency is given as

$$\omega = \tilde{\omega}T \tag{2.32}$$

Substituting the assumed solutions into Equation 2.30 gives

$$\begin{aligned} \nabla^2\phi + \frac{\omega^2}{v^2}\phi &= \nabla^2\phi + k_p^2\phi = 0 \\ \nabla^2\psi + \omega^2\psi &= \nabla^2\psi + k_s^2\psi = 0 \end{aligned} \tag{2.33}$$

where k_p is the dimensionless wavenumber associated with the pressure wave and k_s is the dimensionless wavenumber associated with the shear wave. We employ the method of separation of variables to obtain the solutions to the two equations. Hence, defining the space dependent $\boldsymbol{\phi_1} = X_pZ_p$ and $\boldsymbol{\psi_1} = X_sZ_s$, using the definition of the Laplace operator and substituting them into the above equations gives

$$\partial_x^2X_pZ_p + \partial_z^2X_pZ_p + k_pX_pZ_p = 0 \tag{2.34}$$

$$\partial_x^2X_sZ_s + \partial_z^2X_sZ_s + k_sX_sZ_s = 0 \tag{2.35}$$

To further simplify the equations, we introduce a separation constants k_{px} and k_{sx}. In theory these represent the longitudinal and shear wavenumbers propagating in the x-direction. Taking Equation 2.34, we now obtain two independent differential equations

$$\begin{aligned} d_x^2X_p + k_{px}^2X_p &= 0 \\ d_z^2Z_p + (k_p^2 - k_{px}^2)Z_p &= 0 \end{aligned} \tag{2.36}$$

where $(k_p^2 - k_{px}^2) = k_{pz}^2$. This is done for Equation 2.35 as well. The general solution to the ODEs is obtained gives the following potential functions

$$\begin{aligned}\phi_1(x,z) &= (C_{p1}e^{-ik_{px}x} + C_{p2}e^{ik_{px}x})(B_{p1}e^{-ik_{pz}(z-1)} + B_{p2}e^{ik_{pz}z}) \\ \psi_1(x,z) &= (C_{s1}e^{-ik_{sx}x} + C_{s2}e^{ik_{sx}x})(B_{s1}e^{-ik_{sz}(z-1)} + B_{s2}e^{ik_{sz}z})\end{aligned} \tag{2.37}$$

To obtain the unknown coefficients, we establish an eigen value problem using the homogeneous boundary conditions described in the next section. An assumption is made here given as $k_{px} = k_{sx} = k_x$, where k_x is referred to as the horizontal wavenumbers. This assumption is made so as to obtain a system of x independent algebraic equations, which can then be solved to obtain the characteristic wavenumbers. The vertical wavenumbers corresponding to the P and S are then given as

$$\begin{aligned}k_{pz} &= \sqrt{k_p^2 - k_x^2} \\ k_{sz} &= \sqrt{k_s^2 - k_x^2}\end{aligned} \tag{2.38}$$

2.5 Boundary conditions for the soil

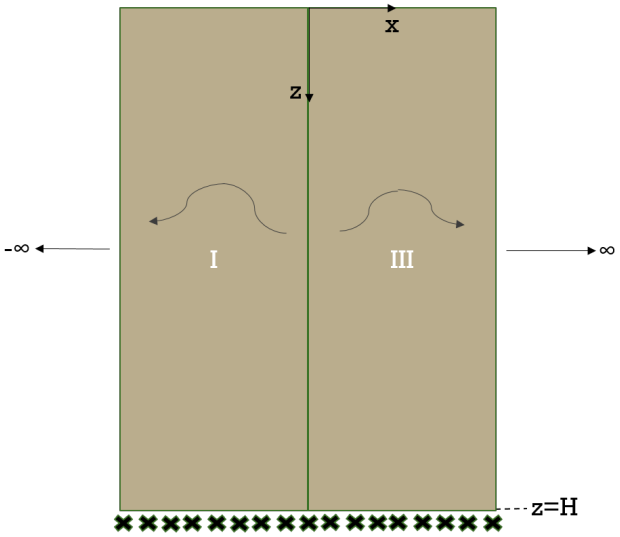

Figure 2.4: ***Elastic waveguides***

Figure 2.4 shows the two domains of soil defined as domain 1 and 3, which represent the soil domain to the left and right of the origin respectively in the waveguide. The general homogeneous boundary conditions used are

$$\begin{aligned} z = 0 \quad & \sigma_{zz}^{(1,3)}(x, z=0) = 0 \quad && \sigma_{xz}^{(1,3)}(x, z=0) = 0 \\ z = H \quad & u_x^{(1,3)}(x, z=H) = 0 \quad && u_z^{(1,3)}(x, z=H) = 0 \end{aligned} \tag{2.39}$$

The superscripts for the displacements and stresses in Equation 2.39 indicate the domain number. Somerfield's radiation condition is used far away from the origin for both the domains, along the horizontal direction. It states that *'Energy radiated from a sources must scatter at infinity, no energy must be radiated from infinity'*.

2.6 Obtaining the stress and displacement solutions

The displacements and stresses are defined as

$$\begin{aligned} u_x &= \partial_x\phi - \partial_z\psi \\ u_z &= \partial_x\psi + \partial_z\phi \\ \sigma_{xx} &= (v^2-2)(\partial_x^2\phi + \partial_z^2\phi) + 2\partial_x^2\phi - 2\partial_x\partial_z\psi \\ \sigma_{zz} &= (v^2-2)(\partial_x^2\phi + \partial_z^2\phi) + 2\partial_x^2\phi + 2\partial_x\partial_z\psi \\ \sigma_{xz} &= 2\partial_x\partial_z\phi + \partial_x^2\psi - \partial_z^2\psi \end{aligned} \tag{2.40}$$

Based on the boundary conditions, a coefficient matrix is derived whose determinant gives the characteristic dispersion equation, from which the wavenumbers were derived. The obtained coefficient matrix is the same for both the waveguides.

The potential functions as a summation of modes for the domains are given as

$$\begin{aligned} \phi^{(1)}(x,z) &= \sum_{n=1}^{\infty} C_n^{(1)} e^{+ik_{x;n}x}[B_{p1}^{(1)} e^{+ik_{p,z;n}(z-1)} + B_{p2}^{(1)} e^{-ik_{p,z;n}z}] \\ \psi^{(1)}(x,z) &= \sum_{n=1}^{\infty} C_n^{(1)} e^{+ik_{x;n}x}[B_{s1}^{(1)} e^{+ik_{p,z;n}(z-1)} + B_{s2}^{(1)} e^{-ik_{p,z;n}z}] \\ \phi^{(3)}(x,z) &= \sum_{n=1}^{\infty} C_n^{(3)} e^{-ik_{x;n}x}[B_{p1}^{(3)} e^{+ik_{p,z;n}(z-1)} + B_{p2}^{(3)} e^{-ik_{p,z;n}z}] \\ \psi^{(3)}(x,z) &= \sum_{n=1}^{\infty} C_n^{(3)} e^{-ik_{x;n}x}[B_{s1}^{(3)} e^{+ik_{p,z;n}(z-1)} + B_{s2}^{(3)} e^{-ik_{p,z;n}z}] \end{aligned} \tag{2.41}$$

Substituting Equation 2.41 in Equation 2.40, the stress and displacement solution modes can then be given as

$$\begin{aligned} u_{x;n}^{(k)} &= C_n^{(k)} X_n^{(k)} Z_{x;n}^{(k)} \\ u_{z;n}^{(k)} &= C_n^{(k)} X_n^{(k)} Z_{z;n}^{(k)} \\ \sigma_{xx;n}^{(k)} &= C_n^{(k)} X_n^{(k)} Z_{xx;n}^{(k)} \\ \sigma_{xz;n}^{(k)} &= C_n^{(k)} X_n^{(k)} Z_{xz;n}^{(k)} \\ \sigma_{zz;n}^{(k)} &= C_n^{(k)} X_n^{(k)} Z_{zz;n}^{(k)} \qquad\qquad k = 1,3 \end{aligned} \tag{2.42}$$

where $X_n^{(1)} = e^{ik_{x;n}x}$, $X_n^{(3)} = e^{-ik_{x;n}x}$ and the Z eigenmodes are given as

$$\begin{aligned} Z_{x;n} &= ia_x k_x Z_{p;n} - \partial_z Z_{s;n} \\ Z_{z;n} &= ia_x k_x Z_{s;n} + \partial_z Z_{p;n} \\ Z_{xx;n} &= -k_{x;n}^2 v^2 Z_{p;n} + (v^2-2)\partial_z^2 Z_{p;n} - 2ia_x k_{x;n}\partial_z Z_{s;n} \\ Z_{zz;n} &= -k_{x;n}^2 v^2 Z_{p;n} - (v^2-2)\partial_z^2 Z_{p;n} v^2 + 2ia_x k_{x;n}\partial_z Z_{s;n} \\ Z_{xz;n} &= 2ia_x\partial_z Z_{p;n} - \partial_z^2 Z_{s;n} - k_{x;n}^2 Z_{s;n} \end{aligned} \tag{2.43}$$

with $a_x = 1$ for a wave moving towards $-\infty$ and $a_x = -1$ for a wave moving towards ∞.

2.6.1 Wavenumbers

The horizontal modal wavenumbers of the soil are the roots of the dispersion equation. The displacements and stress potentials are substituted into the boundary conditions. . Since

the system of equations is homogeneous, it will have non-trivial solutions if an only if the determinant is zero [11]. Combining these four equations, a coefficient matrix is obtained whose determinant gives the dispersion equation.

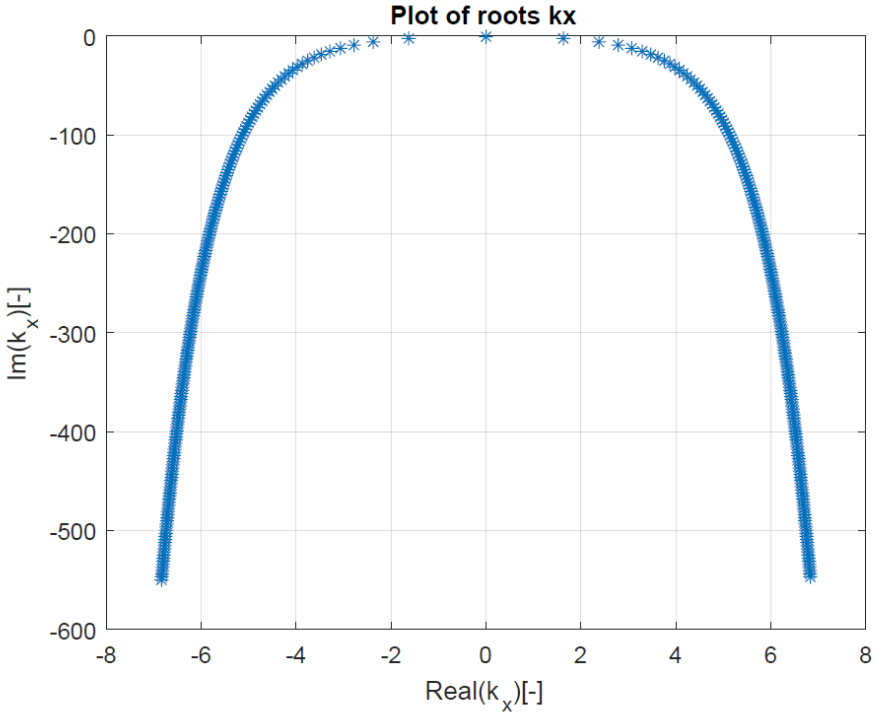

Figure 2.5: ***Normalized Roots(modal horizontal wavenumbers) of the dispersion equation at normalized frequency ω = 1. One real valued root and 400 complex valued roots are shown(while there are infinitely many complex valued roots)***

To comply with the radiation condition, only wavenumbers are chosen such that $Im(k_{x;n}^{(1)}, k_{x;m}^{(3)}) \leq 0$ or the real-valued roots which shift to the lower half-plane when some damping is introduced [11]. Figure 2.5 shows a plot of the normalized horizontal wavenumbers of the soil, for the set of properties given in Table 2.1. In this case, one real-valued root is obtained, satisfying this condition. The real roots correspond to the modes that propagate in space along the x-direction while the complex roots are exponentially decaying modes also referred to as evanescent modes. The number of complex roots are infinite, however we show the roots only in the finite domain. The number of real roots is finite [11].

Table 2.1: ***Soil properties***

Material property	**Value**	**Units**
Shear Modulus(G)	250e5	$\mathrm{N/m^2}$
Mass Density (ρ_s)	1700	$\mathrm{kg/m^3}$
Poisson's ratio(ν_s)	0.4	-

The wavenumbers along the z-direction are calculated using Equation 2.38.

2.6.2 Eigenmodes of the soil

The eigenmodes($Z_{x;n}, Z_{z;n}, Z_{xx;n}, Z_{zz;n}$ and $Z_{xz;n}$) are derived for each wavenumber.These are obtained by solving for the unknown coefficients - B_{p1}, B_{s1}, B_{p2} and B_{s2} for each wavenumber. Since we currently employ homogeneous boundary conditions for the soil hence the value for these coefficients cannot be derived directly. By selecting any three of four equations and solving them, we can obtain three coefficients in terms of the fourth, which then form the eigen vectors corresponding to each wavenumber.

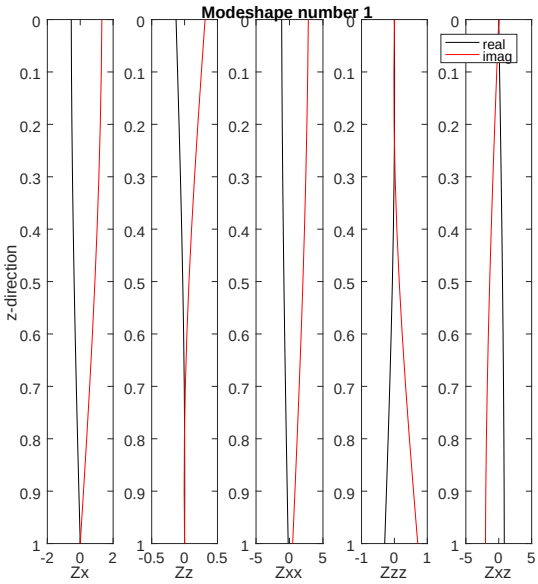

Figure 2.6: ***Eigenmodes - Mode number 1 - Domain 1***

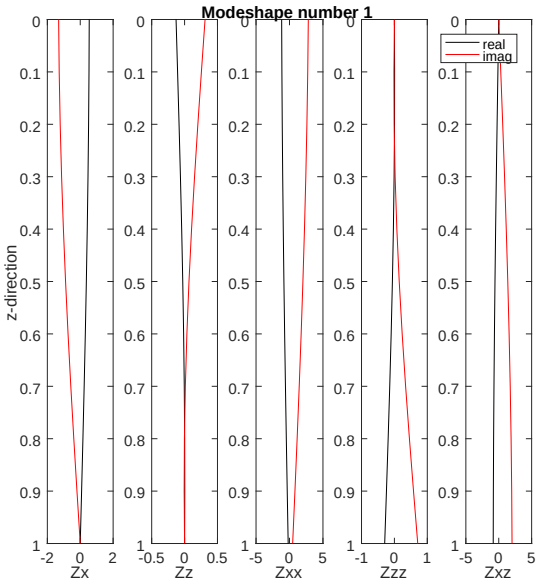

Figure 2.7: ***Eigenmodes - Mode number 1 - Domain 3***

Figure 2.6 shows the eigen modes for Domain 1 and Figure 2.7 shows the eigen modes for Domain 3 for Mode number 1. The $Z_{z;n}, Z_{xx;n}$ and $Z_{zz;n}$ eigenmodes behave the same way for both the domains, whereas $Z_{x;n}$ and $Z_{xz;n}$ behave in the opposite way in both domains.

Chapter 3

Hybrid solution for plate-soil interaction considering a single soil domain

*The proposed hybrid plane strain soil-pile interaction model is a combination of the pile and soil system, where the pile is modelled using Finite element method as Kirchhoff plate elements, which are 2D plane strain Euler-Bernoulli beam elements with modified mass and stiffness matrices to accommodate plate effects due to Poisson's effect. and the soil is modelled as an isotropic elastic waveguide (discussed in Chapter 1). Hence, the beam is modelled using "**Plate elements**". To combine both entities into a single model, the interface between the beam and the soil is discretized using distinct points(referred to as locations to differentiate them from nodes, which are distinct points on the plate between interconnected elements). The method involves obtaining an independent frequency dependent stiffness matrix of the soil waveguide evaluated based on displacements at the various locations on the interface due to stresses acting on each individual locations. This is then coupled with the plate mass and stiffness matrices together, to obtain the plate-soil dynamic stiffness matrix. The current chapter considers the pile-soil interaction method considering domain 3.*

3.1 Discretizing the Soil domain

To obtain the stiffness matrix of soil at the interface between the plate and the soil, we translate the nodal contact forces (shear and normal) between the beam and the soil, on to the beam as shown in Figure 3.1. The nodal contact forces on the plate are imposed as equivalent stresses on the soil. To distinguish the discretization of the soil interface from the plate, the elements in beam will be equivalently called segments or cells on the soil interface. Similarly the nodes on the plate will be referred to as locations on the soil interface.

A triangular distribution of the stress is assumed for both the shear as well as the normal stresses. This distribution will be referred to as $N(z)$. The imposed contact stress is different at the end locations and the intermediate locations. This can be seen in Figure 3.2. e refers to the segment length, which varies depending on the number of segments along the interface. The horizontal dimension shows the amplitude of the stress imposed.

An additional parameter $\tilde{R}$ is introduced, which refers to the radius of the plate or half the width of the plate. This is also made dimensionless to make it consistent with the soil quantities.

$$R = \frac{\tilde{R}}{H} \tag{3.1}$$

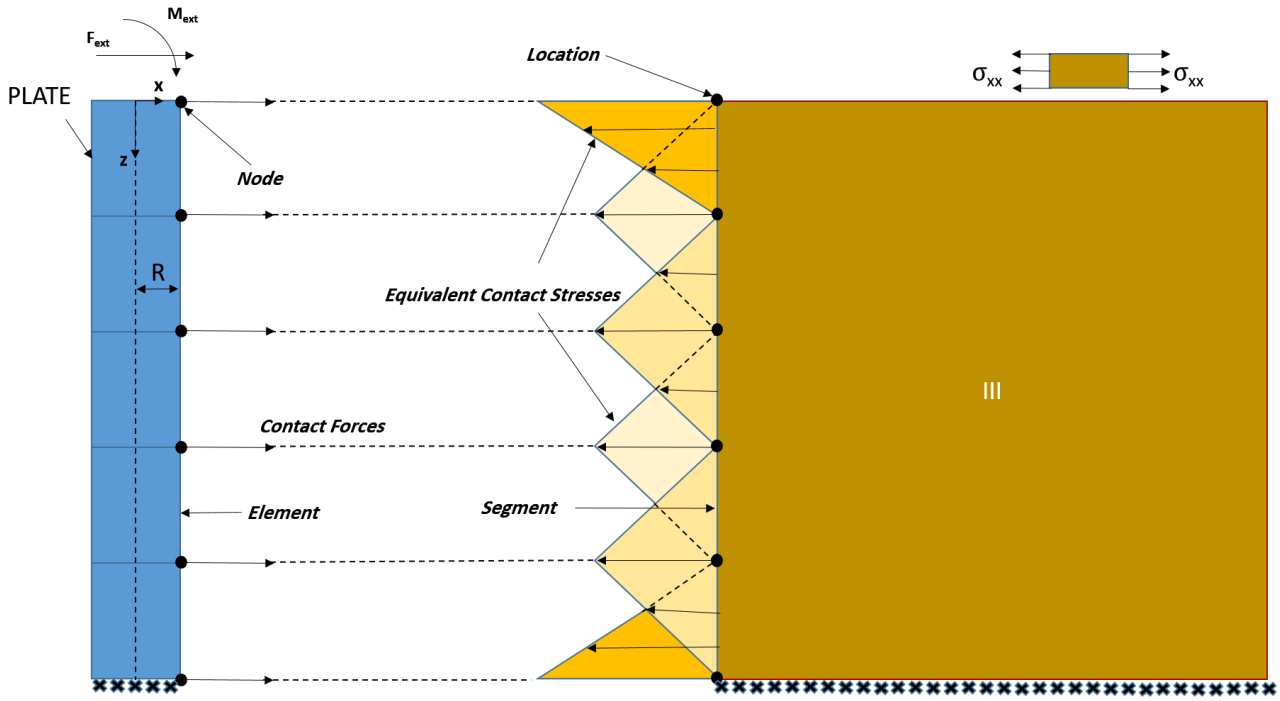

Figure 3.1: *Translation of contact forces from beam to the soil*

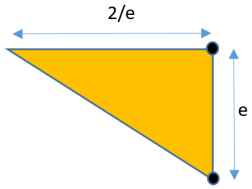

(a) *Imposed top stress*

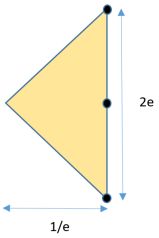

(b) *Imposed intermediate stress*

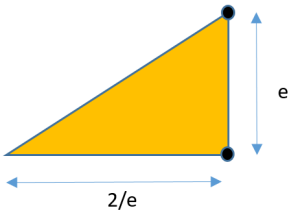

(c) *Imposed bottom stress*

Figure 3.2

3.1.1 Deriving the stresses and displacements

The procedure for obtaining the stresses and displacements in the soil, due to the applied normal or shear distributed stress is given as follows

1. We use two sets of interface conditions to obtain the terms of the stiffness matrix. The first set of interface conditions are -

$$\begin{aligned}\sigma_{xx;1}^{(3;m)}(x=R,z) &= \sum_{n=1}^{\infty} C_{1;n}^{(3;m)} X_n^{(3)}(R) Z_{xx;n}^{(3)}(z) = F(z,z_m)\\ \sigma_{xz;1}^{(3;m)}(x=R,z) &= \sum_{n=1}^{\infty} C_{1;n}^{(3;m)} X_n^{(3)}(R) Z_{xz;n}^{(3)}(z) = 0\end{aligned} \tag{3.2}$$

The second set of interface conditions are -

$$\begin{aligned}\sigma_{xz;2}^{(3;m)}(x=R,z) &= \sum_{n=1}^{\infty} C_{2;n}^{(3;m)} X_n^{(3)}(R) Z_{xz;n}^{(3)}(z) = F(z,z_m) \\ \sigma_{xx;2}^{(3;m)}(x=R,z) &= \sum_{n=1}^{\infty} C_{2;n}^{(3;m)} X_n^{(3)}(R) Z_{xx;n}^{(3)}(z) = 0\end{aligned} \tag{3.3}$$

where

$$\begin{aligned}F(z,z_m) &= N(z-z_m) \\ \int_0^1 F(z,z_m)dz &= 1\end{aligned} \tag{3.4}$$

Equation 3.2 shows the stress boundary conditions considering non-zero normal stresses imposed on the interface, and Equation 3.3 shows the stress boundary conditions considering non-zero shear stresses imposed. It should be noted that each set of boundary conditions is separately solved to obtain the stresses and displacements. Each set of displacements is used to fill the entries of the stiffness matrix, which will be obtained later. $F(z,z_m)$ is the triangular distribution of the contact stress at the location $z=z_m$, which can be observed in Figure 3.1 and Figure 3.2 and was explained earlier in the chapter. z_m refers to the m^{th} location on the plate-soil interface. For the stress and displacement fields, the first part of the superscript refers to the soil domain.

When using the second set of boundary conditions, it should be noted that at the top location($z=0$), there is an incompatibility with respect to the shear stress.The shear stress imposed at the mudline ($z=0$) is zero (from the boundary conditions at $z=0$ used to obtain the Z eigen modes, refer section 1.5), however imposing a non-zero value of shear force is imposed at the top. This will be later shown. Although the incompatibility does exist, it does not seem to have any significant effect for the current study with the single domain of soil.

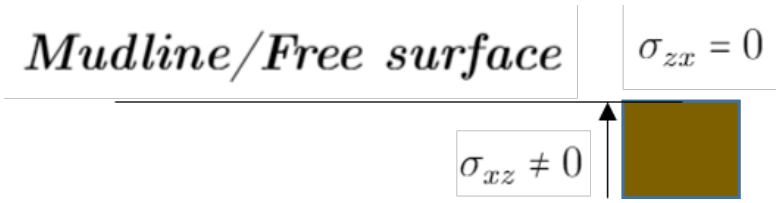

Figure 3.3: ***Shear stress incompatibility at the top location***

2. We multiply each set of the above conditions with a particular eigen function and integrate over z to obtain a truncated set of algebraic equations independent of z [11].

$$\begin{aligned}\int_0^1 \sigma_{xx;1}^{(3;m)}(x=R,z)Z_{x;q}(z)dz &= \int_0^1 F(z,z_m)Z_{x;q}(z)dz \\ \int_0^1 \sigma_{xz;1}^{(3;m)}(x=R,z)Z_{z;q}(z)dz &= 0\end{aligned} \tag{3.5}$$

$$\begin{aligned}\int_0^1 \sigma_{xz;2}^{(3;m)}(x=R,z)Z_{z;q}(z)dz &= \int_0^1 F(z,z_m)Z_{z;q}(z)dz \\ \int_0^1 \sigma_{xx;2}^{(3;m)}(x=R,z)Z_{x;q}(z)dz &= 0\end{aligned} \tag{3.6}$$

3. These individual set of linear equations are used to solve for the unknown coefficients $C_{i;n}$ where $i=[1,2]$ for the two sets of interface conditions used. Steps 4 and 5 are shown for the first set of boundary conditions given in Equation 3.5. These were followed for the second set (Equation 3.6) as well.

4. For every stress $F(z, z_m)$, with Equation 3.5, we obtain a $q \times n$ matrix of coefficients $C_{i;n}$ on the left side and a column vector of dimensions $q \times 1$ in the right side. This can be represented in matrix form as

$$\begin{bmatrix} A_{11} & \cdots & \cdots & \cdots & \cdots & A_{1n} \\ \vdots & \ddots & & & & \vdots \\ A_{q1} & & \ddots & & & A_{qn} \\ B_{11} & & & \ddots & & B_{1n} \\ \vdots & & & & \ddots & \vdots \\ B_{q1} & \cdots & \cdots & \cdots & \cdots & B_{qn} \end{bmatrix}_{2q\times n} \begin{bmatrix} C_{1;1}^{(m)} \\ \vdots \\ C_{1;n}^{(m)} \end{bmatrix}_{n\times 1} = \begin{bmatrix} P_{1;1}^{(m)} \\ \vdots \\ P_{1;q}^{(m)} \\ 0 \\ \vdots \\ 0 \end{bmatrix}_{2q\times 1} \tag{3.7}$$

where

$$\begin{aligned} A_{qn} &= X_n^{(3)}(R) \int_0^1 Z_{xx;n}^{(3)}(z) Z_{x;q}^{(3)}(z).dz \\ B_{qn} &= X_n(R) \int_0^1 Z_{xz;n}^{(3)}(z) Z_{z;q}^{(3)}(z) dz \\ P_{1;q}^{(3;m)} &= \int_0^1 F(z, z_m) Z_{x;q}^{(3)}(z).dz \end{aligned}$$

This can be represented as $\mathbf{DC_1 = P_1}$, where

$$\mathbf{D} = \begin{bmatrix} A_{11} & \cdots & \cdots & \cdots & \cdots & A_{1n} \\ \vdots & \ddots & & & & \vdots \\ A_{q1} & & \ddots & & & A_{qn} \\ B_{11} & & & \ddots & & B_{1n} \\ \vdots & & & & \ddots & \vdots \\ B_{q1} & \cdots & \cdots & \cdots & \cdots & B_{qn} \end{bmatrix}, \quad \mathbf{C_1^{(3;m)}} = \begin{bmatrix} C_{1;1}^{(3;m)} \\ \vdots \\ C_{1;n}^{(3;m)} \end{bmatrix}, \quad \mathbf{P^{(m)}} = \begin{bmatrix} P_{1;1}^{(3;m)} \\ \vdots \\ P_{1;q}^{(3;m)} \\ 0 \\ \vdots \\ 0 \end{bmatrix}$$

Here **D** is a $2q \times n$ matrix and **P** is a $2q \times 1$ matrix.

5. We then obtain the coefficients $C_{1;n}$ using the Moore - Penrose pseudoinverse (see Appendix B for more detail). The Moore-Penrose pseudoinverse is used to find the best fit(least squares) solution to a set of linear equations which lack a unique solution(overdetermined system).

$$\mathbf{C_i^{(3;m)}} = \mathbf{D^{-1}P_i^{(3;m)}} \tag{3.8}$$

6. The displacement and stress fields for both set of boundary conditions can then be obtained as

$$\begin{aligned} \sigma_{xx;1}^{(3;m)} &= \sum_{n=1}^{\infty} C_{1;n}^{(3;m)} X_n^{(3)}(R) Z_{xx;n}^{(3)}(z) \\ u_{x;1}^{(3;m)} &= \sum_{n=1}^{\infty} C_{1;n}^{(3;m)} X_n^{(3)}(R) Z_{x;n}^{(3)}(z) \\ u_{z;1}^{(3;m)} &= \sum_{n=1}^{\infty} C_{1;n}^{(3;m)} X_n^{(3)}(R) Z_{z;n}^{(3)}(z) \\ \sigma_{xz;2}^{(3;m)} &= \sum_{n=1}^{\infty} C_{2;n}^{(3;m)} X_n^{(3)}(R) Z_{xz;n}^{(3)}(z) \\ u_{x;2}^{(3;m)} &= \sum_{n=1}^{\infty} C_{2;n}^{(3;m)} X_n^{(3)}(R) Z_{x;n}^{(3)}(z) \\ u_{z;2}^{(3;m)} &= \sum_{n=1}^{\infty} C_{2;n}^{(3;m)} X_n^{(3)}(R) Z_{z;n}^{(3)}(z) \end{aligned} \tag{3.9}$$

3.2 Number of segments vs number of soil modes

To obtain an accurate stiffness matrix of the soil at the interface, the obtained displacements $u_{x;i}^{(m)}$,$u_{z;i}^{(m)}$, must be converged, indicating that they remain constant with increasing number of modes considered. For accuracy, the displacement fields should be non-oscillatory in nature. However, since we currently impose stresses, we begin with discretizing the interface and checking to obtain smooth stress profiles. These are compared with the imposed stress distributions, which are the triangular stresses. An extensive study is performed based on convergence of stresses and displacements varying the number of modes and the number of segments for two cases, stress imposed at the top($z = 0$) and stress imposed at an intermediate location. The location at the tip($z = H$) is not considered since that boundary is fixed, hence need not be considered when evaluating the stiffness matrix. The analysis is performed using horizontal wavenumbers obtained for normalized frequency $\omega = 1$. Up to 400 wavenumbers(modes) and 100 segments were considered . Stress and displacement convergence plots were made considering a variation of the number of soil modes for a given segment length.

3.2.1 Convergence Studies - displacement and stress profiles

The plate-soil interface was discretized in segments starting from 10 up to 100 segments. Convergence plots for stress and displacement were used to identify the minimum number of modes to be considered for each segment length.Errors in the stresses were plotted against the stress distribution imposed to get an idea of how fast the stress and displacement fields converge. Convergence in displacement along with their non-oscillatory nature was used to obtain the ideal number of soil modes to be considered.

Normal Stress (σ_{xx}) imposed

Figure 3.4 and Figure 3.5 show the applied and obtained normal stress distributions for the stress imposed on the first and third location respectively. Figure 3.6 and Figure 3.7 show the plots of the stress profile across the depth of the soil, for a normal stress imposed at the top and intermediate locations respectively. As the number of soil modes considered are increased, the profile becomes smoother. Similar plots have been made considering 10, 20,30,50 and 100 elements across the domain. These can be found in Appendix D.

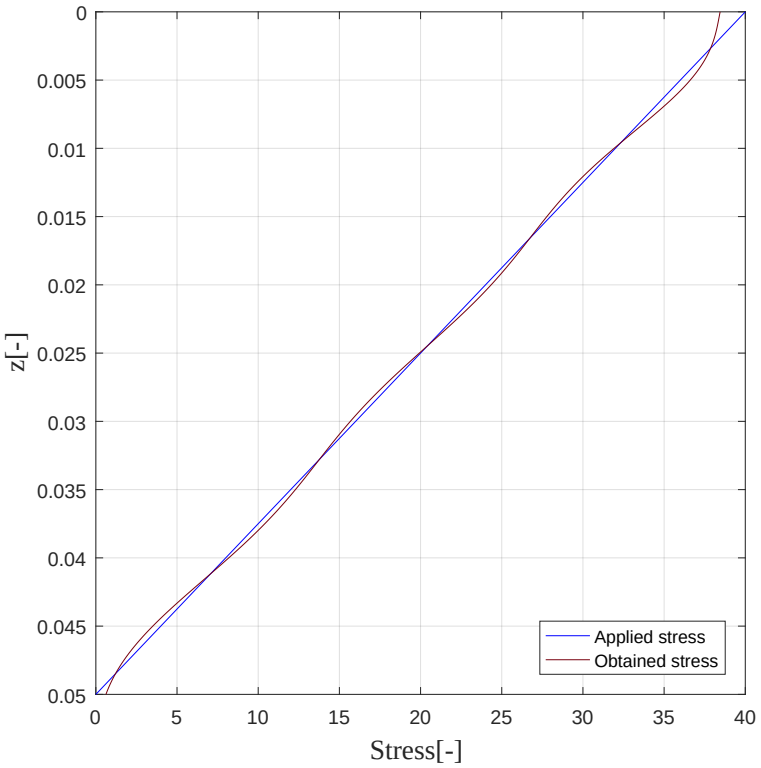

Figure 3.4: ***20 segments and 200 modes - soil-plate interface - Comparing imposed and obtained stress at the top location***

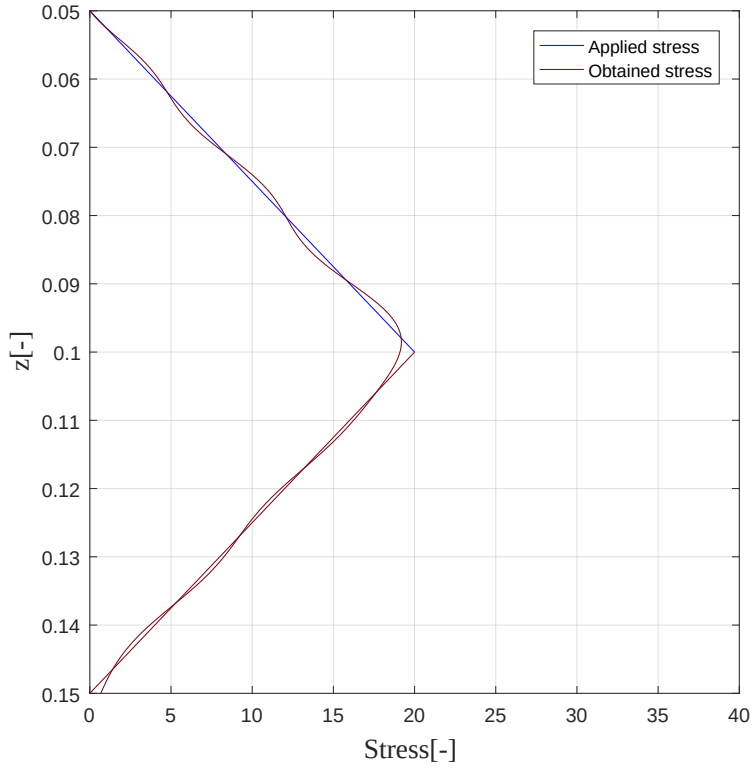

Figure 3.5: ***20 segments and 200 modes - soil-plate interface - Comparing imposed and obtained normal stress at the intermediate location***

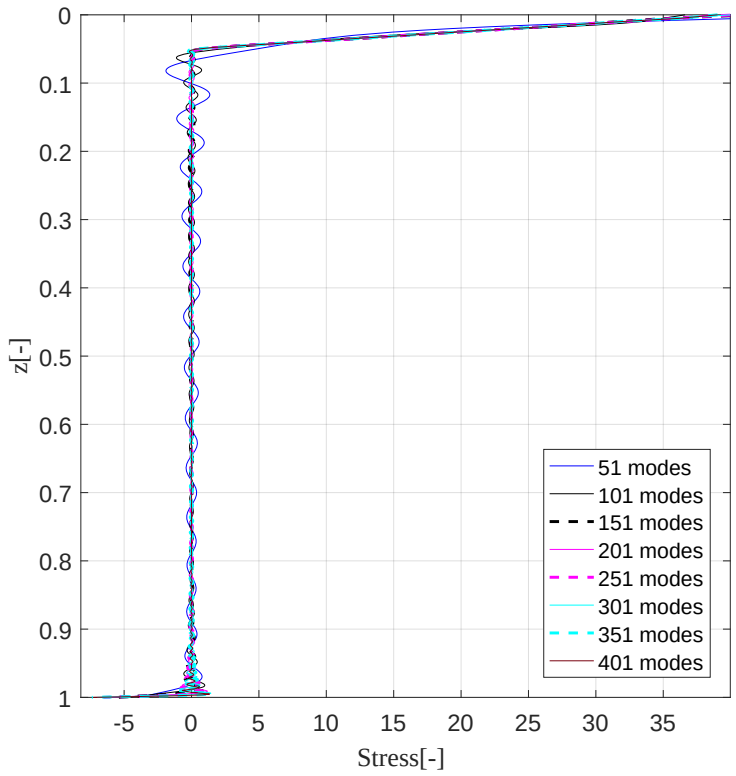

Figure 3.6: ***20 segments - Stress profile σ_{xx} for stress imposed at top location-Variation considering number of soil modes***

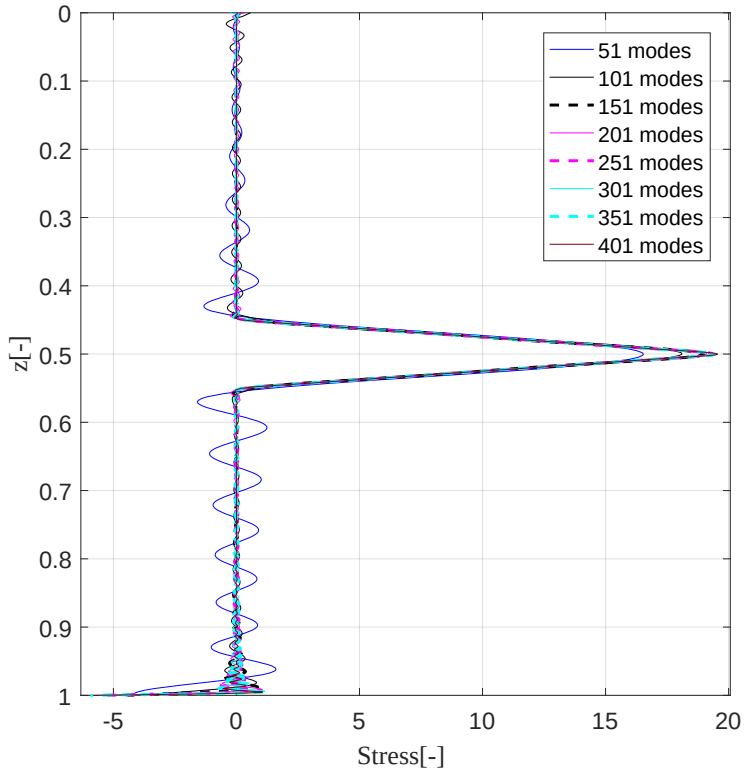

Figure 3.7: ***20 segments - Stress profile σ_{xx} for stress imposed at intermediate location(z=0.5) - Variation considering number of soil modes***

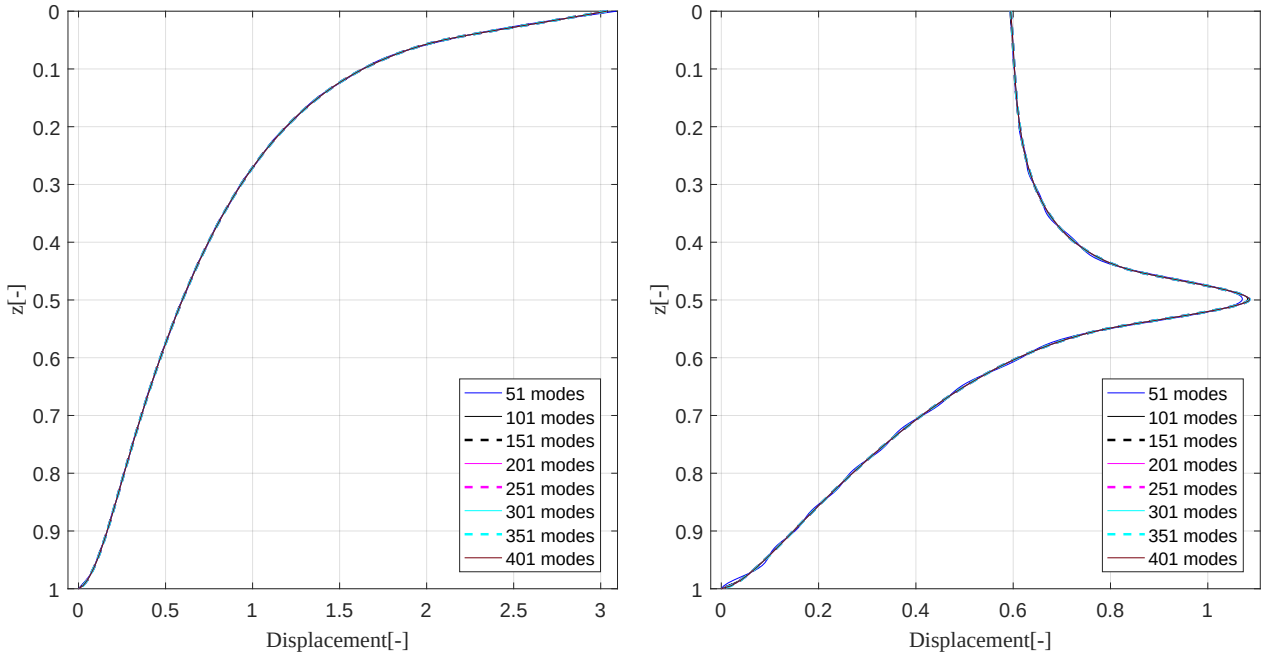

Figure 3.8: ***(Left) 20 segments - Displacement u_x for stress imposed at top location-Variation considering number of soil modes,(Right) 20 segments - Displacement u_x for stress imposed at intermediate location(z=0.5) - Variation considering number of soil modes***

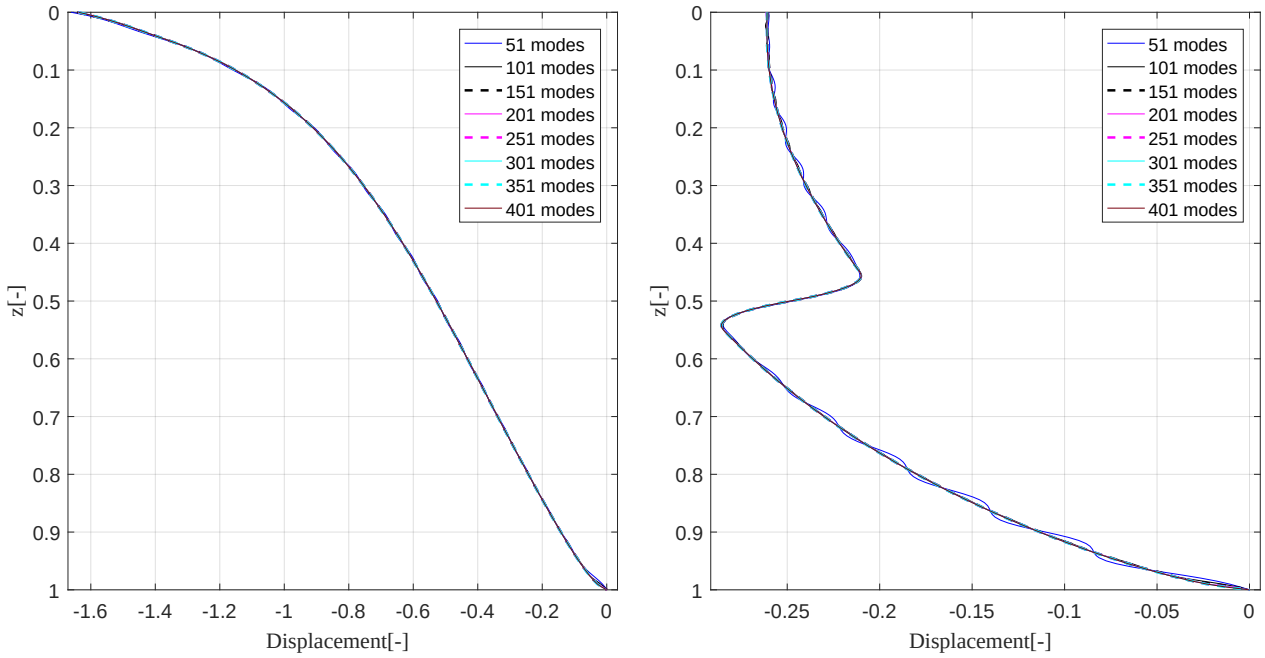

Figure 3.9: ***(Left) 20 segments - Displacement u_z for stress imposed at top location-Variation considering number of soil modes,(Right) 20 segments - Displacement u_z for stress imposed at intermediate location($z = 0.5$) - Variation considering number of soil modes***

Figure 3.8 shows the u_x displacement profile for a σ_{xx} stress acting at the top location(left) and intermediate location (right) with increasing number of modes considered. In this case the domain 3 boundary is discretized with 20 segments. As the number of modes are increased, a smoother profile is obtained. Convergence plots for 10, 30, 50 and 100 segments

can be found in Appendix D.

Figure 3.9 shows the u_z displacement profile for a σ_{xx} stress acting at the top location(Left) and intermediate location (right) with increasing number of modes considered. It can be observed that the peak value of the displacement u_z is close to 50% that of the u_x. This is quite significant, considering the Poisson's ratio of 0.4.

Error analysis for the stress field

Figure 3.12 shows the relative error in the stress at the top and intermediate location calculated as follows

$$\epsilon_{\sigma_{xx}} = \frac{1}{p-1}\sum_{r=1}^{p-1}\frac{|\sigma_{xx;o}(z=z_r) - \sigma_{xx;i}(z=z_r)|}{|\sigma_{xx;i}(z=z_r)|} \tag{3.10}$$

where $\sigma_{xx;o}(z=z_r)$ is the obtained value of the stress and $\sigma_{xx;i}(z=z_r)$ is the imposed value of the stress at $z=z_r$. p is the total number of locations across the interface.

We can observe that for the intermediate location, considering more modes reduces the error. Furthermore, as the number of segments increase, the length of each segment reduces, hence higher modes (smaller wavelengths) are required. Considering 400 soil modes, convergence in stresses is not reached for 50 and 100 segments. More modes should be considered. For the case of the stress imposed at an intermediate location, we observe that error increases for 50 and 100 segments beyond considering 250 soil modes. This is not what is expected and is caused, due to highly ill conditioned matrices when calculating the modal coefficients. Tikhonov regularization [4] and truncated singular value decompostion (Moore-Penrose pseudo inverse) can be used for rank deficient systems. Also, for the stress applied to the top location, the magnitude of the stress is twice that of intermediate stresses and this is distributed over half the length, higher modes are required for convergence.

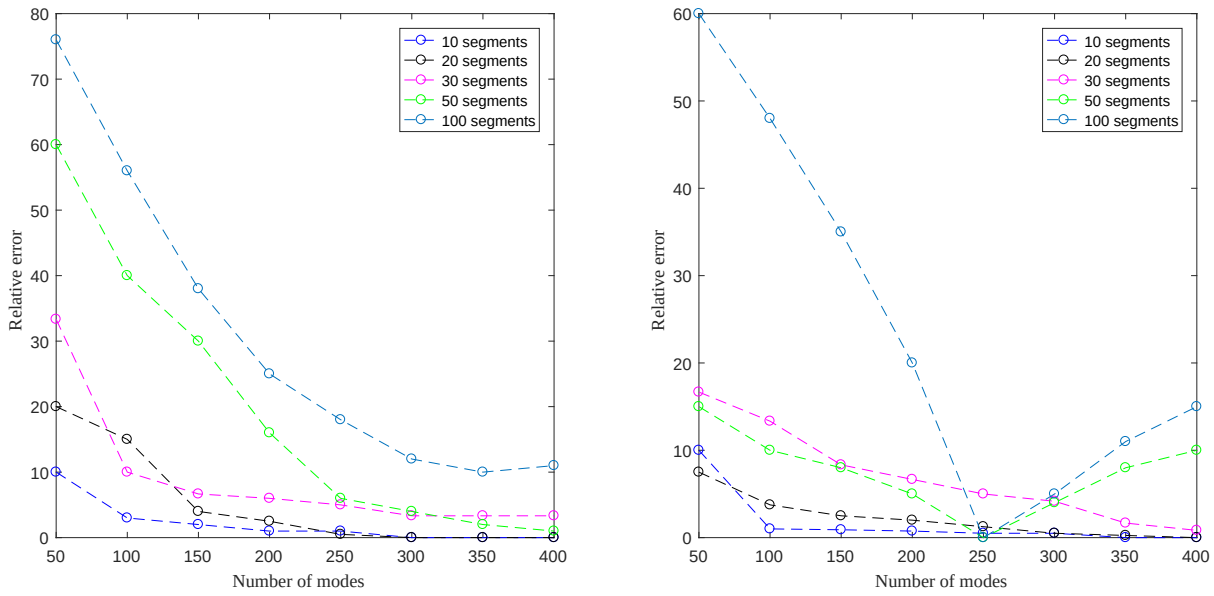

Figure 3.10: ***Error analysis for stresses*** σ_{xx} ***at an (Left) intermediate location(***$z = 0.5$***) and (Right) top location (***$z = 0$***)***

Convergence of displacements

The relative change in displacements with increasing soil modes is calculated using the following formula

$$\epsilon_{u_{x/z}} = \frac{1}{p-1}\sum_{r=1}^{p-1}\frac{\left|u_{x/z;(n=q)}(z=z_r) - u_{x/z;(n=q-1)}(z=z_r)\right|}{\left|u_{x/z;(n=q-1)}(z=z_r)\right|} \tag{3.11}$$

where $q = [50; 100; 150; 200; 250; 300; 350; 400]$ is the number of soil modes that are considered. It should be noted that the value of the number of modes refers to the number of complex wavenumbers. It should be noted that an additional real wavenumber is also considered.

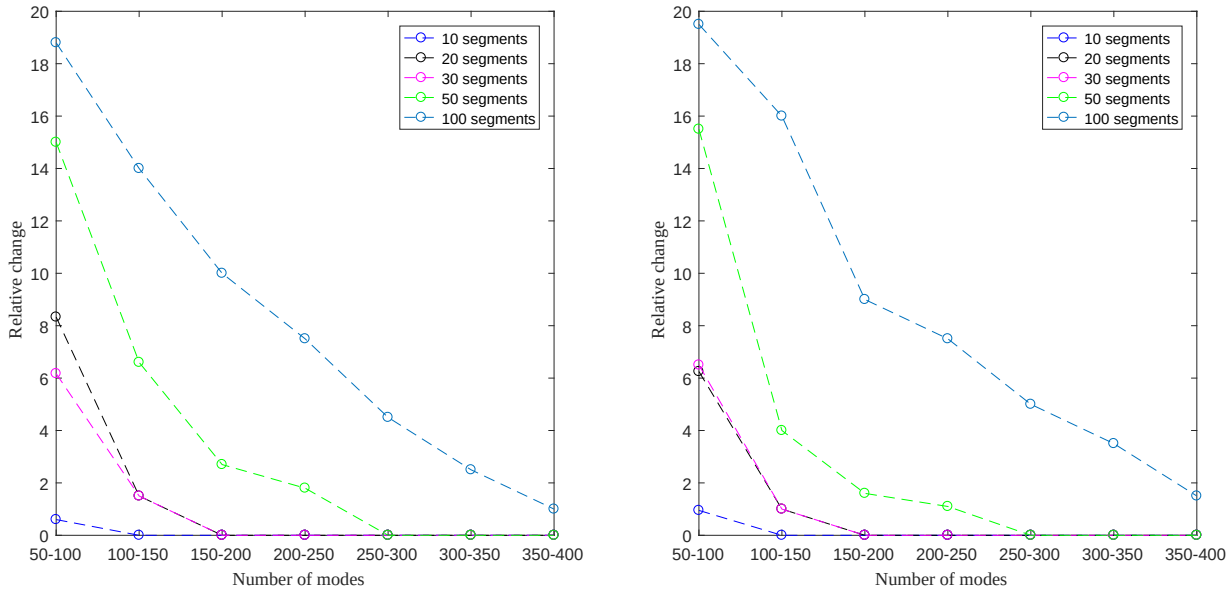

Figure 3.11: ***Convergence for Displacement*** u_z ***at an (Left) intermediate location(***$z = 0.5$***) and (Right) top location (***$z = 0$***)s***

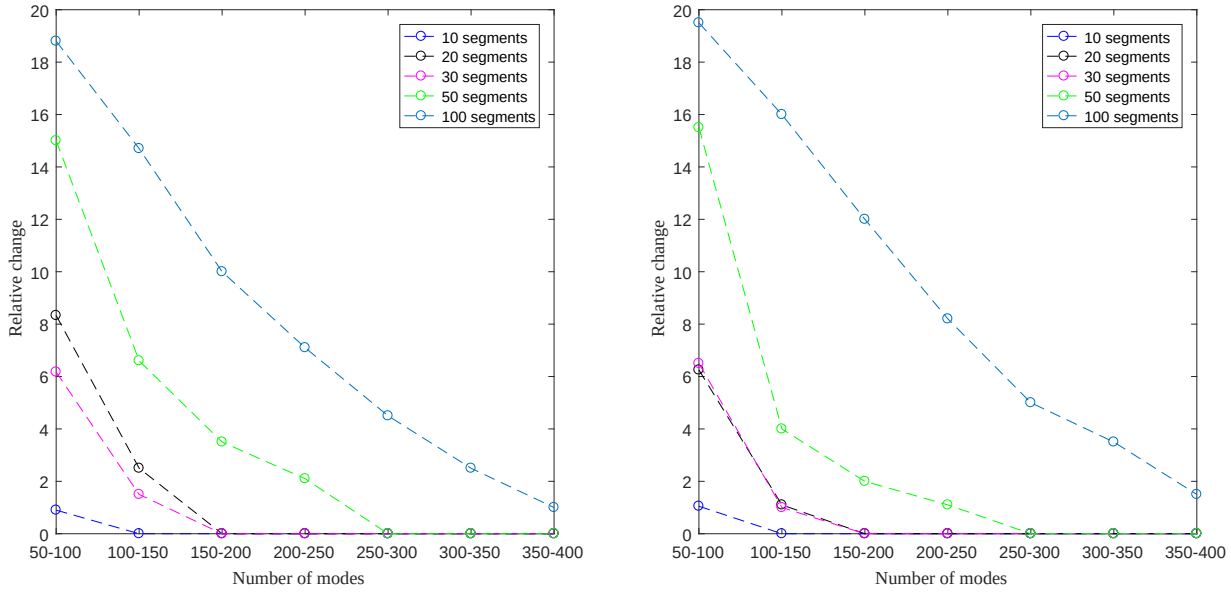

Figure 3.12: ***Convergence of Displacement*** u_x ***at an (left) intermediate location(***$z = 0.5$***) and (right) top location (***$z = 0$***)***

Figure 3.11 shows the convergence plots for displacement field u_x for stress imposed at top and mid-location, Figure 3.12 shows the convergence plots for displacement field u_z for

stress imposed at top and mid-location. Comparing the plots of the displacements with that of the stresses, we observe that displacements converge faster than stresses. For 50 segments, displacements converge with 300 modes, whereas the stress is still not converged.This is expected since stresses are defined as the derivatives of displacements.

Based on the convergence plots of the displacements, the number of modes for each element length is selected. The number of modes are based on the relative change dropping to zero. This is summarized in Table 3.1.

Table 3.1: ***Number of segments vs number of modes***

Number of segments	*Length of segment[-]*	*Number of modes*
10	0.1	101
20	0.05	151
30	0.033	151
50	0.02	251
100	0.01	401

3.3 Deriving the stiffness matrix of soil

The stiffness matrix for the soil waveguide at the interface is obtained using displacements $u_{x;1}^{(3;m)}$,$u_{z;1}^{(3;m)}$,$u_{x;2}^{(3;m)}$ and $u_{z;2}^{(3;m)}$. If the plate - soil interface is discretized into $m-1$ segments with m locations, then the displacement can be related to the applied stress as

$$\mathbf{U_{s;3}} = \mathbf{Q_{s;3}}\mathbf{F_{s;3}} \tag{3.12}$$

where the entries of the compliance matrix are given as

$$\begin{aligned}
Q^{(3)}_{s;(2m-1)(2p-1)} = u^{(3;m)}_{x;1,p} &= \sum_{n=1}^{\infty} C^{(3;m)}_{1,n} X^{(3)}_n(R) Z^{(3)}_{x;n}(z=z_p) \\
Q^{(3)}_{s;(2m-1)(2p)} = u^{(3;m)}_{x;2,p} &= \sum_{n=1}^{\infty} C^{(3;m)}_{2,n} X^{(3)}_n(R) Z^{(3)}_{x;n}(z=z_p) \\
Q^{(3)}_{s;(2m)(2p-1)} = u^{(3;m)}_{z;1,p} &= \sum_{n=1}^{\infty} C^{(3;m)}_{1,n} X^{(3)}_n(R) Z^{(3)}_{z;n}(z=z_p) \\
Q^{(3)}_{s;(2m)(2p)} = u^{(3;m)}_{z;2,p} &= \sum_{n=1}^{\infty} C^{(3;m)}_{2,n} X^{(3)}_n(R) Z^{(3)}_{z;n}(z=z_p)
\end{aligned} \tag{3.13}$$

where $\mathbf{Q_{s;3}}$ is a $2m \times 2m$ compliance matrix since $m = p$. The stiffness matrix $\mathbf{K_s}$ is obtained as

$$\mathbf{K_{s;3}} = (\mathbf{Q_{s;3}})^{-1} \tag{3.14}$$

Here $\mathbf{K_{s;3}}$ can be represented as

$$\mathbf{K_{s;3}} = \begin{array}{c} \begin{matrix} u^{(3)}_{x;1} & u^{(3)}_{z;1} & u^{(3)}_{x;2} & & u^{(3)}_{x;m} & u^{(3)}_{z;m} \\ \downarrow & \downarrow & \downarrow & & \downarrow & \downarrow \end{matrix} \\ \begin{bmatrix} k_{11} & k_{12} & k_{13} & \cdots & k_{1(2m-1)} & k_{1(2m)} \\ k_{21} & k_{22} & k_{23} & \cdots & k_{2(2m-1)} & k_{2(2m)} \\ k_{31} & k_{32} & k_{33} & \cdots & k_{3(2m-1)} & k_{3(2m)} \\ \vdots & \vdots & \vdots & \vdots & \vdots & \vdots \\ k_{(2m-1)1} & k_{(2m-1)2} & k_{(2m-1)3} & \cdots & k_{(2m-1)(2m-1)} & k_{(2m-1)2m} \\ k_{(2m)1} & k_{(2m)2} & k_{(2m)3} & \cdots & k_{(2m)(2m-1)} & k_{(2m)2m} \end{bmatrix} \end{array} \begin{matrix} \leftarrow F^{(3)}_{xx;1} \\ \leftarrow F^{(3)}_{xz;1} \\ \leftarrow F^{(3)}_{xx;2} \\ \\ \\ \leftarrow F^{(3)}_{xx;m} \\ \leftarrow F^{(3)}_{xz;m} \end{matrix} \tag{3.15}$$

$F^{(3)}_{xx;m}$ and $F^{(3)}_{xz;m}$ represent the normal and shear interaction forces respectively at the m^{th} location and $u^{(3)}_{x;m}, u^{(3)}_{z;m}$ represent the displacements of the soil in the x and z direction respectively at the same location. The obtained stiffness matrix is a dimensionless stiffness matrix. To make it dimensional, we can use the following relationships

$$\tilde{\mathbf{U}}_{\mathbf{s;3}} = \mathbf{U}_{s;3} H \tag{3.16}$$

which is obtained using Equation 2.18. The dimensional force vector $\tilde{\mathbf{F}}_{\mathbf{s;3}}$ is *force/unit thickness* which in terms of the dimensionless force vector $\mathbf{F_{s;3}}$ can be obtained as

$$\tilde{F}^{(3)}_{s;i} = \frac{\tilde{\sigma}\tilde{A}_s}{\tilde{t}_s} = \frac{GH^2\sigma A_s}{Ht_s} = GHF^{(3)}_{s;i} \tag{3.17}$$

where t_s is the thickness of the soil layer, A_s is the area of the cross-section of the soil layer corresponding a single element length, $\tilde{F}_{s;i}$ is any element of the dimensional force vector, and $F_{s;i}$ is the corresponding element in the dimensionless force vector. Parameters t_s and A_s are introduced to obtain the units for the force vector and hence make the stiffness matrix dimensional. Using the relation in Equation 3.16, the dimensional displacement vector can now be obtained as

$$\tilde{\mathbf{K}}_{\mathbf{s;3}} = G\mathbf{K_{s;3}} \tag{3.18}$$

Here $\mathbf{U_{s;3}}$ and $\mathbf{K_{s;3}}$ are the dimensionless displacement vector and Stiffness matrix respectively, and $\tilde{\mathbf{U}}_{\mathbf{s;3}}$ and $\tilde{\mathbf{K}}_{\mathbf{s;3}}$ are the dimensional displacement vector and Stiffness matrix. G is the shear modulus of the soil and H is the depth of the considered domain, in this case also equal to the length of the beam.

3.4 Modelling the plate

To model the plate, we use the 2D Euler Bernoulli beam elements with modified plate stiffness. This is an extension from the Euler Bernoulli beam theory, to the Kirchhoff-Love theory used for thin plates, which is its extension. The most important assumption of the theory [27] is that *'straight lines normal to the mid-surface (Neutral axis) remain straight after deformation.'*

These assumptions will be later used to obtain the relation between the degrees of freedom of the plate and soil. Furthermore, the stresses and displacements across the width of the plate can be obtained based on the above assumptions. Plate elements have two nodes per element, with two degrees of freedom per node. This choice was made to obtain a simple way of representing plate behavior. The beam element mass and stiffness matrices have been obtained from [15].

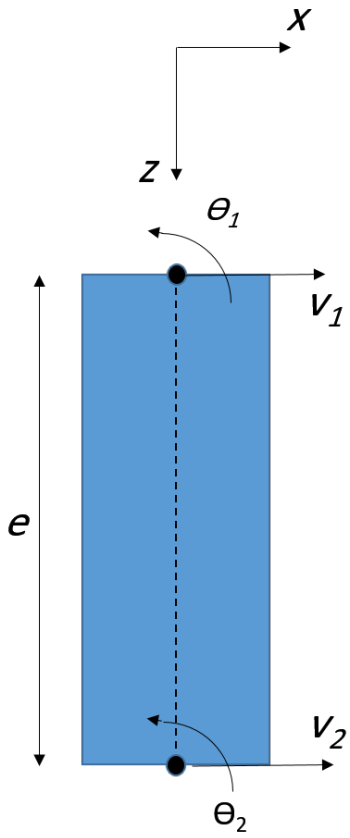

Figure 3.13: ***Kirchhoff plate element***

Figure 3.13 shows an Kirchhoff plate element with two degrees of freedom per node. v_1 and v_2 are the displacements and θ_1 and θ_2 are the rotations at the respective nodal locations.

The stiffness matrix has been modified by replacing the stiffness of the beam EI by the plate stiffness $\frac{EI}{1-\nu^2}$. Instead of using the total mass of the element, mass per unit thickness is considered. The modified mass and stiffness matrices are employed for in-plane bending. The mass and stiffness matrices for one Kirchhoff plate element are given as -

$$\tilde{M}_b = \frac{m_b}{420}\begin{bmatrix} 156 & 22L & 54 & -13L \\ 22L & 4L^2 & 13L & -3L^2 \\ 54 & 13L & 156 & -22L \\ -13L & -3L^2 & -22L & 4L^2 \end{bmatrix} \tag{3.19}$$

$$\tilde{K}_b = \frac{D_b}{L^3}\begin{bmatrix} 12 & 6L & -12 & 6L \\ 6L & 4L^2 & -6L & 2L^2 \\ -12 & -6L & 12 & -6L \\ 6L & 2L^2 & -6L & 4L^2 \end{bmatrix} \tag{3.20}$$

where $m_b = \rho_b A_b L$ is the mass of the element per unit thickness, ρ_b is the mass density, $A_b = 2R$ is the area of the cross-section of the element for unit thickness, and L is the length of the element. The '~' is used to signify that the quantities are dimensional. D_b is the plate stiffness given by $D_b = \frac{Eh^3}{12(1-\nu^2)}$ where E is the Young's modulus of the plate element, h is the depth of the cross-section given by $h = 2R$ and ν is the Poisson's ratio. Plate stiffness D_b has the dimension $\mathrm{Pa.m^3}$, as compared to the beam stiffness which has the dimension $\mathrm{Pa.m^4}$. The mass and stiffness matrices are assembled using [7].

3.4.1 Validation of the modified plate mass and stiffness matrices

The mass and stiffness matrices are validated by comparing the first three natural frequencies of the analytical equation with that of the numerical results. This was done with 20 elements for the FEM model and using the parameter values shown in Table 3.2.

Table 3.2: ***Plate element properties***

Material property	***Value***	***Units***
Young's Modulus(E)	210e9	$\mathrm{N/m^2}$
Mass Density (ρ_b)	7800	$\mathrm{kg/m^3}$
Radius(R)	0.2	m
Length(L)	1	m
Poisson's ratio(ν)	0.3	-

The results are shown in Table 3.3

Table 3.3: ***Comparing Natural frequencies - Analytical and FEM***

Analytical(ω_a)[Hz]	**FEM**(ω_f)[Hz]	**% Error** $= \lvert\omega_a - \omega_f\rvert/\lvert\omega_a\rvert$
2208.2	2208.309	0.001
13840	13839.3	0.005
38767	38750.36	0.042

The analytical frequency of the Kirchhoff plate [24] was obtained using the following formula -

$$\omega_n = \beta_n^2 \sqrt{\frac{D_b}{m_b}} \tag{3.21}$$

where β_n are the roots of the characteristic dispersion equation derived for a cantilever Euler-Bernoulli beam in the considered domain.

3.5 Plate-soil system

This section explains the derivation of the dynamic plate-soil stiffness matrix. Two cases are evaluated - Slip and Non-slip. In the slip case, the shear reaction forces at the vertical interface from the soil are neglected. For the non-slip case, the shear reaction from the soil is included.

In the frequency domain, the equilibrium of the plate-soil system is given as-

$$(-\tilde{\mathbf{M}}_\mathbf{b}\tilde{\omega}^2 + \tilde{\mathbf{K}}_\mathbf{b})\tilde{\mathbf{U}}_\mathbf{b} = \tilde{\mathbf{F}}_\mathbf{ext} + \tilde{\mathbf{F}}_\mathbf{s;3} \tag{3.22}$$

where $\tilde{\mathbf{F}}_\mathbf{s;3} = \tilde{\mathbf{K}}_\mathbf{s;3}\tilde{\mathbf{U}}_\mathbf{s;3}$ with

$$\tilde{\mathbf{U}}_\mathbf{b} = \begin{bmatrix} \tilde{W}_1 \\ \tilde{\phi}_1 \\ \tilde{W}_2 \\ \tilde{\phi}_2 \\ \vdots \\ \tilde{W}_m \\ \tilde{\phi}_m \end{bmatrix}, \quad \tilde{\mathbf{U}}_\mathbf{s;3} = \begin{bmatrix} \tilde{u}^{(3)}_{x;1} \\ \tilde{u}^{(3)}_{z;1} \\ \tilde{u}^{(3)}_{x;2} \\ \tilde{u}^{(3)}_{z;2} \\ \vdots \\ \tilde{u}^{(3)}_{x;m} \\ \tilde{u}^{(3)}_{z;m} \end{bmatrix}, \quad \tilde{\mathbf{F}}_\mathbf{ext} = \begin{bmatrix} \tilde{F}_1 \\ \tilde{M}_1 \\ \tilde{F}_2 \\ \tilde{M}_2 \\ \vdots \\ \tilde{F}_m \\ \tilde{M}_m \end{bmatrix} \tag{3.23}$$

The displacements of the soil can be translated to corresponding displacements and rotations of the beam. At the soil-plate interface

$$\begin{aligned} \tilde{W}_m &= \tilde{u}^{(3)}_{x;m} \\ \tilde{\phi}_m &= -\frac{\tilde{u}^{(3)}_{z;m}}{\tilde{R}} \end{aligned} \tag{3.24}$$

where $\tilde{W}_m$ and $\tilde{\phi}_m$ are the displacement and rotation at the m^{th} location of the beam. $\tilde{R} = RH$ is half the dimensional width of the plate. Figure 3.14 shows how the second relationship in Equation 3.24 is derived.The positive direction of the rotation of cross-section of the beam section is also indicated, and is based on the right hand thumb rule indicated in [30].

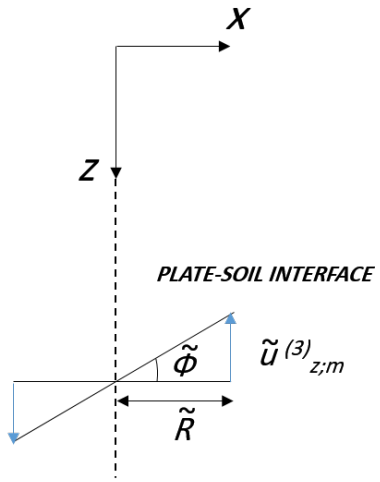

Figure 3.14: ***Rotational compatibility***

The translation of the normal and shear forces to the corresponding shear force and bending moment on the plate is done as shown in Figure 3.15 and Figure 3.16

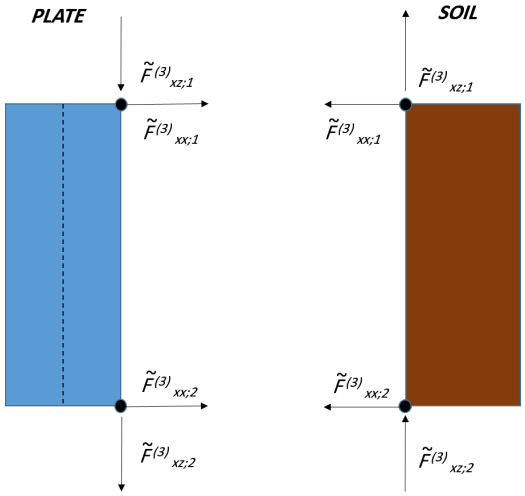

Figure 3.15: ***Translation of forces from Soil to plate - Domain 3***

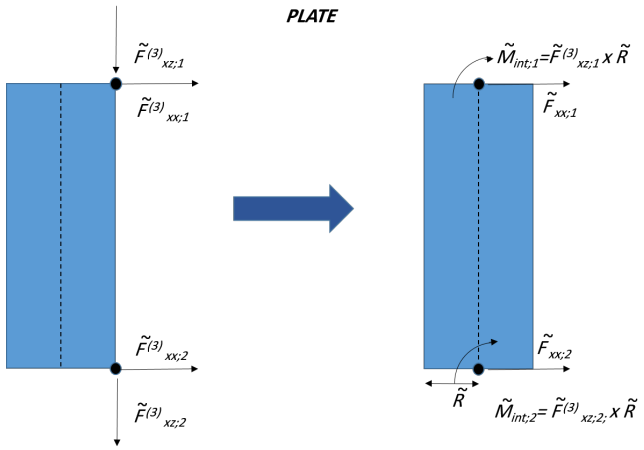

Figure 3.16: ***Moments due to shear forces***

The force vector $\tilde{F}_{s;3}$ from the soil can be written as -

$$\tilde{\mathbf{F}}_{\mathbf{s;3}} = \begin{bmatrix} \tilde{F}^{(3)}_{xx;1} \\ \tilde{F}^{(3)}_{xz;1} \\ \tilde{F}^{(3)}_{xx;2} \\ \tilde{F}^{(3)}_{xz;2} \\ \vdots \\ \tilde{F}^{(3)}_{xx;m} \\ \tilde{F}^{(3)}_{xz;m} \end{bmatrix} = \begin{bmatrix} \tilde{F}^{(1)}_{xx} \\ \frac{-\tilde{M}^{(1)}_{int}}{\tilde{R}} \\ \tilde{F}^{(2)}_{xx} \\ \frac{-\tilde{M}^{(2)}_{int}}{\tilde{R}} \\ \vdots \\ \tilde{F}^{(m)}_{xx} \\ \frac{-\tilde{M}^{(m)}_{int}}{\tilde{R}} \end{bmatrix} \tag{3.25}$$

where $\tilde{M}^{(m)}_{int}$ are the nodal bending moments due to the interaction shear force $\tilde{F}^{(m)}_{xz}$ from the soil. The negative sign for the bending moment comes due to the positive sign convention for the plate elements shown in Figure 3.13. Using Equations Equation 3.25 and Equation 3.24, the dimensional stiffness matrix of the soil is modified to make it compatible with beam dynamic stiffness matrix as follows

$$\tilde{\mathbf{K}}^{(\mathbf{mod})}_{\mathbf{s;3}} = G \begin{bmatrix} \tilde{W}_1 & \tilde{\phi}_1\tilde{R} & \tilde{W}_2 & & \tilde{W}_m & \tilde{\phi}_m\tilde{R} & \\ \downarrow & \downarrow & \downarrow & & \downarrow & \downarrow & \\ k_{11} & -k_{12}\tilde{R} & k_{13} & \cdots & k_{1(2m-1)} & -k_{1(2m)}\tilde{R} & \leftarrow F^{(1)}_{xx} \\ -k_{21}\tilde{R} & k_{22}\tilde{R}^2 & -k_{23}\tilde{R} & \cdots & -k_{2(2m-1)}\tilde{R} & k_{2(2m)}\tilde{R}^2 & \leftarrow M^{(1)}_{int} \\ k_{31} & -k_{32}\tilde{R} & k_{33} & \cdots & k_{3(2m-1)} & -k_{3(2m)}\tilde{R} & \leftarrow F^{(2)}_{xx} \\ \vdots & \vdots & \vdots & \vdots & \vdots & \vdots & \\ k_{(2m-1)1} & -k_{(2m-1)2}\tilde{R} & k_{(2m-1)3} & \cdots & k_{(2m-1)(2m-1)} & -k_{(2m-1)2m}\tilde{R} & \leftarrow F^{(m)}_{xx} \\ -k_{(2m)1}\tilde{R} & k_{(2m)2}\tilde{R}^2 & -k_{(2m)3}\tilde{R} & \cdots & -k_{(2m)(2m-1)}\tilde{R} & k_{(2m)2m}\tilde{R}^2 & \leftarrow M^{(m)}_{int} \end{bmatrix} \tag{3.26}$$

where k_{mp} are the elements of the dimensionless soil stiffness matrix from Equation 3.15. $\tilde{\mathbf{K}}^{(\mathbf{mod})}_{\mathbf{s;3}}$ represents the modified stiffness matrix for the non-slip case. The derivation of the stiffness matrix for the slip case is shown in section 1.5.2.

3.5.1 Plate and soil properties

Table 3.4 and Table 3.5 give the plate and soil properties respectively used for the analysis.

Table 3.4: ***Plate element properties***

Material property	***Value***	***Units***
Young's Modulus(E)	210e9	$\mathrm{N/m^2}$
Mass Density (ρ_b)	7800	$\mathrm{kg/m^3}$
Radius(R)	1	m
Length(L)	25	m
Poisson's ratio(ν_b)	0.3	-

Table 3.5: ***Soil properties***

Material property	***Value***	***Units***
Shear Modulus(G)	250e5	$\mathrm{N/m^2}$
Mass Density (ρ_s)	1700	$\mathrm{kg/m^3}$
Poisson's ratio(ν_s)	0.4	-
Height of soil continuum(H)	25	m

3.5.2 Slip

For the slip case, we neglect the shear reaction forces from the soil at the vertical interface are neglected. The relative change in displacement and rotation considering shear stresses, would give us an idea about the contribution of shear to the stiffness of the soil. The modified stiffness matrix for the slip case is given by

$$\tilde{\mathbf{K}}^{(\mathbf{mod})}_{\mathbf{s;3;slip}} = G \begin{array}{c} \begin{matrix} \tilde{W}_1 \downarrow & \tilde{\phi}_1\tilde{R} \downarrow & \tilde{W}_2 \downarrow & & \tilde{W}_m \downarrow & \tilde{\phi}_m\tilde{R} \downarrow \end{matrix} \\ \begin{bmatrix} k_{11} & 0 & k_{13} & \cdots & k_{1(2m-1)} & 0 \\ 0 & 0 & 0 & \cdots & 0 & 0 \\ k_{31} & 0 & k_{33} & \cdots & k_{3(2m-1)} & 0 \\ \vdots & \vdots & \vdots & \vdots & \vdots & \vdots \\ k_{(2m-1)1} & 0 & k_{(2m-1)3} & \cdots & k_{(2m-1)(2m-1)} & 0 \\ 0 & 0 & 0 & \cdots & 0 & 0 \end{bmatrix} \begin{matrix} \leftarrow F^{(1)}_{xx} \\ \leftarrow M^{(1)}_{int} \\ \leftarrow F^{(2)}_{xx} \\ \\ \leftarrow F^{(m)}_{xx} \\ \leftarrow M^{(m)}_{int} \end{matrix} \end{array} \tag{3.27}$$

where $k_{11}...k_{(2m-1)2m}$ are the elements of the stiffness matrix $\mathbf{K_{s;3}}$. Using the relations in Equation 3.24, $\tilde{\mathbf{U}}_\mathbf{b}$ can be related to $\tilde{\mathbf{U}}_{\mathbf{s;3}}$. The equilibrium equation for the plate-soil system can then be written as -

$$\begin{aligned} (-\tilde{\mathbf{M}}_\mathbf{b}\tilde{\omega}^2 + \tilde{\mathbf{K}}_\mathbf{b})\tilde{\mathbf{U}}_\mathbf{b} &= \tilde{\mathbf{F}}_\mathbf{ext} + \tilde{\mathbf{K}}^{(\mathbf{mod})}_{\mathbf{s;3;slip}}\tilde{\mathbf{U}}_\mathbf{b} \\ \implies (-\tilde{\mathbf{M}}_\mathbf{b}\tilde{\omega}^2 + \tilde{\mathbf{K}}_\mathbf{b} - \tilde{\mathbf{K}}^{(\mathbf{mod})}_{\mathbf{s;3;slip}})\tilde{\mathbf{U}}_\mathbf{b} &= \tilde{\mathbf{F}}_\mathbf{ext} \\ \implies \tilde{\mathbf{K}}_\mathbf{d}\tilde{\mathbf{U}}_\mathbf{b} &= \tilde{\mathbf{F}}_\mathbf{ext} \end{aligned} \tag{3.28}$$

where $\tilde{\omega} = \frac{c_s}{H}\omega$ is the dimensional circular frequency, with c_s is the shear wave speed in soil. The factor $\frac{c_s}{H}$ is obtained using Equation 2.32. $\tilde{\mathbf{K}}_\mathbf{d}$ is the dimensional dynamic stiffness matrix for the plate-soil system.

Note: For the non-slip case, we include all the entries in the soil stiffness matrix (the matrix is given in Equation 1.26. This can be substituted in Equation 3.28 to solve for the plate-soil system.

3.6 Results

This section explains the main results of the plate-soil system with a single domain of soil. Both cases of slip and non-slip were analyzed. A weighted plot of the soil stiffness matrix for both cases is analyzed first. This is followed by validation of the plate-soil model. In order to validate the plate-soil model, the results were compared with those obtained from a reference solution method described in Appendix A, where the plate and soil are modelled as a continuous system. This will be henceforth be referred to as the benchmark solution. The case of a unit normalized force applied to the top node is used to validate the cases of slip and non-slip. Validation involved a check with the displacement, rotational, shear force and bending moment profile across the depth of the plate as a convergence study. Additionally, the normal and shear interaction force distribution at the interface across the soil profile were also examined as well as the natural frequencies of the plate-soil system.

3.6.1 Slip

Figure 3.17 shows the weighted plot of the modified soil stiffness matrix $\tilde{\mathbf{K}}^{(\mathbf{mod})}_{\mathbf{s;3;slip}}$. The last two rows (corresponding to the last location) have not been shown due to the clamped end. The stiffness entries corresponding to these rows would be much higher than the other stiffness entries in the matrix. To obtain a square matrix, the last two columns have also not been shown. The matrix is almost perfectly symmetric except for entries in the first row.

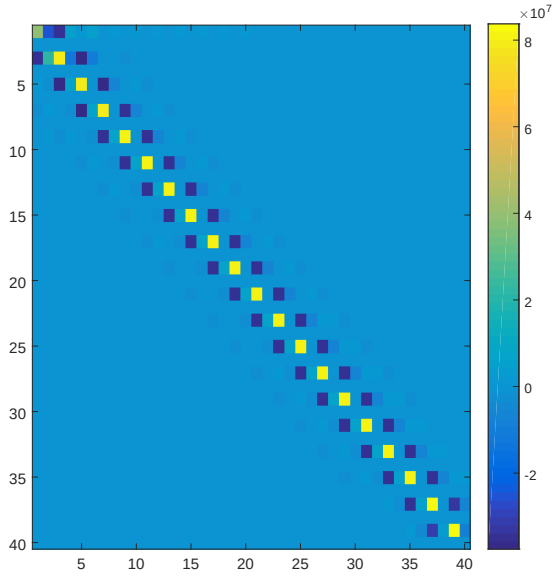

Figure 3.17: ***Weighted plot of the soil stiffness matrix*** $\mathbf{K_{s;3;slip}}$

We now move on to the results of the pile-soil system. The case of unit force imposed at the top node is considered for validation. The boundary conditions imposed are

$$\begin{aligned} F = 1 \quad M = 0, \qquad z = 0 \\ W = 0 \quad \phi = 0, \qquad z = H \end{aligned} \tag{3.29}$$

Figure 3.18 shows the convergence plot for the displacement profile of the plate and Figure 3.19 shows the convergence plot for the rotation profile across the plate length. The displacement is normalized using domain depth H.

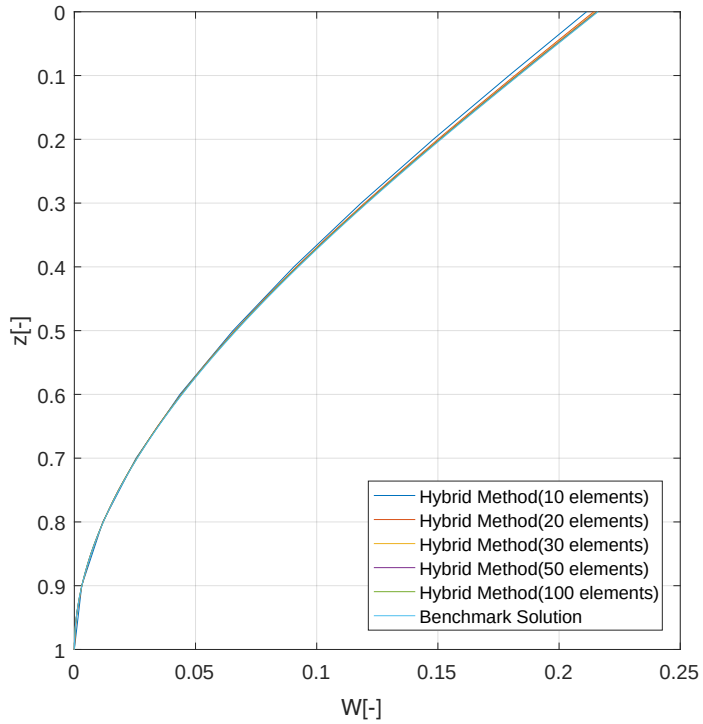

Figure 3.18: ***Convergence study - Displacement profile of the plate - unit lateral force at the top***

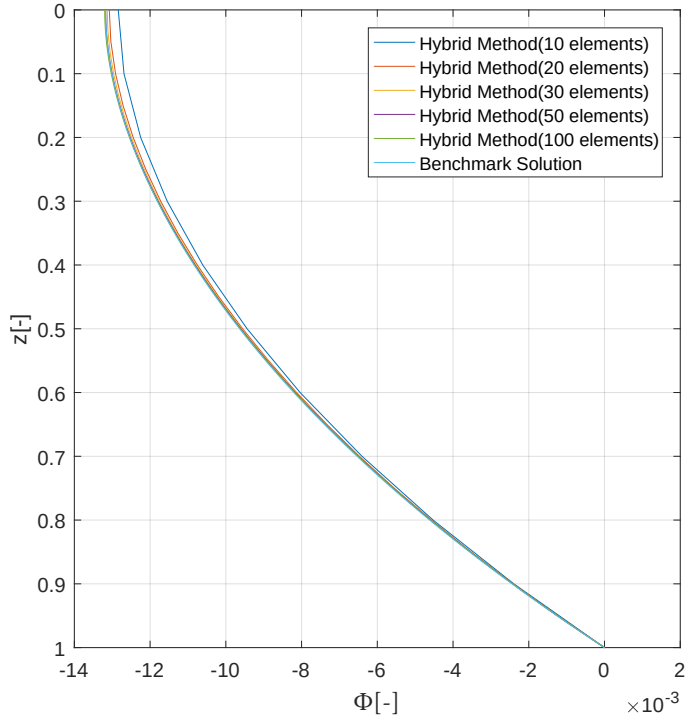

Figure 3.19: ***Convergence study - Rotation profile of the plate - Unit lateral force at the top***

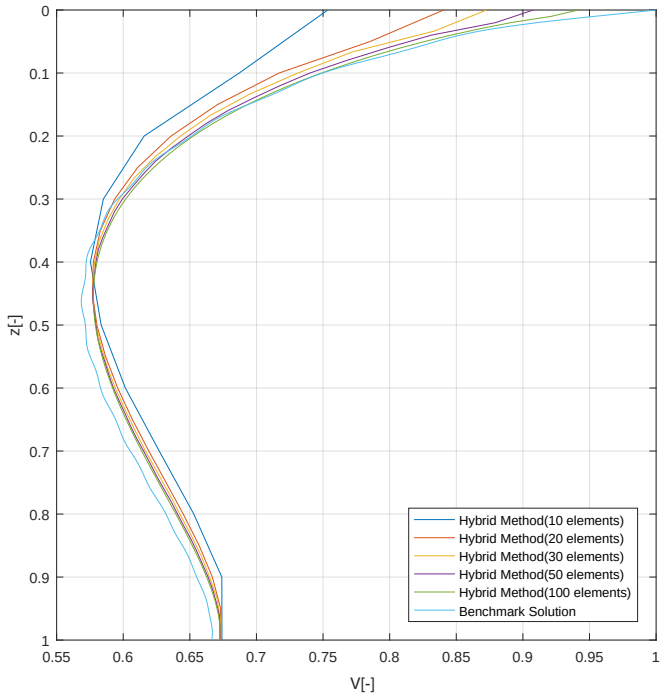

Figure 3.20: ***Convergence study - Shear force profile of the plate - unit lateral force at the top***

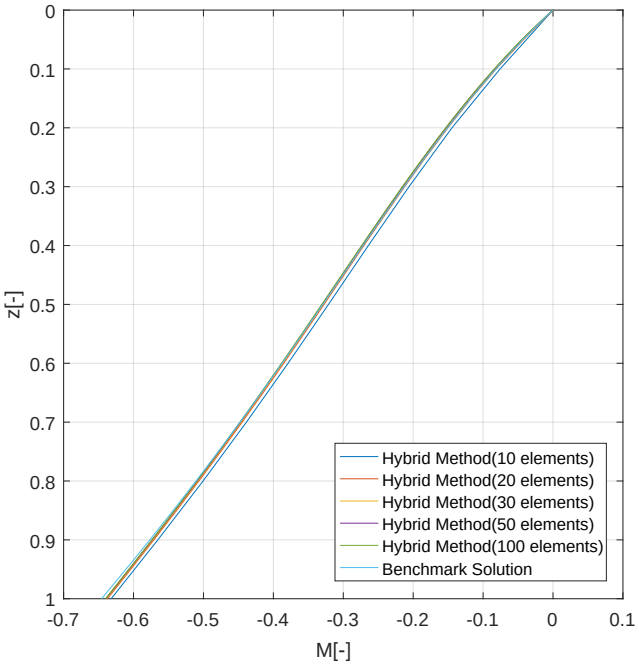

Figure 3.21: ***Convergence study - Bending Moment profile of the plate - Unit lateral force at the top***

Figure 3.20 shows the convergence plot of the shear force profile across the plate depth and Figure 3.21 shows the convergence plot for the bending moment profile across the plate depth. The shear and bending moment are normalized. A normalization factor of H^2/D_b was

used for the Shear force and H/D_b for the bending moment. These relations can be obtained from the benchmark model described in Appendix A.

It is observed that with the displacement and rotation, convergence is obtained with 20 elements. The average relative difference is maximum at the top and has a value of 0.01 % and 0.005% across the depth for displacement. Similarly for rotation it is 0.4% and 0.01% as an average across the depth.These are calculated as follows, and will be used for all quantities.

$$\epsilon_{top} = \frac{|S_o(z=0) - S_a(z=0)|}{|S_a(z=0)|} \tag{3.30}$$

$$\epsilon_{avg} = \frac{1}{p-1} \sum_{r=1}^{p-1} \frac{|S_o(z=z_r) - S_a(z=z_r)|}{|S_a(z=z_r)|} \tag{3.31}$$

where S_a is the benchmark value and S_o is the Hybrid method value. p is the total number of nodes considered.

Comparing the shear force and bending moment profile, with 50 elements, the average relative difference at the top is reduced to 1.2 % and 0.05% across the depth. The shear force at the top however has the largest relative difference of 16% and an average relative difference of 4.5% the depth. Increasing the number of elements could reduce this as already observed. However, one needs to then use more soil modes as well, since with 100 segments, it was observed that the displacement still hadn't fully converged. Additionally, it should be noted that since both models have not been validated yet, it is still difficult to predict which model has more accuracy.

3.6.2 Non-Slip

Figure 3.22 shows the weighted plot of the modified soil stiffness matrix $\tilde{\mathbf{K}}_{\mathbf{s;3}}^{(\mathbf{mod})}$. The last two rows (corresponding to the last location) have not been shown due to the clamped end. The stiffness entries corresponding to these rows would be much higher than the other stiffness entries in the matrix. To obtain a square matrix, the last two columns have also not been shown. The matrix is almost perfectly symmetric except for entries in the first row.

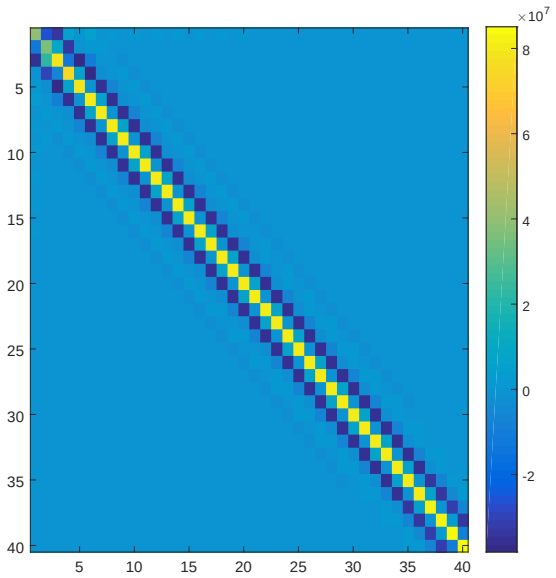

Figure 3.22: ***Weighted plot of the soil stiffness matrix*** $\mathbf{K_{s;3}}$

Similar to the slip case, a convergence study is performed and the Hybrid model is compared to the benchmark model.

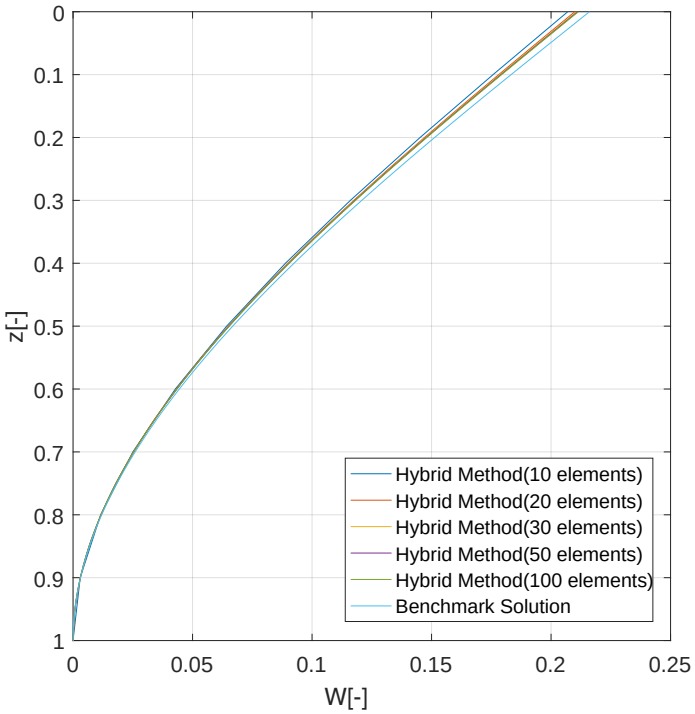

Figure 3.23: ***No slip - Convergence study - Displacement profile of the plate - unit lateral force at the top***

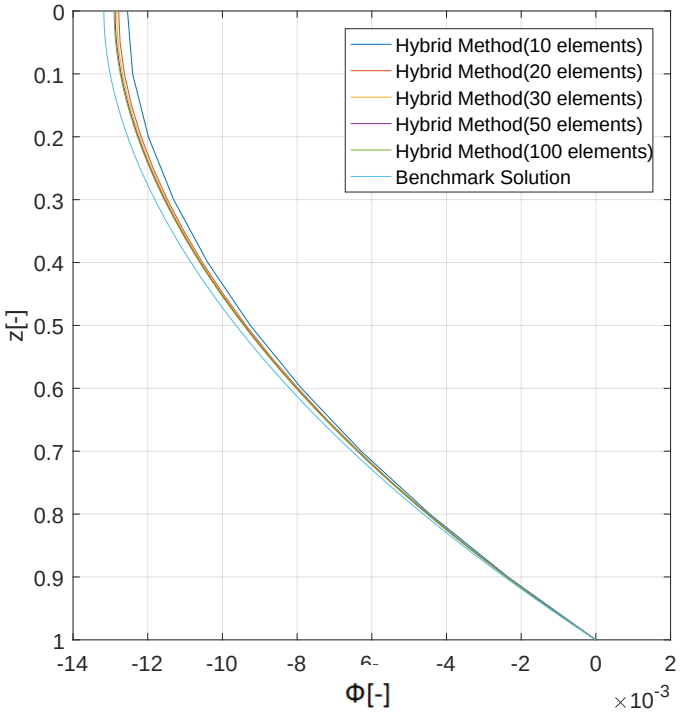

Figure 3.24: ***No slip - Convergence study - Rotation profile of the plate - unit lateral force at the top***

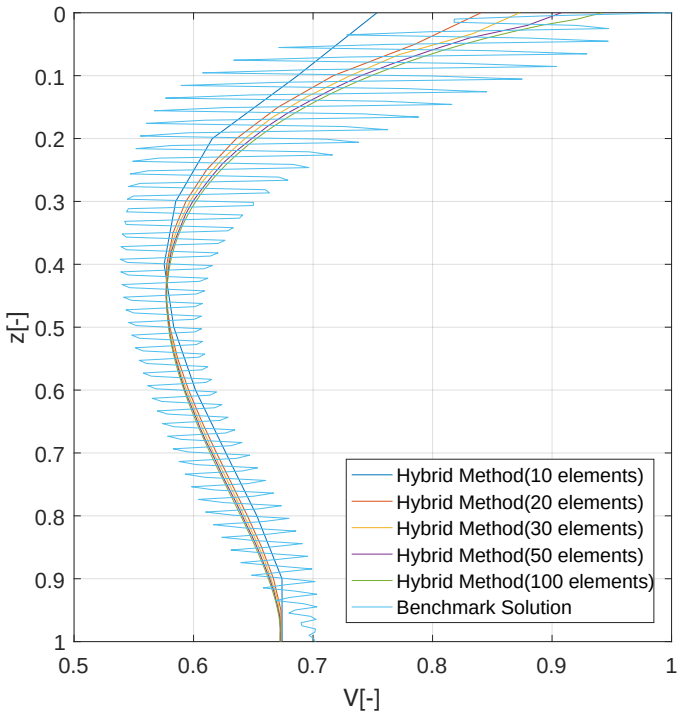

Figure 3.25: ***No slip - Convergence study - Shear force profile of the plate - Unit lateral force at the top***

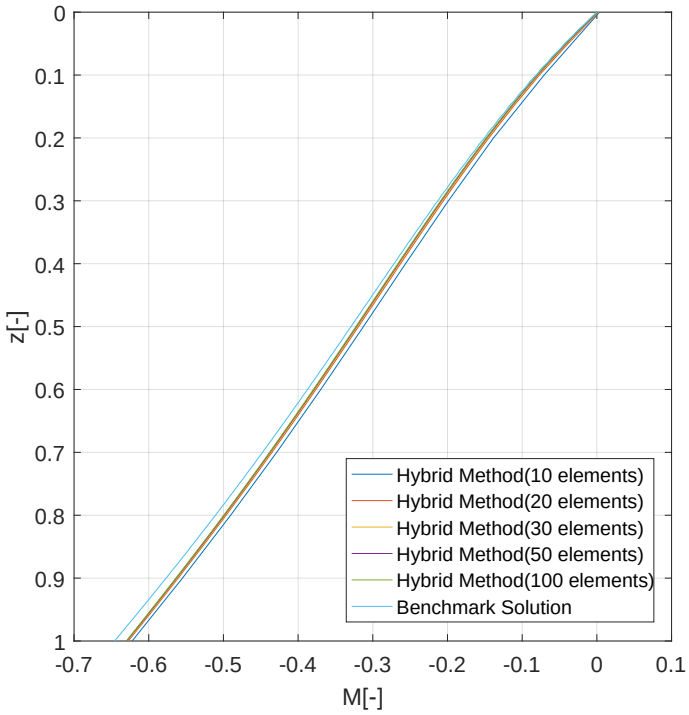

Figure 3.26: ***No slip - Convergence study - Bending Moment profile of the plate - unit lateral force at the top***

Figure 3.23 shows the displacement profile of the plate in response to the unit force. The boundary conditions imposed are same as for the slip case given in Equation 3.29. Figure 3.24, Figure 3.25 and Figure 3.26 show the rotation, shear force and bending moment

profile for the same. As the number of elements across the depth is increased, the hybrid solution converges to the benchmark solution. In the shear force plot, we can observe that the highly oscillatory nature of the benchmark solution is overcome by the hybrid solution, with a slight mismatch close to the tip ($z = H$). The least square fitting method is used for the shear force distribution to get a smooth profile (see Appendix C for a detailed implementation).

3.6.3 Comparing slip and non-slip

Between the slip and non-slip case, in the hybrid method, an average relative difference of all quantities (displacement, rotation, shear force and bending moment) is observed to be less than 1%. In the benchmark solution however, a relative difference of 5% is observed at the tip for the shear force.

3.6.4 Interaction force distribution in the soil at the interface

This section discusses the interaction forces in the soil at the interface for the non-slip case. These are calculated as

$$\tilde{\mathbf{F}}_{\mathbf{s;3}} = \tilde{\mathbf{K}}_{\mathbf{s;3}} \tilde{\mathbf{U}}_{\mathbf{s;3}} \tag{3.32}$$

where $\tilde{\mathbf{F}}_{\mathbf{s;3}}$ is the soil interaction force vector.

Normal interaction force distribution

Figure 3.27 shows the normal interaction force distribution across the profile with various number of segments.

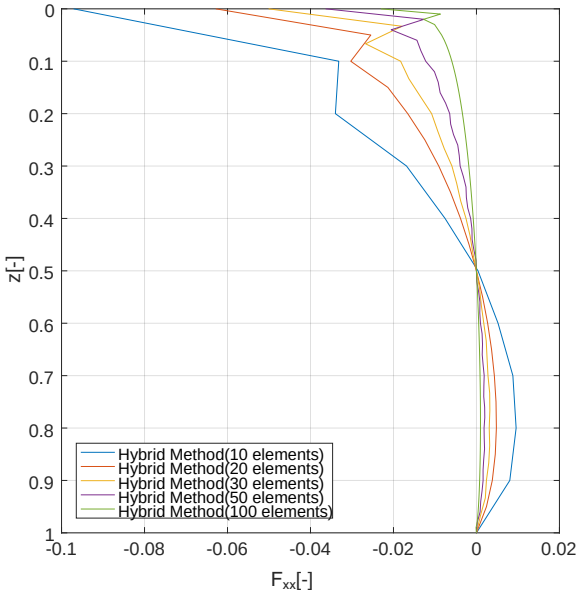

Figure 3.27: ***No slip - Normal interaction force distribution in the soil at the interface*** ***($x = R$)***

F_{xx} refers to the normalized normal force distribution. As the number of segments increase, the curve becomes smoother. A jump is observed at the top close to $z = 0$. The width of this kink is spread across two segments, and its amplitude reduces with increasing the number of segments across the profile.

Shear interaction force distribution

Figure 3.28 shows the imposed and obtained Shear stress distribution at the top. It is observed that for shear stress imposed at $z = 0$, the obtained shear stress distribution shows a different behavior from the imposed distribution.

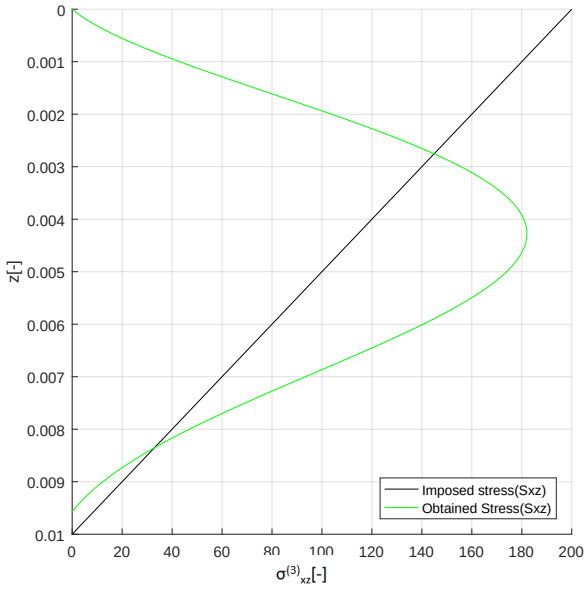

Figure 3.28: ***Imposed and obtained Shear stress distribution at the top - Considering 100 segments and 400 soil modes***

When deriving the soil stiffness matrix, for the location at the top, a non-zero value of shear force is imposed, however when deriving the eigen functions of the soil, the shear stress at the free surface was imposed as zero.

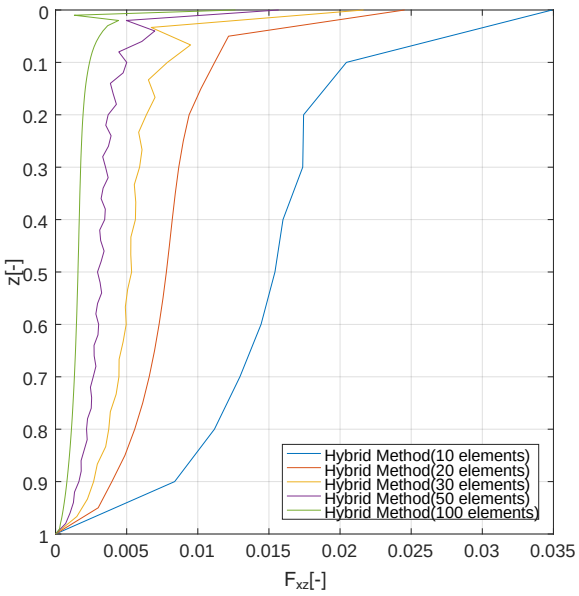

Figure 3.29: ***No slip - Shear interaction force distribution in the soil at the interface ($x = R$)***

Figure 3.29 shows the plot of the shear force across the soil at the interface. F_{xz} represents the shear interaction forces between the pile and the soil at the plate-soil interface. Similar to the normal interaction force distribution, a kink is observed close to the top, and spreads over two segments. The value of the shear interaction force at the top reduces as the number of segments are increased across the domain depth. The stiffness entries corresponding the the shear force at the top location are imposed as non-zero. Hence a non-zero value of shear force is obtained at the top.

3.7 Summary and Conclusion

The chapter discusses the hybrid soil-pile interaction model with a single domain (domain 3), where the pile is modeled using Kirchoff plate elements. The soil is modeled as an elastic waveguide. By applying a unit force(in the form of normal and shear stress) at each location, the corresponding u_x and u_z displacements are derived, at each location, which can then be used to form the compliance matrix, and hence the stiffness matrix. For the top location, a shear stress incompatibility occurs at the corner. However,this does not have any influence on the dynamic behavior of the soil.

To get an accurate estimation of the displacements, a convergence study was conducted. Up to 100 segments across the soil domain depth at the interface and 401 soil modes were considered for the study. For each segment length, the number of soil modes for converged non-oscillatory displacement fields at the interface were determined.

Two cases were analyzed - Slip and non - slip. In the slip case the stiffness entries due to the shear interaction forces at the interface were neglected. A weighted plot of the soil stiffness matrix shows a symmetric plot except for the first row and column. For the non-slip case, the fully populated soil stiffness matrix is considered. A weighted plot of the soil stiffness matrix shows a symmetric plot except for the first two rows. The soil stiffness matrix was derived for each segment length and a convergence study was done for the plate-soil system. With 100 segments, and 401 soil modes, the results match well with the benchmark solution, for the two cases discussed, slip and non-slip. For the slip case, comparing the shear force profile with the benchmark solution, a slight difference is obtained at the top ($z = 0$), which reduces when the number of segments are increased. The number of segments required for shear force convergence (greater than 100 segments) is found to be much higher than that obtained for the other quantities (up to 20 segments). For the non-slip case, the hybrid method gives a smoother profile of the shear force as compared to the oscillatory nature of the shear force profile in the benchmark solution with a slight mismatch between the two at the tip.

Comparing the slip and non-slip case, the average variation in all quantites (displacement, rotation, bending moment and shear force) is less that 1 %. However in the bench mark solution, a relative difference of 5% is observed at the tip in the shear force.

The normal and shear interaction force distribution in the soil gives a uniform profile with a kink close to the top, which extends over the length of two segments. The amplitude of the kink reduces as the element length reduces.

In conclusion, the hybrid method is in good agreement with the benchmark method with an improvement in the distribution of the shear force profile across the plate length.

Chapter 4

Solution for a waveguide with cavity excited by a stress applied at the cavity surface

For monopile foundations currently used in the industry, the embedded length/diameter of the pile ranges from 3 to 7. In this range, the pile behaves as a rigid pile, and hence soil below the tip could have an influence on the dynamic behavior of the pile. Hence, an additional domain of soil called the tip domain (domain 4) is introduced into the model in addition to domain 1 and 3. This chapter describes the soil model including the tip domain, which is essentially the problem of a waveguide with a cavity (rectangular in this case). The eigen modes of domain 4 are derived as a modification of the eigen modes of domain 1 and 3, which can be used to obtain the stresses and displacements in the domain. Using the boundary and interface conditions, the displacements and stresses due to a normal and shear stress imposed at each location can be derived. Additionally, locations are introduced at the tip. Due to stress imposed on these locations, domain 4 has an inhomogeneous component for the displacements and stresses in addition to its homogeneous component. The corresponding displacement profiles at the boundaries and the tip can then be used to obtain the stiffness matrix of the soil.

4.1 Model description

Domains 1 (left), 3 (right) and 4 (tip) are combined in this formulation to obtain the complete soil domain, which is then coupled to the plate via the discretized plate-soil interfaces as shown in Figure 4.1. Additionally, parameter $\tilde{L}$ is introduced, which gives the depth from which the tip domain begins. This is made dimensionless using the same normalizing factor H as was used in for other length parameters (Refer to Equation 2.18).

$$L = \frac{\tilde{L}}{H} \tag{4.1}$$

Locations are introduced at the tip. Stresses and displacements for the domain will have a homogeneous and inhomogeneous component. The homogeneous component is obtained for the homogeneous boundary conditions similar to domain 1 or 3, and can be derived using the same Z eigen modes by modifying the local vertical coordinate, hence referred to as z_{mod} for the domain in terms of the global coordinate z. When a stress is imposed on domain 1 or 3 boundary, the tip domain has homogeneous boundary conditions, and hence only the homogeneous component of the stresses and displacements. The inhomogeneous component is present only when a stress is imposed on locations on the tip domain.

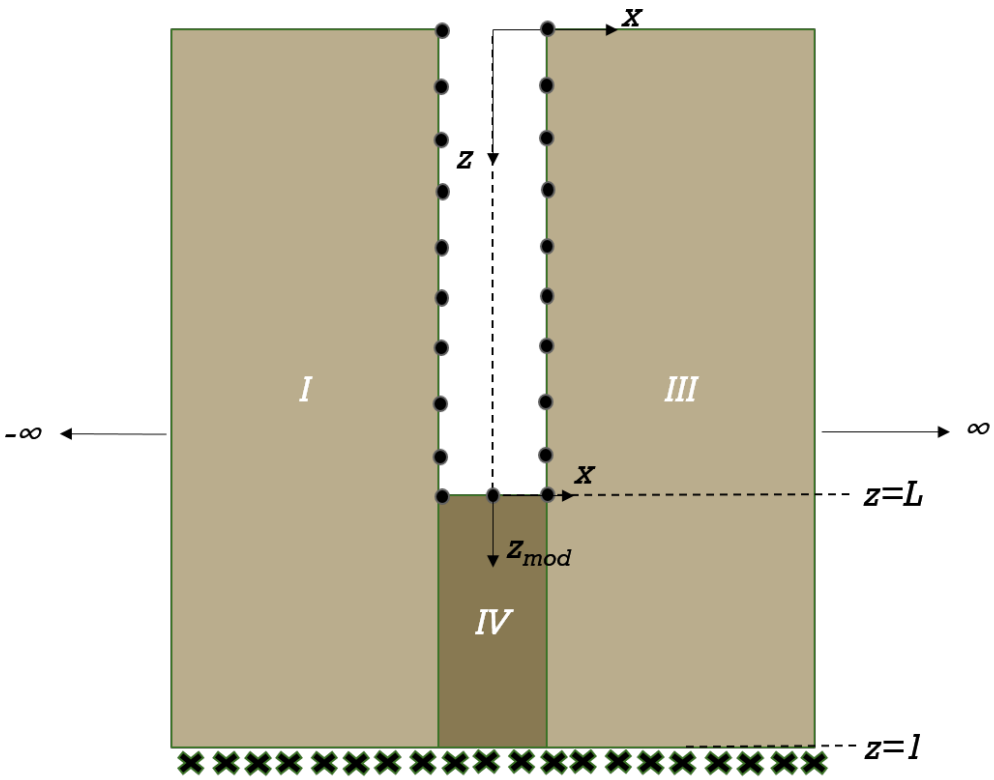

Figure 4.1: ***Soil with tip domain***

Figure 4.1 shows the three domains of the soil along with the local tip coordinate system.

4.2 Tip domain coordinate system

For obtaining the homogeneous component of the stresses and displacements in the tip domain, the Z eigen modes used are a modified form of the Z eigen modes used for domain 1 and 3 (see section 1.6.2). This is possible since both domain 4 (Tip domain) and domain 1 or 3, have the same homogeneous boundary conditions for this analysis and dimensionless dispersion equation for the wavenumbers. The local origin for the domain lies a $\tilde{x} = 0, \tilde{z} = \tilde{L}$ with the domain depth $H - \tilde{L}$, where $\tilde{x}$ and $\tilde{z}$ are the dimensional global coordinates. The global x coordinate can be retained since there is no change in that direction, however the local coordinate system undergoes two changes with respect to the local z coordinate. A shift of local origin and a scaling of the domain depth. Figure 4.1 shows the model in terms of dimensionless coordinates. The following steps are taken to obtain z_{mod} in terms of z - .

- The global dimensional z coordinate $\tilde{z}$ in terms of the local coordinate is given by

$$\tilde{z} = \tilde{z}_{mod} + \tilde{L} \tag{4.2}$$

  where $\tilde{L}$ is the dimensional depth of plate.

- The dimensionless global coordinate is given by

$$z = \frac{\tilde{z}_{mod}}{H} + \frac{\tilde{L}}{H} = \frac{\tilde{z}_{mod}}{H} + L \tag{4.3}$$

  where L is the dimensionless depth of the plate.

- The relation between the dimensional and dimensionless local coordinate is given by

$$\tilde{z}_{mod} = (H - \tilde{L}) z_{mod} \tag{4.4}$$

  The domain depth H is used as a normalizing factor in the global coordinate system. With regard to local tip coordinate system, the tip domain depth is $H - \tilde{L}$, and is hence used as the normalizing factor. This is essentially a scaling.

- Substituting Equation 4.4 in Equation 4.3, we get the local dimensionless coordinate in terms of the global dimensionless coordinate as

$$z_{mod} = \frac{z - L}{1 - L} \tag{4.5}$$

The Z eigen modes for the homogeneous component of the tip domain are given as

$$Z_{xx}^{(4-)}(z) = Z_{xx}^{(1)}(z_{mod}), \quad Z_{xz}^{(4-)}(z) = Z_{xz}^{(1)}(z_{mod}), \quad Z_{x}^{(4-)}(z) = Z_{x}^{(1)}(z_{mod}), \quad Z_{z}^{(4-)}(z) = Z_{z}^{(1)}(z_{mod}) \tag{4.6}$$

$$Z_{xx}^{(4+)}(z) = Z_{xx}^{(3)}(z_{mod}), \quad Z_{xz}^{(4+)}(z) = Z_{xz}^{(3)}(z_{mod}), \quad Z_{x}^{(4+)}(z) = Z_{x}^{(3)}(z_{mod}), \quad Z_{z}^{(4+)}(z) = Z_{z}^{(3)}(z_{mod}) \tag{4.7}$$

4.3 Solution to the problem of cavity in the waveguide for interaction stress imposed on locations on Domain 1 or 3 boundary

This section describes the solution procedure adopted for obtaining the stresses and displacements due to the a stress on any location on domain 1 or 3 boundary. Intermediate locations refer to all locations on the soil boundary except the first and last location. The first location is referred to as the top location and the last location as the corner at the tip. The following steps are taken when solving the system for a normal interaction stress imposed on an intermediate or top location on domain 1. Similar steps can be taken for a shear stress on domain 1 boundary and normal and shear stress imposed on domain 3 boundary.

4.3.1 Boundary and interface Conditions

At $x{=}{-}R$, the boundary and interface conditions imposed are

$$\sigma_{xx}^{(1)}(x = -R, z) = \sum_{n=1}^{\infty} C_n^{(1)} X_n^{(1)}(-R) Z_{xx;n}^{(1)}(z) = \begin{cases} F(z, z_m) & \text{for } z{=}\ 0 \text{ to } L \\ \sigma_{xx}^{(4,h)}(x = -R, z) & \text{for } z{=}L \text{ to } 1 \end{cases}$$

$$\sigma_{xz}^{(1)}(x = -R, z) = \sum_{n=1}^{\infty} C_n^{(1)} X_n^{(1)}(-R) Z_{xz;n}^{(1)}(z) = 0 = \begin{cases} & \text{for } z = 0 \text{ to } L \\ \sigma_{xz}^{(4,h)}(x = -R, z) & \text{for } z = L \text{ to } 1 \end{cases}$$

$$\begin{aligned} u_x^{(1)}(x = -R, z) &= \sum_{n=1}^{\infty} C_n^{(1)} X_n^{(1)}(-R) Z_{x;n}^{(1)}(z) = u_x^{(4,h)}(x = -R, z) \quad \text{for } z = L \text{ to } 1 \\ u_z^{(1)}(x = -R, z) &= \sum_{n=1}^{\infty} C_n^{(1)} X_n^{(1)}(-R) Z_{z;n}^{(1)}(z) = u_z^{(4,h)}(x = -R, z) \quad \text{for } z = L \text{ to } 1 \end{aligned} \tag{4.8}$$

where $F(z, z_m)$ is the triangular stress as described in Equation 3.4. The superscript h is used to indicate that this is the homogeneous component of the tip domain. Similarly the boundary and interface conditions at $x = R$ are given as

$$\begin{aligned}
\sigma_{xx}^{(3)}(x=R,z) &= \sum_{n=1}^{\infty} C_n^{(3)} X_n^{(3)}(R) Z_{xx;n}^{(3)}(z) = \begin{cases} 0 & \text{for } z = 0 \text{ to } L \\ \sigma_{xx}^{(4,h)}(x=R,z) & \text{for } z = L \text{ to } 1 \end{cases} \\
\sigma_{xz}^{(3)}(x=R,z) &= \sum_{n=1}^{\infty} C_n^{(3)} X_n^{(3)}(R) Z_{xz;n}^{(3)}(z) = 0) = \begin{cases} 0 & \text{for } z = 0 \text{ to } L \\ \sigma_{xz}^{(4,h)}(x=R,z) & \text{for } z = L \text{ to } 1 \end{cases} \\
u_x^{(3)}(x=R,z) &= \sum_{n=1}^{\infty} C_n^{(3)} X_n^{(3)}(R) Z_{x;n}^{(3)}(z) = u_x^{(4,h)}(x=R,z) \quad \text{for } z = L \text{ to } 1 \\
u_z^{(3)}(x=R,z) &= \sum_{n=1}^{\infty} C_n^{(3)} X_n^{(3)}(R) Z_{z;n}^{(3)}(z) = u_z^{(4,h)}(x=R,z) \quad \text{for } z = L \text{ to } 1
\end{aligned} \tag{4.9}$$

where the stresses and displacements in the tip domain are given as

$$\begin{aligned}
\sigma_{xx}^{(4,h)} &= \sum_{n=1}^{\infty} C_n^{(4+)} X_n^{(4+,h)} Z_{xx;n}^{(4+,h)}(z) + \sum_{n=1}^{\infty} C_n^{(4-)} X_n^{(4-,h)} Z_{xx;n}^{(4-,h)}(z) \\
\sigma_{xz}^{(4,h)} &= \sum_{n=1}^{\infty} C_n^{(4+)} X_n^{(4+,h)} Z_{xz;n}^{(4+,h)}(z) + \sum_{n=1}^{\infty} C_n^{(4-)} X_n^{(4-,h)} Z_{xz;n}^{(4-,h)}(z) \\
u_x^{(4,h)} &= \sum_{n=1}^{\infty} C_n^{(4+)} X_n^{(4+,h)} Z_{x;n}^{(4+,h)}(z) + \sum_{n=1}^{\infty} C_n^{(4-)} X_n^{(4-,h)} Z_{x;n}^{(4-,h)}(z) \\
u_z^{(4,h)} &= \sum_{n=1}^{\infty} C_n^{(4+)} X_n^{(4+,h)} Z_{z;n}^{(4+,h)}(z) + \sum_{n=1}^{\infty} C_n^{(4-)} X_n^{(4-,h)} Z_{z;n}^{(4-,h)}(z)
\end{aligned} \tag{4.10}$$

where $X_n^{(4+)} = e^{-ik_{x;n}x}$ and $X_n^{(4-)} = e^{+ik_{x;n}x}$. Waves travelling in both directions $x = -R$ and $x = R$ should be considered to obtain the total solution for the tip domain.

4.3.2 Solving the overdetermined system

To solve the system of equations, we multiply each of the 12 boundary and interface conditions with a particular eigen function and integrate over z to obtain a truncated set of linear equations [11]. This can be written as

$$\int_0^L \sigma_{xx;n}^{(1)}(x=-R,z) Z_{x;q}^{(1)}(z) dz = \int_0^L F(z,z_m) Z_{x;q}^{(1)}(z).dz \tag{1.11}$$

$$\int_L^1 \sigma_{xx;n}^{(1)}(x=-R,z) Z_{x;q}^{(1)}(z) dz = \int_L^1 \sigma_{xx;n}^{(4,h)}(x=-R,z) Z_{x;q}^{(1)}(z) dz \tag{1.12}$$

$$\int_0^L \sigma_{xz;n}^{(1)}(x=-R,z) Z_{z;q}^{(1)}(z) dz = 0 \tag{1.13}$$

$$\int_L^1 \sigma_{xz;n}^{(1)}(x=-R,z) Z_{z;q}^{(1)}(z) dz = \int_L^1 \sigma_{xz;n}^{(4,h)}(x=-R,z) Z_{z;q}^{(1)}(z) dz \tag{1.14}$$

$$\int_L^1 u_{x;n}^{(1)}(x=-R,z) Z_{xx;q}^{(4-,i)}(z) dz = \int_L^1 u_{x;n}^{(4,h)}(x=-R,z) Z_{xx;q}^{(4-,h)}(z) dz \tag{1.15}$$

$$\int_L^1 u_{z;n}^{(1)}(x=-R,z) Z_{xz;q}^{(4-,h)}(z) dz = \int_L^1 u_{z;n}^{(4,h)}(x=-R,z) Z_{xz;q}^{(4-,h)}(z) dz \tag{1.16}$$

$$\int_0^L \sigma_{xx;n}^{(3)}(x=R,z) Z_{x;q}^{(3)}(z) dz = 0 \tag{1.17}$$

$$\int_L^1 \sigma_{xx;n}^{(3)}(x=R,z) Z_{x;q}^{(3)}(z) dz = \int_L^1 \sigma_{xx;n}^{(4,h)}(x=R,z) Z_{x;q}^{(3)}(z) dz \tag{1.18}$$

$$\int_0^L \sigma_{xz;n}^{(3)}(x=R,z)Z_{z;q}^{(3)}(z)dz = 0 \tag{1.19}$$

$$\int_L^1 \sigma_{xz;n}^{(3)}(x=R,z)Z_{z;q}^{(3)}(z)dz = \int_L^1 \sigma_{xz;n}^{(4,h)}(x=R,z)Z_{z;q}^{(3)}(z)dz \tag{1.20}$$

$$\int_L^1 u_{x;n}^{(3)}(x=R,z)Z_{xx;q}^{(4+,h)}(z)dz = \int_L^1 u_{x;n}^{(4,h)}(x=R,z)Z_{xx;q}^{(4+,h)}(z)dz \tag{1.21}$$

$$\int_L^1 u_{z;n}^{(3)}(x=R,z)Z_{xz;q}^{(4+,h)}(z)dz = \int_L^1 u_{z;n}^{(4,h)}(x=R,z)Z_{xz;q}^{(4+,h)}(z)dz \tag{1.22}$$

The respective relations for the stresses and displacements in the individual domains are substituted to obtain the final equations. Here $n = q$. These are then be reduced to matrix form given as

$$A_{qn}^{(1)}C_n^{(1)} = P_q^{(1)} \tag{4.23}$$

$$B_{qn}^{(1)}C_n^{(1)} = D_{qn}^{(4+)}C_n^{(4+)} + D_{qn}^{(4-)}C_n^{(4-)} \tag{4.24}$$

$$E_{qn}^{(1)}C_n^{(1)} = 0 \tag{4.25}$$

$$G_{qn}^{(1)}C_n^{(1)} = H_{qn}^{(4+)}C_n^{(4+)} + H_{qn}^{(4-)}C_n^{(4-)} \tag{4.26}$$

$$I_{qn}^{(1)}C_n^{(1)} = J_{qn}^{(4+)}C_n^{(4+)} + J_{qn}^{(4-)}C_n^{(4-)} \tag{4.27}$$

$$K_{qn}^{(3)}C_n^{(3)} = M_{qn}^{(4+)}C_n^{(4+)} + M_{qn}^{(34-)}C_n^{(4-)} \tag{4.28}$$

$$N_{qn}^{(3)}C_n^{(3)} = 0 \tag{4.29}$$

$$O_{qn}^{(3)}C_n^{(3)} = Q_{qn}^{(34+)}C_n^{(4+)} + Q_{qn}^{(34-)}C_n^{(4-)} \tag{4.30}$$

$$S_{qn}^{(3)}C_n^{(3)} = 0 \tag{4.31}$$

$$T_{qn}^{(3)}C_n^{(3)} = U_{qn}^{(34+)}C_n^{(4+)} + U_{qn}^{(34-)}C_n^{(4-)} \tag{4.32}$$

$$V_{qn}^{(3)}C_n^{(3)} = W_{qn}^{(34+)}C_n^{(4+)} + W_{qn}^{(34-)}C_n^{(4-)} \tag{4.33}$$

$$X_{qn}^{(3)}C_n^{(3)} = Y_{qn}^{(34+)}C_n^{(4+)} + Y_{qn}^{(34-)}C_n^{(4-)} \tag{4.34}$$

where

$$\begin{aligned}
A_{qn}^{(1)} &= X_n^{(1)}(-R)\int_0^L Z_{xx;n}^{(1)}(z)Z_{x;q}^{(1)}(z)dz \\
P_q^{(1)} &= \int_0^L F(z,z_m)Z_{x;q}^{(1)}(z)dz \\
B_{qn}^{(1)} &= X_n^{(1)}(-R)\int_L^1 Z_{xx;n}^{(1)}(z)Z_{x;q}^{(1)}(z)dz \\
D_{qn}^{(4+)} &= X_n^{(4+,h)}(-R)\int_L^1 Z_{xx;n}^{(4+,h)}(z)Z_{x;q}^{(1)}(z)dz \\
D_{qn}^{(4-)} &= X_n^{(4-,h)}(-R)\int_L^1 Z_{xx;n}^{(4-,h)}(z)Z_{x;q}^{(1)}(z)dz
\end{aligned} \tag{4.35}$$

$$\begin{aligned}
E_{qn}^{(1)} &= X_n^{(1)}(-R)\int_0^L Z_{xz;n}^{(1)}(z)Z_{z;q}^{(1)}(z)dz \\
G_{qn}^{(1)} &= X_n^{(1)}(-R)\int_L^1 Z_{xz;n}^{(1)}(z)Z_{z;q}^{(1)}(z)dz \\
H_{qn}^{(4+)} &= X_n^{(4+,h)}(-R)\int_L^1 Z_{xz;n}^{(4+,h)}(z)Z_{z;q}^{(1)}(z)dz \\
H_{qn}^{(4-)} &= X_n^{(4-,h)}(-R)\int_L^1 Z_{xz;n}^{(4-,h)}(z)Z_{z;q}^{(1)}(z)dz
\end{aligned} \tag{4.36}$$

$$
\begin{aligned}
I_{qn}^{(1)} &= X_n^{(1)}(-R)\int_L^1 Z_{x;n}^{(1)}(z)Z_{xx;q}^{(4-,h)}(z)dz \\
J_{qn}^{(4+)} &= X_n^{(4+,h)}(-R)\int_L^1 Z_{x;n}^{(4+,h)}(z)Z_{xx;q}^{(4-,h)}(z)dz \\
J_{qn}^{(4-)} &= X_n^{(4-,h)}(-R)\int_L^1 Z_{x;n}^{(4-,h)}(z)Z_{xx;q}^{(4-,h)}(z)dz
\end{aligned} \tag{4.37}
$$

$$
\begin{aligned}
K_{qn}^{(1)} &= X_n^{(1)}(-R)\int_L^1 Z_{z;n}^{(1)}(z)Z_{xz;q}^{(4-,h)}(z)dz \\
M_{qn}^{(4+)} &= X_n^{(4+,h)}(-R)\int_L^1 Z_{z;n}^{(4+,h)}(z)Z_{xz;q}^{(4-,h)}(z)dz \\
M_{qn}^{(4-)} &= X_n^{(4-,h)}(-R)\int_L^1 Z_{z;n}^{(4-,h)}(z)Z_{xz;q}^{(4-,h)}(z)dz
\end{aligned} \tag{4.38}
$$

$$
\begin{aligned}
N_{qn}^{(3)} &= X_n^{(3)}(R)\int_0^L Z_{xx;n}^{(3)}(z)Z_{x;q}^{(3)}(z)dz \\
O_{qn}^{(3)} &= X_n^{(3)}(R)\int_L^1 Z_{xx;n}^{(3)}(z)Z_{x;q}^{(3)}(z)dz \\
Q_{qn}^{(4+)} &= X_n^{(4+,h)}(R)\int_L^1 Z_{xx;n}^{(4+,h)}(z)Z_{x;q}^{(3)}(z)dz \\
Q_{qn}^{(4-)} &= X_n^{(4-,h)}(R)\int_L^1 Z_{xx;n}^{(4-,h)}(z)Z_{x;q}^{(3)}(z)dz
\end{aligned} \tag{4.39}
$$

$$
\begin{aligned}
S_{qn}^{(3)} &= X_n^{(3)}(R)\int_0^L Z_{xz;n}^{(3)}(z)Z_{z;q}^{(3)}(z)dz \\
T_{qn}^{(3)} &= X_n^{(3)}(R)\int_L^1 Z_{xz;n}^{(3)}(z)Z_{z;q}^{(3)}(z)dz \\
U_{qn}^{(4+)} &= X_n^{(4+,h)}(R)\int_L^1 Z_{xz;n}^{(4+,h)}(z)Z_{z;q}^{(3)}(z)dz \\
U_{qn}^{(4-)} &= X_n^{(4-,h)}(R)\int_L^1 Z_{xz;n}^{(4-,h)}(z)Z_{z;q}^{(3)}(z)dz
\end{aligned} \tag{4.40}
$$

$$
\begin{aligned}
V_{qn}^{(3)} &= X_n^{(3)}(R)\int_L^1 Z_{x;n}^{(3)}(z)Z_{xx;q}^{(4+,h)}(z)dz \\
W_{qn}^{(4+)} &= X_n^{(4+,h)}(R)\int_L^1 Z_{x;n}^{(4+,h)}(z)Z_{xx;q}^{(4+,h)}(z)dz \\
G_{qn}^{(4-)} &= X_n^{(4-,h)}(R)\int_L^1 Z_{x;n}^{(4-,h)}(z)Z_{xx;q}^{(4+,h)}(z)dz
\end{aligned} \tag{4.41}
$$

$$
\begin{aligned}
X_{qn}^{(3)} &= X_n^{(3)}(R)\int_L^1 Z_{z;n}^{(3)}(z)Z_{xz;q}^{(4+,h)}(z)dz \\
Y_{qn}^{(4+)} &= X_n^{(4+,h)}(R)\int_L^1 Z_{z;n}^{(4+,h)}(z)Z_{xz;q}^{(4+,h)}(z)dz \\
Y_{qn}^{(4-)} &= X_n^{(4-,h)}(R)\int_L^1 Z_{z;n}^{(4-,h)}(z)Z_{xz;q}^{(4+,h)}(z)dz
\end{aligned} \tag{4.42}
$$

The overdetermined system of equations is solved in one go using the pseudo inverse (For more detail refer to Appendix B). Equation 4.23 to Equation 4.34 are combined as follows.

$$
\begin{bmatrix}
[A_{qn}^{(1)}] & 0 & 0 & 0 \\
\vdots & \vdots & \vdots & \vdots \\
[K_{qn}^{(1)}] & [M_{qn}^{(4+)}] & [M_{qn}^{(4-)}] & 0 \\
0 & 0 & 0 & [N_{qn}^{(3)}] \\
\vdots & \vdots & \vdots & \vdots \\
0 & [Y_{qn}^{(4+)}] & [Y_{qn}^{(4-)}] & [X_{qn}^{(3)}]
\end{bmatrix}_{12q\times 4n}
\begin{bmatrix} C_n^{(1)} \\ C_n^{(4+)} \\ C_n^{(4-)} \\ C_n^{(3)} \end{bmatrix}_{4n\times 1}
=
\begin{bmatrix} [P_n^{(1)}] \\ \vdots \\ 0 \\ 0 \\ \vdots \\ 0 \end{bmatrix}_{12q\times 1} \tag{4.43}
$$

This can be represented as

$$\mathbf{DC} = \mathbf{P} \implies \mathbf{C} = \mathbf{D^{-1}P} \tag{4.44}$$

where $\mathbf{D^{-1}}$ refers to the pseudo inverse. Using these coefficients, the stresses and displacements for all the soil domains can be determined. The following changes need to implemented to find the stresses and displacements for shear stress imposed at domain 1 boundary and a normal and shear stress imposed on the domain 3 boundary. For the shear stress imposed on domain 1

$$P_q^{(1)} = \int_0^L F(z, z_m) Z_{z;q}^{(1)}(z) dz \tag{4.45}$$

This should be added to the right side of Equation 4.25
For normal stress on domain 3

$$P_q^{(3)} = \int_0^L F(z, z_m) Z_{x;q}^{(3)}(z) dz \tag{4.46}$$

This should be added to the right side of Equation 4.29
For shear stress on domain 3

$$P_q^{(3)} = \int_0^L F(z, z_m) Z_{z;q}^{(3)}(z) dz \tag{4.47}$$

This should be added to the right side of Equation 4.31

Additionally, the right side of Equation 4.24 is made zero for each of the above cases. It should be noted that it is the multiplication with the Z eigen modes that varies for each case depending on the stress that is imposed. The entire system of 12 equations should be solved in one go for stress imposed at each location.

The results for the analysis with a normal stress imposed at the top, intermediate and corner locations are discussed in section 1.6. The following section explains the analysis of the waveguide with cavity for stresses imposed on the tip domain.

4.4 Stress imposed on tip domain - Imhomogeneous component of the tip domain

The stresses and displacements due to an excitation imposed on locations on the surface of the tip domain form the inhomogeneous component of the tip domain, which stems due to the non-homogeneous boundary conditions of the tip domain. The imposed triangular stresses are similar to the stress imposed on domain 1 or 3 boundary, where the equivalent force due to the stress is unity. To represent this stress, an exponential fourier expansion is used. [25] has been used to obtain the expansion. Figure 4.2 shows the tip domain with a three locations as an example.

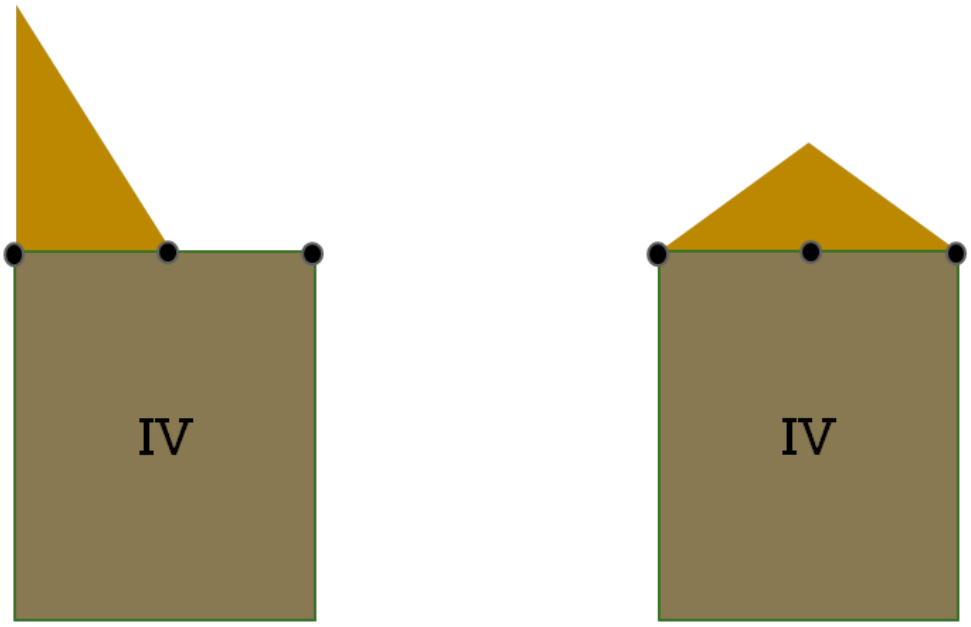

(a) ***Stress imposed at the corner*** **(b)** ***Stress imposed at an intermediate location***

Figure 4.2: ***Stress imposed on the tip domain***

4.4.1 Imposed stress as a Fourier expansion

Assuming the period of the function (triangular stress distribution) equal to the width of the tip domain i.e. $2R$, the fourier exponential expansion can be written as

$$F(x, x_r) = \sum_{p=-\infty}^{\infty} C_{p;r} e^{i2\pi nx/2R} = \sum_{p=-N}^{N} C_{p;r} e^{i\pi nx/R} \tag{4.48}$$

where $2N + 1$ fourier components are considered. Here $F(x, x_r)$ represents the triangular stress distribution imposed on the tip. x_r represents the rth location on the tip domain. The unknown coefficients can then be derived as

$$C_{m;r} = \frac{1}{2R} \int_{-R}^{R} F(x, x_r) e^{-i\pi mx/R} dx \tag{4.49}$$

Equation 4.49 can be obtained using the orthogonality property of the exponential components.

$$\int_{-R}^{R} e^{i\pi nx/R} e^{-i\pi mx/R} dx = 2R\delta_{nm} \tag{4.50}$$

4.4.2 Convergence of stresses

A convergence study was done to obtain the minimum number of Fourier components required for a converged stress profile for each segment length. This is important to obtain accurate Z functions for the domain across its width ($-R$ to R). This is shown in Figure 4.3 for the tip discretized by two segments (3 locations), and a normal stress imposed on the intermediate (in this case, second) location.

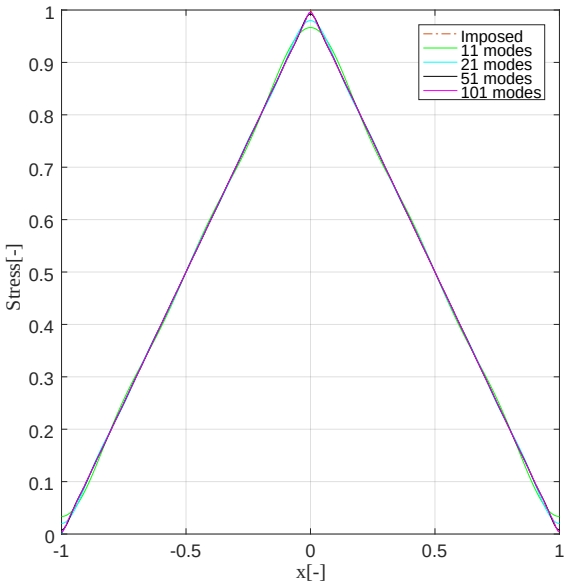

Figure 4.3: ***Tip Domain with 3 locations - Normal Stress imposed on the intermediate location - Convergence plot***

Table 4.1 gives the number of fourier components to be considered for each segment length. Up to 6 segments were considered for the discretization. It should be noted that the number of components is based on the stresses imposed on the corner location, whose peak magnitude is twice that of the intermediate stresses distributed over half the length.

Table 4.1: ***Number of segments vs number of fourier components for the tip required for convergence***

Number of segments	*Length of segment[-]*	*Number of modes*
2	1	51
4	0.5	75
6	0.33	101

4.4.3 Obtaining the inhomogeneous component of the tip domain

The inhomogeneous component of the tip domain can be obtained using the displacement and stress functions for the soil medium and the inhomogeneous boundary conditions. The general expressions for the displacements and stresses are summarized for convenience.

$$\begin{aligned} u_x &= \partial_x\phi - \partial_z\psi \\ u_z &= \partial_x\psi + \partial_z\phi \\ \sigma_{xx} &= (\upsilon^2 - 2)(\partial_x^2\phi + \partial_z^2\phi) + 2\partial_x^2\phi - 2\partial_x\partial_z\psi \\ \sigma_{zz} &= (\upsilon^2 - 2)(\partial_x^2\phi + \partial_z^2\phi) + 2\partial_x^2\phi + 2\partial_x\partial_z\psi \\ \sigma_{xz} &= 2\partial_x\partial_z\phi + \partial_x^2\psi - \partial_z^2\psi \end{aligned} \tag{4.51}$$

Substituting the expressions for potentials (obtained from Equation 2.34 into Equation 4.51) , the displacement and stress inhomogeneous components for a stress imposed at location x_p

can be represented as

$$\begin{aligned} u_{x;p}^{(4,i;r)} &= X_p^{(4,i)} Z_{x;p}^{(4,i;r)} \\ u_{z;p}^{(4,i;r)} &= X_p^{(4,i)} Z_{z;p}^{(4,i;r)} \\ \sigma_{xx;p}^{(4,i;r)} &= X_p^{(4,i)} Z_{xx;p}^{(4,i;r)} \\ \sigma_{zz;p}^{(4,i;r)} &= X_p^{(4,i)} Z_{zz;p}^{(4,i;r)} \\ \sigma_{xz;p}^{(4,i;r)} &= X_p^{(4,i)} Z_{xz;p}^{(4,i;r)} \end{aligned} \tag{4.52}$$

where $X_p^{(4,i)} = e^{ik_{x;p}x}$. The boundary conditions for the tip domain for the case of an imposed normal stress are given by

$$\begin{aligned} u_x(x, z = H) &= 0 \\ u_z(x, z = H) &= 0 \\ \sigma_{xz}(x, z = L) &= 0 \\ \sigma_{zz}(x, z = L) &= \sum_{p=-N}^{N} C_{p;r} e^{i\pi n x/R} \end{aligned} \tag{4.53}$$

Comparing the expression for $X_p^{(4,i)}$ with the imposed fourier expansion, the horizontal wavenumbers $k_{x;n}^{(4,i)}$ for the tip domain can be obtained as

$$X_p^{(4,i)} = e^{ik_{x;p}^{(4,i)}x} = e^{i\pi p x/R} \tag{4.54}$$

giving

$$k_{x;p}^{(4,i)} = \pi p/R \tag{4.55}$$

We use Equation 4.55 and the inhomogeneous boundary conditions to obtain the Z functions for the tip domain. Hence, we can solve for the unknown coefficients $B_{p1;p}^{(4,i;r)}$,$B_{s1;p}^{(4,i;r)}$,$B_{p2;p}^{(4,i;r)}$ and $B_{s2;p}^{(4,i;r)}$ for each fourier component using the boundary conditions in Equation 4.53 as

$$\begin{bmatrix} P_{Z_x^{(4,i)}(z=H)} & Q_{Z_x^{(4,i)}(z=H)} & S_{Z_x^{(4,i)}(z=H)} & T_{Z_x^{(4,i)}(z=H)} \\ P_{Z_z^{(4,i)}(z=H)} & Q_{Z_z^{(4,i)}(z=H)} & S_{Z_z^{(4,i)}(z=H)} & T_{Z_z^{(4,i)}(z=H)} \\ P_{Z_{xz}^{(4,i)}(z=L)} & Q_{Z_{xz}^{(4,i)}(z=L)} & S_{Z_{xz}^{(4,i)}(z=L)} & T_{Z_{xz}^{(4,i)}(z=L)} \\ P_{Z_{zz}^{(4,i)}(z=L)} & Q_{Z_{zz}^{(4,i)}(z=L)} & S_{Z_{zz}^{(4,i)}(z=L)} & T_{Z_{zz}^{(4,i)}(z=L)} \end{bmatrix} \begin{bmatrix} B_{p1;p}^{(4,i)} \\ B_{p2;p}^{(4,i)} \\ B_{s1;p}^{(4,i)} \\ B_{s2;p}^{(4,i)} \end{bmatrix} = \begin{bmatrix} 0 \\ 0 \\ 0 \\ C_{p;r} \end{bmatrix} \tag{4.56}$$

where P, Q, S and T are the corresponding multipliers of the coefficients $B_{p1;p}^{(4,i;r)}$,$B_{s1;p}^{(4,i;r)}$,$B_{p2;p}^{(4,i;r)}$ and $B_{s2;p}^{(4,i;r)}$ in the inhomogeneous set of boundary conditions. The inhomogeneous displacement and stress fields can then be obtained as

$$\begin{aligned} u_x^{(4,i;r)} &= \sum_{p=-N}^{N} X_p^{(4,i)} Z_{x;p}^{(4,i;r)} \\ u_z^{(4,i;r)} &= \sum_{p=-N}^{N} X_p^{(4,i)} Z_{z;p}^{(4,i;r)} \\ \sigma_{xx}^{(4,i;r)} &= \sum_{p=-N}^{N} X_p^{(4,i)} Z_{xx;p}^{(4,i;r)} \\ \sigma_{zz}^{(4,i;r)} &= \sum_{p=-N}^{N} X_p^{(4,i)} Z_{zz;p}^{(4,i;r)} \\ \sigma_{xz}^{(4,i;r)} &= \sum_{p=-N}^{N} X_p^{(4,i)} Z_{xz;p}^{(4,i;r)} \end{aligned} \tag{4.57}$$

Similarly, the stresses and displacements can also be obtained for imposed shear stress on the tip domain.

4.4.4 Solution for waveguide with a cavity for stress imposed on the tip domain

The obtained inhomogeneous components are now added to the homogeneous components of the tip domain to obtain the complete solution, which can be then used to solve for the stresses and displacements across all three domains.

At $x{=}{-}R$, the boundary and interface conditions imposed are

$$\begin{aligned}
\sigma_{xx}^{(1)}(x=-R,z) = \sum_{n=1}^{\infty} C_n^{(1)} X_n^{(1)}(-R) Z_{xx;n}^{(1)}(z) &= 0 && \text{for } z{=}\ 0 \text{ to } L \\
&= \sigma_{xx}^{(4,h)}(x=-R,z) + \sigma_{xx}^{(4,i;r)}(x=-R,z) && \text{for } z{=}L \text{ to } 1 \\
\sigma_{xz}^{(1)}(x=-R,z) = \sum_{n=1}^{\infty} C_n^{(1)} X_n^{(1)}(-R) Z_{xz;n}^{(1)}(z) &= 0 && \text{for } z = 0 \text{ to } L \\
&= \sigma_{xz}^{(4,h)}(x=-R,z) + \sigma_{xz}^{(4,i;r)}(x=-R,z) && \text{for } z = L \text{ to } 1 \\
u_{x}^{(1)}(x=-R,z) = \sum_{n=1}^{\infty} C_n^{(1)} X_n^{(1)}(-R) Z_{x;n}^{(1)}(z) &= u_{x}^{(4,h)}(x=-R,z) + u_{x}^{(4,i;r)}(x=-R,z) && \text{for } z = L \text{ to } 1 \\
u_{z}^{(1)}(x=-R,z) = \sum_{n=1}^{\infty} C_n^{(1)} X_n^{(1)}(-R) Z_{z;n}^{(1)}(z) &= u_{z}^{(4,h)}(x=-R,z) + u_{z}^{(4,i;r)}(x=-R,z) && \text{for } z = L \text{ to } 1
\end{aligned} \tag{4.58}$$

Similarly the boundary and interface conditions at $x = R$ are given as

$$\begin{aligned}
\sigma_{xx}^{(3)}(x=R,z) = \sum_{n=1}^{\infty} C_n^{(3)} X_n^{(3)}(R) Z_{xx;n}^{(3)}(z) &= 0 && \text{for } z = 0 \text{ to } L \\
&= \sigma_{xx}^{(4,h)}(x=R,z) + \sigma_{xx}^{(4,i;r)}(x=R,z) && \text{for z} = L \text{ to } 1 \\
\sigma_{xz}^{(3)}(x=R,z) = \sum_{n=1}^{\infty} C_n^{(3)} X_n^{(3)}(R) Z_{xz;n}^{(3)}(z) &= 0 && \text{for } z = 0 \text{ to } L \\
&= \sigma_{xz}^{(4,h)}(x=R,z) + \sigma_{xz}^{(4,i;r)}(x=R,z) && \text{for } z = L \text{ to } 1 \\
u_{x}^{(3)}(x=R,z) = \sum_{n=1}^{\infty} C_n^{(3)} X_n^{(3)}(R) Z_{x;n}^{(3)}(z) &= u_{x}^{(4,h)}(x=R,z) + u_{x}^{(4,i;r)}(x=R,z) && \text{for } z = L \text{ to } 1 \\
u_{z}^{(3)}(x=R,z) = \sum_{n=1}^{\infty} C_n^{(3)} X_n^{(3)}(R) Z_{z;n}^{(3)}(z) &= u_{z}^{(4,h)}(x=R,z) + u_{z}^{(4,i;r)}(x=R,z) && \text{for } z = L \text{ to } 1
\end{aligned} \tag{4.59}$$

The above functions were multiplied by a particular Z eigen function and integrated over the domain length. The choice of eigen mode is the same as shown in Equation 4.11 through 4.22. The set of equations are then solved in one go using pseudo-inverse to obtain the unknown coefficients.

4.5 Results - stress imposed at top and intermediate locations on domain 1 boundary and on the tip domain

This section discusses the main results for two sets of analysis - 1. Stress imposed on the domain 1 boundary, 2. Stress imposed on the tip (domain 4), for top and intermediate locations. Since this is a symmetric problem with respect to the global coordinate system, the results for stress imposed on the domain 3 boundary should be similar in magnitude (both stress and displacement profile). For the first study, up to 50 segments and 401 soil modes were considered. For the study with the tip domain, up to 6 segments were considered across the tip domain surface. Convergence studies were done to obtain the number of soil modes required for converged non-oscillatory displacement profiles for various segment lengths. The case for stress imposed at the corner location for both domain 1 and 4 will be explained in section 1.6.

4.5.1 Properties of the soil domain

Table 4.2 summarizes the domain properties used for the three domain analysis. The values used are chosen since the reference solution, which is used for validating the plate-soil interaction model, was evaluated for these values.

Table 4.2: ***Soil domain properties***

Parameter	***Value***	***Units***
Embedded length of plate(L)	50	m
Domain 1 or 3 depth (H)	100	m
Diameter(D)	2	m
Embedded Length/Diameter(L/D)	25	-

4.5.2 Normal stress imposed at mid location of domain 1 - stress and displacement profiles at domain 1 and 3 boundary

The results are shown for the case of a normal stress imposed at the intermediate location on the boundary of domain 1. For this case, domain 1 and 3 are discretized into 20 segments and 101 modes were found to give converged non-oscillatory displacement profiles. Figure 4.4 and Figure 4.5 show the normal and shear stresses at the boundary and interfaces between the domains considering 20 segments and 101 soil modes. This jump is expected since there is a change in material properties (from cavity to soil material). From Figure 4.6(a), the maximum displacement is obtained around $z = 0.25$, which is expected due to the peak of the normal stress triangle acting at that location. Continuity of stresses and displacements can be observed at the interface except close to the tip ($z = L$) as indicated in Figure 4.6(a). A slight discontinuity in displacements is observed close to the tip at both corners $x = -R, R$. This is a consequence of the imbalance of moments close to the corner and is explained in greater detail in section 1.6. We continue to work with these displacements since the relative difference between the displacements from domain 1 and 4 boundary as well as 3 and 4 at the tip was found to be less than 5 %, for stresses imposed at the top or intermediate locations in domain 1 or 3.

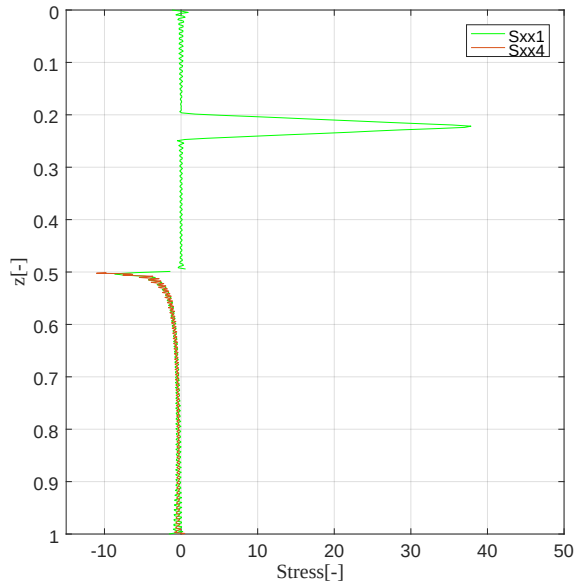

(a) $\sigma_{xx}^{(1)}$ ***and*** $\sigma_{xx}^{(4)}$ ***at*** $x = -R$

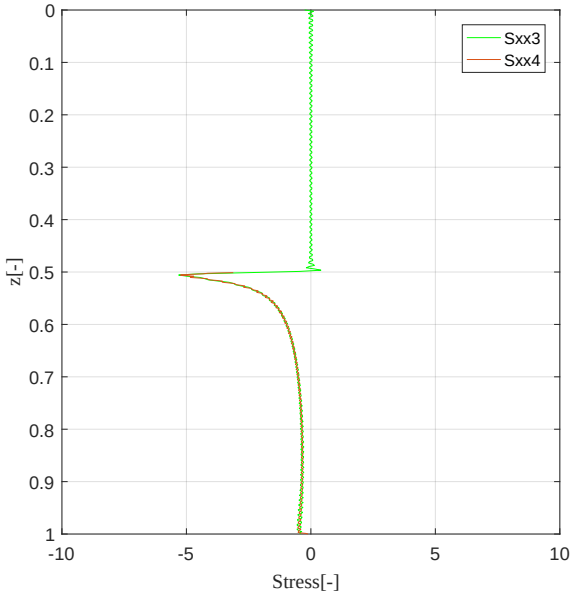

(b) $\sigma_{xx}^{(3)}$ ***and*** $\sigma_{xx}^{(4)}$ ***at*** $x = R$

Figure 4.4: ***Normal stresses*** σ_{xx} ***at the domain 1 and 3 boundaries and the interface between domain 1 and 4, 3 and 4 for*** $L = 0.5$ ***for a normal stress imposed at the mid location on Domain 1, considering 20 segments and 101 soil modes. Note: Each figure has a different scale to have a clear view of the stress profile***

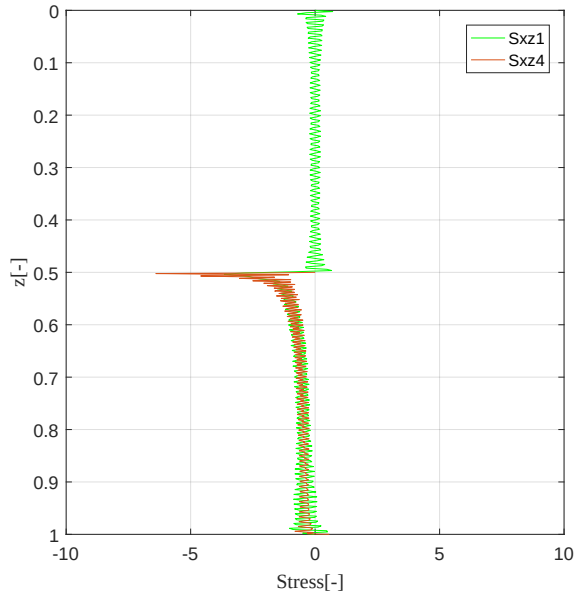

(c) $\sigma_{xz}^{(1)}$ ***and*** $\sigma_{xz}^{(4)}$ ***at*** $x = -R$

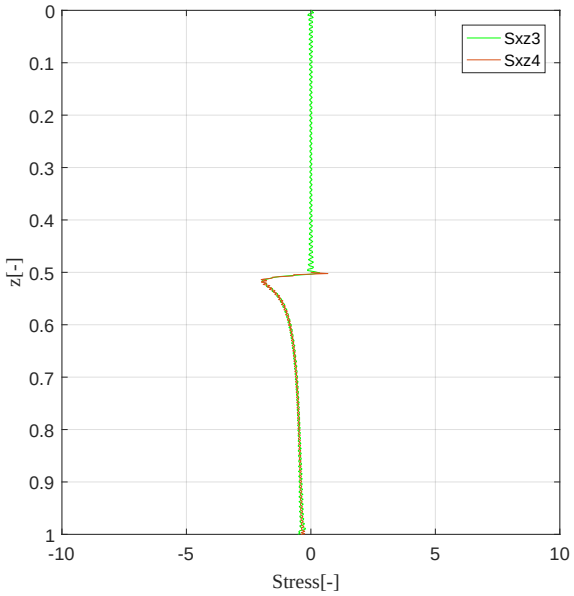

(d) $\sigma_{xz}^{(3)}$ ***and*** $\sigma_{xz}^{(4)}$ ***at*** $x = R$

Figure 4.5: ***Shear stresses*** σ_{xz}***at the domain 1 and 3 boundaries and the interface between domain 1 and 4, 3 and 4 for*** $L = 0.5$ ***for a normal stress imposed at the mid location on Domain 1, considering 20 segments and 101 soil modes. Note: Each figure has a different scale to have a clear view of the stress profile***

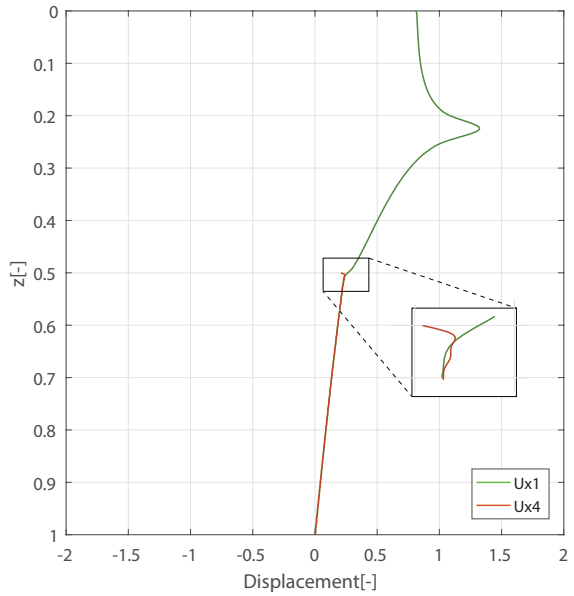

(a) $u_x^{(1)}$ ***and*** $u_x^{(4)}$ ***at*** $x = -R$

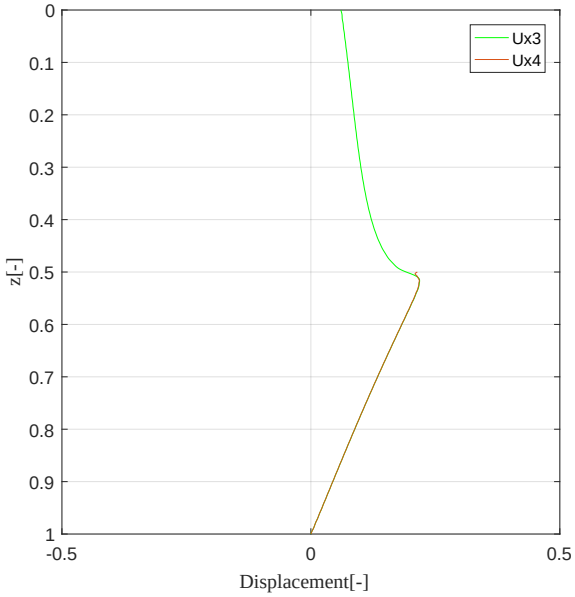

(b) $u_x^{(3)}$ ***and*** $u_x^{(4)}$ ***at*** $x = R$

Figure 4.6: ***Displacements*** u_x ***at the domain 1 and 3 boundaries and the interface between domain 1 and 4, 3 and 4 for*** $L = 0.5$ ***for a normal stress imposed at the mid location on domain 1, considering 20 segments and 101 soil modes. Note: Each figure has a different scale to have a clear view of the displacement profile***

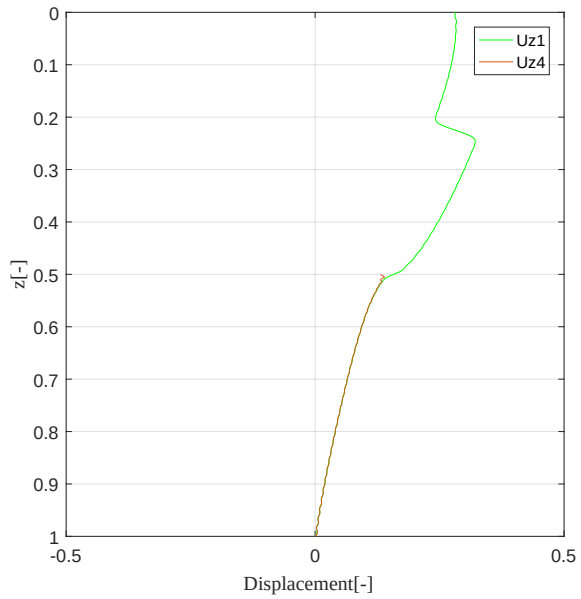

(a) $u_z^{(1)}$ ***and*** $u_z^{(4)}$ ***at*** $x = -R$

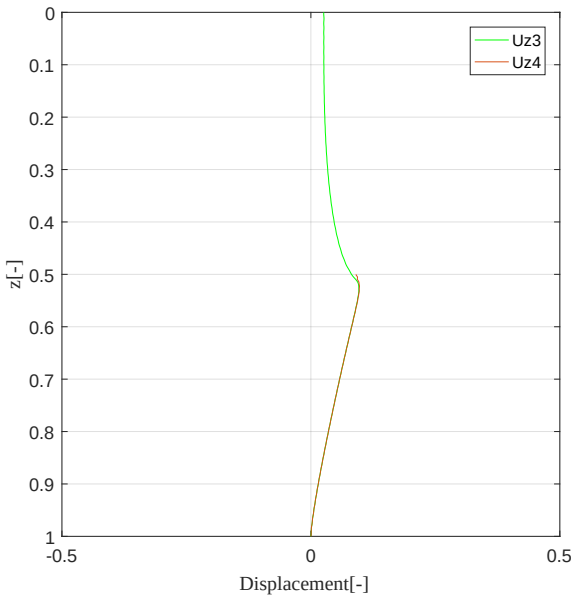

(b) $u_z^{(3)}$ ***and*** $u_z^{(4)}$ ***at*** $x = R$

Figure 4.7: ***Displacements*** u_z ***at the domain 1 and 3 boundaries and the interface between domain 1 and 4, 3 and 4 for*** $L = 0.5$ ***for a normal stress imposed at the mid location on domain 1, considering 20 segments and 101 soil modes. Note: Each figure has a different scale to have a clear view of the displacement profile***

4.5.3 Number of segments vs number of soil modes

Similar to the single domain analysis (refer section 3.2.1), the number of soil modes to the number of segments was obtained, so that the displacements are converged and non-oscillatory in nature. Up to 50 segments and 401 soil modes were considered across Domain 1 and 3. For the study, stress imposed at the top location and an intermediate location (in this case mid location) were used.

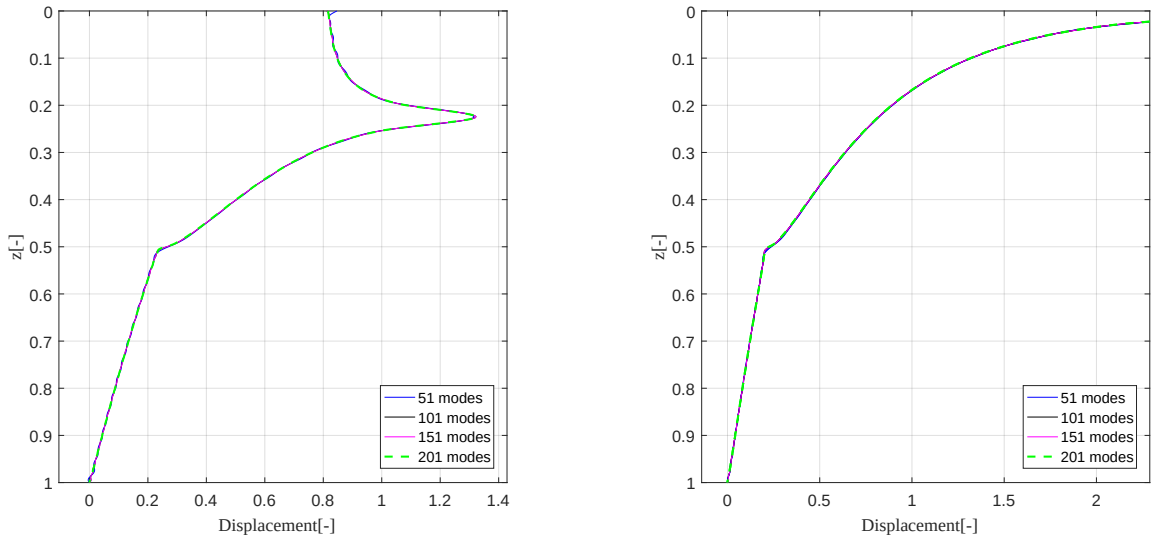

(a) ***Convergence plot - $u_x^{(1)}$ at $x = -R$ - Normal stress at mid location*** **(b)** ***Convergence plot - $u_x^{(1)}$ at $x = -R$ - Normal stress at top location***

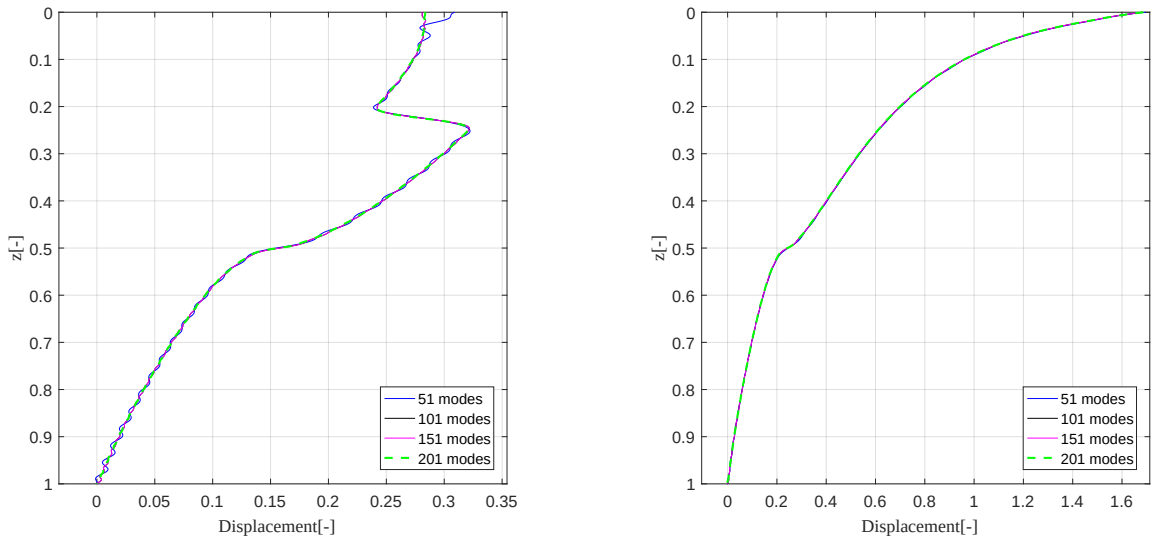

(c) ***Convergence plot - $u_z^{(1)}$ at $x = -R$ - Normal stress at mid location*** **(d)** ***Convergence plot - $u_z^{(1)}$ at $x = -R$ - Normal stress at top location***

Figure 4.8: ***Convergence plots for displacements - domain 1 discretized with 20 segments***

Figure 4.8(a) and (c) show the convergence plots for displacements u_x and u_z for normal stress acting on the mid location on domain 1 considering 20 segments. Figure 4.8(b) and (d) shows the convergence plots for displacements u_x and u_z for normal stress acting on the top location on Domain 1 considering 20 segments. The case of stress applied to the corner was currently not considered due to discontinuity in displacements observed at the tip corner. This will be discussed in detail later in section 1.6. Figure 4.9 shows the average

change in the displacements across the locations considering number of soil modes for two cases considered. These were calculated using the formula in Equation 3.11. These were used as the basis to obtain the number of soil modes required for different segment lengths.

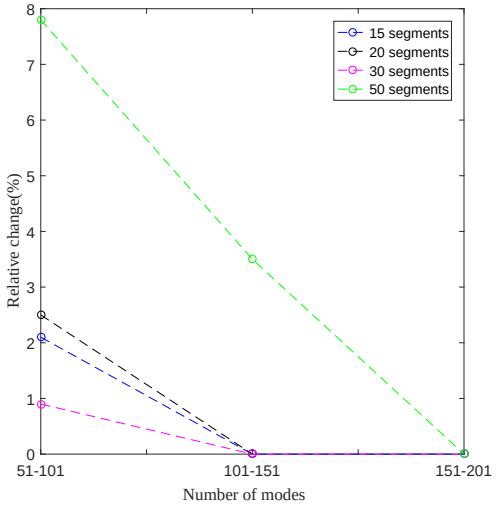

(a) ***Convergence plot - $u_x^{(1)}$ at $x = -R$ - Normal stress at mid location***

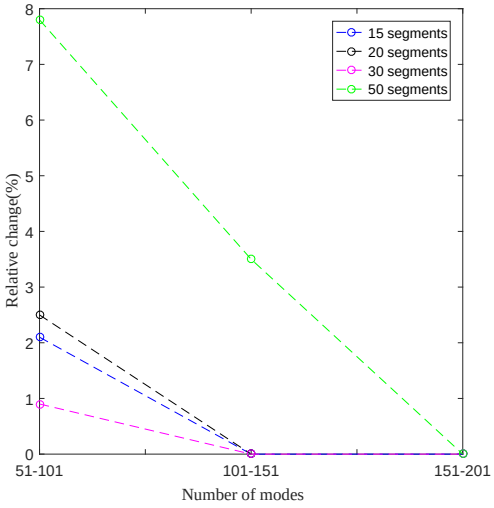

(b) ***Convergence plot - $u_x^{(1)}$ at $x = -R$ - Normal stress at top location***

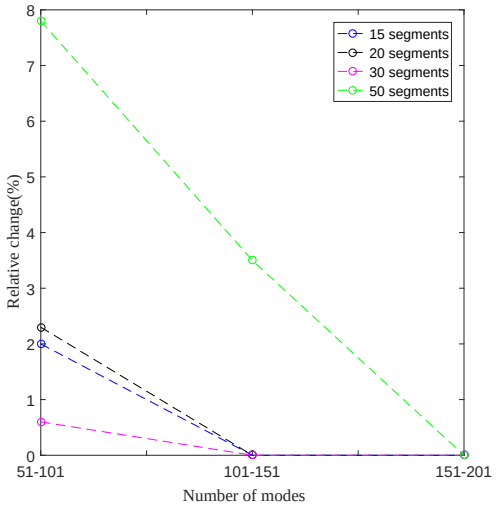

(c) ***Convergence plot - $u_z^{(1)}$ at $x = -R$ - Normal stress at mid location***

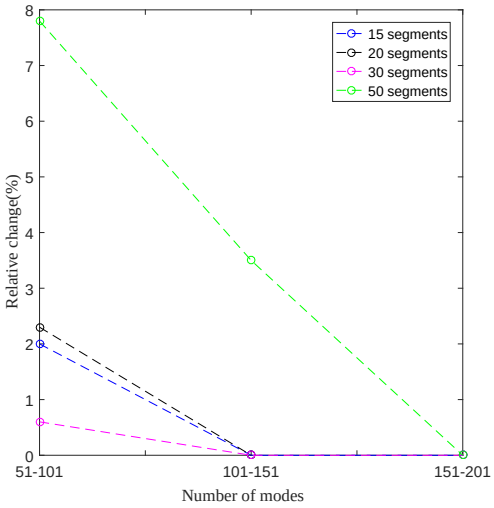

(d) ***Convergence plot - $u_z^{(1)}$ at $x = -R$ - Normal stress at top location***

Figure 4.9: ***Convergence plots for displacements with varying number of segments***

Based on the convergence plots, the number of soil modes required for each segment length is summarized in Table 4.3. The number of modes are selected such that there is no relative change in the displacements.

Table 4.3: ***Number of segments vs number of modes***

Number of segments	*Length of segment[-]*	*Number of modes*
15	0.1	51
20	0.05	101
30	0.033	101
50	0.02	201

4.5.4 Normal stress imposed on tip domain at an intermediate location

Figure 4.10 and Figure 4.11 shows the displacement profiles u_x and u_z respectively at $x = -R, R$ for a normal stress imposed at the tip at the fourth location. The tip is discretized using 4 segments. A slight mismatch in the displacements is observed at the corners, which has been explained in the following section. The number of soil modes utilized is the same as given in Table 4.4 (which shows the number of soil modes required at the corner) for stress imposed at each location at the tip, as these were found to be sufficient for non-oscillatory displacement profiles.

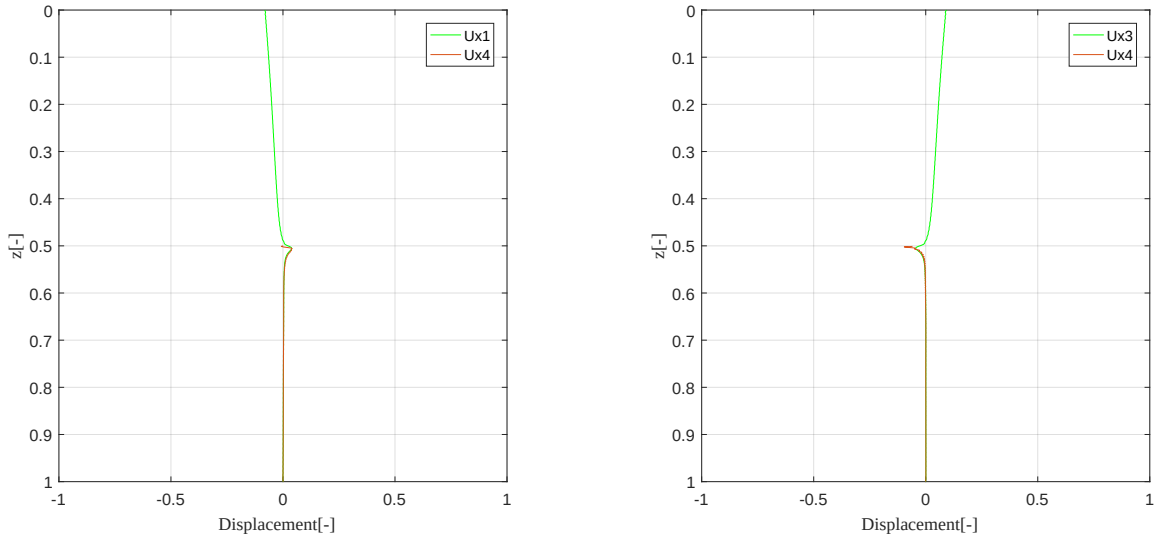

(a) $u_x^{(1)}$ ***and*** $u_x^{(4)}$ ***at*** $x = -R$ **(b)** $u_x^{(3)}$ ***and*** $u_x^{(4)}$ ***at*** $x = R$

Figure 4.10: ***Displacement profile of*** u_x ***at the the boundaries*** $x = -R, R$ ***for modified normal stress imposed at the tip on location 4, where the tip is discretized into 4 segments***

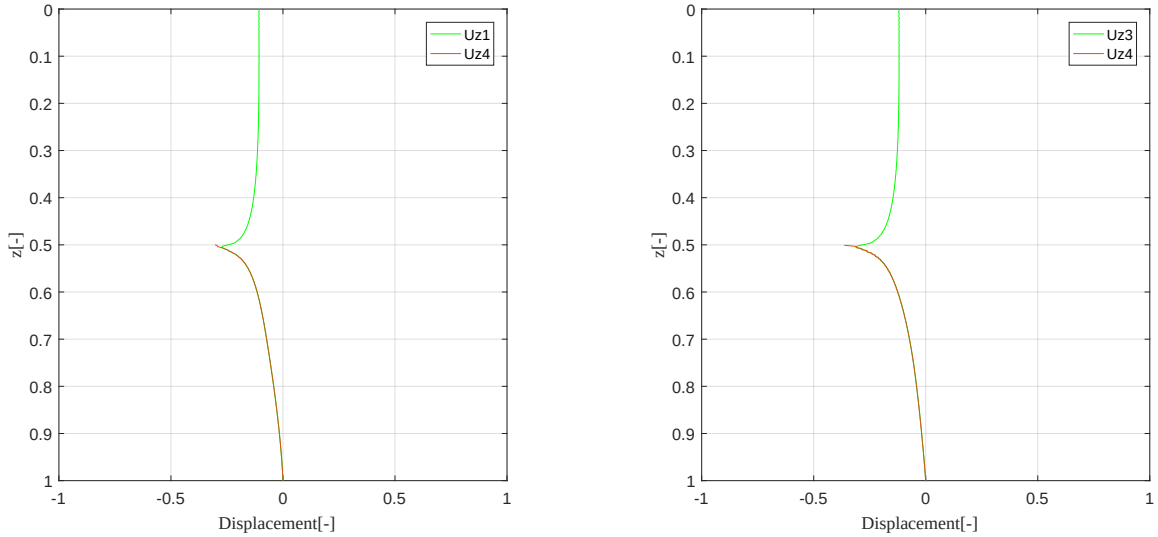

(c) $u_z^{(1)}$ ***and*** $u_z^{(4)}$ ***at*** $x = -R$ **(d)** $u_z^{(3)}$ ***and*** $u_z^{(4)}$ ***at*** $x = R$

Figure 4.11: ***Displacement profile of*** u_z ***at the the boundaries*** $x = -R, R$ ***for modified normal stress imposed at the tip on location 4, where the tip is discretized into 4 segments***

4.6 What happens at the corner?

This section describes two important aspects of the corner - 1. The imbalance of bending moment for the soil element in the tip domain close to the corner and 2. the large jump in stresses at the corner for the case of a shear or normal stress imposed at the corner location on both domain 1 and 4 boundaries. The section begins with a brief description on the physical phenomena that occurs at the corner followed by the results obtained when a stress is imposed at the corner. Discontinuity of displacements is observed for stresses imposed at any location on the boundary of any of the domains. This is observed to be more pronounced when the stress is imposed at the corner location on both domain 1 and 4 boundaries. Additionally, for the triangular stress distribution imposed at the corner of domain 4, the Gibbs phenomenon is observed. This is only dependent on the imposed stress distribution and the behavior of the fourier components close at a discontinuity and does not have anything to do with the physical phenomena observed at the corner. Due to the effects of the corner, two alternatives for the stress imposed at the corner location are suggested and the obtained results are shown.

4.6.1 Physical phenomena observed at the corner

Sharp corners in elastic media generally give rise to stress concentrations or stress jumps. This has been observed in multiple problems. *Maria Comninou* studied the problem of an elastic wedge on a half space with perfect contact ,where wedge angle above 77.5^0(including 90^0) gives irregularities in the stress field at the corner, when the wedge is relatively soft compared to the half space [8]. In Finite Element analysis, contact stress problems in elastic media close to sharp edges show sudden jumps, and are generally solved by increasing the discretization of the elements close to the edge. Another alternative suggested by *Hu.et.al* [19] was the use of higher order elements (using higher order polynomials - order higher than 2, to represent the displacement field) close to the edges. He studied the case of a 3D rectangular plate resting on elastic half space using direct boundary element method in combination with finite element method.

A jump in stresses is also observed at the corner in the current study for stresses imposed on the top or intermediate location, The behavior of the stress fields at the interface is however smoother, as compared to the case where the stress is imposed at the corner, where even large jumps in stresses are observed along with highly oscillatory stress fields at the interface. This is shown in Figure 4.12. The jump is seen in both normal and shear stress which could be since they are inherently coupled in a continua. Even though the stresses are highly oscillatory in nature, it is the convergence of the displacements that is most important to obtain the stiffness matrices. For locations at the corners, it was observed that the number of soil modes required for convergence was much higher than for the top and intermediate locations. This can be observed in the convergence plots in Figure 4.13 and is summarized in Table 4.4. The number of soil modes required for convergence for the corner location considering 20 segments,is already around 401 modes, hence increasing the discretization close to the corner is not the best alternatively for computational efficiency.

Figure 4.12 shows the shear and normal stress on domain 1 boundary for the case of a shear stress imposed at the corner. Figure 4.13 shows the convergence plots for the displacement profiles at the domain 1 boundary due to a shear stress acting at the corner location.

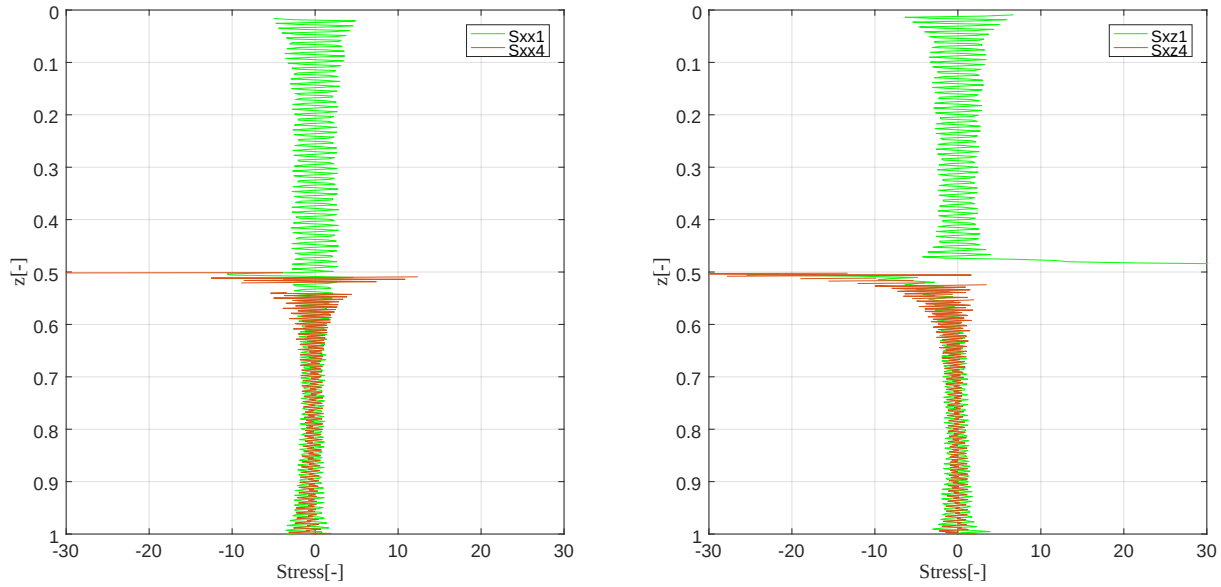

(a) $\sigma_{xx}^{(1)}$ ***and*** $\sigma_{xx}^{(4)}$ ***at*** $x = -R$ **(b)** $\sigma_{xz}^{(1)}$ ***and*** $\sigma_{xz}^{(4)}$ ***at*** $x = -R$

Figure 4.12: ***Shear stress imposed at the corner - stresses at the interface between Domain 1 and 4***

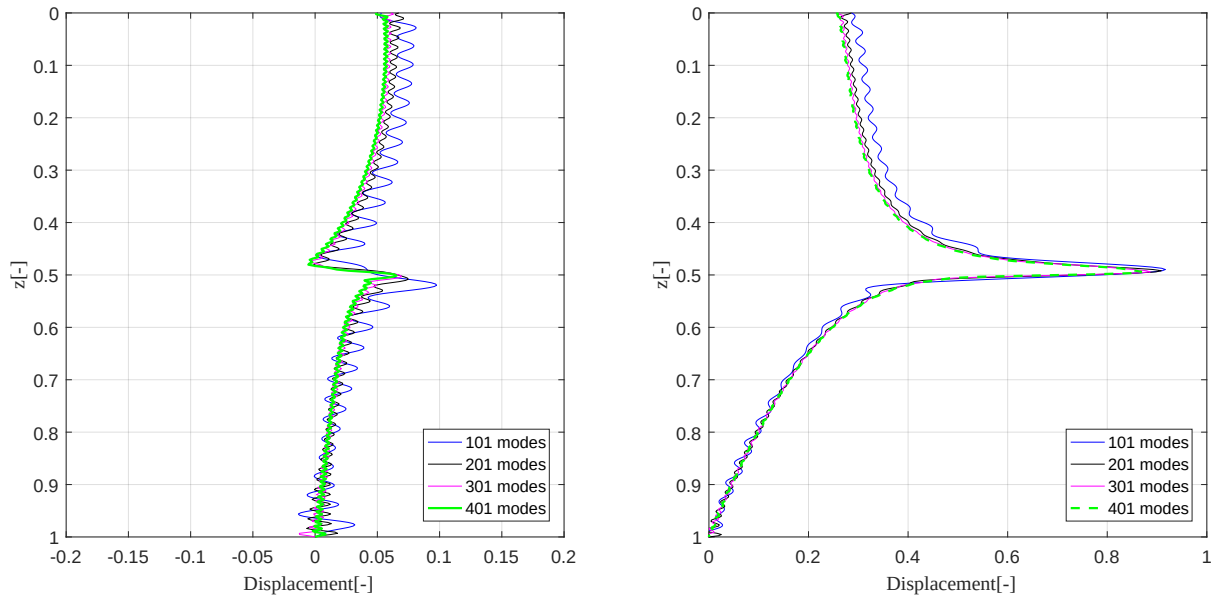

(a) $u_x^{(1)}$ ***at*** $x = -R$ **(b)** $u_z^{(1)}$ ***at*** $x = -R$

Figure 4.13: ***Convergence plots - shear stress imposed at the corner***

Table 4.4: ***Number of segments vs number of modes at the corner***

Number of segments	*Length of segment[-]*	*Number of modes*
15	0.1	301
20	0.05	301
30	0.033	351
50	0.02	401

Apart from the increased requirement of soil modes (Table 4.4), the difference in obtained displacements at the tip is much larger at the interface between Domain 1 and 4, 3 and 4.

A slight discontinuity in displacements is observed at the corners in both domain 1 and 3 boundaries independent of where the excitation is given on the cavity boundary. Hence, to get a better understanding of the what happens at the corner, we should consider the equilibrium of stresses for the soil element at the corner. As already shown in Figure 4.12, the stress profiles are highly oscillatory close to the corner, and hence it is difficult to make any inferences. The corners can be directly related to the top ($x = -R, R, z = 0$) for the case when a shear stress is applied on the domain boundary. This was already discussed in section 3.6.4. Due to the imposed boundary conditions when deriving the eigen functions of domain 1 or 3, a shear stress incompatibility occurs at the top. Although this incompatibility exists at the top, it does not seem to have any direct effect on the displacements (as seen in section 3.6.4 with the interaction force distribution at the interface), however, for the corners at the tip, this results in a discontinuity of displacements between domain 1 and 4. In classical continua, to maintain the bending moment equilibrium, the shear stresses across the perpendicular faces of an element must exist together and be equal. Due to the absence of the shear stresses at the top, an imbalance in bending moments is created. Figure 4.14 shows the stresses across a square soil element at the corner when the domain is discretized with 20 segments. e refers to the length of a single segment. It can be seen that there is slight shift in the peak value of the shear stress ($\sigma_{xz}(x = R, z = 0)$) at the top (due to the imposed boundary conditions) as compared to imposed stress indicated by the black line . Although the normal stress (σ_{xx})is imposed as zero at the top, a large non-zero value (Shear stress peak value: 45, Normal stress peak: -25) is obtained. This could be so that the bending moment equilibrium can be obtained for the element. A similar situation occurs at the corners as well with respect to the soil element in domain 4, however it is difficult to observe this due to the highly oscillatory nature of the stresses.

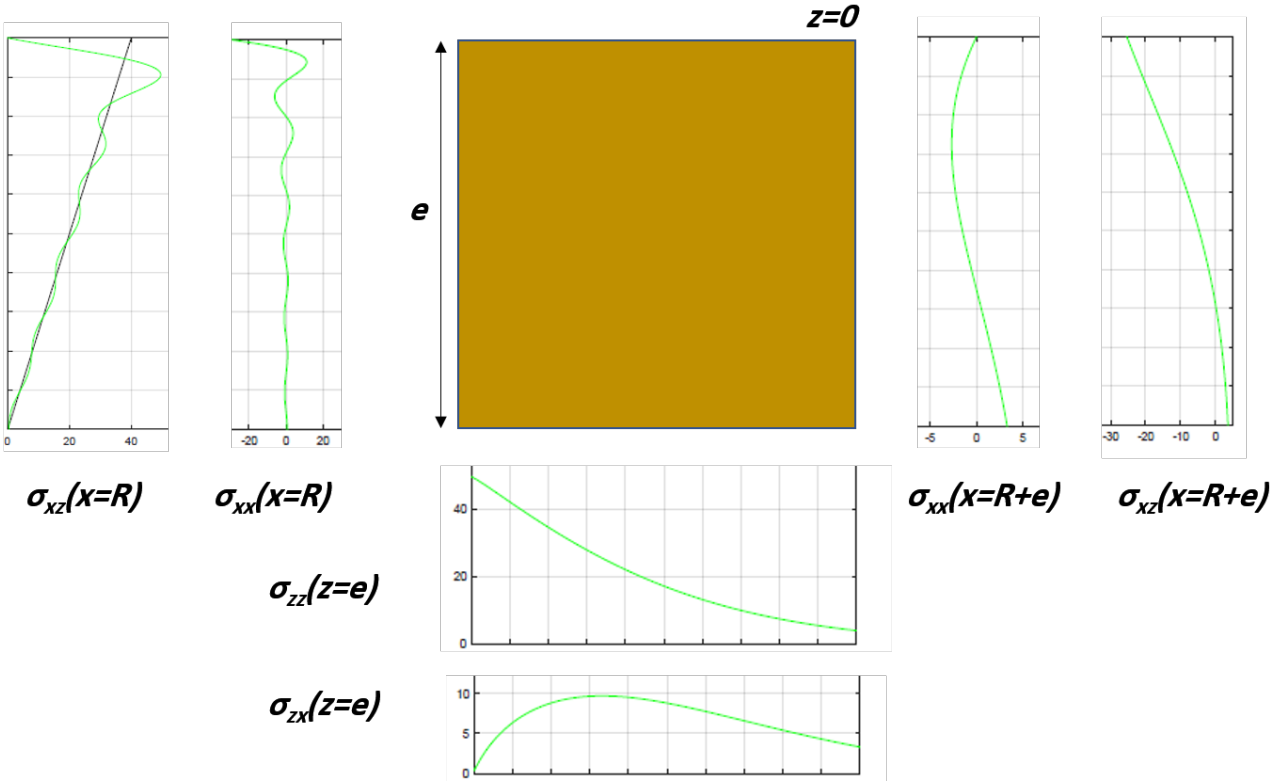

Figure 4.14: ***Stresses at the top corner soil element($z = 0$) for a shear stress applied to the top location - 20 segments across Domain 1 boundary***

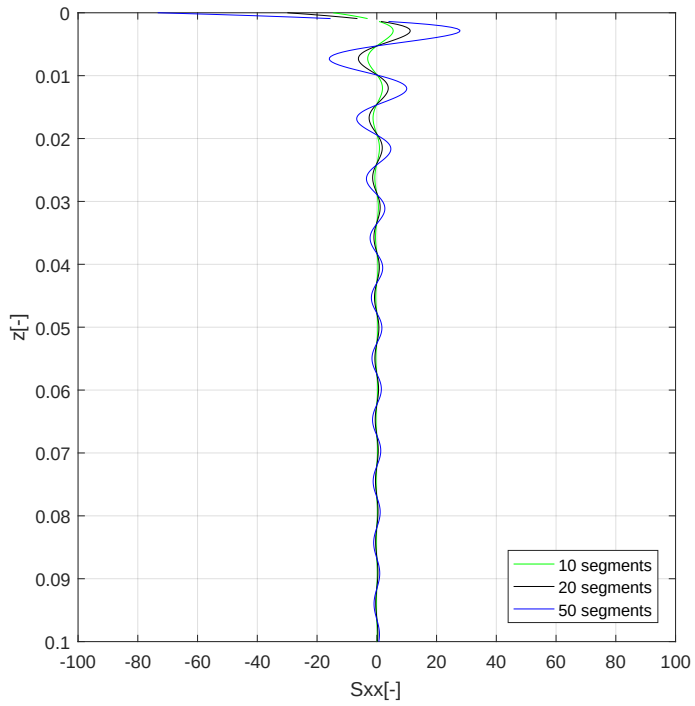

Figure 4.15: ***Normal stress (σ_{xx}) close to the top corner soil element ($z = 0$) for a shear stress applied to the top location - varying segments across domain 1 boundary***

Figure 4.15 shows the normal stress distribution close to the top corner element for varying element lengths, for a shear stress imposed at the top location. With increasing number of segments, the value of the normal stress at the top also increases, which could be to attain moment equilibrium, since with reducing segment length, the lever arm for the normal force across the element also reduces, hence resulting in the increased stress close to the top its effect is seen in the normal soil interaction force for the plate embedded in a waveguide (can be seen in section 5.2.1.3).

When a shear or a normal stress is imposed at the tip location on Domain 1 or 3, the obtained stresses are highly oscillatory in nature. Also the jump in the stresses at the corner is much higher as compared to when stresses are imposed at the top and intermediate locations. Stress value transits from a high tensile stress value to a high compressive stress value at $z = L$ (from $z = L^-$ to $z = L^+$), however for the top and intermediate locations, it changes from a value close to 0 to a high non-zero compressive value. This would imply that the stress gradient is quite large ,and the eigen modes might not be able to handle such jumps at the corner. Hence, higher order polynomial functions would be required to accurately represent these jumps.

Hence for the case of a stress imposed at the corner, an imbalance of moments occurs, in addition to which the large stress gradient occurs, which results in the highly oscillatory nature of the stresses and results in a larger difference in the displacements between the domains at the tip. For the two cases of a normal and shear stress imposed on domain 1 boundary corner location, the displacements fields at domain 1 and 3 boundary is shown.

Shear stress imposed at the corner of domain 1

Figure 4.16 and Figure 4.17 show the u_x and u_z displacements profiles at Domain 1 and 3 boundary due to a shear stress acting at the corner of domain 1 boundary.

For the corner location at $x = -R$, a relative difference of 67 % between $u_x^{(4)}$ and $u_x^{(1)}$ and 50 % between $u_z^{(4)}$ and $u_z^{(1)}$ is observed. Also, a relative difference of 20 % between $u_x^{(4)}$ and $u_x^{(3)}$ and 20 % between $u_z^{(4)}$ and $u_z^{(3)}$ is observed at $x = R$.

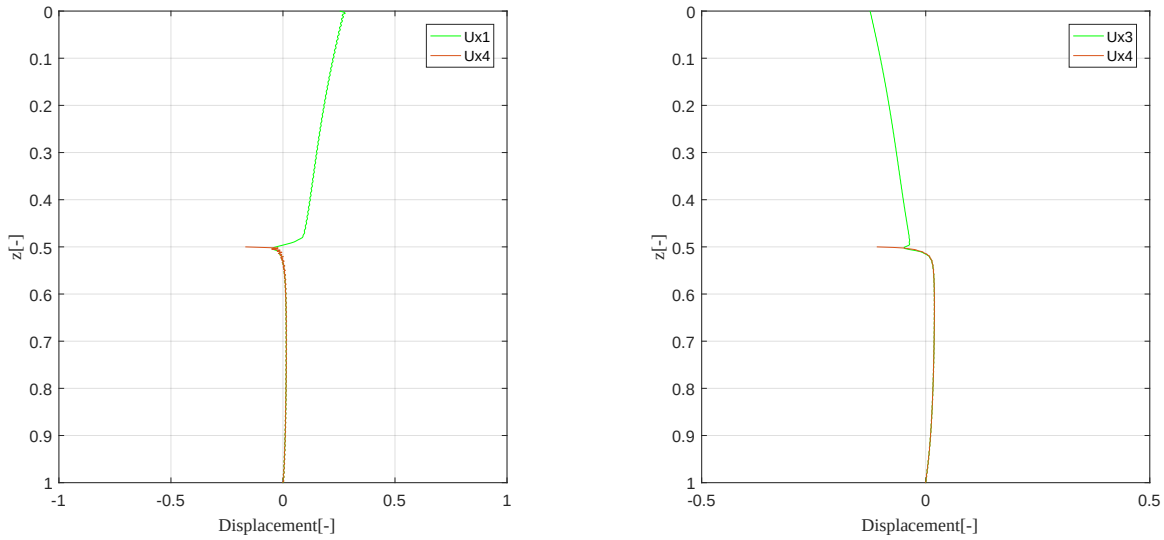

(a) $u_x^{(1)}$ ***and*** $u_x^{(4)}$ ***at*** $x = -R$ **(b)** $u_x^{(3)}$ ***and*** $u_x^{(4)}$ ***at*** $x = R$

Figure 4.16: u_x ***displacements at the Domain 1 and 3 boundaries and the interface between domain 1 and 4, 3 and 4 for*** $L = 0.5$ ***- Shear stress imposed at the corner of domain 1. Note: Each figure has a different scale to have a better view of the displacement profile***

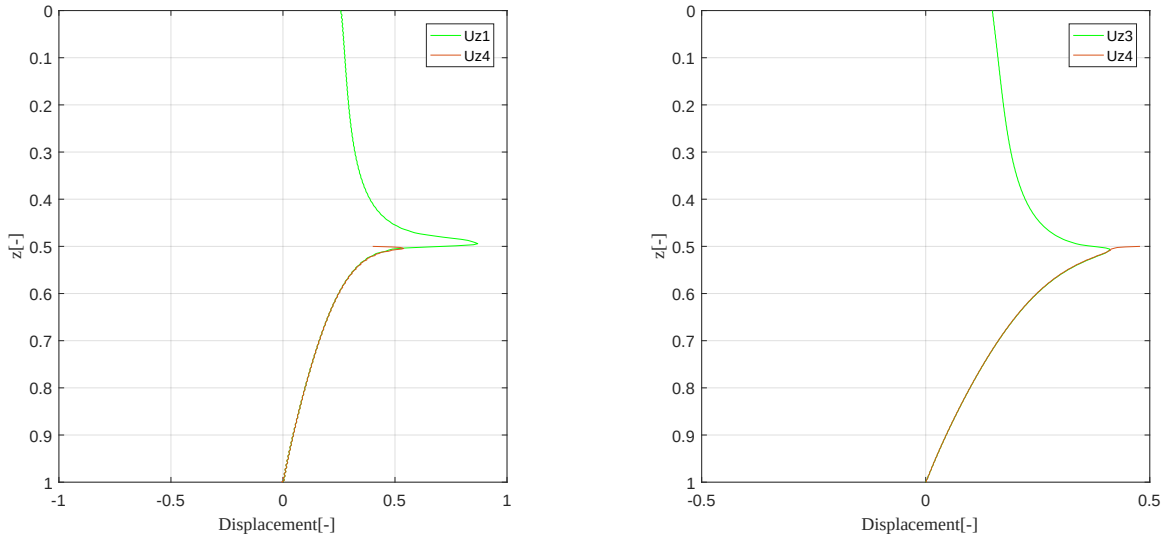

(a) $u_z^{(1)}$ ***and*** $u_z^{(4)}$ ***at*** $x = -R$ **(b)** $u_z^{(3)}$ ***and*** $u_z^{(4)}$ ***at*** $x = R$

Figure 4.17: u_z ***displacements at the Domain 1 and 3 boundaries and the interface between domain 1 and 4, 3 and 4 for*** $L = 0.5$ ***- Shear stress imposed at the corner of domain 1. Note: Each figure has a different scale to have a better view of the displacement profile***

Normal stress imposed at the corner

Figure 4.18 and Figure 4.19 show the u_x and u_z displacements profiles at Domain 1 and 3 boundary due to a shear stress acting at the corner of Domain 1 boundary.

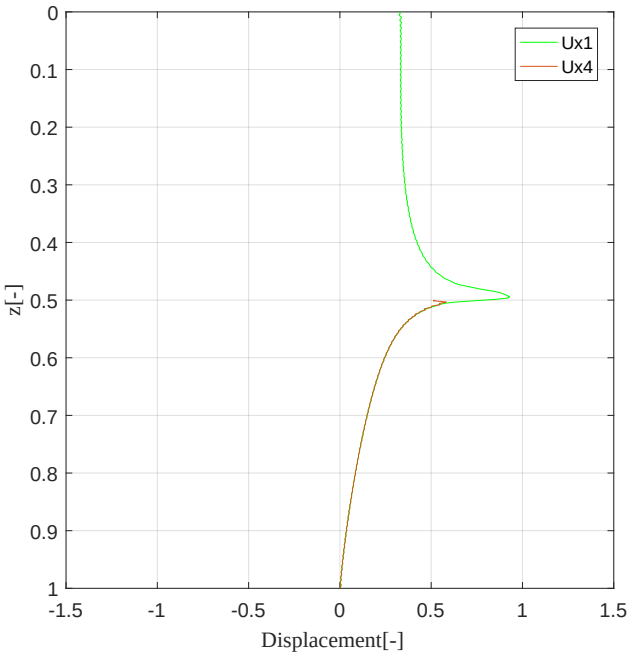

(a) $u_x^{(1)}$ ***and*** $u_x^{(4)}$ ***at*** $x = -R$

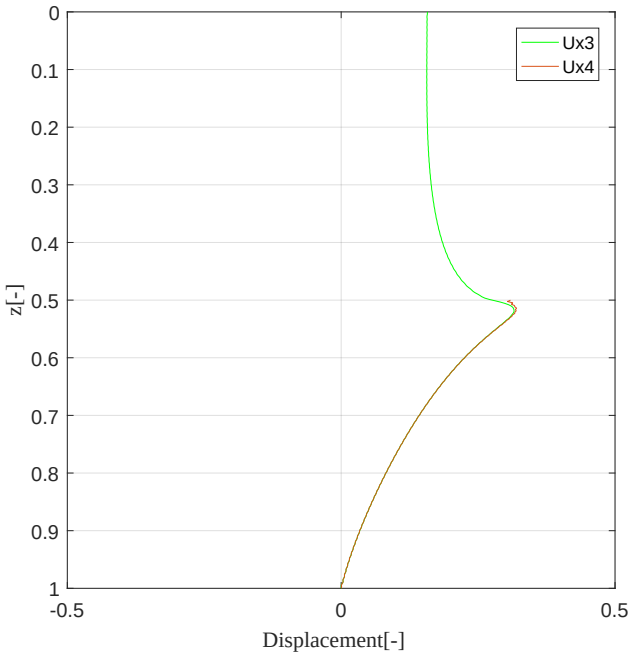

(b) $u_x^{(3)}$ ***and*** $u_x^{(4)}$ ***at*** $x = R$

Figure 4.18: u_x ***displacements at the Domain 1 and 3 boundaries and the interface between domain 1 and 4, 3 and 4 for*** $L = 0.5$ ***- Normal Stress imposed at the corner of domain 1. Note: Each figure has a different scale to have a better view of the displacement profile***

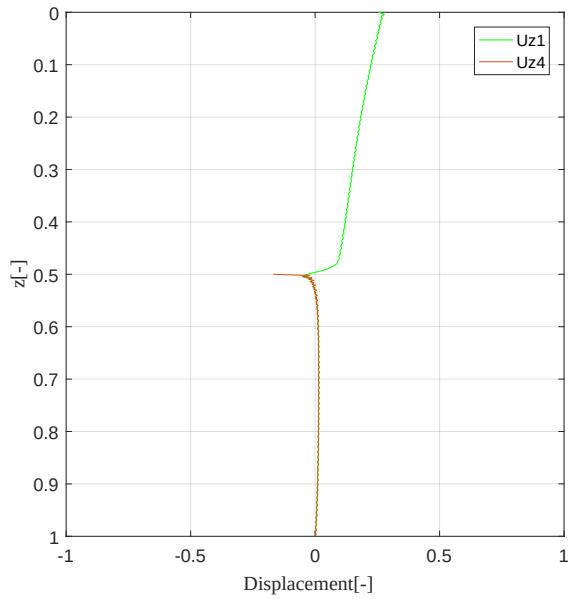

(a) $u_z^{(1)}$ ***and*** $u_z^{(4)}$ ***at*** $x = -R$

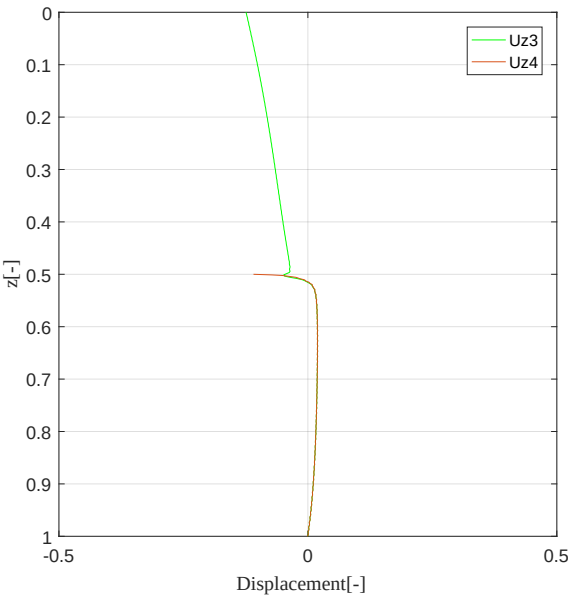

(b) $u_z^{(3)}$ ***and*** $u_z^{(4)}$ ***at*** $x = R$

Figure 4.19: u_z ***displacements at the Domain 1 and 3 boundaries and the interface between domain 1 and 4, 3 and 4 for*** $L = 0.5$ ***- Normal Stress imposed at the corner of domain 1. Note: Each figure has a different scale to have a better view of the displacement profile***

A relative difference of 50 % between $u_x^{(4)}$ and $u_x^{(1)}$ and 67 % between $u_z^{(4)}$ and $u_z^{(1)}$ is observed. Also, a relative difference of 2 % between $u_x^{(4)}$ and $u_x^{(3)}$ and 15 % between $u_z^{(4)}$

and $u_z^{(3)}$ is observed at $x = R$. The effect of the jump is less pronounced as compared to the application of a shear stress.

Similarly, the case of stress imposed at the corner location of domain 4 boundary is discussed. Following this the alternatives will be proposed and the corresponding results will be shown.

4.6.2 Considering the location at the corner of the tip domain

The location at the corner of the tip domain is considered. Figure 4.20 shows the *Gibbs phenomenon* observed close to the corner.

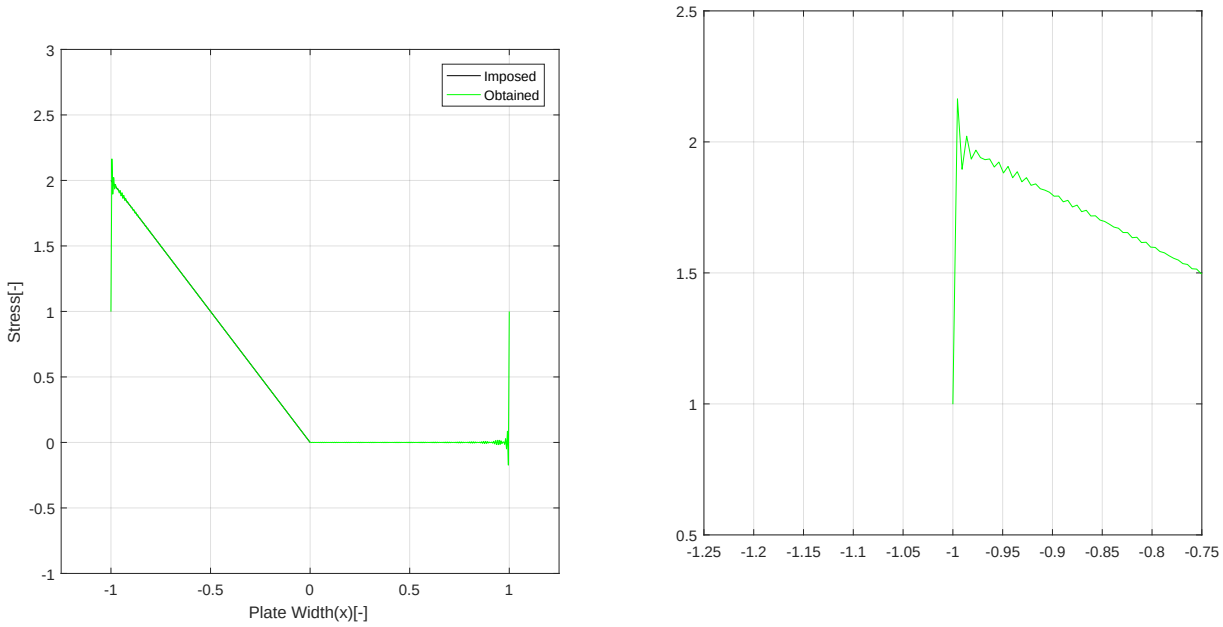

(a) ***Stress imposed at corner location - Tip Domain*** **(b)** ***Gibbs Phenomenon - close to corner*** ($x = -R$)

Figure 4.20: ***Stress as a Fourier representation***

As explained earlier in the section, the stress jump close to the corner for stresses imposed at the corner affects the continuity of the displacements at the interface between domain 1 and 4, and 3 and 4. Furthermore, the number of soil modes required for convergence of displacements is also higher. For the tip domain, in addition to the above, stress imposed at the tip corner also suffers from Gibbs phenomenon which occurs close to the domain boundaries (in this case, $x = -R, R$) essentially due to the imposed stress distribution, which drops from the triangle peak to 0, hence a large discontinuity. The Gibbs phenomenon refers to the manner in which the Fourier series for a periodic function overshoots the values of the function on either side of a discontinuity [25]. Furthermore, we also observe wiggles close to the discontinuity, which get pushed closer and closer to the discontinuity as the number of terms in the fourier series is increased. This Gibbs phenomenon is shown in Figure 4.20(b).

Due to the overshoot at the boundaries, the inhomogeneous stress components derived for the tip domain give erroneous estimations at the interface (essentially the corners).

4.6.3 Modifications for the corner - for corner location on domain 1,3 and 4

Although the effects at the corner cannot be completely eliminated, alternatives are suggested to reduce the inaccuracies. Two assumptions, one with respect to the corner stress distribution for Domain 1 and 3, and another with respect to the Domain 4 are introduced. These are shown in Figure 4.21.

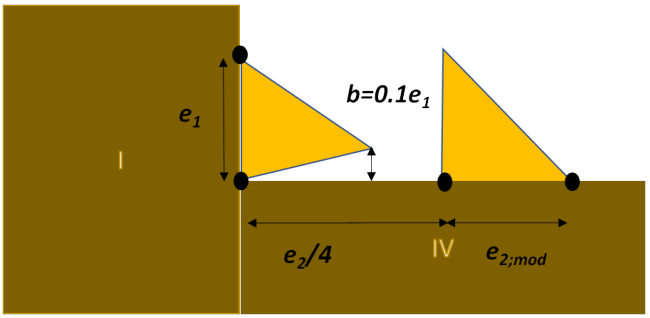

Figure 4.21: ***Modifications at the corner location***

Stress imposed at the corner of domain 1 or 3 - Apex shifted triangle

The right angled stress triangle distribution imposed at the corner is modified with the apex shifted slightly away from the corner, such that the value of the stress at the corner is zero. This reduces the stress gradient at the corner, as well as improves the continuity of displacements between the domains. Due to the shift, the centroid of the stress triangle now shifts further away from the corner (initially located at one-third segment length from the corner). An additional parameter b is introduced here, which represents the shift in the apex as a fraction of the segment length. The small value of b was selected so that the shift in the centroid of the stress triangle is not much. The value of $0.1e_1$ for the shift was used to have a close approximation, where e_1 is the segment length on Domain 1 or 3 boundary (see Figure 4.21).

Corner stress imposed at the tip domain 4 - Apex shifted triangle with a shift in corner location

For the corner stress on domain 4, the Gibbs phenomena is an additional effect at the corner. Furthermore, as the number of segments across the domain increase, the number of fourier components required for convergence also increase, resulting in the wiggles (and the overshoot) getting closer and closer to the corner. Hence, the locations on the tip domain were slightly shifted inwards. Furthermore, a sudden jump (discontinuity) would again give rise to wiggles, hence the apex of the triangle was slightly shifted inwards ($0.05e_2$) where e_2 is the segment length along tip domain. Based on the length of the segment up to which the wiggles were observed, the shift of the corner locations was done, and then the locations were equally spaced. The new length will be referred to as $e_{2;mod}$ (see Figure 4.21). The number of modes for varying segment lengths were found to be the same as that summarized in Table 4.1. The length up to which the wiggles were observed was close to $0.2e_2$ for each segment length, hence the shift was approximated to a value of $0.25e_2$.

Figure 4.22 shows the fourier expansion distribution of the stress close to the corner after implementing the modification with respect to the domain 4 corner. This is for a case for two segments which are used to discretize the tip domain. The horizontal axis is in normalized coordinates with $R = 1$.

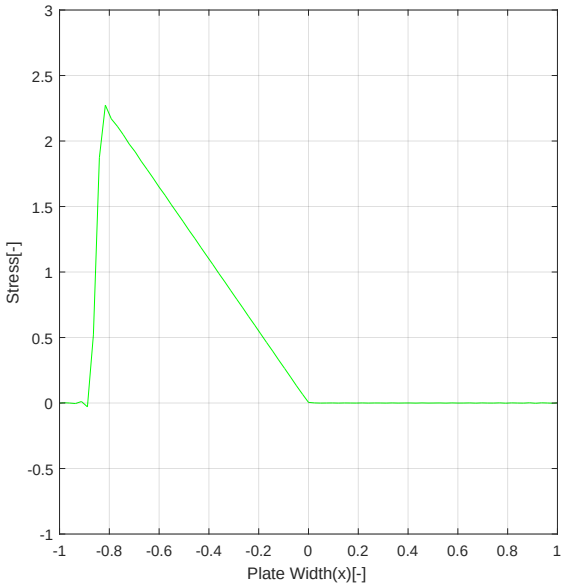

Figure 4.22: ***Modified stress at the tip - stress imposed close to the corner*** $x = -R$***. Note: the horizontal axis is normalized with*** $R = 1$***)***

Based on the the above assumptions, the stresses and displacements in the three soil domains for stress imposed at the corners of domain 1 and 3 and all locations on domain 4 were obtained. The results from one such analysis for stress imposed on domain 1 boundary and domain 4 boundary follow.

Displacements due to stress at the corner - domain 1 or 3

Figure 4.24 shows the displacement profiles for u_x and u_z at domain 1 and 3 boundaries for the modified shear stress imposed at the corner.

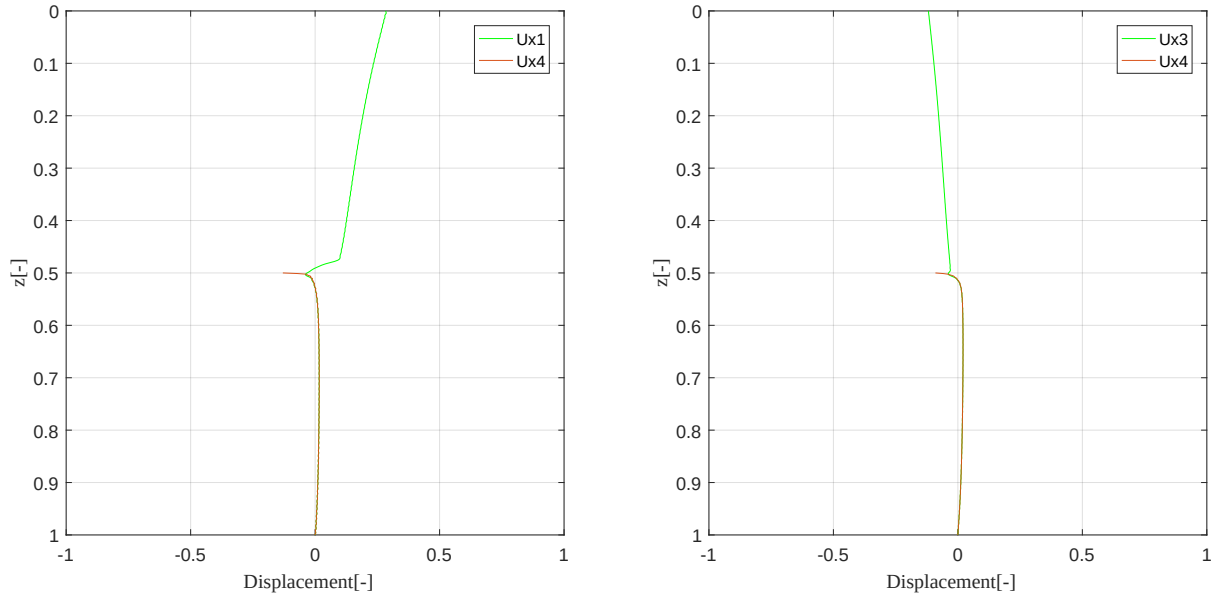

(a) $u_x^{(1)}$ ***and*** $u_x^{(4)}$ ***at*** $x = -R$ **(b)** $u_x^{(3)}$ ***and*** $u_x^{(4)}$ ***at*** $x = R$

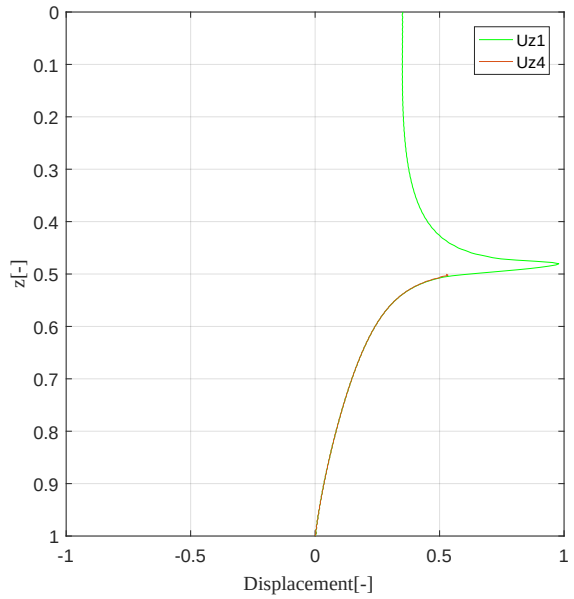

(c) $u_z^{(1)}$ *and* $u_z^{(4)}$ *at* $x = -R$

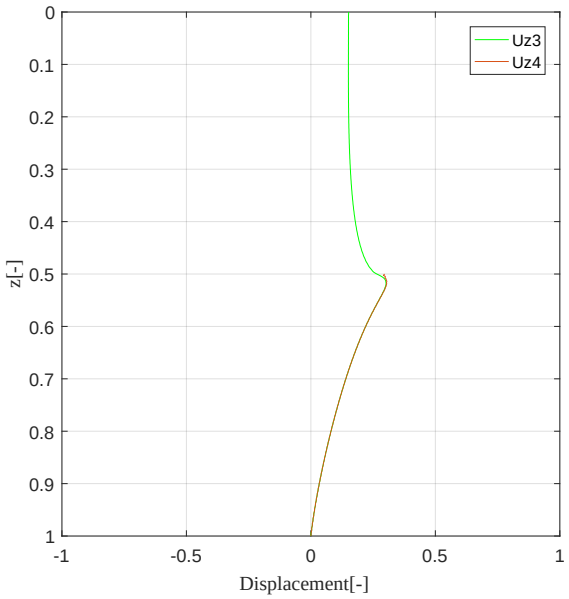

(d) $u_z^{(3)}$ *and* $u_z^{(4)}$ *at* $x = R$

Figure 4.24: ***Displacement profile of*** u_x ***and*** u_z ***at the the boundaries*** $x = -R, R$ ***for modified shear stress imposed at the corner on Domain 1***

We observe that the with regard to the displacements u_x, the continuity of displacements is maintained at the tip. With regard to the displacements u_z, a relative difference of 37 % at the interface of domain 1 and 4 and a relative difference of 30 % at the interface of domain 3 and 4 is seen at the corner. Since there is a slight shift in the apex of the triangle, the peak displacement position will vary. A relative difference of 9 % was found between the peak displacement before and after the modification in u_x at the domain 1 boundary and a relative difference of 13 % at the domain 3 boundary. The values for u_z were 4 % and 2 % respectively. The average relative change across the boundary ($z = 0$ to L), which was 4 % and 2 % for u_x at Domain 1 and 3 boundaries, and 3 % and 0.7 % for u_z at Domain 1 and 3 boundaries.

Similar range of values were also obtained for displacements u_x and u_z for a modified normal stress imposed at the corner. Due to the shifted triangle, the stress gradient at the tip is reduced, although the stresses are highly oscillatory in nature. Furthermore, it is possible that due to the shifted triangle, the bending moment imbalance is reduced close to the corner since the u_x displacements show better continuity at the tip, however the imbalance is not completely eliminated since the there is a mismatch in the u_z displacements, although reduced as compared to the initial case (see Figure 4.18 and Figure 4.19).

Displacements due to the shifted triangle - domain 4

Figure 4.26 shows the displacement profile at the two boundaries $x = -R, R$ for a modified normal stress acting close to the corner at $x = -R$. The range of errors(in terms of the difference between the displacements between Domain 1 and 4 at $z = L$)), is in the same range as in Figure 4.10.

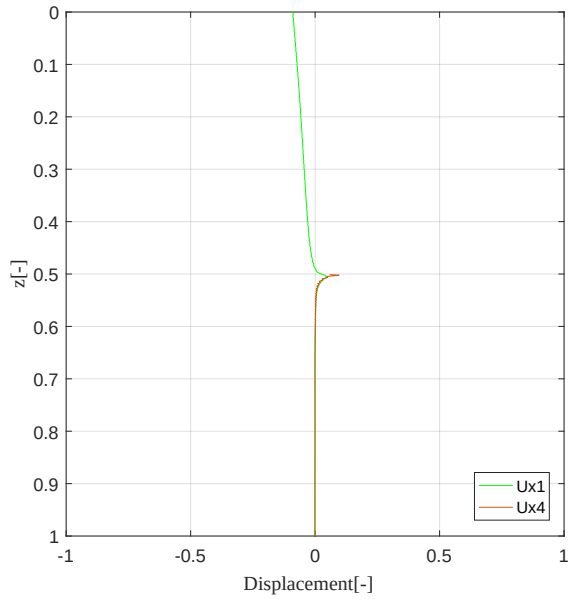

(a) $u_x^{(1)}$ ***and*** $u_x^{(4)}$ ***at*** $x = -R$

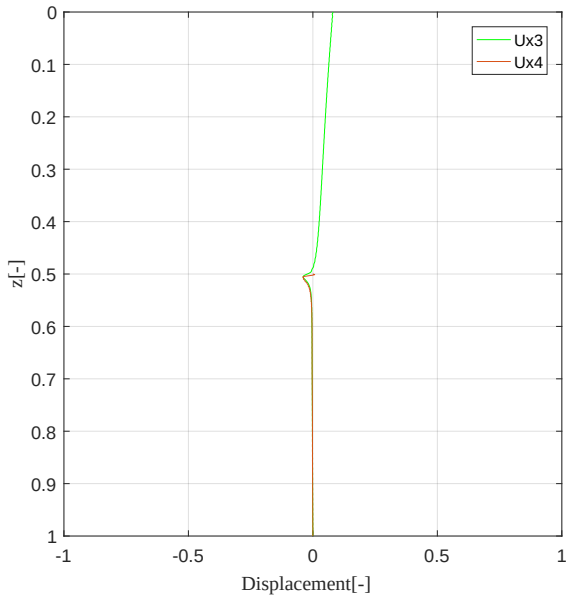

(b) $u_x^{(3)}$ ***and*** $u_x^{(4)}$ ***at*** $x = R$

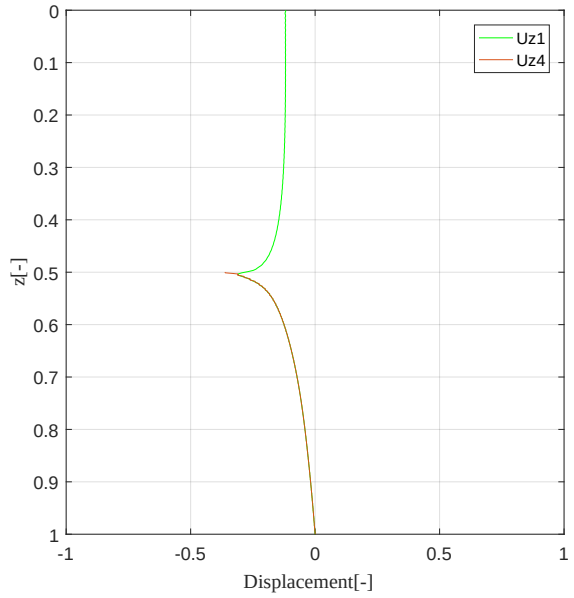

(a) $u_z^{(1)}$ ***and*** $u_z^{(4)}$ ***at*** $x = -R$

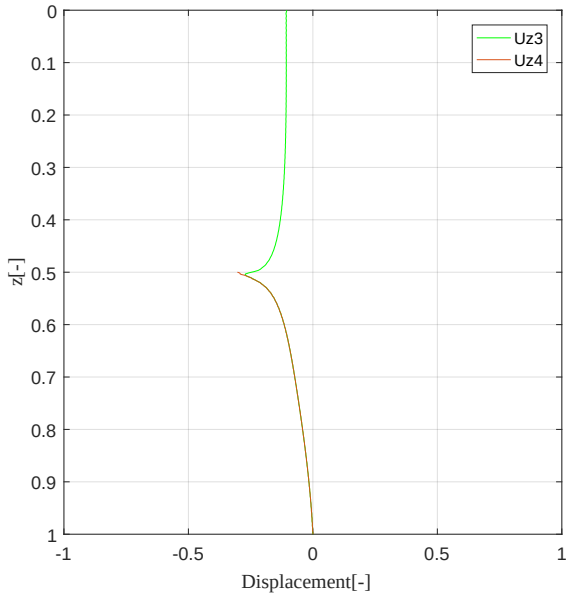

(b) $u_z^{(3)}$ ***and*** $u_z^{(4)}$ ***at*** $x = R$

Figure 4.26: ***Displacement profile of*** u_x ***and*** u_z ***at the the boundaries*** $x = -R, R$ ***for modified normal stress imposed at the corner of domain 4 close to*** $x = -R$***, for the tip discretized into 4 segments***

4.7 Summary and Conclusion

The chapter discusses the model for the soil continuum including the 3 domains - domain 1 (Left), domain 3(Right) and domain 4(tip domain), which is essentially the problem of a cavity in an elastic waveguide. Locations are introduced on the tip domain, in addition to the boundaries of domain 1 and 3. The tip domain fields (stress and displacement fields)

can have two components - homogeneous (with homogeneous boundary conditions) and inhomogeneous (when inhomogeneous boundary conditions are applied).

The eigen modes for the tip domain are derived as a modification of the eigen functions of domain 1 and 3, since all three domains have the same set of homogeneous boundary condition as well as the dimensionless dispersion equation. The solution procedure for obtaining the stresses and displacements in all three domains, due to stresses imposed on the locations is introduced, which forms a system of 12 equations, to be solved for stress imposed on each location (normal and shear).

Convergence studies are done to obtain the number soil modes required for converged non-oscillatory displacement profile at the domain boundaries. For the case of an excitation (shear or normal stress) on domain 1 or 3 boundary, the convergence study is done considering up to 50 segments. Based on the convergence study, it is observed that the number of soil modes required for converged non-oscillatory displacement profiles is much higher close to the corner than for stress imposed on the top and intermediate locations. A slight discontinuity in displacements between domain 1 and 4, 3 and 4 is observed at the corner, which is due to the bending moment imbalance with respect to the corner soil element in domain 4. For stresses (normal or shear) imposed close to the corner, the highly oscillatory stress profiles are obtained. The jump in stresses close to the corner is much larger when the apex of the stress triangle lies at the corner, leading to a large stress gradient. These are not well represented by the modal functions that are currently employ. Hence as an alternative, a slight shift in the apex of the triangles away from the corner is suggested.

When a stress (normal or shear) is applied on domain 4, the total field (stresses or displacements) is now a sum of the homogeneous and inhomogeneous component. The triangular stresses imposed are represented as a Fourier series. A convergence study is done considering up to 6 segments to obtain the number of Fourier components required for converged stress distribution. The number of soil modes required for all locations at the tip were found to be equal to the number of soil modes required for the case of stress imposed at the corner. Similar to the approach used for the corner on domain 1 or 3, a large oscillatory stress profile was obtained for stresses imposed at the tip domain corner. The difference in the displacements between the interacting domains was relatively large (in the range of 67 %), Additionally, the Gibbs phenomenon was also observed at the corner due to the large discontinuity in the original stress distribution. Hence, as an alternative, a slight shift in the triangular distribution as well as its apex was suggested. With this the error is reduced to 30%.

With the obtained stress and displacement solutions, the stiffness matrix derived can be combined with the plate mass and stiffness matrices to obtain the complete dynamic plate-soil stiffness matrix. This will be explained in detail in the next chapter.

Chapter 5

Hybrid solution for a plate embedded in a wave guide - a plane strain problem

This chapter describes the procedure for deriving the stiffness matrices which can then be combined with the plate mass and stiffness matrices to obtain the dynamic stiffness matrices for the entire system (section 5.1 and 5.2). Validation is done by comparing the results with the Benchmark solution (explained in detail in Appendix A), for the two cases of slip and non-slip, as done for the single domain analysis. An additional case study is discussed with different set of domain parameters, where some important observations with respect to the tip are made.

5.1 Assembling the Global stiffness matrix of the soil at the cavity boundary

Using the displacements obtained from the analysis of the three domain soil system (see section 4.4 and 4.5), the global stiffness matrix is derived. This stiffness matrix contains entries from all the locations in the three domains. This is then split into individual stiffness matrices for each domain, using the relations of force and displacement compatibility at the three boundaries(I - $x = -R, z = 0$ to L, II - $x = R, z = 0$ to L and III - $z = L, x = -R$ to R) between the plate and soil.

The horizontal and vertical displacements obtained for stresses acting on the j^{th} location on domain 1 or 3 are denoted as $u_{x;v}^{(t;j)}$ and $u_{z;v}^{(t;j)}$ and for the k^{th} location on the tip (domain 4) are given as $u_{x;v}^{(t;k)}$ and $u_{z;s}^{(t;k)}$, with $t = [1, 3]$ signifying the domain number and $v = [1, 2]$ with 1 for normal stress and 2 for shear stress imposed at the location. m can be used for both domains since, for both domain 1 and 3, the number of locations are the same, since these then have to be connected to the nodes on the plate. For displacements due to stresses on domain 4, a slightly different convention is used due to the presence of the inhomogeneous component. The homogeneous component of the displacements are given as $u_{x;s}^{(4,h;m)}$ and $u_{z;v}^{(4,h;j)}$, and the inhomogeneous component $u_{x;v}^{(4,i;j)}$ and $u_{z;v}^{(4,i;j)}$ at the m^{th} location. This is similarly taken for the r locations on the tip. To obtain the global stiffness matrix, we first derive the global compliance matrix. The total number of locations are $2m + r$, where m and r are the total number of locations assumed in the domain 1/3 and domain 4 boundary respectively. Therefore, the compliance matrix is of size $(4m+2r)$ x $(4m+2r)$. The equilibrium equation with the compliance matrix can be written as

$$\mathbf{u_{s;g}} = \mathbf{Q_{s;g}} \mathbf{F_{s;g}} \tag{5.1}$$

where $\mathbf{u_{s;g}} = \begin{bmatrix} [\mathbf{u_{s;1}}]_{2m\ x\ 1} \\ [\mathbf{u_{s;3}}]_{2m\ x\ 1} \\ [\mathbf{u_{s;4}}]_{2r\ x\ 1} \end{bmatrix}$, $\mathbf{Q_{s;g}} = \begin{bmatrix} [\mathbf{Q_{11}}]_{2m\ x\ 2m} & [\mathbf{Q_{13}}]_{2m\ x\ 2m} & [\mathbf{Q_{14}}]_{2m\ x\ 2r} \\ [\mathbf{Q_{31}}]_{2m\ x\ 2m} & [\mathbf{Q_{33}}]_{2m\ x\ 2m} & [\mathbf{Q_{34}}]_{2m\ x\ 2r} \\ [\mathbf{Q_{41}}]_{2r\ x\ 2m} & [\mathbf{Q_{43}}]_{2r\ x\ 2m} & [\mathbf{Q_{44}}]_{2r\ x\ 2r} \end{bmatrix}$ and $\mathbf{F_{s;g}} = \begin{bmatrix} [\mathbf{F_{s;1}}]_{2m\ x\ 1} \\ [\mathbf{F_{s;3}}]_{2m\ x\ 1} \\ [\mathbf{F_{s;4}}]_{2m\ x\ 1} \end{bmatrix}$

the subscript $'g'$ indicates that these belong to the global system. These can be further elaborated as

$$\mathbf{u_{s;1}} = \begin{bmatrix} u_x^{(1;1)} \\ u_z^{(1;1)} \\ u_x^{(1;2)} \\ u_z^{(1;2)} \\ \vdots \\ \vdots \\ u_x^{(1;m)} \\ u_z^{(1;m)} \end{bmatrix}, \mathbf{u_{s;3}} = \begin{bmatrix} u_x^{(3;1)} \\ u_z^{(3;1)} \\ u_x^{(3;2)} \\ u_z^{(3;2)} \\ \vdots \\ \vdots \\ u_x^{(3;m)} \\ u_z^{(3;m)} \end{bmatrix}, \mathbf{u_{s;4}} = \begin{bmatrix} u_x^{(4;1)} \\ u_z^{(4;1)} \\ u_x^{(4;2)} \\ u_z^{(4;2)} \\ \vdots \\ \vdots \\ u_x^{(4;r)} \\ u_z^{(4;r)} \end{bmatrix} \tag{5.2}$$

and

$$\mathbf{F_{s;1}} = \begin{bmatrix} F_x^{(1;1)} \\ F_z^{(1;1)} \\ F_x^{(1;2)} \\ F_z^{(1;2)} \\ \vdots \\ \vdots \\ F_x^{(1;m)} \\ F_z^{(1;m)} \end{bmatrix}, \mathbf{F_{s;3}} = \begin{bmatrix} F_x^{(3;1)} \\ F_z^{(3;1)} \\ F_x^{(3;2)} \\ F_z^{(3;2)} \\ \vdots \\ \vdots \\ F_x^{(3;m)} \\ F_z^{(3;m)} \end{bmatrix}, \mathbf{F_{s;4}} = \begin{bmatrix} F_x^{(4;1)} \\ F_z^{(4;1)} \\ F_x^{(4;2)} \\ F_z^{(4;2)} \\ \vdots \\ \vdots \\ F_x^{(4;r)} \\ F_z^{(4;r)} \end{bmatrix} \tag{5.3}$$

Here $\mathbf{u_{s;1}}$,$\mathbf{u_{s;3}}$ and $\mathbf{u_{s;4}}$ represent the displacements at the locations in domain 1,3 and 4 respectively, and $\mathbf{F_{s;1}}$,$\mathbf{F_{s;3}}$ and $\mathbf{F_{s;4}}$ represent the soil interaction forces in the three domains. The entries of the individual elements of the compliance matrix can be obtained as

$$\begin{aligned} Q_{11;(2j-1)(2p-1)} &= u_{x;1,p}^{(1;j)} = u_{x;1}^{(1;j)}(x = -R, z = z_p) \\ Q_{11;(2j-1)(2p)} &= u_{x;2,p}^{(1;j)} \\ Q_{11;(2j)(2p-1)} &= u_{z;1,p}^{(1;j)} \\ Q_{11;(2j)(2p)} &= u_{z;2,p}^{(1;j)}) \end{aligned} \tag{5.4}$$

and

$$\begin{aligned} Q_{13;(2j-1)(2p-1)} &= u_{x;1,p}^{(3;j)} = u_{x;1}^{(3;j)}(x = -R, z = z_p) \\ Q_{13;(2j-1)(2p)} &= u_{x;2,p}^{(3;j)} \\ Q_{13;(2j)(2p-1)} &= u_{z;1,p}^{(3;j)} \\ Q_{13;(2j)(2p)} &= u_{z;2,p}^{(3;j)} \end{aligned} \tag{5.5}$$

and

$$\begin{aligned} Q_{14;(2j-1)(2k-1)} &= u_{x;1,k}^{(4;j)} = u_{x;1}^{(4;j)}(x = x_k, z = L) \\ Q_{14;(2j-1)(2k)} &= u_{x;2,k}^{(4;j)} \\ Q_{14;(2j)(2k-1)} &= u_{z;1,k}^{(4;j)} \\ Q_{14;(2j)(2k)} &= u_{z;2,k}^{(4;j)} \end{aligned} \tag{5.6}$$

where $j = 1,..,m$, $p = 1,..,m$ and $k = 1,..,r$. Similarly the entries for the matrices $\mathbf{Q_{31}}$,$\mathbf{Q_{33}}$ and $\mathbf{Q_{34}}$ can be obtained.The entries of the matrices $\mathbf{Q_{41}}$,$\mathbf{Q_{43}}$ and $\mathbf{Q_{44}}$ are given as

$$\begin{aligned} Q_{41;(2k-1)(2p-1)} &= u^{(1;k)}_{x;1,p} = u^{(1;k)}_{x;1}(x = -R, z = z_p) \\ Q_{41;(2k-1)(2p)} &= u^{(1;k)}_{x;2,p} \\ Q_{41;(2k)(2p-1)} &= u^{(1;k)}_{z;1,p} \\ Q_{41;(2k)(2p)} &= u^{(1;k)}_{z;2,p} \end{aligned} \tag{5.7}$$

and

$$\begin{aligned} Q_{43;(2k-1)(2p-1)} &= u^{(3;k)}_{x;1,p} = u^{(3;r)}_{x;1}(x = -R, z = z_p) \\ Q_{43;(2k-1)(2p)} &= u^{(3;k)}_{x;2,p} \\ Q_{43;(2k)(2p-1)} &= u^{(3;k)}_{z;1,p} \\ Q_{43;(2k)(2p)} &= u^{(3;k)}_{z;2,p} \end{aligned} \tag{5.8}$$

and

$$\begin{aligned} Q_{44;(2k-1)(2y-1)} &= u^{(4,h;k)}_{x;1,y} + u^{(4,i;k)}_{x;1,y} = u^{(4,h;k)}_{x;1}(x = x_y, z = L) + u^{(4,i;k)}_{x;1}(x = x_y, z = L) \\ Q_{44;(2k-1)(2y)} &= u^{(4,h;k)}_{x;2,y} + u^{(4,i;k)}_{x;2,y} \\ Q_{44;(2k)(2y-1)} &= u^{(4,h;k)}_{z;1,y} + u^{(4,i;k)}_{x;2,y} \\ Q_{44;(2k)(2y)} &= u^{(4,h;k)}_{z;2,y} + u^{(4,i;k)}_{x;2,y} \end{aligned} \tag{5.9}$$

where $y = 1,..,r$. The global stiffness matrix can then be obtained as

$$\mathbf{K_{s;g}} = \mathbf{Q^{-1}_{s;g}} \tag{5.10}$$

The soil stiffness matrix is made dimensional (from Equation 3.16 and Equation 3.17) as

$$\tilde{\mathbf{K}}_{\mathbf{s;g}} = G\mathbf{K_{s;g}} \tag{5.11}$$

where G is the shear stiffness of the soil. Similar to $\mathbf{Q_{s;g}}$, $\tilde{\mathbf{K}}_{\mathbf{s;g}}$ can be represented as

$$\tilde{\mathbf{K}}_{\mathbf{s;g}} = \begin{bmatrix} [\tilde{\mathbf{K}}_{\mathbf{11}}]_{\text{2m x 2m}} & [\tilde{\mathbf{K}}_{\mathbf{13}}]_{\text{2m x 2m}} & [\tilde{\mathbf{K}}_{\mathbf{14}}]_{\text{2m x 2r}} \\ [\tilde{\mathbf{K}}_{\mathbf{31}}]_{\text{2m x 2m}} & [\tilde{\mathbf{K}}_{\mathbf{33}}]_{\text{2m x 2m}} & [\tilde{\mathbf{K}}_{\mathbf{34}}]_{\text{2m x 2r}} \\ [\tilde{\mathbf{K}}_{\mathbf{41}}]_{\text{2m x 2m}} & [\tilde{\mathbf{K}}_{\mathbf{43}}]_{\text{2m x 2m}} & [\tilde{\mathbf{K}}_{\mathbf{44}}]_{\text{2m x 2r}} \end{bmatrix} \tag{5.12}$$

This will be later used to derive the domain stiffness matrices.

5.2 Assembling the domain stiffness matrices

The stiffness matrix of the three domains can be derived from the global stiffness matrix. The order of the plate stiffness and mass matrix should be equal to the order of the stiffness matrix of the surrounding soil, so that they can be combined to obtain the dynamic plate-soil stiffness matrix. This is done by breaking the global soil stiffness matrix and implementing the relationships between the degrees of freedom of the plate and the soil at the three boundaries. For Domain 1 and 3, this relationship is indicated in Figure 5.1.

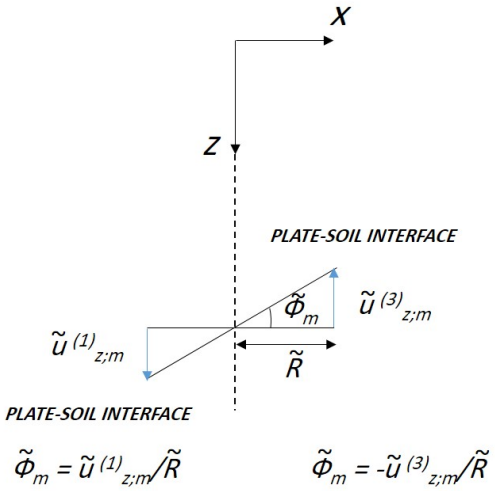

Figure 5.1: ***Rotational compatibility between plate and soil***

It should be noted that, in the plate, there is a single node present at each point, where the location in the soil domain is present. Hence, for compatibility, the horizontal displacements for both domain 1 and 3 should be the same at each node. Similarly, the rotations should also be the same, since in the Kirchhoff plate theory, it is assumed that plane cross-sections remain plane before and after bending. The difference in sign comes due to the adopted sign convention. Hence, the degrees of freedom of the soil in terms of those of the plate are given as

$$\begin{aligned} \tilde{u}_x^{(1;m)} &= \tilde{u}_x^{(3;m)} = \tilde{W}_m \\ \tilde{u}_z^{(1;m)} &= \tilde{\phi}_m \tilde{R} \\ \tilde{u}_z^{(3;m)} &= -\tilde{\phi}_m \tilde{R} \end{aligned} \tag{5.13}$$

where $\tilde{W}_m$ is the plate displacement at the node m. For the tip domain locations, the compatibility between the degrees of freedom of the plate and the soil are expressed in Figure 5.2. This is shown for the tip discretized to 4 segments. This is based on the same assumption of the Kirchhoff plate theory that plane sections remain plane before and after bending.

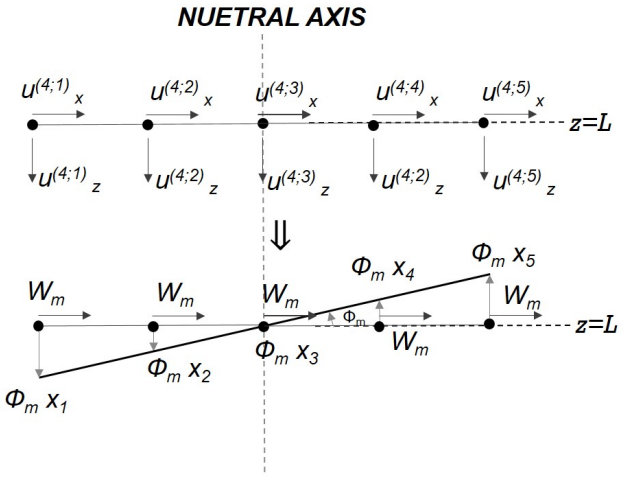

Figure 5.2: ***Displacement and rotational compatibility at the tip***

Using these relationships, the global stiffness matrix can now to modified, relating the

interaction forces between the soil and plate and the degrees of freedom of the plate. Considering the interaction forces in domain 1

$$\tilde{\mathbf{F}}_{\mathbf{s;1}} = \tilde{\mathbf{K}}_{\mathbf{11}}\tilde{\mathbf{u}}_{\mathbf{s;1}} + \tilde{\mathbf{K}}_{\mathbf{13}}\tilde{\mathbf{u}}_{\mathbf{s;3}} + \tilde{\mathbf{K}}_{\mathbf{14}}\tilde{\mathbf{u}}_{\mathbf{s;4}} \tag{5.14}$$

$$\implies \begin{bmatrix} F_{xx}^{(1;1)} \\ F_{xz}^{(1;1)} \\ F_{xx}^{(1;2)} \\ F_{xz}^{(1;2)} \\ \vdots \\ F_{xx}^{(1;m)} \\ F_{xz}^{(1;m)} \end{bmatrix} = \begin{bmatrix} \begin{bmatrix} K_{11}^{(11)} & \cdots & K_{1(2m)}^{(11)} \\ \vdots & \ddots & \vdots \\ K_{(2m)1}^{(11)} & \cdots & K_{(2m)2m}^{(11)} \end{bmatrix} \begin{bmatrix} K_{11}^{(13)} & \cdots & K_{1(2m)}^{(13)} \\ \vdots & \ddots & \vdots \\ K_{(2m)1}^{(13)} & \cdots & K_{(2m)2m}^{(13)} \end{bmatrix} \begin{bmatrix} K_{11}^{(14)} & \cdots & K_{1(2r)}^{(14)} \\ \vdots & \ddots & \vdots \\ K_{(2m)1}^{(14)} & \cdots & K_{(2m)2r}^{(14)} \end{bmatrix} \end{bmatrix} \begin{bmatrix} u_x^{(1;1)} \\ u_z^{(1;1)} \\ u_x^{(1;2)} \\ u_z^{(1;2)} \\ \vdots \\ u_x^{(1;m)} \\ u_z^{(1;m)} \\ u_x^{(3;1)} \\ u_z^{(3;1)} \\ u_x^{(3;2)} \\ u_z^{(3;2)} \\ \vdots \\ u_x^{(3;m)} \\ u_z^{(3;m)} \\ u_x^{(4;1)} \\ u_z^{(4;1)} \\ u_x^{(4;2)} \\ u_z^{(4;2)} \\ \vdots \\ u_x^{(4;r)} \\ u_z^{(4;r)} \end{bmatrix} \tag{5.15}$$

Substituting the relationships in Figure 5.2 and Equation 5.13, we get

$$\implies \begin{bmatrix} F_{xx}^{(1;1)} \\ F_{xz}^{(1;1)} \\ F_{xx}^{(1;2)} \\ F_{xz}^{(1;2)} \\ \vdots \\ F_{xx}^{(1;m)} \\ F_{xz}^{(1;m)} \end{bmatrix} = \begin{bmatrix} \begin{bmatrix} K_{11}^{(11)} & \cdots & K_{1(2m)}^{(11)} \\ \vdots & \ddots & \vdots \\ K_{(2m)1}^{(11)} & \cdots & K_{(2m)2m}^{(11)} \end{bmatrix} \begin{bmatrix} K_{11}^{(13)} & \cdots & K_{1(2m)}^{(13)} \\ \vdots & \ddots & \vdots \\ K_{(2m)1}^{(13)} & \cdots & K_{(2m)2m}^{(13)} \end{bmatrix} \begin{bmatrix} K_{11}^{(14)} & \cdots & K_{1(2r)}^{(14)} \\ \vdots & \ddots & \vdots \\ K_{(2m)1}^{(14)} & \cdots & K_{(2m)2r}^{(14)} \end{bmatrix} \end{bmatrix} \begin{bmatrix} W_1 \\ \phi_1 R \\ W_2 \\ \phi_2 R \\ \vdots \\ W_m \\ \phi_m R \\ W_1 \\ -\phi_2 R \\ W_2 \\ -\phi_2 R \\ \vdots \\ W_m \\ -\phi_m R \\ W_m \\ \phi_m R \\ W_m \\ \phi_m R \\ \vdots \\ W_m \\ -\phi_m R \end{bmatrix} \tag{5.16}$$

Is shoudl be noted that m is used explicitly to indicate the last location (at the tip) in all the following expressions. The stiffness matrix can then be reduced. This is shown for a normal interaction force in Equation 5.17.

$$F^{(1;j)} = (K_{j1}^{(11)} + K_{j1}^{(13)})W_1 + (K_{j2}^{(11)} - K_{j2}^{(13)})\phi_1 R \cdots (K_{j(2m-1)}^{(11)} + K_{j(2m-1)}^{(13)})W_m + (K_{j(2m)}^{(11)} - K_{j(2m)}^{(13)})\phi_m R$$

$$F^{(1;j)} = \begin{bmatrix} (K_{j1}^{(11)} + K_{j1}^{(13)}) & (K_{j2}^{(11)} - K_{j2}^{(13)})R & \cdots & (K_{j(2m-1)}^{(11)} + K_{j(2m-1)}^{(13)} + \Sigma_{k=1}^{r} K_{q(2k-1)}^{(14)}) & (K_{1(2m)}^{(11)} - K_{1(2m)}^{(13)})R + \Sigma_{k=1}^{r} K_{j(2k)}^{(14)} x_k \end{bmatrix} \begin{bmatrix} W_1 \\ \phi_1 \\ \vdots \\ W_m \\ \phi_m \end{bmatrix}$$

In condensed form, this reads

$$F^{(1;j)} = \begin{bmatrix} K_{j1}^{(1;mod)} & K_{j2}^{(1;mod)} & \cdots & K_{j(2m-1)}^{(1;mod)} & K_{j(2m)}^{(1;mod)} \end{bmatrix} \begin{bmatrix} W_1 \\ \phi_1 \\ \vdots \\ W_m \\ \phi_m \end{bmatrix} \tag{5.17}$$

where $K_{pq}^{(1;mod)}$ are the modified entries of the stiffness matrix. The subscripts xx and xz have been removed in Equation 5.17 since this relation can be applied for all the interaction force entries for all domain boundaries. Similarly, the relations for the soil interaction forces at each location are obtained in terms of the plate degrees of freedom. Furthermore, the same steps can be used to obtain the stiffness matrix for domain 3 and domain 4. It should be noted that we are currently working with interaction forces, and these forces need to be made compatible with the internal forces in the plate. The interaction forces from domain 1 are translated as shown in Figure 5.3, Figure 5.4 and Equation 5.19.

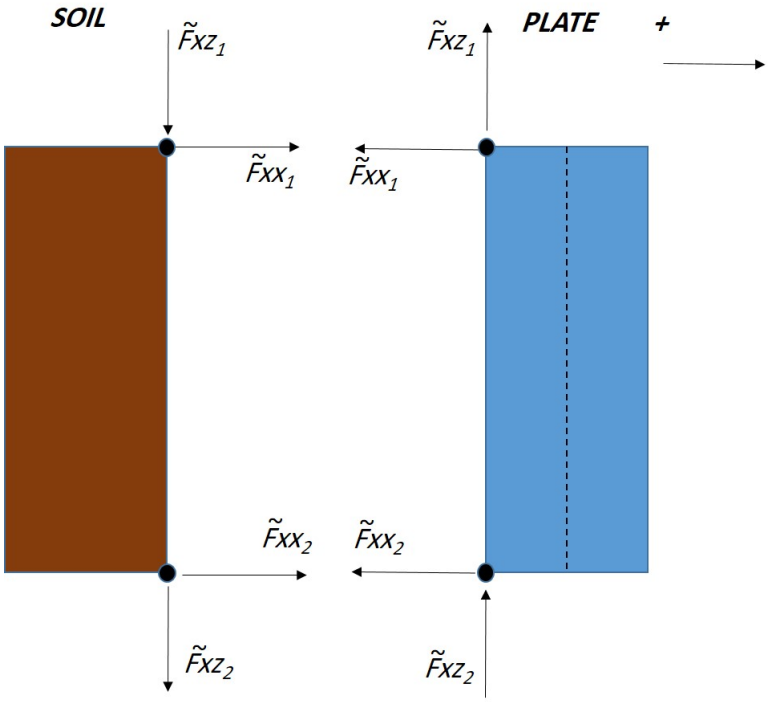

Figure 5.3: ***Translation of forces from soil to plate - domain 1***

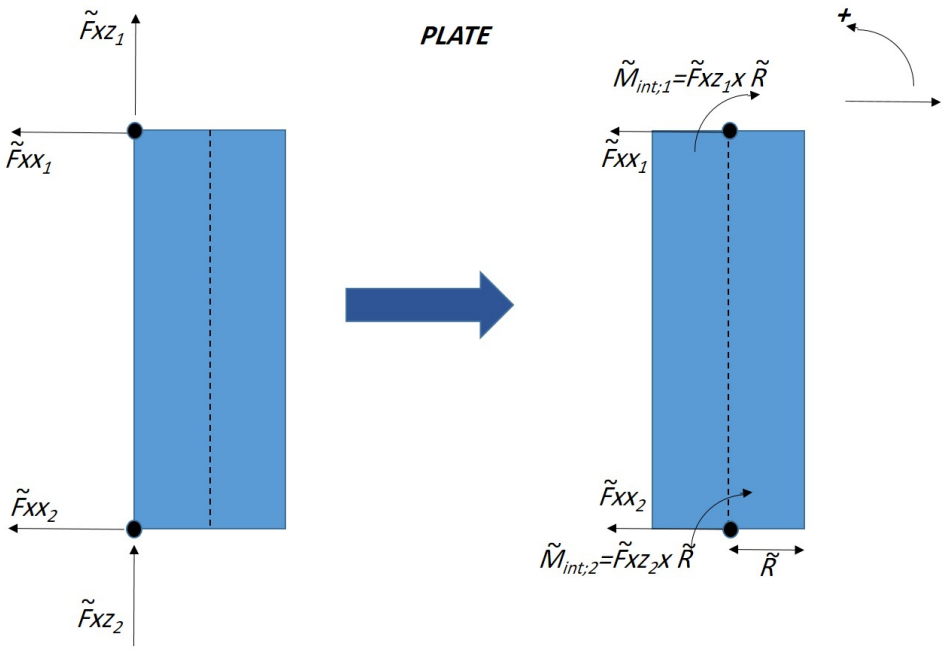

Figure 5.4: ***Moments due to shear forces***

The interaction forces from domain 1 are translated to the plate, as shown in Figure 5.3 and Figure 5.4.The relations are summarized for convenience.

$$\tilde{\mathbf{F}}_{\mathbf{s;1}} = \begin{bmatrix} \tilde{F}_{xx}^{(1;1)} \\ \tilde{F}_{xz}^{(1;1)} \\ \tilde{F}_{xx}^{(1;2)} \\ \tilde{F}_{xz}^{(1;2)} \\ \vdots \\ \tilde{F}_{xx}^{(1;m)} \\ \tilde{F}_{xz}^{(1;m)} \end{bmatrix} = \begin{bmatrix} -\tilde{F}_{xx}^{(1;1)} \\ -\frac{\tilde{M}_{int}^{1;1)}}{\tilde{R}} \\ -\tilde{F}_{xx}^{(1;2)} \\ -\frac{\tilde{M}_{int}^{(1;2)}}{\tilde{R}} \\ \vdots \\ -\tilde{F}_{xx}^{(1;m)} \\ -\frac{\tilde{M}_{int}^{(1;m)}}{\tilde{R}} \end{bmatrix} \tag{5.18}$$

The interaction forces from domain 3 are translated to the plate, as shown in Figure 3.15, Figure 3.16 and Equation 3.25. The relations are summarized for convenience.

$$\tilde{\mathbf{F}}_{\mathbf{s;3}} = \begin{bmatrix} \tilde{F}_{xx}^{(3;1)} \\ \tilde{F}_{xz}^{(3;1)} \\ \tilde{F}_{xx}^{(3;2)} \\ \tilde{F}_{xz}^{(3;2)} \\ \vdots \tilde{F}_{xx}^{(3;m)} \\ \tilde{F}_{xz}^{(3;m)} \end{bmatrix} = \begin{bmatrix} \tilde{F}_{xx}^{(3;1)} \\ \frac{-\tilde{M}_{int}^{3;1)}}{\tilde{R}} \\ \tilde{F}_{xx}^{(3;2)} \\ \frac{-\tilde{M}_{int}^{(3;2)}}{\tilde{R}} \\ \vdots \\ \tilde{F}_{xx}^{(3;m)} \\ \frac{-\tilde{M}_{int}^{(3;m)}}{\tilde{R}} \end{bmatrix} \tag{5.19}$$

The translation of interaction forces from the soil to the plate at the tip is shown in Figure 5.5. The obtained shear force and bending moment essentially acts as boundary conditions at the tip.

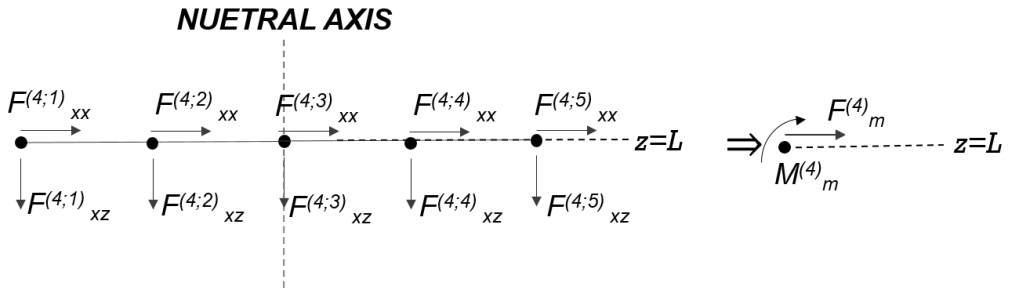

Figure 5.5: ***Interaction forces translated from soil to plate at the tip*** ($z = L$)

The interaction forces at the tip are given as

$$\tilde{\mathbf{F}}_{\mathbf{s;4}} = \begin{bmatrix} \tilde{F}_{xx}^{(4;1)} \\ \tilde{F}_{xz}^{(4;1)} \\ \tilde{F}_{xx}^{(4;2)} \\ \tilde{F}_{xz}^{(4;2)} \\ \vdots \\ \tilde{F}_{xx}^{(4;r)} \\ \tilde{F}_{xz}^{(4;r)} \end{bmatrix} \tag{5.20}$$

Using the reduction technique introduced in Equation 5.17, the soil interaction forces at the tip are given as

$$F^{(4;k)} = \begin{bmatrix} K_{k1}^{(4;mod)} & K_{k2}^{(4;mod)} R & \cdots & K_{k(2m-1)}^{(4;mod)} & K_{k(2m)}^{(4;mod)} R \end{bmatrix} \begin{bmatrix} W_m \\ \phi_m \\ \vdots \\ W_m \\ \phi_m \end{bmatrix}$$

$$= \begin{bmatrix} (K_{q1}^{(4;mod)} + K_{k3}^{(4;mod)} \cdots + K_{k(2m-1)}^{(4;mod)}) & (K_{k2}^{(4;mod)} + K_{k4}^{(4;mod)} \cdots + K_{k(2m)}^{(4;mod)}) R \end{bmatrix} \begin{bmatrix} W_m \\ \phi_m \end{bmatrix} \tag{5.21}$$

To obtain the shear force $F_m^{(4)}$ and bending moment $M_m^{(4)}$ at the tip, we combine the entries of the interaction force vector in the following way

$$\begin{aligned} F_m^{(4)} &= \sum_{k=1}^{r} F_{xx}^{(4;k)} \\ M_m^{(4)} &= \sum_{k=1}^{r} F_{xz}^{(4;k)} x_k \end{aligned} \tag{5.22}$$

5.3 Plate-soil system

The equilibrium equation for the plate-soil system can then be derived considering the stiffness matrices of all three domains

$$(-\tilde{\mathbf{M}}_{\mathbf{b}}\tilde{\omega}^2 + \tilde{\mathbf{K}}_{\mathbf{b}})\tilde{\mathbf{U}}_{\mathbf{b}} = \tilde{\mathbf{F}}_{\mathbf{ext}} + \tilde{\mathbf{F}}_{\mathbf{s;1}} + \tilde{\mathbf{F}}_{\mathbf{s;3}} + \tilde{\mathbf{F}}_{\mathbf{s;4}} \tag{5.23}$$

where $\tilde{\mathbf{F}}_{\mathbf{s;1}} = \tilde{\mathbf{K}}_{\mathbf{s}}^{(\mathbf{1;mod})}\tilde{\mathbf{U}}_{\mathbf{b}}$, $\tilde{\mathbf{F}}_{\mathbf{s;3}} = \tilde{\mathbf{K}}_{\mathbf{s}}^{(\mathbf{3;mod})}\tilde{\mathbf{U}}_{\mathbf{b}}$ and $\tilde{\mathbf{F}}_{\mathbf{s;4}} = \tilde{\mathbf{K}}_{\mathbf{s}}^{(\mathbf{4;mod})}\tilde{\mathbf{U}}_{\mathbf{b}}$. The term "$mod$" is used to indicate that the stiffness entries of the soil stiffness matrices have been modified based

of the degrees of freedom of the plate. Furthermore, the force vector from the tip domain is given as

$$\tilde{\mathbf{F}}_{\mathbf{s;4}} \begin{bmatrix} 0 \\ 0 \\ \vdots \\ F_m^{(4)} \\ M_m^{(4)} \end{bmatrix} \tag{5.24}$$

The stiffness matrix of the plate-soil system then becomes

$$\begin{aligned} (-\tilde{\mathbf{M}}_{\mathbf{b}}\tilde{\omega}^2 + \tilde{\mathbf{K}}_{\mathbf{b}} - \tilde{\mathbf{K}}_{\mathbf{s}}^{(\mathbf{1;mod})} - \tilde{\mathbf{K}}_{\mathbf{s}}^{(\mathbf{3;mod})} - \tilde{\mathbf{K}}_{\mathbf{s}}^{(\mathbf{4;mod})})\tilde{\mathbf{U}}_{\mathbf{b}} &= \tilde{\mathbf{F}}_{\mathbf{ext}} \\ \tilde{\mathbf{K}}_{\mathbf{d}}\tilde{\mathbf{U}}_{\mathbf{b}} &= \tilde{\mathbf{F}}_{\mathbf{ext}} \end{aligned} \tag{5.25}$$

where $\tilde{\mathbf{K}}_{\mathbf{d}}$ is the dynamic plate-soil stiffness matrix.

5.4 Results

This section explains the results for the plate-soil system for a plate embedded in an elastic waveguide. Two case studies are done, the first where L/D ratio of the plate is 25 and the second where L/D is 12.5. It should be noted that the depth of the waveguide varies in both cases, hence these two studies cannot be compared directly, however some interesting results are obtained from both the studies. The main results elaborated include the displacement, rotation, shear force and bending moment convergence plots for the plate-soil system with respect to increasing segments on domain 1 or 3 boundary as well as increasing segments along domain 4 tip. The interaction forces in the soil at the the vertical interface as well as the tip are also analyzed.

5.4.1 Case study 1

This case study was performed using the domain parameters given in Table 4.2.Up to 50 segments were considered across the boundary of domain 1 or 3, and up to 6 segments across the tip domain boundary. Relative difference at the tip for the quantities mentioned is used as the basis for convergence. These are calculated using Equation 5.26.

$$\epsilon_Q = \frac{|Q_b - Q_h|}{|Q_b|} \tag{5.26}$$

where ϵ_Q is the relative difference in the quantity obtained, Q_b is the value of the quantity in the benchmark solution and Q_h is the quantity in the hybrid solution. The boundary condition at the top used for the analysis is

$$W = 1 \quad \phi = 0, \quad z = 0 \tag{5.27}$$

Two cases are analyzed: Slip and non-slip.

2.4.1.1 Slip

For the slip case, we neglect the shear contributions of the soil at the interface to the dynamic response of the plate, meaning, we neglect the stiffness contributions of the degree of freedom u_z. This was explained in detail in section 3.5.2. It should be noted that this is done only for domain 1 and 3, since we choose to have non-zero boundary conditions at the

tip. Figure 5.6 shows the weighted plot of the real entries of the soil stiffness matrix obtained for domain 1 at $x = -R$ ($\tilde{K}_{s;1;slip}$) or domain 3 ($\tilde{K}_{s;3;slip}$) at $x = R$.

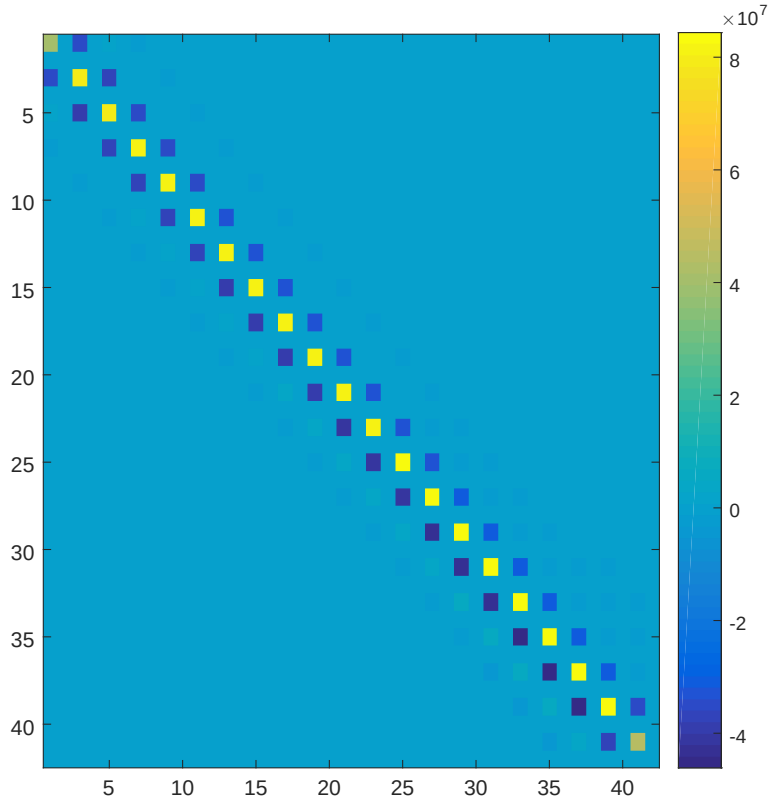

Figure 5.6: ***Weighted plot of real entries of the soil stiffness matrix evaluated for domain 3*** ($\tilde{K}_{s;3;slip}$) ***at*** $x = R$ ***or domain 1 at*** $x = -R$ ***- slip (Note: the units are in*** N/m^2

$'Weighted'$ refers to the relative scaling of all the entries in the matrix with respect to the entry with the highest entries. This can be understood from the color, although the values indicated are the exact values. The obtained matrix is not completely symmetric, which is not expected, as compared to the stiffness matrix for the single domain analysis, which is almost completely symmetric except for some entries associated with the top location (see Figure 3.17). This can be in the diagonal line of entries on either side of the main diagonal. A relative difference lies between 4 to 18% with the maximum relative difference observed for the first row and column, closer to the right top corner.

Displacement and rotation plot - Varying the number of segments across the tip

Figure 5.7 shows the displacement and rotation for the plate considering 20 segments across domain 1 and 3.The number of segments across the tip domain is varied from 2 to 6 segments. The relative error in the displacement and rotation with varying number of segments across the tip is shown in Figure 5.8. The legend entry for the hybrid method can be understood as follows - **'20 d1/3 2 d4'** indicates that there are 20 segments across domain 1 and 3 boundary and 2 segments across domain 4 boundary. The remaining entries can be interpreted in the same manner.

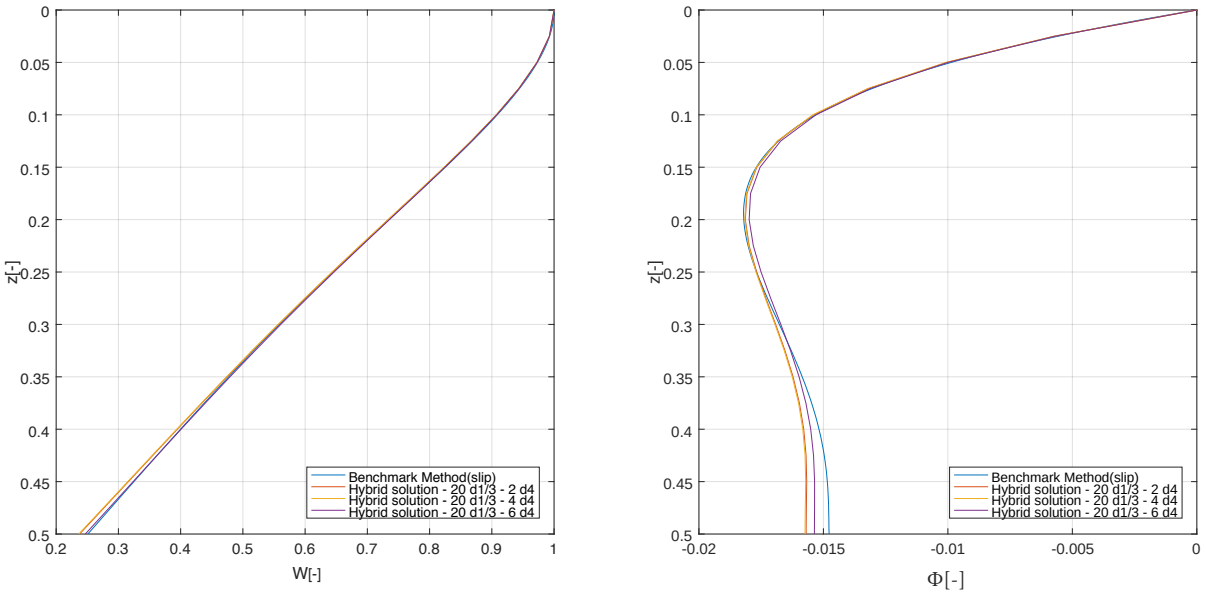

(a) **(b)**

Figure 5.7: ***Convergence plot - (a)Displacement and (b)Rotation - Plate considering 20 segments across domain 1 or 3 - Varying the number of segments across the tip***

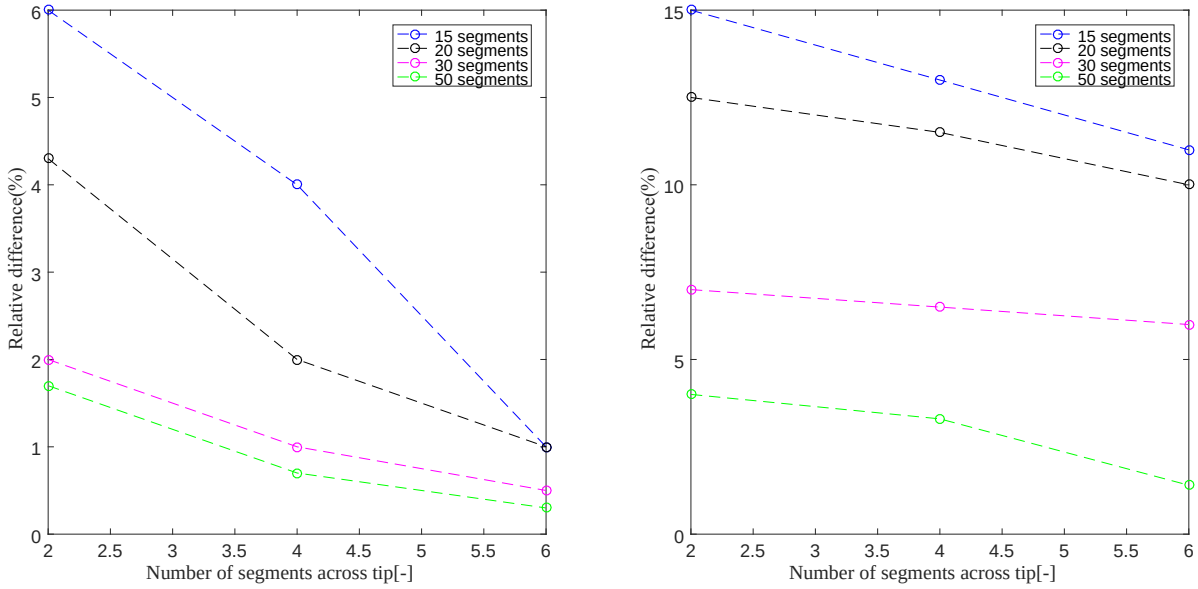

(a) ***Displacement*** **(b)** ***Rotation***

Figure 5.8: ***Relative difference with varying number of segments at the tip (Note: The scale for the vertical axis is different in each case)***

Increasing the number of segments across the tip reduces the relative difference at the tip although the change is observed to be small.

Shear Force and bending moment plot - Varying the number of segments across the tip

Figure 5.9 shows the shear force and bending moment plots considering 20 segments across domain 1 and 3 boundary with varying the number of segments across the tip. Least square fitting (described in Appendix C) was done for the benchmark solution for a smoother profile for comparison.

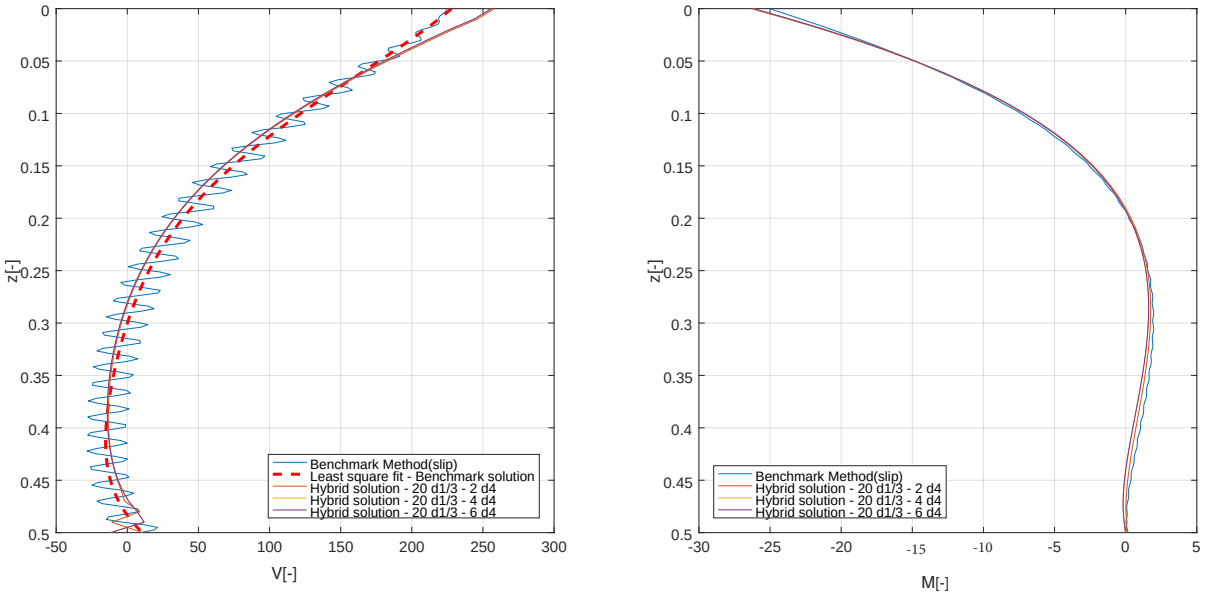

(a) **(b)**

Figure 5.9: ***Convergence plot - (a)Shear force and (b)Bending moment - Plate considering 20 segments across domain 1 or 3 - Varying the number of segments across the tip***

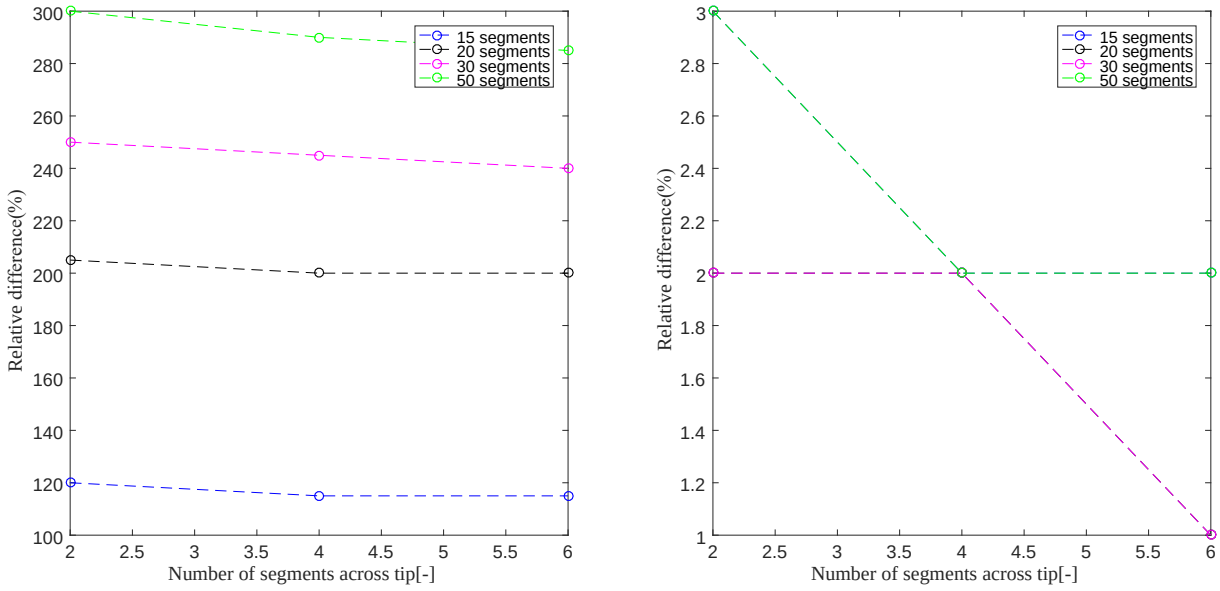

(a) ***Shear Force*** **(b)** ***Bending moment***

Figure 5.10: ***Relative difference with varying number of segments at the tip***

Figure 5.10 shows the relative difference in the bending moment and shear force with respect to the benchmark solution for varying number of segments across the tip.

It is observed that relative difference in the shear force and bending moment at the tip increases with increase in the number of segments across Domain 1 and 3. Increasing the number of segments across the tip does not influence the solution much. For the shear force at the tip, the relative difference is large since the value obtained for the hybrid solution is negative whereas the benchmark solution is positive. With increasing the number of segments, the shear force is observed to become more and more negative.

In the benchmark method, the boundary conditions at the tip given as the bending moment and shear force are evaluated from the stress distribution across the tip alone, however in the hybrid method, the contributions are included from the last location on domain 1 and 3 in addition to the tip.

Hence, to make a fair comparison, we subtract the shear force contribution of the last location on domain 1 and 3 boundary from the shear force value at the tip. This is also done for the bending moment as well. For the slip case, it does not make a difference with regard to the bending moment, since the shear force contributions for the last location are currently neglected.

Figure 5.11 shows the shear force plot after the modification. m is the last node.

$$\begin{aligned} V^{(i)}_{m;mod} &= V^{(i)}_{m;hybrid} - F^{(1;m)}_{xx} + F^{(3;m)}_{xx} \\ M^{(i)}_{m;mod} &= M^{(i)}_{m;hybrid} - M^{(1;m)}_{int} - M^{(3;m)}_{int} \end{aligned} \tag{5.28}$$

where $V^{(i)}_{m;mod}$ and $M^{(i)}_{m;mod}$ are the modified shear force and bending moment at the tip.

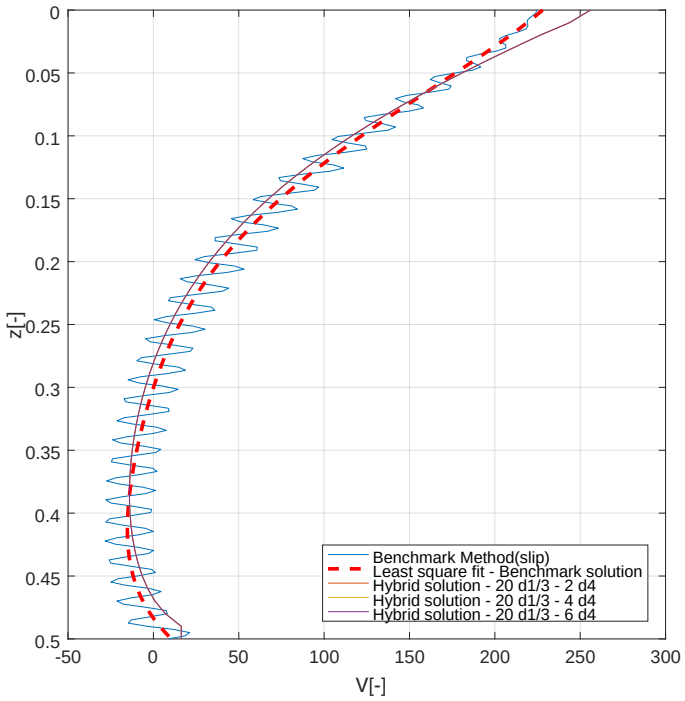

Figure 5.11: ***Shear force plot considering 50 segments across Domain 1 and 3 with the modification***

The relative difference is now around 50 % at the tip, however now this is a fair comparison.

Varying the number of segments across Domain 1 and 3

As we have now established, that value at the tip does not change much by increasing the number of segments across the tip, we now discuss the influence of varying the number of segments across domain 1 and 3 to observe the sensitivity of the model to changes in domain 1 and 3. For further studies in this section, we will consider 6 segments across Domain 4.

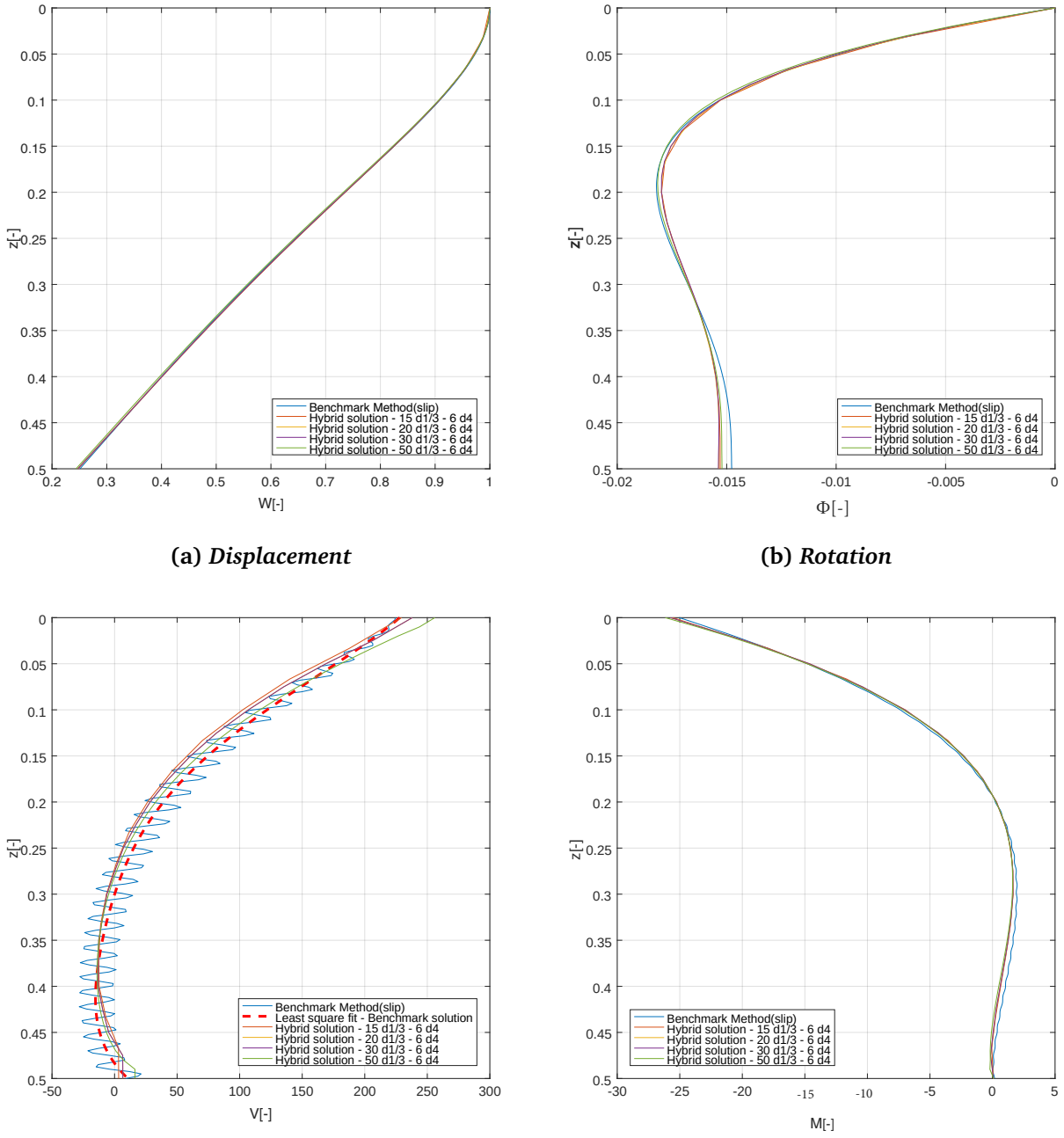

(a) ***Displacement*** **(b)** ***Rotation***

(c) ***Shear Force*** **(d)** ***Bending Moment***

Figure 5.12: ***Convergence plot - Varying the number of segments across the domain 1 and 3 - with 6 segments across the tip -slip***

Figure 5.12 shows the convergence plots for the displacement, rotation,shear force and bending moment. With respect to the displacements, with 15 segments already, the relative error at the tip is less than 6 %. The rotation profile for the hybrid solution and benchmark solution match except at the tip. With 50 segments, the error is less than 5 % at the tip.

With regard to the shear force profile, the relative difference in the value at the top $z = 0$ increases with increasing the number of segments. The value at the tip convergences to the benchmark value. There is some uncertainty in the bench mark solution with respect to the shear force profile as well due to its oscillatory nature. The bending moment profile for the hybrid solution matches well with the benchmark solution.

2.4.1.2 Non-Slip

For the non-slip case, the fully populated stiffness matrices of Domain 1 and 3 are considered in the plate-soil system. Figure 5.13 shows the weighted plot for the soil stiffness matrix $\tilde{\mathbf{K}}_{\mathbf{s;1}}$ or $\tilde{\mathbf{K}}_{\mathbf{s;3}}$

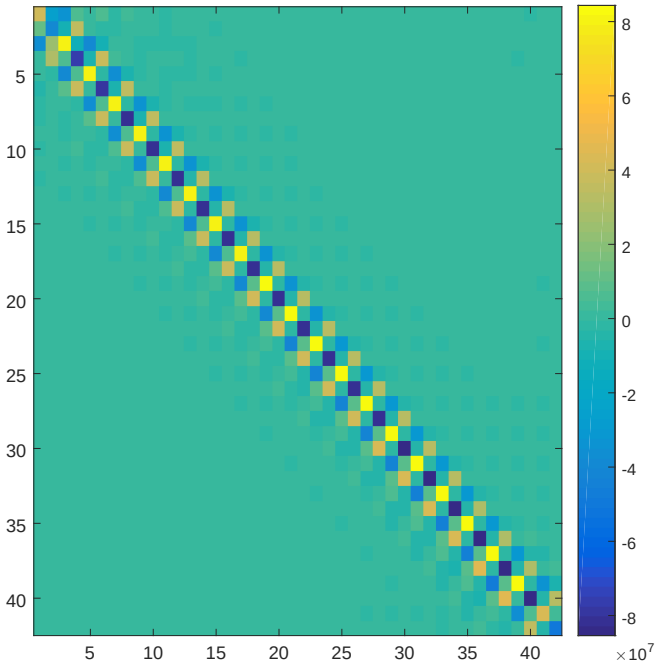

Figure 5.13: ***Weighted plot of soil stiffness matrix*** $\tilde{\mathbf{K}}_{\mathbf{s;1}}$ ***or*** $\tilde{\mathbf{K}}_{\mathbf{s;3}}$ ***- non-slip***

Similar to the slip case, the stiffness matrix is not symmetric. A relative difference lies between 4 to 18% with the maximum relative difference observed for the first two rows and columns, closer to the right top corner.

With regards to the sensitivity of the discretization in the tip domain, the discretization at the tip shows no influence on the dynamic behavior of the plate. A converged reference solution for the non-slip was not obtained. With the hybrid method, the solutions for the non-slip case were obtained. These were compared with the slip case.

Figure 5.14 shows the displacement, rotation, shear force and bending moment plots for the non-slip case. Additionally the reference solution for the slip case are also plotted to make a direct comparison.

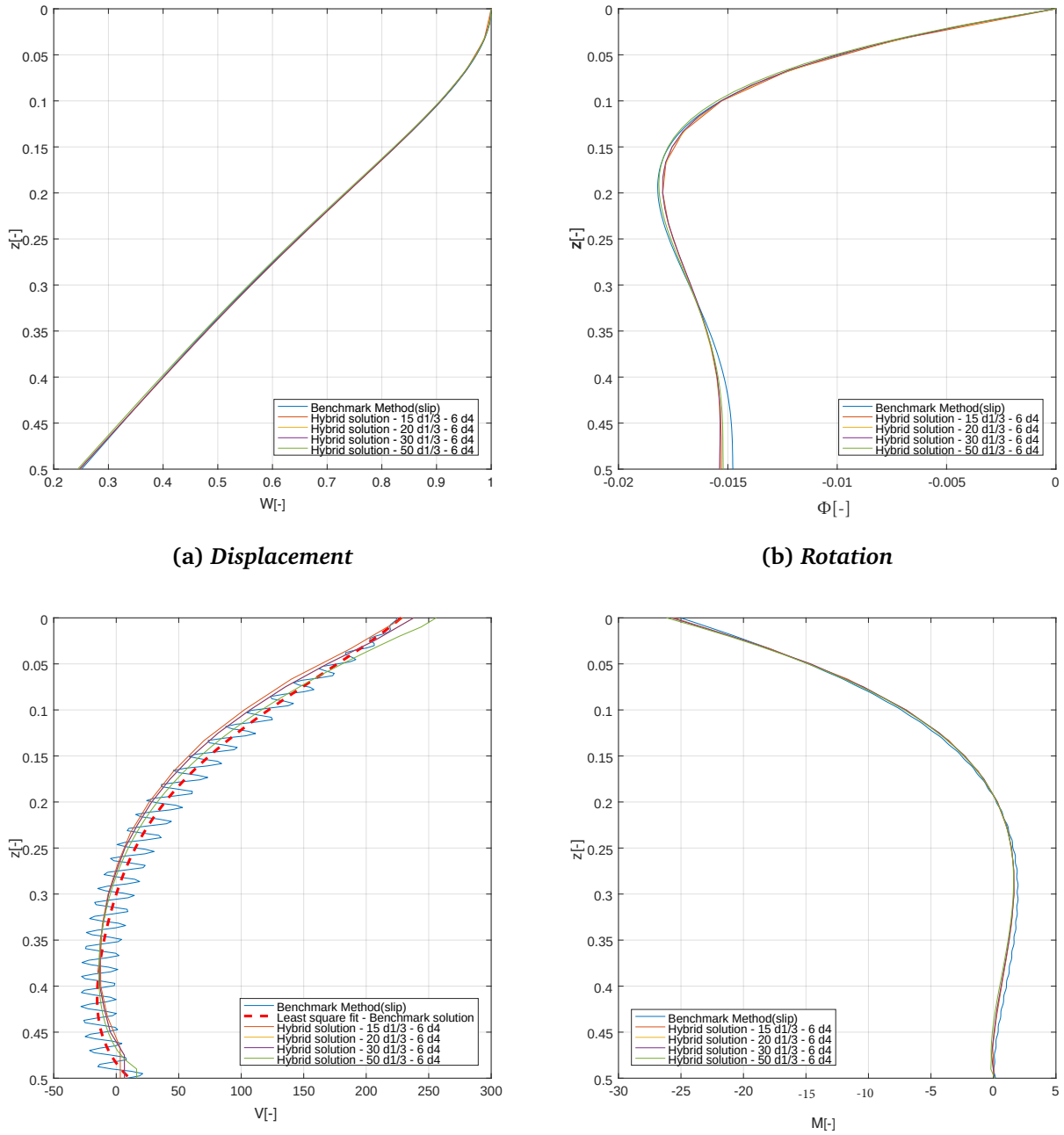

(a) ***Displacement***

(b) ***Rotation***

(c) ***Shear Force***

(d) ***Bending Moment***

Figure 5.14: ***Convergence plot - Varying the number of segments across the domain 1 and 3 - with 6 segments across the tip -non-slip***

Comparing the slip and the non-slip case, we observe that the relative difference in displacement at the tip is less than 1 %. The average change (calculated using Equation 3.11 across the depth of the plate was observed to be less than 1 %. The average change here indicated the average of the relative difference for the quantity at all nodes along the plate. With respect to the rotation profile, the change at the tip is less than 5% as well for the average change across depth. Similar values were obtained Bending moment distribution. For the shear force distribution, a relative change of less than 1% at the tip was observed. With respect to the average change, it was around 4%. The value at the top and tip were almost the same, however, the change was observed within the plate depth.

2.4.1.3 Interaction force distribution

The shear and normal interaction force distribution in the soil at $x = -R$ is shown in Figure 5.15 and Figure 5.16 respectively.

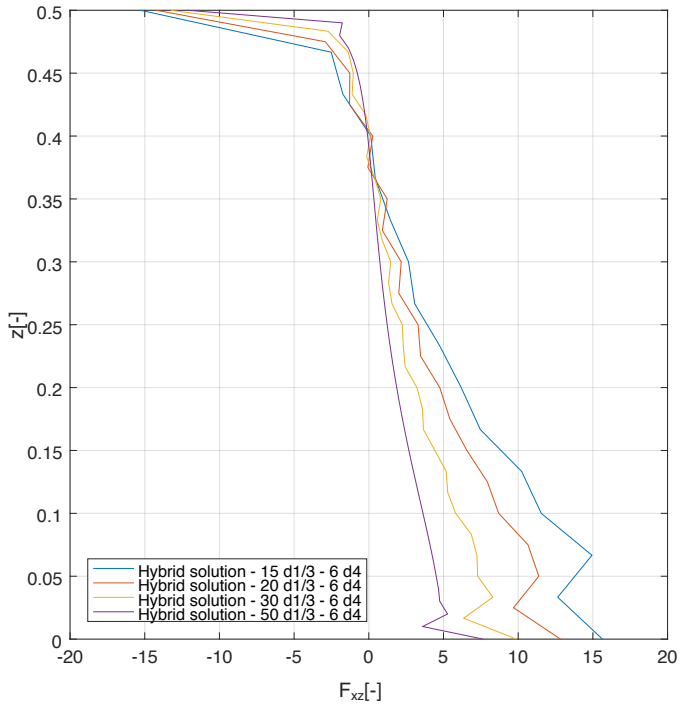

Figure 5.15: ***Shear interaction force distribution at*** $x = -R$

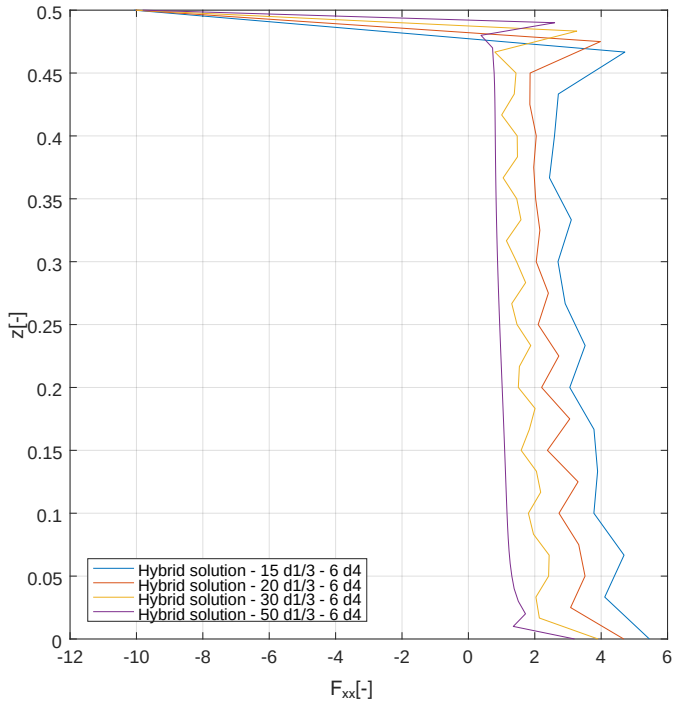

Figure 5.16: ***Normal interaction force distribution at*** $x = -R$

Since the change in the dynamic behavior of the plate is observed to be independent of the discretization at the tip in the current study, for the results of the interaction force along domain 1 and 3 boundary, we assume the number of segments to be constant across the tip.

A large jump at the top $z = 0$ is observed in the shear interaction force distribution. This is due to the imposed non-zero value of shear force at these locations, however the boundary conditions dictate a zero value for the shear stress at the top when obtaining the domain 1 and 3 eigen modes. The magnitude of the shear interaction force reduces at the top with increasing number of segments, however the change is very small. In the single domain analysis, this was observed to converge to a very small value (see Figure 3.29). A small jump close to the tip is also observed.

A large jump at the top is also observed for the normal interaction force distribution at the top. This could be attributed to the bending moment imbalance at the top which was explained in Section 4.7 since the magnitude of the normal interaction at the top does not decrease as the number of segments across domain 1 and 3 is increased. In the single domain analysis, this was observed to converge to a very small value (see Figure 3.27)A jump is also observed at the tip, however the jump is less pronounced.

The soil interaction forces at the tip in domain 4 (computed using Equation 5.21) are shown in Figure 5.17. It compares the force distribution obtained at tip for a discretization of 20 and 50 segments across Domain 1 and 3.

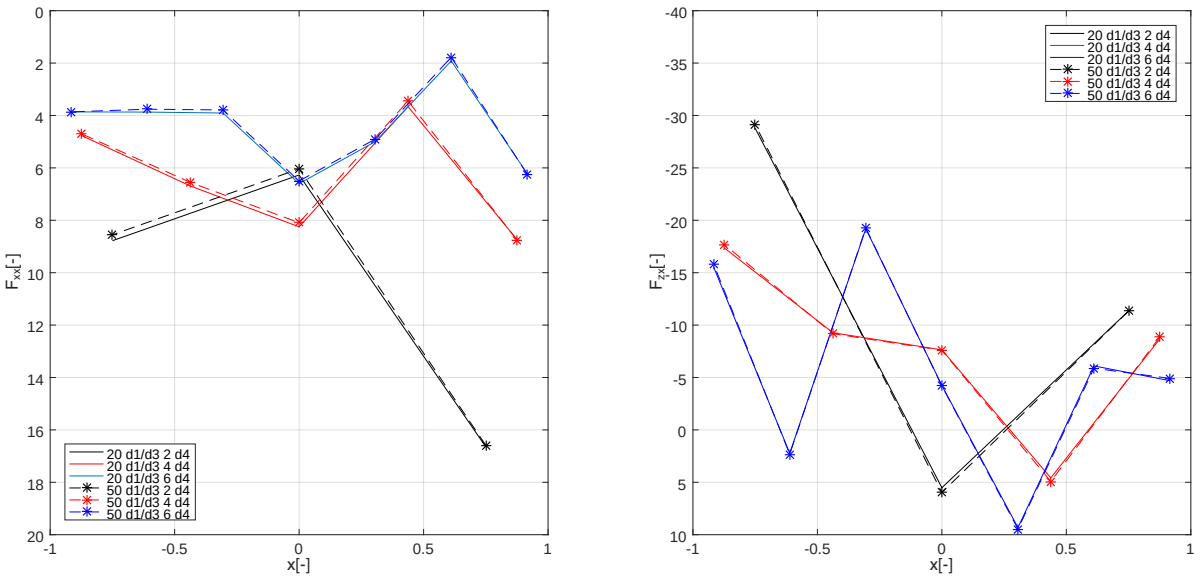

(a) ***Normal interaction force*** **(b)** ***Shear interaction force***

Figure 5.17: ***Tip interaction forces - Convergence study***

It is observed that they are almost exactly the same, which indicates that for this case, increasing the discretization across domain 1 and 3 does not influence the soil interaction forces at the tip.

Hence with respect to tip, it is observed that for the current study, neither the discretization across domain 4 (shown in Figure 5.14) nor the discretization across domain 1 and 3) has an influence on the reactions at the top.

5.4.2 Case study 2

This section discusses a second study performed for the smaller L/D ratio of the plate as compared to the first study, in this case 12.5. The objective of the study is to investigate if reducing the L/D ratio has an influence on the dynamic behavior of the plate embedded in the waveguide. The domain parameters are summarized in Table 5.1. For the given set of parameters up to 20 segments, across domain 1 and 3, could be considered with 401 soil modes for obtaining non-oscillatory displacement convergence plots (see Appendix E for convergence plots. Hence the results shown are limited to those with 20 segments across domain 1 and 3. The number segments across the tip varied up to 6, as done in the main case study. Appendix E shows the number of fourier components used for each segment length for converged stress distribution at the tip. Some additional observations with regard to the influence of the tip are made.

Table 5.1: ***Soil domain properties***

Parameter	***Value***	***Units***
Embedded length of plate(L)	25	m
Domain 1 or 3 depth (H)	50	m
Diameter(D)	2	m
Embedded Length/Diameter(L/D)	12.5	-

5.4.2.1 Slip

The displacement and rotation plot for the slip case are shown in Figure 5.18.

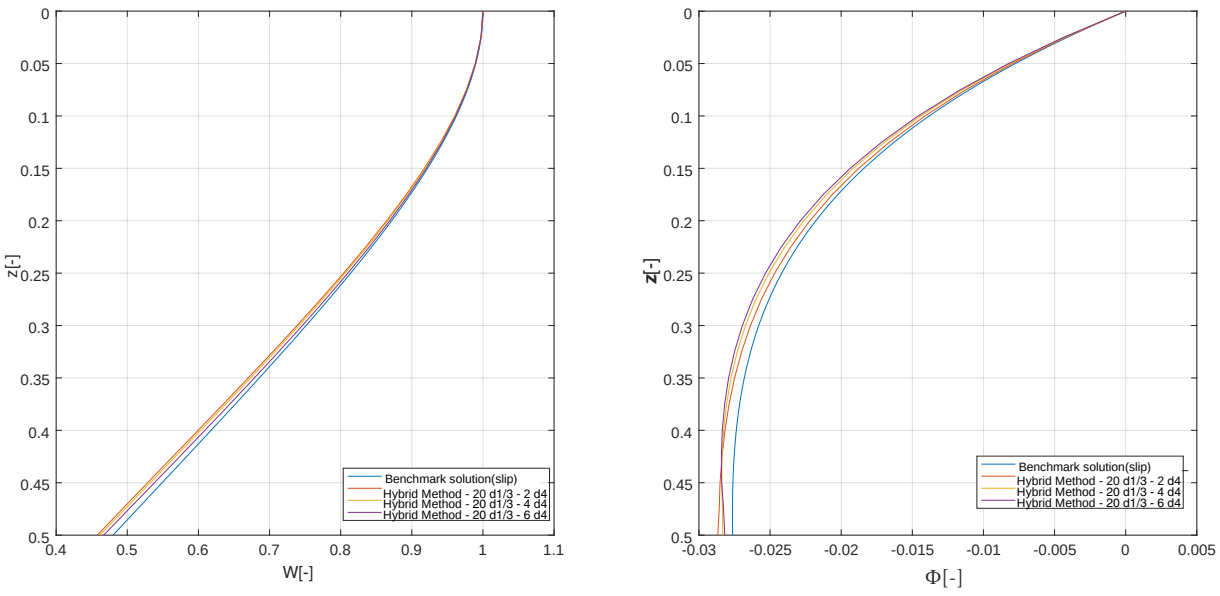

(a) **(b)**

Figure 5.18: ***Convergence plot - (a)Displacement and (b)Rotation - Plate considering 20 segments across domain 1 or 3 - Varying the number of segments across the tip - slip case***

With increasing the number of segments across the tip domain, the solution is seen to converge to the benchmark solution. Furthermore, it can be observed that varying the number

of segments influences pile deflection and rotation across its length.

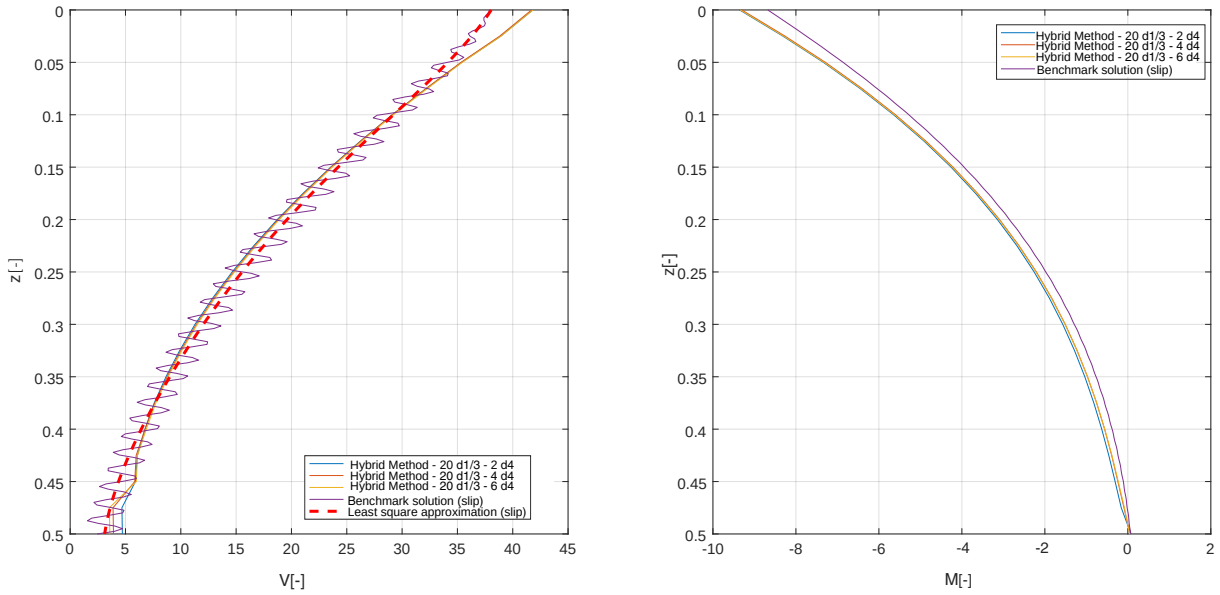

(a) ***Shear Force*** **(b)** ***Bending moment***

Figure 5.19: ***Convergence plot - (a)Shear force and (b)Bending moment - Plate considering 20 segments across domain 1 or 3 - Varying the number of segments across the tip - slip case***

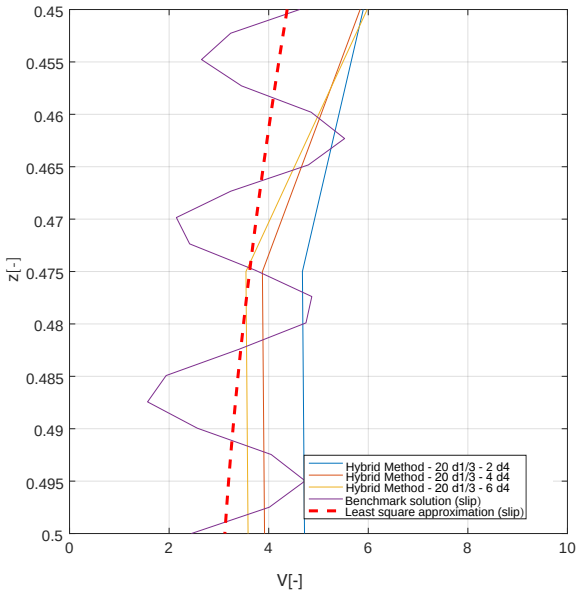

Figure 5.20: ***Shear force distribution at*** $x = -R$ ***close to the tip***

Figure 5.19 shows the shear force and bending moment of the plate for varying number of segments across the depth of the plate. With regard to the shear force distribution, similar to the main case study, a deviation at the top is observed. In the bending moment distribution, a constant difference of 8-10 % is observed through the profile, however it converges to the benchmark solution at the tip.

Figure 5.20 shows the shear force distribution close to the tip. It is observed that as the number of segments is increased, the value at the tip for the hybrid method goes closer to

the benchmark solution showing the influence of the tip discretization. Hence discretization at the tip is shown to affect the reaction forces at the tip as well. It should be noted that this is the modified shear force value obtained using Equation 5.28. Additionally a small kink is observed just above the tip.

5.4.2.2 Non-slip

Figure 5.21 shows the displacement, rotation, shear force and bending moment plot for the non-slip case, with 20 segments across the Domain 1 and 3 boundary, and varying number of segments across the tip domain.

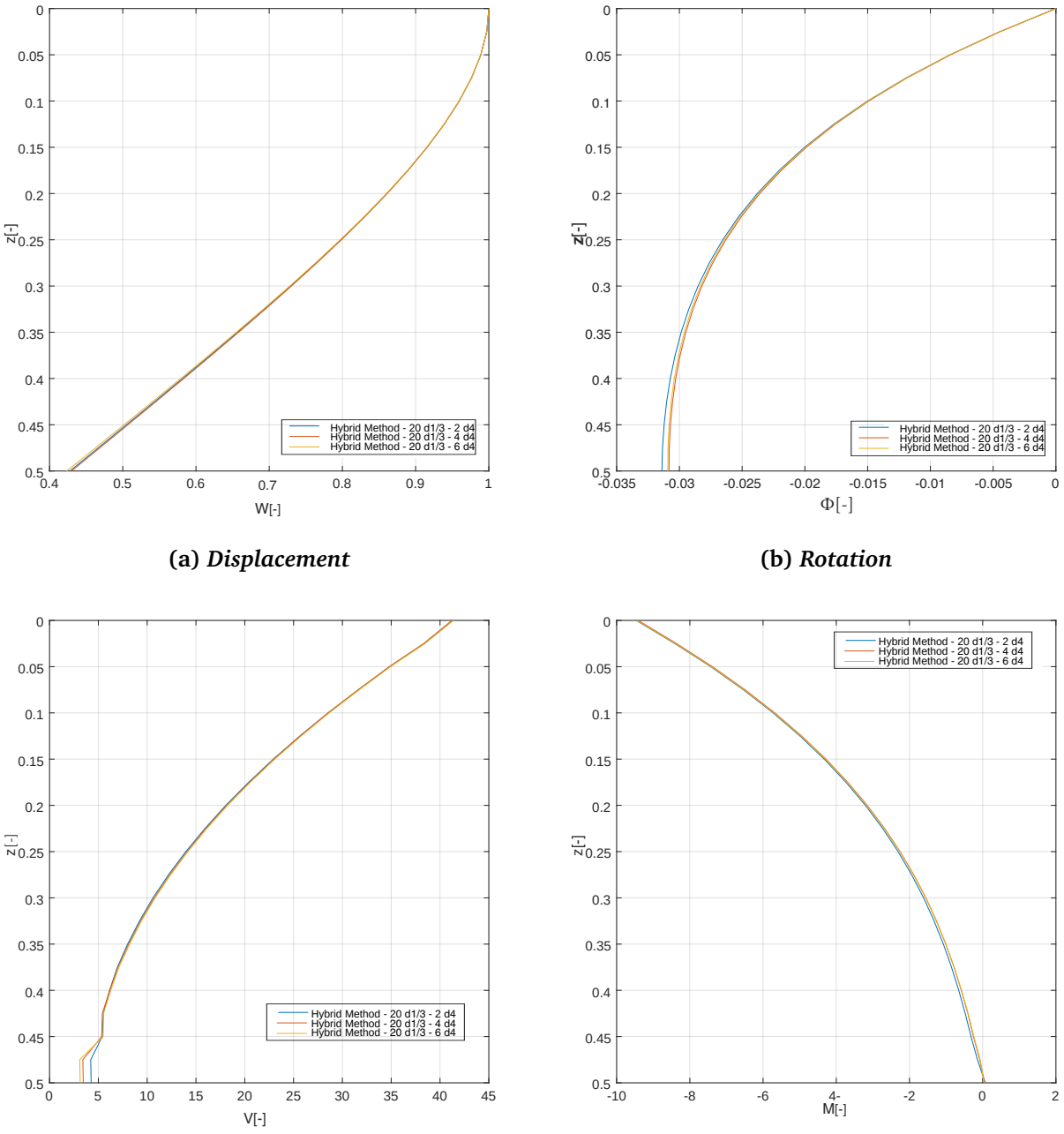

(a) ***Displacement***

(b) ***Rotation***

(c) ***Shear Force***

(d) ***Bending Moment***

Figure 5.21: ***Convergence plot - Varying the number of segments across the domain 1 and 3 - with 6 segments across the tip -non-slip***

As seen from the figure, varying the number of segments across the tip domain has a localized effect close to the tip most prominent in the shear force plot.

5.4.2.3 Comparing Non-slip and Slip

Figure 5.22 shows the plots comparing the slip and non-slip case.

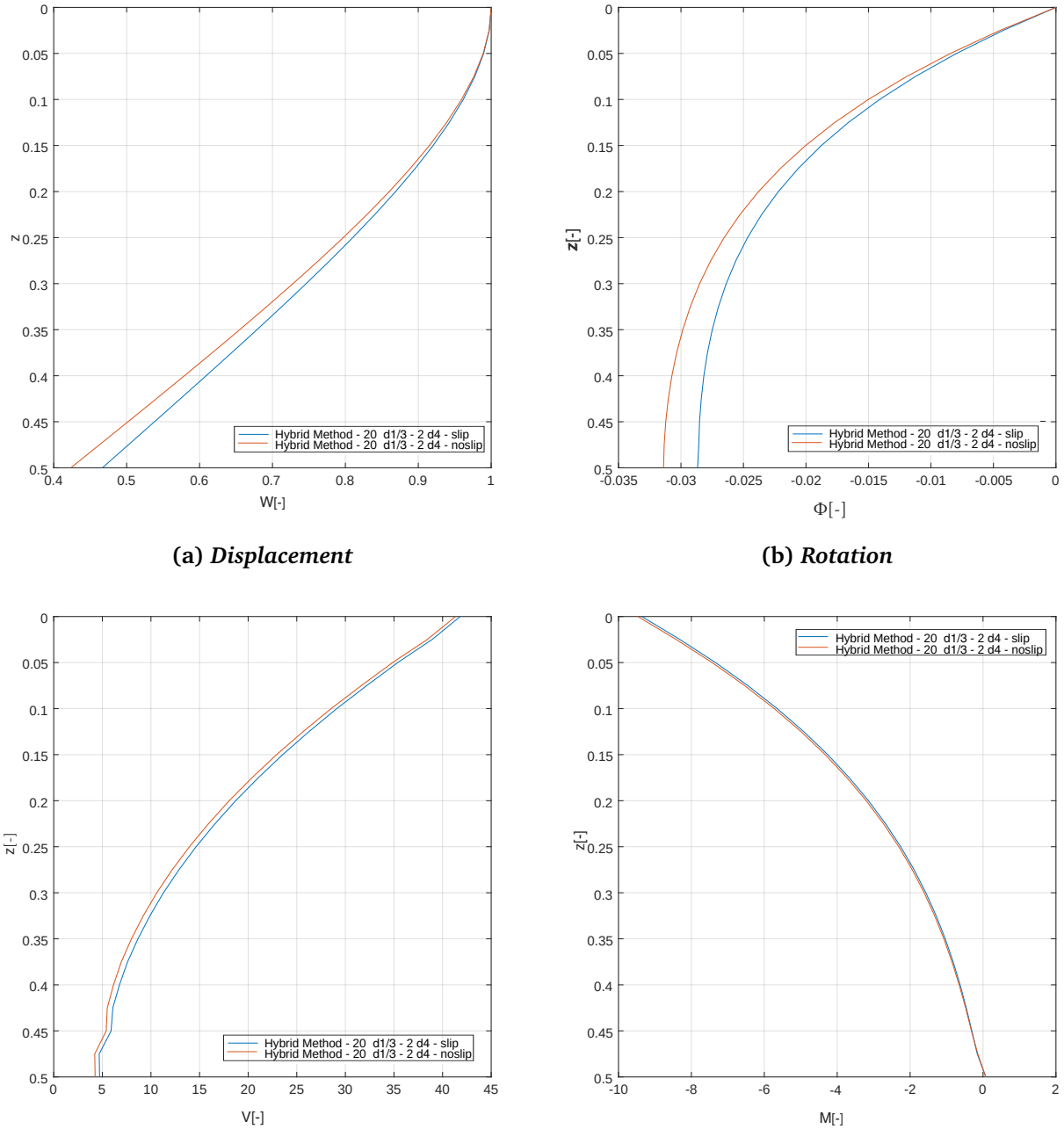

(a) ***Displacement*** **(b)** ***Rotation***

(c) ***Shear Force*** **(d)** ***Bending Moment***

Figure 5.22: ***Comparing Slip and Non-slip - 20 segments across domain 1 and 3 boundary and 2 segments across tip domain***

With regard to the displacement plot, a relative difference of 12 % is observed at the tip. For the rotation plot, a relative difference of 15 % is observed at the tip. With respect to the Bending moment distribution, a relative difference of less the 2 % is observed, and for the shear force distribution, an average difference of 5 % is observed across the entire

profile including the top and the tip. As compared to the previous case study (see section 2.4.1.2), we see a significant change from the slip to the non-slip case and this could be due to the reduction in the L/D ratio. Additionally, comparing the shear force at the tip (see Figure 5.14), 40 % increase in the magnitude is observed in case study 2 as compared to case study 1 (for the non-slip case), which indicates that reducing the L/D ratio increases the reaction at the tip, which is important to note.

5.5 Summary and Conclusion

The chapter describes the hybrid solution for plate embedded in an elastic waveguide. Using the displacement fields obtained from the previous chapter, the global stiffness matrix for the soil is derived at the cavity boundary. This is then split into individual domain stiffness matrices using force and displacement compatibility relations between the degrees of freedom of the plate and soil, which can then be combined with the plate mass and stiffness matrices to obtain the dynamic soil-pile stiffness matrix.

Two case studies were discussed. The first study follows directly from the previous chapter with the L/D ratio for the plate as 25 (highly flexible) and soil domain depth of H =100m. Similar to the single domain analysis, the hybrid and benchmark method were compared using the displacement, rotation, shear force and bending moment profiles across the depth of the plate. The hybrid method gave a smoother profile and removes the oscillatory nature of the shear force distribution (which is also observed with the single domain anaalysis). Based on convergence studies,it was observed varying the number of segments at the tip had very little influence on the dynamic behavior of the plate. Similar to the single domain analysis, two cases of slip and non-slip were analyzed. Less than 1 % relative change between the displacement at the tip, and 4% between the rotation at the tip was observed for the slip case. The hybrid method gives a converged solution for the non-slip case which is not obtained in the benchmark solution. However, negligible change is observed from the slip to non-slip case. With regard to the soil interaction forces, a large jump for the shear and normal interaction forces was observed close to the top ($z = 0$). Furthermore the magnitude of the jump does not reduce with increasing number of segments across domain 1 and 3 boundary. The large jump in normal force could be due to the bending moment imbalance for the top soil element. This also exists in the single domain study, however, the effect disappears as the number of segments are increased. Analysis of the tip boundary interaction forces, shows that the varying the number of segments across domain 1 and 3 boundary has no effect on the magnitude of the interaction forces. It can be established that the hybrid method is in good agreement with the benchmark solution.

In the second case study, a smaller L/D of 12.5 (still flexible) and $H = 50$ m domain depth is used. In the slip case, increasing the discretization of the tip domain has an influence on the rotation an displacement profile of the plate across the length. With the shear force distribution, it was observed that varying the number of segments across the tip domain boundary has a local effect close to the tip. For the non-slip case, the discretization at the tip has a local effect close to the tip for all quantities particularly the shear force distribution. Comparing the slip and non-slip case, significant changes are observed in all quantities except the bending moment, which was not observed in the previous case study. This could be due to the reduction in the L/D ratio.

Comparing the two case studies, three observations were made regarding the reduction of the L/D ratio. Firstly, the sensitivity of the dynamic behavior of the plate to the variation of segments at the tip. Secondly, a significant change from slip to non-slip behavior. For practical applications this could be important since the non-slip case is more realistic. Thirdly,

the increase in the magnitude of the shear force (around) 40%) due to the reduction in the L/D ratio.

Chapter 6

Conclusions and Recommendations

This chapter gives the most important conclusions of this research and recommendations for future research. Conclusions are split into three parts. First, conclusions for the hybrid solution for the plate-soil system considering a single domain of soil are given. This is followed by the conclusions from the study on a waveguide with a cavity subjected to excitation on the cavity surface. Finally, the conclusions from the hybrid solution method for plate embedded in a waveguide are presented. This is followed by the recommendations.

6.1 Hybrid solution for the plate-soil interaction with a single soil domain

The major conclusions of the analysis are

- **Number of segments vs number of soil modes**

  As the segment length, the number of soil modes required for convergence (stress or displacement field) is found to be higher. As the segment length reduces, smaller wavelengths will have higher contribution to the solution, hence the higher modal contributions become significant.

- **Symmetry of the soil stiffness matrices derived at the domain boundaries**

  For both the cases of slip and non-slip, it is observed that the obtained soil stiffness matrices are almost perfectly symmetrical except in the first two rows and columns. The stiffness entries here are associated with the top location $z = 0$

- **Slip vs non-slip**

  Comparing the slip and non-slip case, an average variation of less than 1% is observed for all quantities (displacement, rotation, shear force and bending moment) across the depth of the plate.

- **Hybrid solution vs Benchmark solution**

  The hybrid solution is compared to the benchmark solution for the cases of slip and non-slip. The hybrid solution is in good agreement with the benchmark solution for the

slip when comparing the quantities - displacement, rotation, shear force and bending moment profiles for the slip case. Based on the convergence studies by varying the number of segments across domain 3 boundary, it is observed that significantly larger number of segments are required for the shear force convergence, as compared to the other quantities. For the non-slip case, the hybrid solutions removes the oscillatory nature of the benchmark solution.

- **Shear stress incompatibility at the top corner at the boundary of domain 3**

  Due to the imposed boundary conditions at the top when deriving the eigen modes of the soil, there is shear stress incompatibility at the top. In classical continua, for any continuum element, the shear stresses in the perpendicular faces must be equal to maintain bending moment equilibrium. Although this incompatibility exists, it does not seem to have any considerable effect on the dynamic behavior of the soil.

6.2 Waveguide with a cavity subjected to excitation (as stresses) in the cavity surface

The major conclusions of this analysis are

- **Number of soil modes required for converged non-oscillatory displacement profiles when a stress is imposed on domain 1 or 3 boundary**

  Based on convergence studies with respect to the displacement fields at the boundaries for stress applied to locations on the boundary of domain 1 and 3, it is observed that the number of soil modes required for corner locations are much higher than for the top and intermediate locations

- **Number of soil modes required for converged non-oscillatory displacement profiles when a stress is imposed on domain 4 boundary**

  The number of soil modes required for obtaining converged non-oscillatory displacement profiles for stress imposed on all locations on the domain 4 boundary are the same as the number of soil modes required for the the corner locations on domain 1 and 3.

- **The bottom corner locations - domain 1, 3 and 4**

  At the bottom corner, a discontinuity of displacements between the interacting domains is observed independent of the location where the stress is imposed. This can be attributed to the bending moment imbalance for the corner elements in the domain 4 boundary, due to the imposed homogeneous stress boundary conditions as explained in section 4.6. The relative difference between the displacements of the interacting domains at the corner is observed to be much more pronounced when the stress is imposed at the corner location on domain 1 or 3 boundary since in addition to the bending moment imbalance, the stress gradient is large, and the eigen modes might not be able to accurately capture this change. The triangular stress distribution imposed at the corner of domain 4 is represented as a fourier expansion, which suffers from Gibbs

phenomenon, resulting in an overshoot close to the corner. Hence, two alternatives for modeling the stress distributions imposed at the corner are suggested. For the stress distribution imposed on domain 1 or 3 corner, a shift in the apex of the triangle away from the corner location, and for the stress imposed on the corner of domain 4, a shift in the location away from the corner in addition the a slight shift in the apex of the imposed triangular stress. This is shown to significantly improve the continuity of displacements at the corners.

6.3 Hybrid solution for a plate embedded in an elastic waveguide

The major conclusions of this analysis are

- **Non-symmetric soil stiffness matrices at the boundary of domain 1 and 3**

  The stiffness matrices derived for both the slip as well as the non-slip shows slight asymmetry. The maximum relative difference was observed for the first two rows and columns of the matrices. Slight differences were observed with the diagonal line of stiffness entries above and below the main diagonal.

- **Shear force profile of the plate**

  For the non-slip case, the hybrid method removes the oscillatory nature of the shear force distribution across the length of the plate.

- **Effect of the moment imbalance at the top corners of domain 1 and 3 boundary**

  The normal interaction force distribution for domain 1 and 3 has a large jump close to the corner. The magnitude of the jump does not reduce even when the number of segments across the domain is increased. This could be attributed to the bending moment imabalance occurring close to the top corners. The imbalance in the moment due to the absence of the shear stress at surface of the waveguide is compensated ny the increase in the magnitude of the normal interaction force close to the top corner.

- **Variation of L/D ratio**

  Two case studies were performed for varying L/D ratios (25 and 12.5) with varying waveguide depths (100m and 50m) respectively. For the first study, it is observed that the discretization of the tip domain boundary has no significant influence on the dynamic behavior of the plate. Furthermore, the relative difference in the quantities (displacement, rotation, bending moment and shear force) is negligible comparing the slip and non-slip case. Similarly varying the number of segments across domain 1 or 3 boundary has no significant effect on the interaction forces in the domain 4 boundary. With the second case study with the reduced L/D, it is observed that for the slip case, the discretization at the tip influences the dynamic behavior of the plate along its length. Furthermore, the magnitude of the shear force at the tip is sensitive to the discretization in the tip domain boundary. Comparing the slip and non-slip case, a significant difference is observed in the behavior of the pile. For practical consideration, the non-slip

case should be analyzed since it is more realistic. Furthermore, a 40% increase in the shear force at the corner is observed for L/D of 12.5 as compared to 25. Based on this, it can be concluded that including the tip does have an effect on the dynamic behavior of the plate.

6.4 THE BIGGER PICTURE

The study with the plate embedded in an elastic continuum demonstrated that as the L/D ratio for the plate is reduced, the tip has an influence on the dynamic behavior of the pile. For these case studies, the L/D ratio considered is in the range where the pile is flexible. Therefore, for the monopiles currently manufactured whose L/D ratio lies between 3 and 7, the influence of the tip is bound to be significant.

6.5 Recommendations

Based on the study conducted, it is recommended to consider the influence of the soil below the tip, to more accurately model the soil-structure interaction for current monopile foundations.

The author would like to draw the following recommendations for future research in this topic -

1. Validating the hybrid solution with field experimental results.
2. Incorporating soil inhomogeneity by considering multiple layers of soil around the plate.
3. An extensive study with varying the L/D ratio of the plate in the range of currently designed monopile foundations.
4. For the L/D < 7, the shear deformation in the piles would be significantly large. Reissner plate theory considers transverse shear deformations in its kinematic assumptions, and could be used to model the pile.
5. The plate could be modeled with smoother corners, to avoid the jumps in stresses at the corner
6. Development of a three-dimensional model for the same problem could give more realistic insight.

Appendix A

Benchmark Solution

The benchmark solution is a semi-analytical plate soil interaction model developed by Ir. Frank Renting, as part of TKIW02001 project "DISSTINCT" (Dynamic Interaction between Soil and Structure, Tools and Investigation using Numerical Calculations and Testing), Siemens Wind power. He is the author's mentor through the course of this thesis.

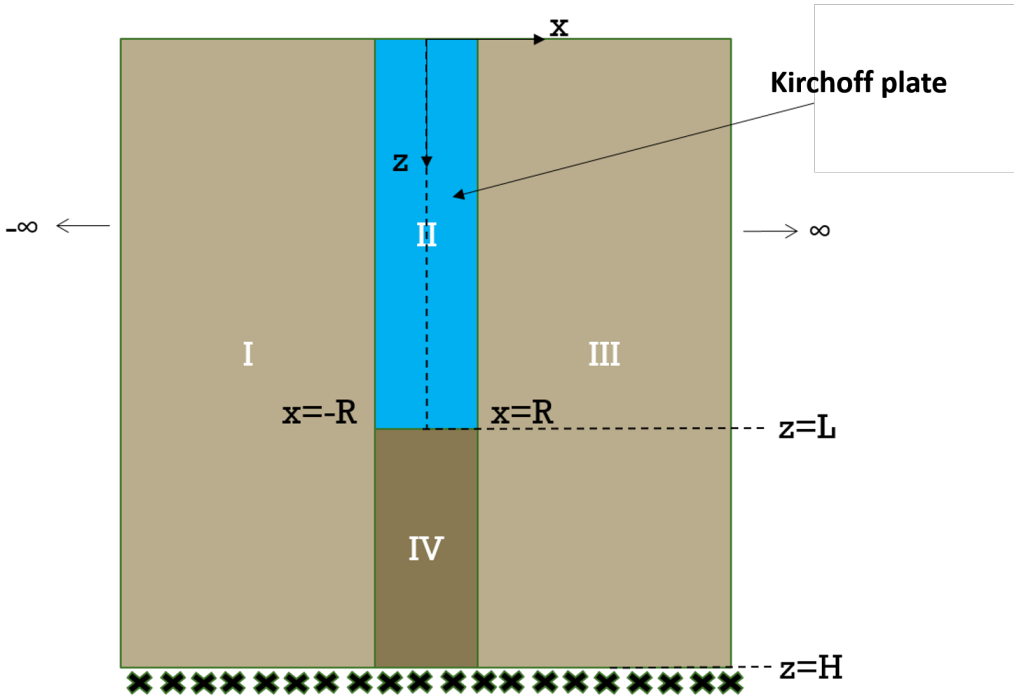

Figure A.1: ***Benchmark plate-soil system***

The Benchmark solution is a dimensionless waveguide Kirchhoff plate interaction problem. The expressions for stresses in the soil for all domains are obtained as indicated in Chapter 2 and Chapter 4 (Tip domain).

A.1 Kinematic relationship

Figure A.2 shows the global reference system used as well as the direction of positive rotation. It can be seen that when moving along $+z$, if W is positive, the rotation is positive.

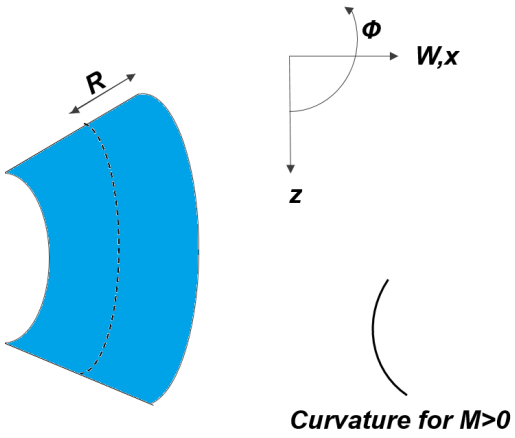

Figure A.2: ***Sign Conventions***

Hence, the Kinematic relationship can be stated as

$$\tilde{\phi} = \partial_{\tilde{z}} \tilde{W} \tag{A.1}$$

A.2 Constitutive relationship

The curvature κ is given as

$$\tilde{\kappa} = \partial_{\tilde{z}} \tilde{\phi} = \partial^2_{\tilde{z}} \tilde{W} \tag{A.2}$$

The relation between the Moment and curvature is given as

$$\tilde{M} = -D_b \tilde{\kappa} \tag{A.3}$$

where $D_b = \frac{EI}{(1-\nu^2)}$ is the plate stiffness

If the reader is interested in how this relationship is derived, they can refer to [30]. The '-' sign comes since the assumed curvature is opposite to that for positive moment.

A.3 Equilibrium relationship

Figure A.3, shows the free body diagram of a small segment of the plate of length Δz.

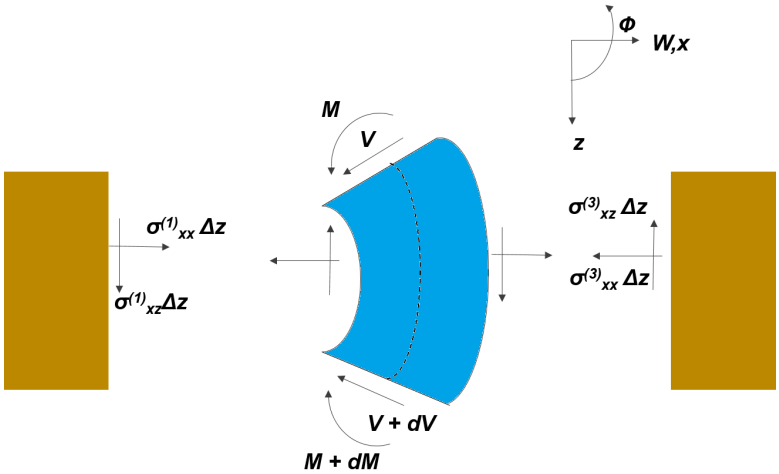

Figure A.3: ***Equilibrium relation***

Taking Horizontal force equilibrium

$$\begin{aligned} -m_b\tilde{\omega}^2 W\tilde{\Delta}\tilde{z} &= -\tilde{\sigma}_{xx}^{(1)}\tilde{\Delta}\tilde{z} + \tilde{\sigma^{(3)}}_{xx}\tilde{\Delta}z - \tilde{V} + \tilde{V} + d\tilde{V} \\ \implies -m_b\tilde{\omega}^2 W &= -\tilde{\sigma}_{xx}^{(1)} + \tilde{\sigma}_{xx}^{(3)} + \tilde{V}^I \end{aligned} \tag{A.4}$$

Equation A.4 is obtained after dividing the previous equation throughout by Δz,
Taking Bending moment equilibrium about the nuetral axis at the top of the element

$$\begin{aligned} -\tilde{M} - d\tilde{M} + \tilde{M} + (\tilde{V} + d\tilde{V})\tilde{\Delta}\tilde{z} - \tilde{\sigma}_{xz}^{(3)}\tilde{R} - -\tilde{\sigma}_{xz}^{(1)}\tilde{R} = 0 \\ \implies \tilde{V}^I = \tilde{M}^{II} + (\tilde{\sigma}^{I,(3)} + \tilde{\sigma}^{I,(1)})\tilde{R} \end{aligned} \tag{A.5}$$

Using Equation A.4 and Equation A.5, the following equation of motion is derived

$$D_b\tilde{w}^{IV} + m_b\partial_{\tilde{t}}^2\tilde{w} = -\tilde{\sigma}_{xx}(\tilde{x} = -\tilde{R}, \tilde{z}) + \tilde{\sigma}_{xx}(\tilde{x} = \tilde{R}, \tilde{z}) + \left(\partial_{\tilde{z}}\tilde{\sigma}_{xz}(\tilde{x} = -\tilde{R}, \tilde{z}) + \partial_{\tilde{z}}\tilde{\sigma}_{xz}(\tilde{x} = \tilde{R}, \tilde{z})\right)\tilde{R} \tag{A.6}$$

$m_b = \rho_b 2R$ is the mass per unit area, ρ_b the density of the plate. The right side is made dimensionless by dividing by μ and substituting the derivatives. This gives

$$w^{IV} + \alpha\partial_t^2 w = \frac{\mu H^3}{D_b}(-\sigma_{xx}^- + \sigma_{xx}^+ + \sigma_{xz}^{I,+} + -\sigma_{xz}^{I,-}) \tag{A.7}$$

where

$$\alpha = \frac{m_b\mu H^4}{\mu T^2 D_b} = \frac{m_b c_s^2 H^2}{D_b} \tag{A.8}$$

The solution to the equation of motion is found in the frequency domain. Assuming harmonic motion in soil,

$$w = W(z)e^{i\omega t} \tag{A.9}$$

The resulting equation is

$$W^{IV}(z) - \beta^4 W(z) = \zeta_0(-\sigma_{xx}^{(1)} + \sigma_{xx}^{(3)} + \sigma_{xz}^{I,(3)} + \sigma_{xz}^{I,(1)}) \tag{A.10}$$

where $\beta^4 = \alpha\omega^2$ and $\zeta_0 = \frac{\mu H^3}{D_b}$
The solution to this equation will be a combination of a homogeneous and a particular solution. The homogeneous part of the solution is given as

$$W_h(z) = C_1^{(2)}e^{-i\beta z} + C_2^{(2)}e^{i\beta z} + C_3^{(2)}e^{-\beta z} + C_4^{(2)}e^{\beta z} \tag{A.11}$$

where the superscript (2) indicates the plate domain. The particular solution is obtained for each stress component separately. The expressions for the stresses are now substituted into the equations. For the normal stress from Domain 1

$$W^{IV}(z) - \beta^4 W(z) = -\zeta_0 \sum_{n=1}^{\infty} C_n^{(1)} X_n^{(1)}(-R) Z_{xx;n}^{(1)} \qquad 0 \le z \le L \tag{A.12}$$

Similarly for the shear stress

$$\begin{aligned} W^{IV}(z) - \beta^4 W(z) &= \zeta_0 R\partial_z\sigma_{xz}^{(1)} \\ &= -\zeta_0 \sum_{n=1}^{\infty} C_n^{(1)} X_n^{(1)}(-R)\partial_z Z_{xz;n}^{(1)} \qquad 0 \le z \le L \end{aligned} \tag{A.13}$$

Similarly equations for Stresses from Domain 3 are also obtained

$$W^{IV}(z) - \beta^4 W(z) = -\zeta_0 \sum_{n=1}^{\infty} C_n^{(3)} X_n^{(3)}(R) Z_{xx;n}^{(3)} \qquad 0 \le z \le L \tag{A.14}$$

$$\begin{aligned} W^{IV}(z) - \beta^4 W(z) &= \zeta_0 R \partial_z \sigma_{xz}^{(3)} \\ &= -\zeta_0 \sum_{n=1}^{\infty} C_n^{(3)} X_n^{(3)}(R) \partial_z Z_{xz;n}^{(3)} \qquad 0 \le z \le L \end{aligned} \tag{A.15}$$

where

$$\begin{aligned} Z_{x;n} &= i a_x k_x Z_{p;n} - \partial_z Z_{s;n} \\ Z_{z;n} &= i a_x k_x Z_{s;n} + \partial_z Z_{p;n} \\ Z_{xx;n} &= -k_{x;n}^2 v^2 Z_{p;n} + (v^2 - 2)\partial_z^2 Z_{p;n} - 2 i a_x k_{x;n} \partial_z Z_{s;n} \\ Z_{zz;n} &= -k_{x;n}^2 v^2 Z_{p;n} - (v^2 - 2)\partial_z^2 Z_{p;n} v^2 + 2 i a_x k_{x;n} \partial_z Z_{s;n} \\ Z_{xz;n} &= 2 i a_x \partial_z Z_{p;n} - \partial_z^2 Z_{s;n} - k_{x;n}^2 Z_{s;n} \end{aligned} \tag{A.16}$$

with $a_x = 1$ for a wave moving towards $-\infty$ and $a_x = -1$ for a wave moving towards ∞.

The particular solutions are found assuming four trial functions for Domain 1 and 3

$$\begin{aligned} W_n^{(k1)} &= A_n^{(k1)} Z_{p;n}^{(k)}(z) \\ W_n^{(k2)} &= A_n^{(k2)} \partial_z^2 Z_{p;n}^{(k)}(z) \\ W_n^{(k3)} &= A_n^{(k3)} \partial_z Z_{s;n}^{(k)}(z) \\ W_n^{(k4)} &= A_n^{(k4)} \partial_z^3 Z_{s;n}^{(k)}(z) \qquad k = 1, 3 \end{aligned}$$

The solution for stresses on each Domain is given as

$$W_n^{(k)} = W_n^{(k1)} + W_n^{(k2)} + W_n^{(k3)} + W_n^{(k4)} \tag{A.17}$$

The total solution for the plate is then given as

$$W(z) = \sum_{n=1}^{\infty} C_n^{(1)} W_n^{(1)} + \sum_{m=1}^{\infty} C_m^{(3)} W_m^{(3)} + \sum_{j=1}^{4} C_j^{(2)} W_j^{(2)} \tag{A.18}$$

The unknown coefficients $C_n^{(m)}$ are determined using the boundary conditions imposed at the two ends of the plate.

A.4 Normalization factors

The Rotation, Shear force and bending moment in the plate are normalized as follows

$$\begin{aligned} \tilde{\phi} &= \frac{\partial \tilde{W}}{\partial \tilde{z}} = \frac{H \partial W}{H \partial z} = \frac{\partial W}{\partial z} = \phi \\ \tilde{M} &= D_b \frac{\partial \tilde{\phi}}{\partial \tilde{z}} = D_b \frac{\partial \phi}{H \partial z} = \frac{D_b}{H} M \\ \tilde{V} &= \frac{\partial \tilde{M}}{\partial \tilde{z}} = D_b \frac{\partial^2 \tilde{\phi}}{\partial \tilde{z}^2} = \frac{D_b}{H^2} V \end{aligned} \tag{A.19}$$

where $\tilde{\phi}, \tilde{M}$ and $\tilde{V}$ are the dimensional quantities and ϕ, M and V are the dimensionless quantities.

A.5 Boundary and Interface conditions

The boundary and interface conditions are given for a unit normalized for acting at the top of the plate.

A.5.1 Hybrid solution for plate-soil system considering a single domain of soil

For the single domain analysis, only Domain 3 is considered, $\sigma_{xx}^{(1)}(x = -R, z) = 0$, $\sigma_{xz}^{(1)}(x = -R, z) = 0$. Two cases were considered - Slip and the non-slip

For the slip case, $\sigma_{xz}^{(3)}(x = R, z) = 0$, and only $\sigma_{xx}^{(3)}(x = -R, z)$ was considered in the RHS of Equation A.6. The complete solution is then given as

$$W(z) = \sum_{m=1}^{\infty} C_m^{(3)} W_m^{(3)} + \sum_{j=1}^{4} C_j^{(2)} W_j^{(2)} \tag{A.20}$$

This has $n+4$ unknowns, which can be solved using the boundary and interface conditions. The interface conditions used for the slip case

$$\phi(z) = -\frac{u_z^{(3)}(x,z)}{R}, W(z) = u_x^{(3)}(x,z) \qquad x = R \tag{A.21}$$

The boundary conditions for the plate used were

$$\begin{aligned} V(z) &= 1, \quad M(z) = 0, \qquad z = 0 \\ W(z) &= 0, \quad \phi(z) = 0, \qquad z = L \end{aligned} \tag{A.22}$$

The system of equations is an overdetermined system, hence the Pseudo-inverse was used to solve the equations simultaneously. For the non-slip case, same set of boundary and interface conditions were used with the consideration of $\sigma_{xz}^{(3)}(x = R, z)$ in Equation A.6.

A.5.2 Hybrid solution for a plate embedded in an elastic waveguide

For this analysis, all three soil domains surrounding the plate were considered.

Equation A.6 shows the plate equilibrium equation that is considered.

The interface conditions used are

$$\begin{aligned} \phi(z) &= -\frac{u_z^{(3)}(x,z)}{R}, W(z) = u_x^{(3)}(x,z) \qquad x = R, 0 < z < L \\ \phi(z) &= \frac{u_z^{(1)}(x,z)}{R}, W(z) = u_x^{(1)}(x,z) \qquad x = -R, 0 < z < L \\ \sigma_{xx}^{(4)}(x,z) &= \sigma_{xx}^{(3)}(x,z), \qquad x = R, L < z < H \end{aligned}$$

$$\begin{aligned} \sigma_{xz}^{(4)}(x,z) &= \sigma_{xz}^{(3)}(x,z), \qquad x = R, L < z < H \\ u_x^{(4)}(x,z) &= u_x^{(3)}(x,z), \qquad x = R, L < z < H \\ u_z^{(4)}(x,z) &= u_z^{(3)}(x,z), \qquad x = R, L < z < H \end{aligned}$$

$$\sigma_{xx}^{(4)}(x,z) = \sigma_{xx}^{(1)}(x,z), \qquad x = -R, L < z < H$$

$$\begin{aligned} \sigma_{xz}^{(4)}(x,z) &= \sigma_{xz}^{(1)}(x,z), \qquad x = -R, L < z < H \\ u_x^{(4)}(x,z) &= u_x^{(1)}(x,z), \qquad x = -R, L < z < H \\ u_z^{(4)}(x,z) &= u_z^{(1)}(x,z), \qquad x = -R, L < z < H \end{aligned} \tag{A.23}$$

The boundary conditions used are

$$\begin{aligned} V(z) &= 1, \quad M(z) = 0, \qquad z = 0 \\ V(z) &= \int_{-R}^{R} \sigma_{zx}^{(4)}.dx, \quad M(z) = \int_{-R}^{R} \sigma_{zz}^{(4)} x.dx, \qquad z = L \end{aligned} \tag{A.24}$$

where the expressions for $\sigma_{zx}^{(4)}, \sigma_{zz}^{(4)}, u_x^{(4)}$ and $u_z^{(4)}$ are given in Equation 4.10.

Appendix B

Pseudo Inverse

A pseudoinverse $\mathbf{A}^+$ of a matrix of a matrix **A** is a generalization of an inverse matrix. The most common use of the pseudoinverse is to compute a 'best fit'(least squares) solution of a system of linear equations that lacks a unique solution. Another use is to find the minimum (Euclidean) norm solution to a system of linear equations with multiple solutions. The *Moore-Penrose Pseudoinverse* was used in this thesis to obtain the solution to an overdetermined system of equations. The function *'pinv'* in MATLAB coding language was used. The theory behind this function is described in detail in this appendix.

For any matrix **A**, there exists a unique pseudoinverse $\mathbf{A}^+$ that satisfies four Penrose conditions:

1. $\mathbf{A}\mathbf{A}^+\mathbf{A} = \mathbf{A}$
2. $\mathbf{A}^+\mathbf{A}\mathbf{A}^+ = \mathbf{A}^+$
3. $\mathbf{A}^+\mathbf{A} = (\mathbf{A}^+\mathbf{A})^*$
4. $\mathbf{A}\mathbf{A}^+ = (\mathbf{A}\mathbf{A}^+)^*$

where $\mathbf{M}^*$ is the conjugate transpose of matrix **M**. If **A** is nonsingular, it is clear that $\mathbf{A}^+ = \mathbf{A}^{-1}$ trivially satisfies the four equations. Since the pseudoinverse is known to be unique, it follows that the pseudoinverse of a nonsingular matrix is the same as the ordinary inverse.

For creating the Pseudo-inverse many methods are available, the most commonly used being QR decomposition and Single value Decomposition (SVD). The function $'pinv'$ is based on SVD, hence we discuss more on this method.

For a matrix **A** of order n x m with rank r, the SVD is

$$\mathbf{A} = \mathbf{U}\mathbf{D}\mathbf{V}^* \tag{B.1}$$

where **U** is a n x n unitary matrix, **V** is a m x m unitary matrix and **D** is a n x m matrix diagonal matrix of singular values of **A**. The singular values are the roots of the eigenvalues of the square matrices $\mathbf{A}^*\mathbf{A}$ or $\mathbf{A}\mathbf{A}^*$, and the number of singular values is equal to the rank of **A**.

$$\mathbf{D} = \begin{bmatrix} \mathbf{S} & 0 \\ 0 & 0 \end{bmatrix} \tag{B.2}$$

where **S** is a r x r matrix of singular values. Rows $\{(n-r)...n\}$ and columns $\{(m-r)...m\}$, of **D** are full of zeros.

For simplicity, SVD can be expressed as

$$\mathbf{A} = \sum_{i=1}^{r} s_i \vec{x}_i \vec{y}_i^* \tag{B.3}$$

where the columns of **U** are $\{x_1 ... x_n\}$ and **V** are $\{y_1 ... y_m\}$ are orthonormal.

In MATLAB, if the value of an element in the matrix is below the tolerance value, it is taken to be zero. The tolerance is calculated as

$$t = \epsilon * max(m, n) * max(\mathbf{D}) \tag{B.4}$$

where ϵ is known as the machine epsilon and is referred to relative error in rounding off. More information on computing the pseudoinverse can be found in [23].

Appendix C

Obtaining the Least square approximation

Mathematically, the Least squares approximation is the problem of approximately solving an overdetermined system of linear equations, where the best approximation is defined as that which minimizes the sum if squared differences between the data values and their corresponding modeled values [1].

Consider an overdetermined system

$$\sum_{j=1}^{n} X_{ij}\beta_j = y_i, (i = 1, 2, ..., m) \tag{C.1}$$

where there are m linear equations with n unknown coefficients, with $m > n$. In matrix form the above equation can be written as

$$\mathbf{X}\beta = y \tag{C.2}$$

where

$$X = \begin{bmatrix} X_{11} & X_{12} & \cdots & X_{1n} \\ X_{21} & X_{22} & \cdots & X_{2n} \\ \vdots & \vdots & \ddots & \vdots \\ X_{m1} & X_{m2} & \cdots & X_{mn} \end{bmatrix}, \quad \beta = \begin{bmatrix} \beta_1 \\ \beta_2 \\ \vdots \\ \beta_n \end{bmatrix}, \quad = \begin{bmatrix} y_1 \\ y_2 \\ \vdots \\ y_n \end{bmatrix} \tag{C.3}$$

Since there is no unique solution, the goal is find the unknown coefficients β which give the $'bestfit'$, which is obtained by solving the quadratic minimization problem

$$\epsilon = \arg_{\beta}\min S(\beta) \tag{C.4}$$

where the function S is given as

$$S(\beta) = \sum_{i=1}^{m} |y_i - \sum_{j=1}^{n} X_{ij}\beta_j|^2 \tag{C.5}$$

This minimization problem as a unique solution provided the n columns of the matrix $\mathbf{X}$ are linearly independent, which can be obtained by solving the normal equation

$$\begin{aligned} (\mathbf{X^T X})\epsilon &= \mathbf{X^T} y \\ \implies \epsilon &= (\mathbf{X^T X})^{-1}\mathbf{X^T} y \end{aligned} \tag{C.6}$$

where ϵ is the coefficient vector of the least squares subspace.

C.1 MATLAB implementation

```
%% Least squares approximation

y = dddW2';% dddW2 - Curve to be fit
a = ZU2';% ZU2 - Equidistant points across the domain
X = [ones(length(dddW2),1),a];% forming X

Eps = pinv(X'*X)*X'*y;% Computing the projection of X on y, giving
   Eps

Ytil = X*Eps;% Best fit line

X1= [ones(length(dddW2),1),a,a.^2,a.^3,a.^4,a.^5,a.^6];% Curve
   fitting using higher order polynomial

%% Plotting

plot(Ytil,a);
```

Appendix D

Hybrid solution for the pile-soil system with a single domain of soil - Convergence plots

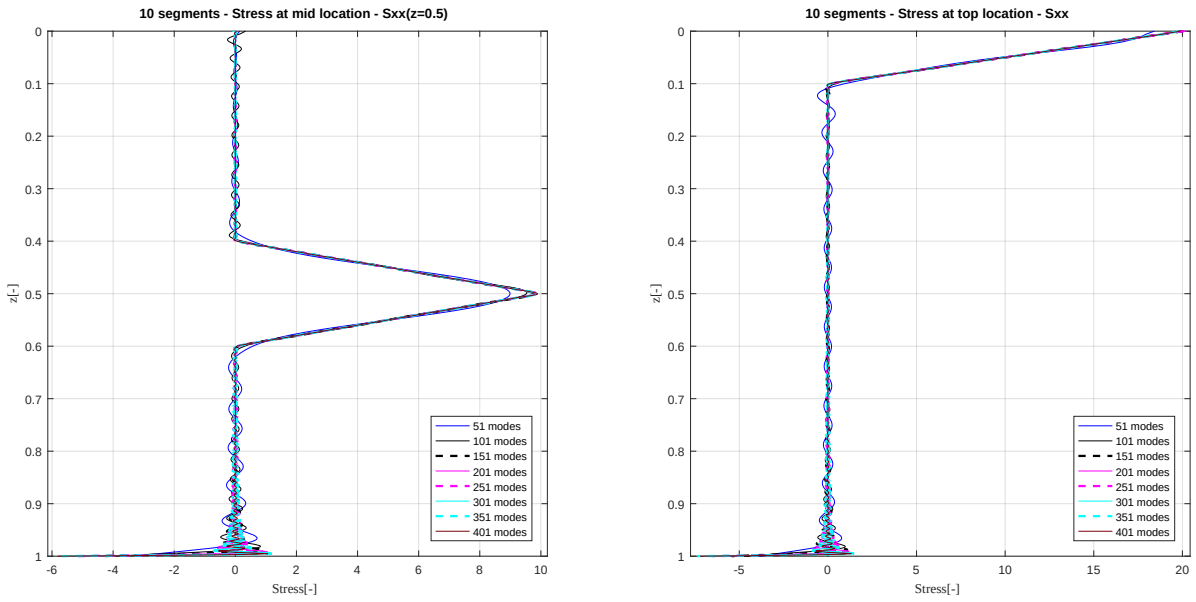

Figure D.1: *Convergence plot - $\sigma_{xx}^{(3)}$ - 10 segments - (a) Stress applied to mid location, (b) Stress applied to top location*

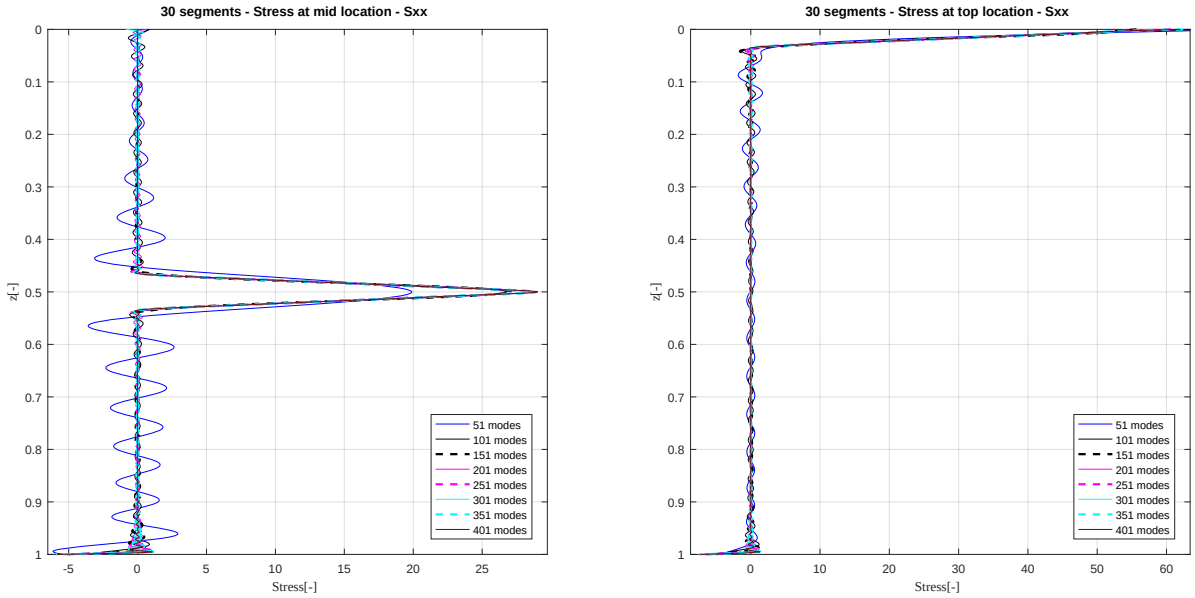

Figure D.2: ***Convergence plot - $\sigma_{xx}^{(3)}$ - 30 segments - (a) Stress applied to mid location, (b) Stress applied to top location***

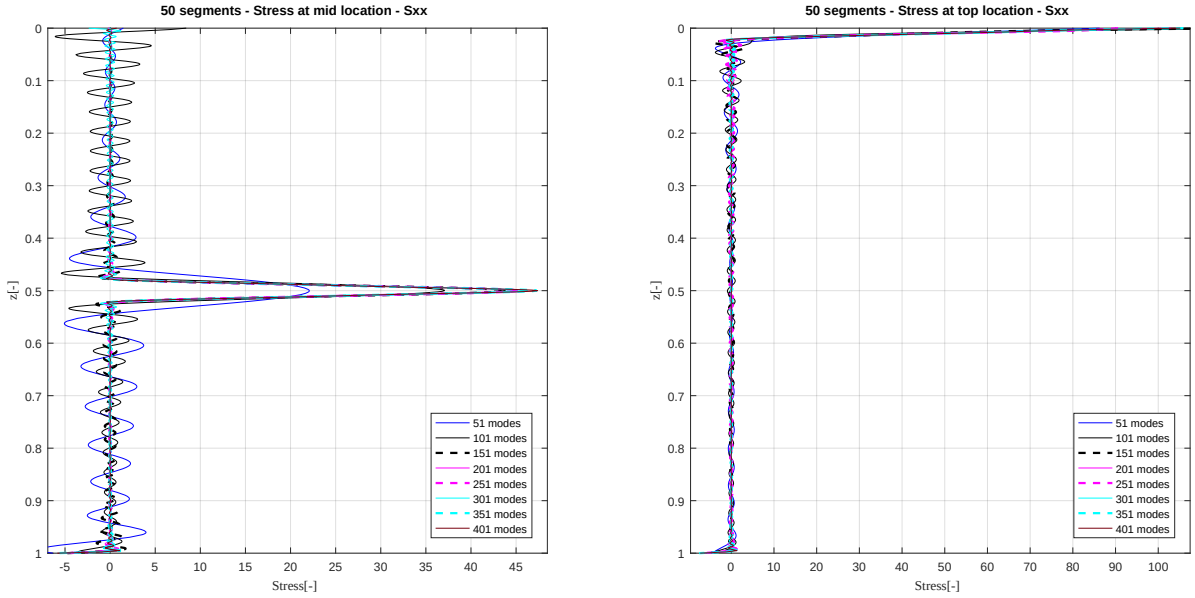

(a) ***$\sigma_{xx}^{(3)}$ at $x = R$ applied at the mid-location***

(b) ***$\sigma_{xx}^{(3)}$ at $x = R$ applied at the top location***

Figure D.3: ***Convergence plot - $\sigma_{xx}^{(3)}$ - 50 segments - (a) Stress applied to mid location, (b) Stress applied to top location***

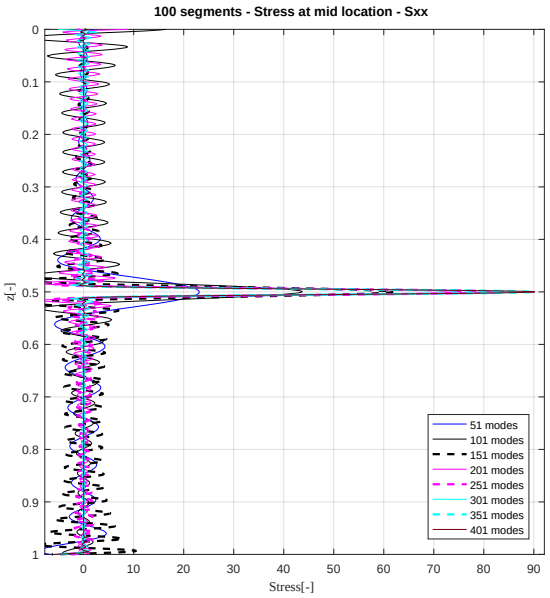

(a) $\sigma_{xx}^{(3)}$ ***at*** $x = R$ ***applied at the mid-location***

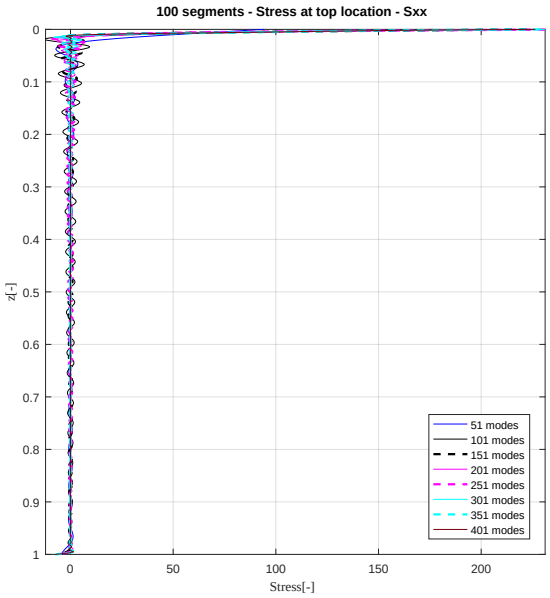

(b) $\sigma_{xx}^{(3)}$ ***at*** $x = R$ ***applied at the top location***

Figure D.4: ***Convergence plot -*** $\sigma_{xx}^{(3)}$ ***- 100 segments - (a) Stress applied to mid location, (b) Stress applied to top location***

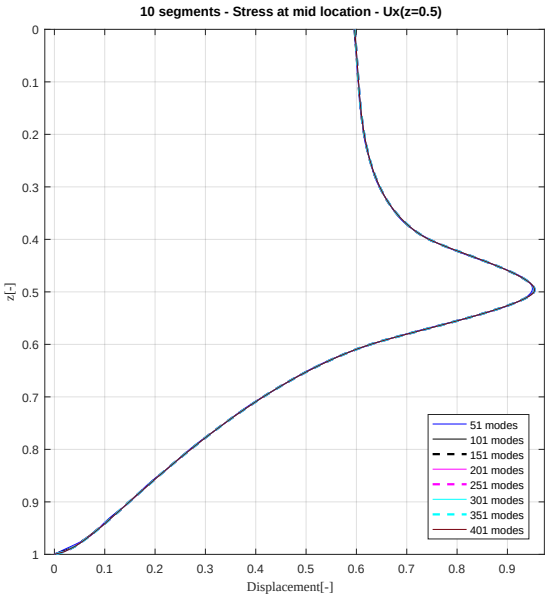

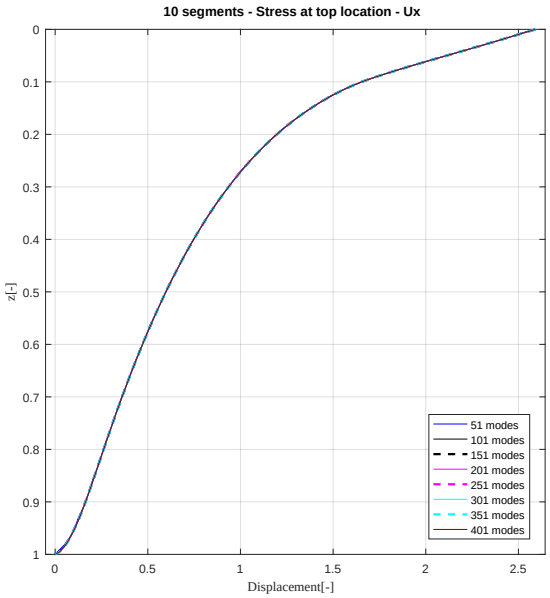

Figure D.5: ***Convergence plot -*** $u_x^{(3)}$ ***- 10 segments - (a) Stress applied to mid location, (b) Stress applied to top location***

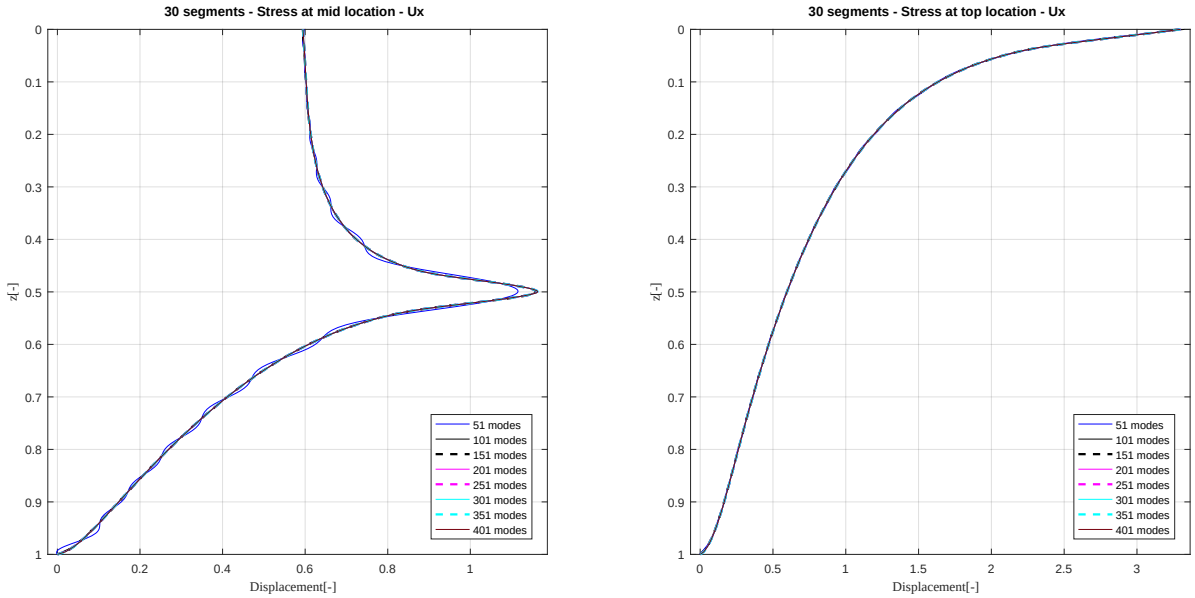

Figure D.6: ***Convergence plot - $u_x^{(3)}$ - 30 segments - (a) Stress applied to mid location, (b) Stress applied to top location***

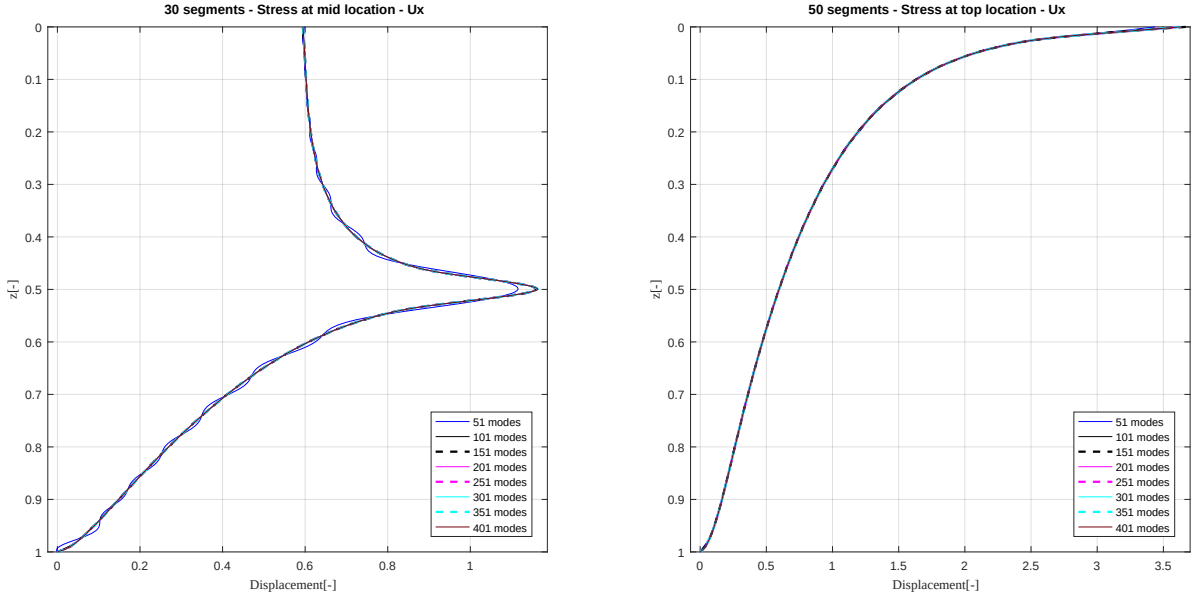

Figure D.7: ***Convergence plot - $u_x^{(3)}$ - 50 segments - (a) Stress applied to mid location, (b) Stress applied to top location***

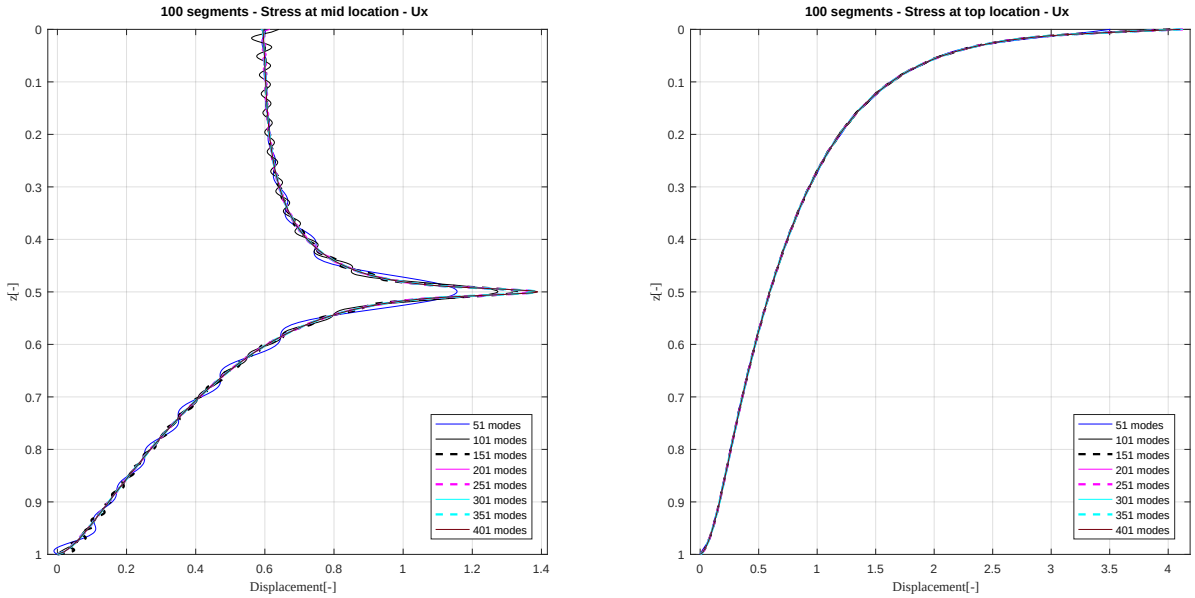

Figure D.8: ***Convergence plot - $u_x^{(3)}$ - 100 segments - (a) Stress applied to mid location, (b) Stress applied to top location***

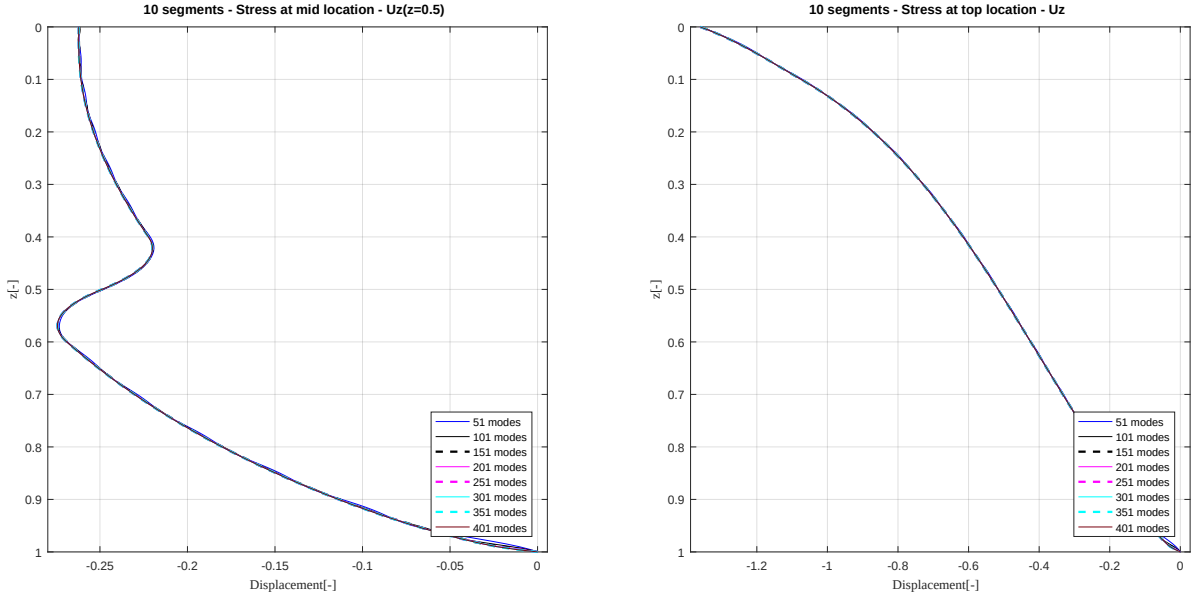

Figure D.9: ***Convergence plot - $u_z^{(3)}$ - 10 segments - (a) Stress applied to mid location, (b) Stress applied to top location***

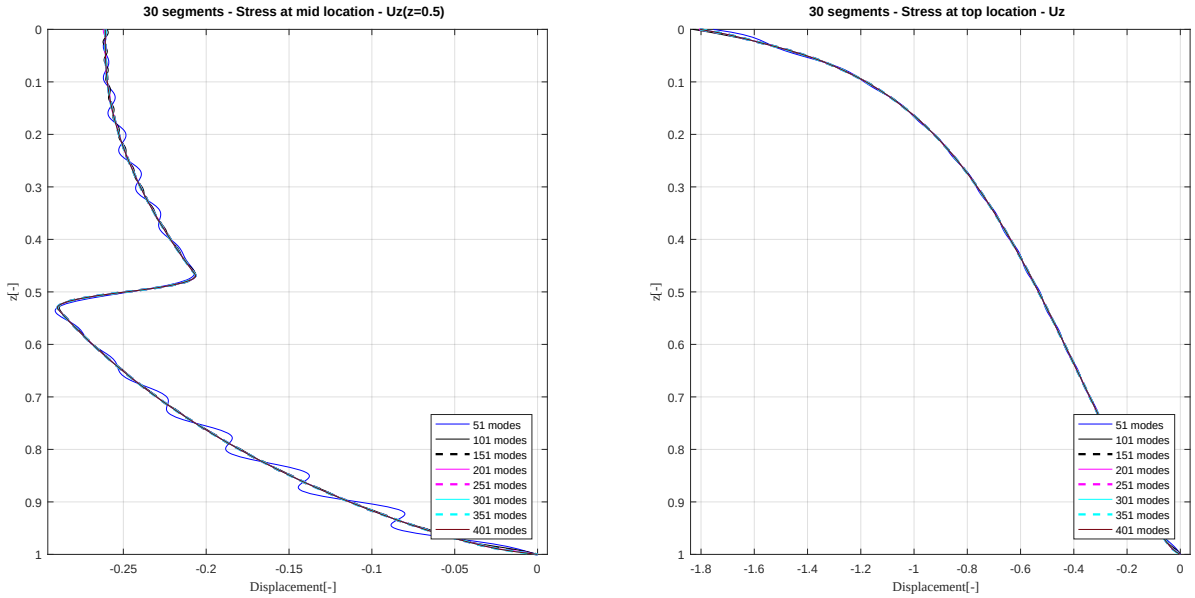

Figure D.10: ***Convergence plot - $u_z^{(3)}$ - 30 segments - (a) Stress applied to mid location, (b) Stress applied to top location***

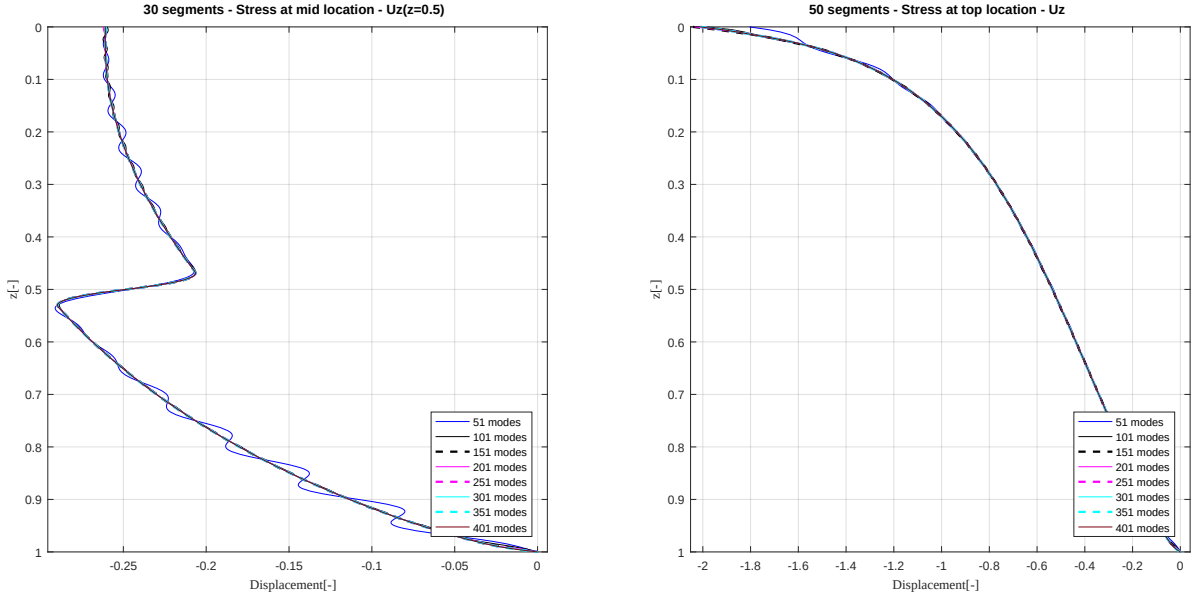

Figure D.11: ***Convergence plot - $u_z^{(3)}$ - 50 segments - (a) Stress applied to mid location, (b) Stress applied to top location***

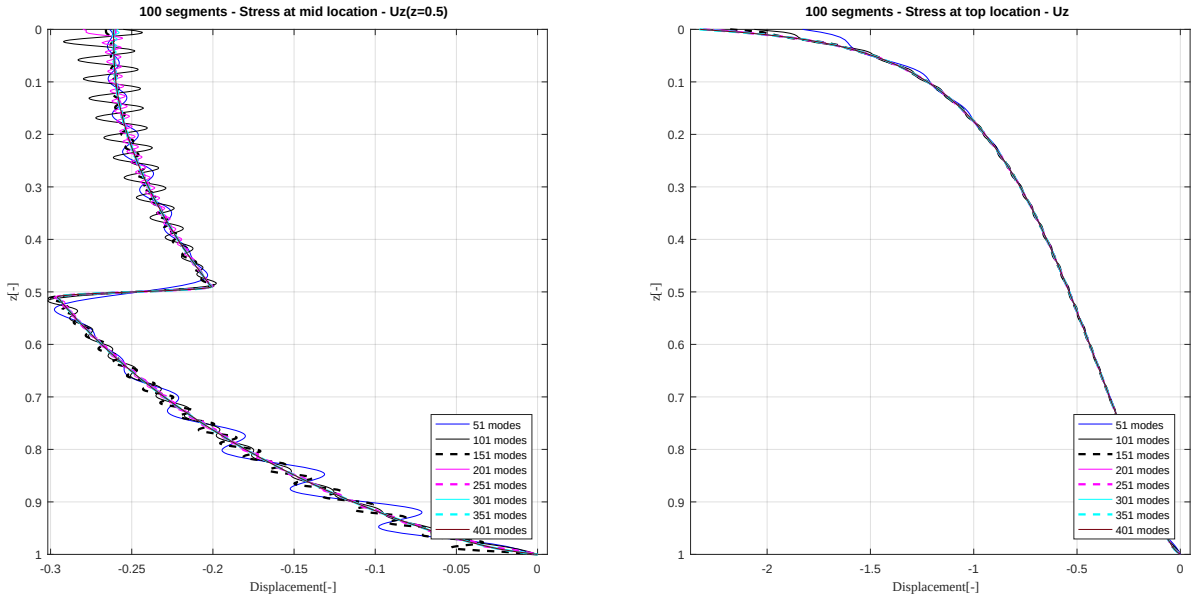

Figure D.12: ***Convergence plot - $u_z^{(3)}$ - 100 segments - (a) Stress applied to mid location, (b) Stress applied to top location***

Appendix E

Waveguide with a cavity subjected to excitation - Convergence studies

E.1 Case study 1 - convergence plots

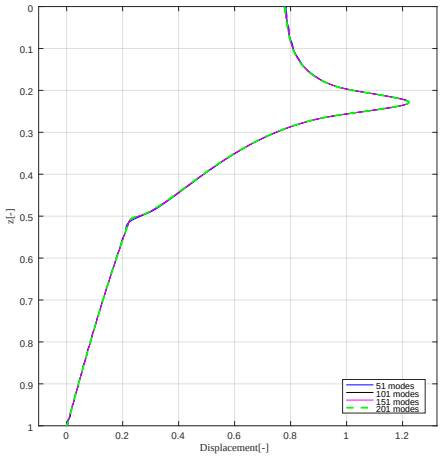

(a) ***Convergence plot - $u_x^{(1)}$ at $x = -R$ - Normal stress at mid location***

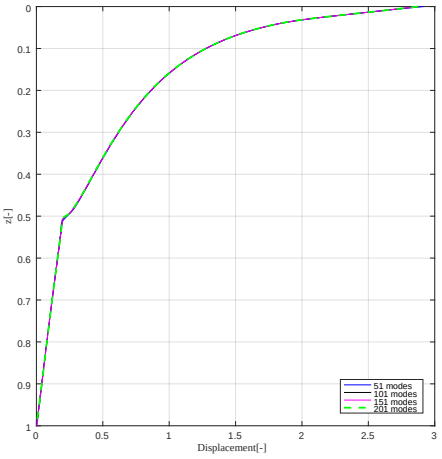

(b) ***Convergence plot - $u_x^{(1)}$ at $x = -R$ - Normal stress at top location***

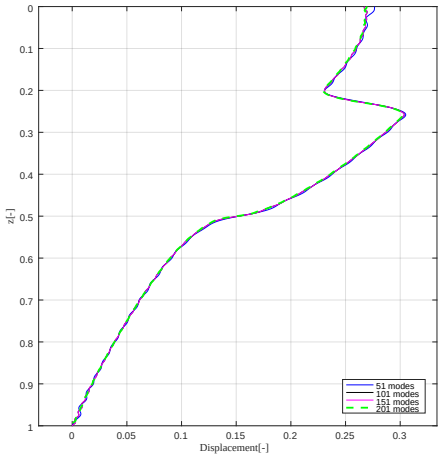

(c) ***Convergence plot - $u_z^{(1)}$ at $x = -R$ - Normal stress at mid location***

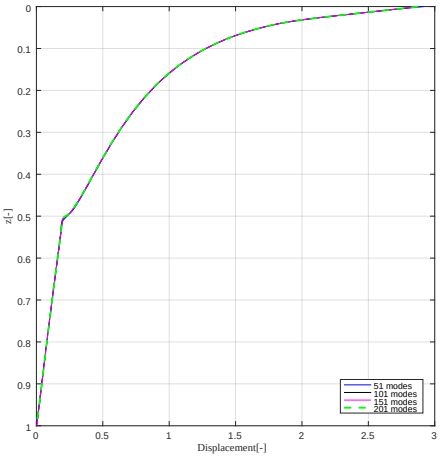

(d) ***Convergence plot - $u_z^{(1)}$ at $x = -R$ - Normal stress at top location***

Figure E.1: ***Convergence plots for displacements with varying number of modes - 15 segments***

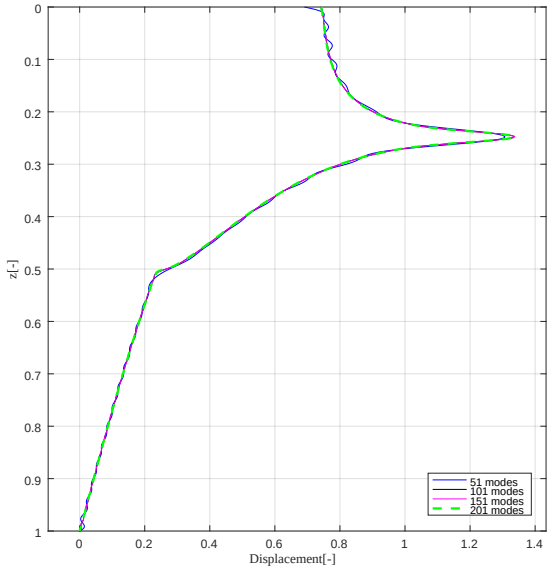

(a) ***Convergence plot -*** $u_x^{(1)}$ ***at*** $x = -R$ ***- Normal stress at mid location***

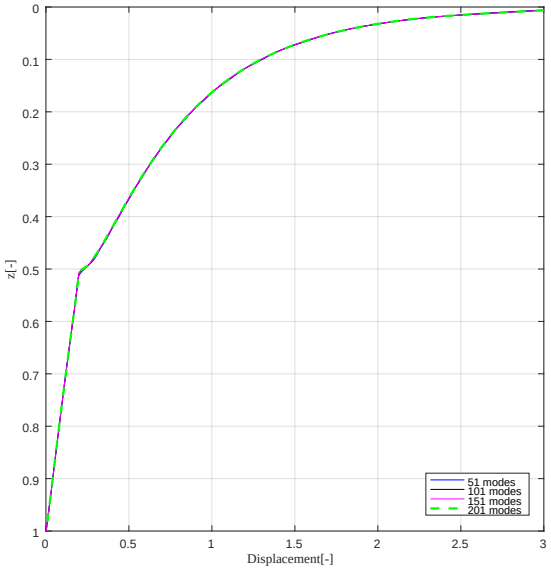

(b) ***Convergence plot -*** $u_x^{(1)}$ ***at*** $x = -R$ ***- Normal stress at top location***

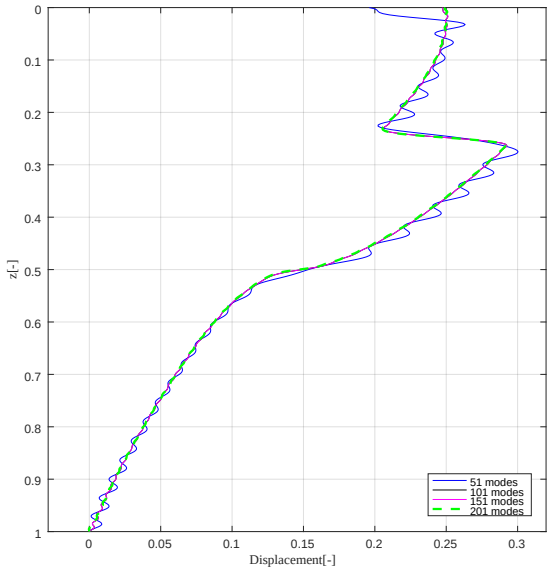

(c) ***Convergence plot -*** $u_z^{(1)}$ ***at*** $x = -R$ ***- Normal stress at mid location***

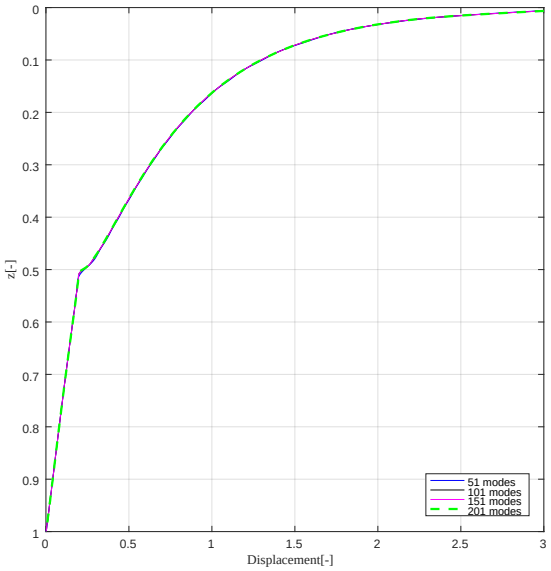

(d) ***Convergence plot -*** $u_z^{(1)}$ ***at*** $x = -R$ ***- Normal stress at top location***

Figure E.2: ***Convergence plots for displacements with varying number of modes - 30 segments***

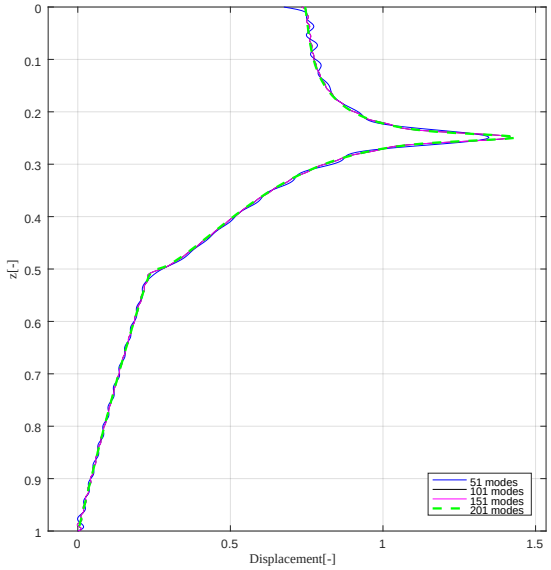

(a) ***Convergence plot - $u_x^{(1)}$ at $x = -R$ - Normal stress at mid location***

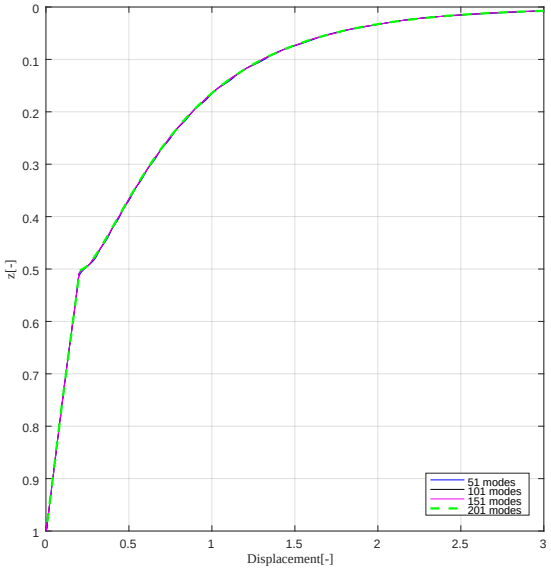

(b) ***Convergence plot - $u_x^{(1)}$ at $x = -R$ - Normal stress at top location***

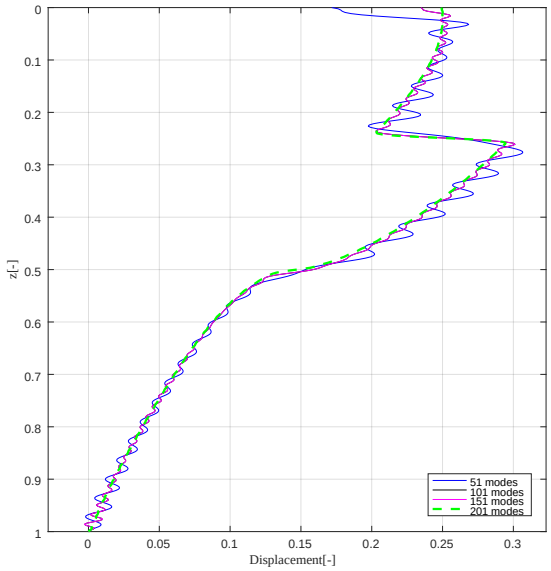

(c) ***Convergence plot - $u_z^{(1)}$ at $x = -R$ - Normal stress at mid location***

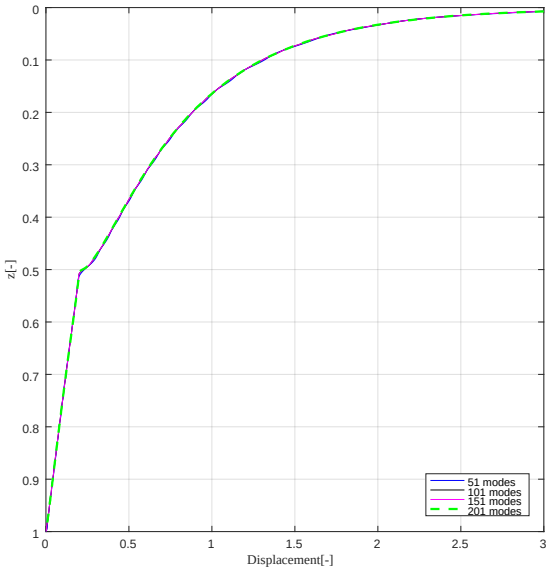

(d) ***Convergence plot - $u_z^{(1)}$ at $x = -R$ - Normal stress at top location***

Figure E.3: ***Convergence plots for displacements with varying number of modes - 50 segments***

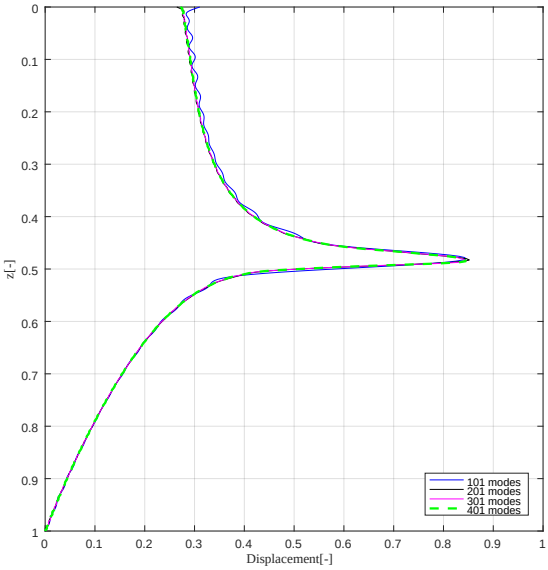

(a) ***Convergence plot -*** $u_x^{(1)}$ ***at*** $x = -R$ ***- Normal stress at corner location***

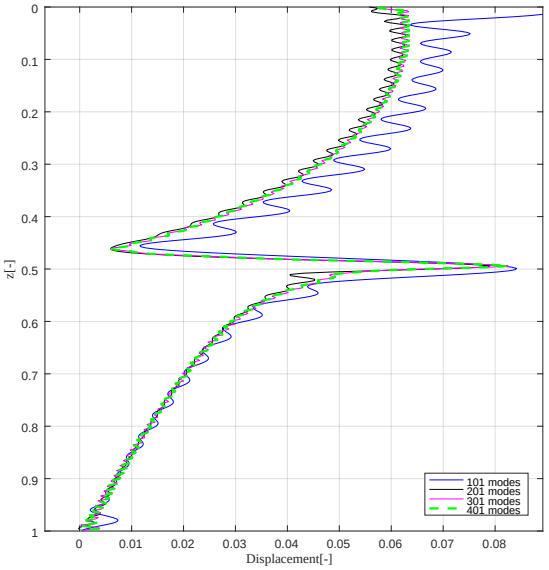

(b) ***Convergence plot -*** $u_z^{(1)}$ ***at*** $x = -R$ ***- Normal stress at corner location***

Figure E.4: ***Convergence plots for displacements with varying number of modes - 15 segments***

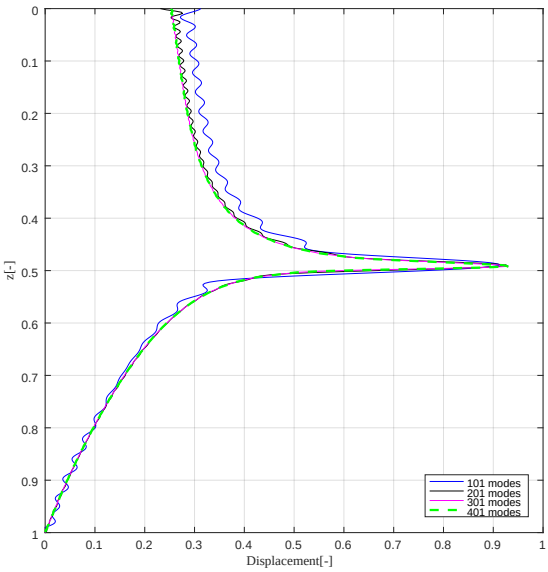

(a) ***Convergence plot -*** $u_x^{(1)}$ ***at*** $x = -R$ ***- Normal stress at corner location***

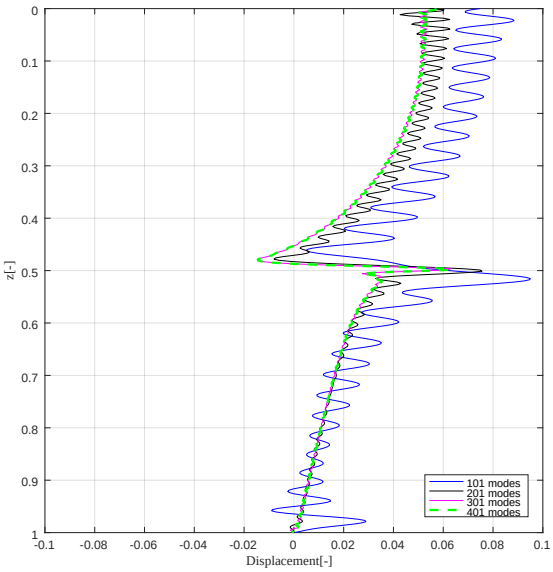

(b) ***Convergence plot -*** $u_z^{(1)}$ ***at*** $x = -R$ ***- Normal stress at corner location***

Figure E.5: ***Convergence plots for displacements with varying number of modes - 30 segments***

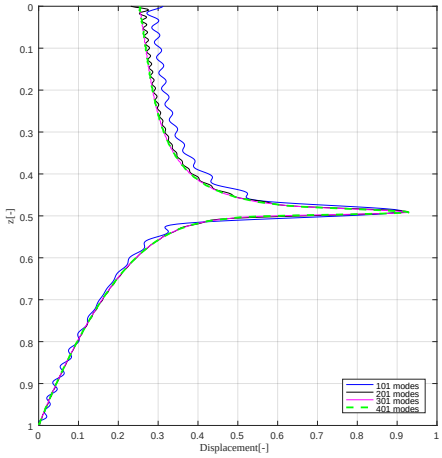

(a) ***Convergence plot - $u_x^{(1)}$ at $x = -R$ - Normal stress at corner location***

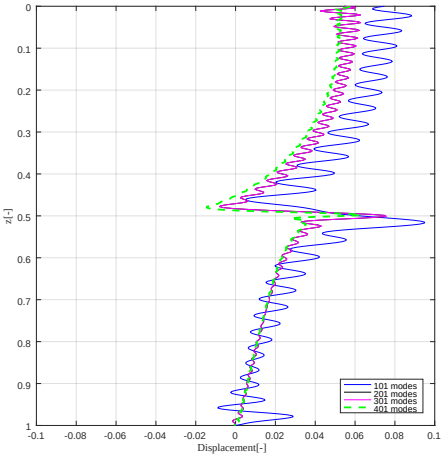

(b) ***Convergence plot - $u_z^{(1)}$ at $x = -R$ - Normal stress at corner location***

Figure E.6: ***Convergence plots for displacements with varying number of modes - 50 segments***

E.2 Case study 2

E.2.1 Requirement of fourier components for convergence

Table E.1: ***Number of segments vs number of modes for the tip***

Number of segments	*Length of segment[-]*	*Number of modes*
2	1	51
4	0.5	75
6	0.33	75

The number of Fourier components for convergence of stress for segments in the tip domain considering the corner location is summarized in Table E.1.

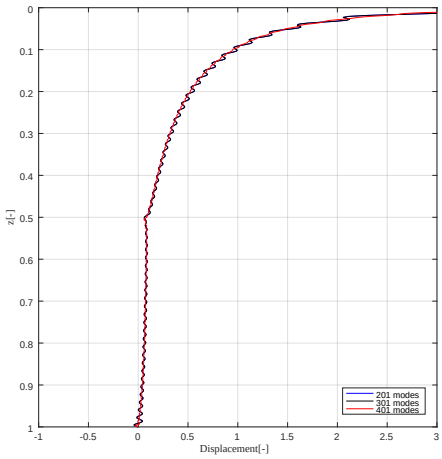

(a) ***Convergence plot - $u_x^{(1)}$ at $x = -R$ - Normal stress at top location***

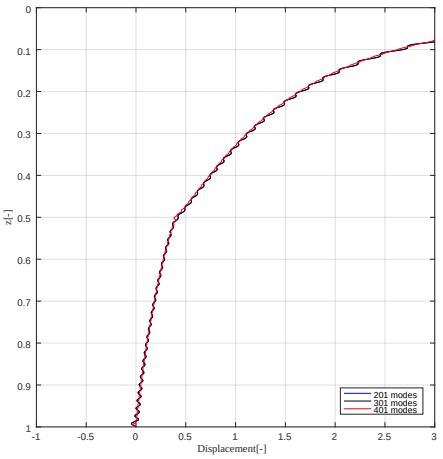

(b) ***Convergence plot - $u_z^{(1)}$ at $x = -R$ - Normal stress at top location***

Figure E.7: ***Convergence plots for displacements with varying number of modes - 20 segments***

Bibliography

[1] Wikipedia - linear least squares (mathematics). https://en.wikipedia.org/wiki/Linear_least_squares_(mathematics).

[2] ACHENBACH, J. Chapter 2 - the linearized theory of elasticity. In *Wave Propagation in Elastic Solids*, J. ACHENBACH, Ed., North-Holland Series in Applied Mathematics and Mechanics. Elsevier, Amsterdam, 1975, pp. 46 – 78.

[3] ACHENBACH, J. D. *Reciprocity in Elastodynamics*. Cambridge Monographs on Mechanics. Cambridge University Press, 2004.

[4] ARMSTRONG, M. MSc Thesis - Seismic Inversion for Identification of Soil Stiffness and Damping for Offshore Wind Turbines(2016).

[5] AZHAR NIYAZ, A., JUNAID AHMED SHAFEEQUE AH., A., MOHD ATIQUE SADIQUE, B., AND ABID NOOR, K. BSc Thesis - Pile Soil Interaction by Finite Element Method in Abaqus(2016).

[6] BYRNE, B. W., AND HOULSBY, G. T. Foundations for offshore wind turbines. *Philosophical Transactions of the Royal Society of London A: Mathematical, Physical and Engineering Sciences 361*, 1813 (2003), 2909–2930.

[7] CHOPRA, A. *Dynamics of Structures: Theory and Applications to Earthquake Engineering*. Civil Engineering and Engineering Mechanics Series. Prentice Hall, 2012.

[8] COMNINOU, M. Stress singularity at a sharp edge in contact problems with friction. *Zeitschrift für angewandte Mathematik and Physik ZAMP 27*, 4 (Jul 1976), 493–499.

[9] COUNCIL, W. E. World energy resources - technical report.

[10] DALEN, K. N. V. Lecture notes CIE5340 Soil Dynamics , part B : Body waves in an elastic continuum & Rayleigh waves at the free surface(2015). 1–34.

[11] DALEN, K. N. V., TSOUVALAS, A., METRIKINE, A. V., AND HOVING, J. S. International Journal of Solids and Structures Transition radiation excited by a surface load that moves over the interface of two elastic layers. *International Journal of Solids and Structures 73-74* (2015), 99–112.

[12] DAMGAARD, M., ZANIA, V., ANDERSEN, L., AND IBSEN, L. Effects of soil–structure interaction on real time dynamic response of offshore wind turbines on monopiles. *Engineering Structures 75* (2014), 388 – 401.

[13] DNV. Design of offshore wind turbines. *DNV-OS-J101 ,1^{st} Edition* (2004).

[14] EWEA. Deep water - the next step for offshore wind energy. *EWEA technical report* (2013).

[15] GAVIN, H. P. Structural Element Stiffness, Mass, and Damping Matrices. *CEE 541 - Structural Dynamics* (2014), 1–33.

[16] GENES, M. C., AND KOCAK, S. Dynamic soil–structure interaction analysis of layered unbounded media via a coupled finite element/boundary element/scaled boundary finite element model. *International Journal for Numerical Methods in Engineering 62*, 6 (2005), 798–823.

[17] GERCEK, H. Poisson's ratio values for rocks. *International Journal of Rock Mechanics and Mining Sciences 44*, 1 (2007), 1 – 13.

[18] HO, A., AND MBISTROVA, A. The european offshore wind energy.

[19] HU, C., AND HARTLEY, G. Analysis of a thin plate on an elastic half-space. *Computers and Structures 52*, 2 (1994), 227–235.

[20] KOUROUSSIS, G., VERLINDEN, O., AND CONTI, C. Finite-dynamic model for infinite media: Corrected solution of viscous boundary efficiency. *Journal of Engineering Mechanics 137*, 7 (2011), 509–511.

[21] KUO, Y.-S., ACHMUS, M., AND ABDEL-RAHMAN, K. *Investigation on the Requirements Regarding the Minimum Embedded Length of Monopiles*.

[22] LESNY, K., PAIKOWSKY, S. G., AND GURBUZ, A. *Scale Effects in Lateral Load Response of Large Diameter Monopiles*. 2007.

[23] MACAUSLAND, R. The moore-penrose inverse and least squares. *MATH 420 - Advanced Topics in Linear Algebra, University of Puger sound* (2014).

[24] METRIKINE, A., AND VROUWENVELDER, A. Wave Dynamics - Part 2, Dynamics of Solids and Structures (CT4140). 1–204.

[25] MORIN, D. Fourier analysis.

[26] PAUL, H. Lecture Notes CIE5340 - Part A - Soil dynamics in urban areas(2016).

[27] REDDY, J. *Theory and analysis of elastic plates and shells*. CRC Press, 2007.

[28] REESE, L., COX, W., AND KOOP, F. Field testing and analysis of laterally loaded piles in stiff clay.

[29] ROCK, M., AND PARSONS, L. Offshore wind energy (2010).

[30] SIMONE, A. *Analysis of Slender Structures - Coursebook CIE4190*. 2011.

[31] TILLESSEN, T. High demand for wind farm installation vessels. *Hansa International Maritime Journal 147* (2010), 170–171.

[32] VERRUIJT, A. *An Introduction to Soil Dynamics*. Theory and Applications of Transport in Porous Media. Springer Netherlands, 2009.

[33] WEGENER, P. MSc Thesis - A Critical Evaluation of the Current Design Standard for Offshore Wind Turbine Monopile Foundations.

[34] W.S.HALL, AND G.OLIVETO. The semi-analytical fundamental-solution-less scaled boundary finite-element method to model unbounded soil. *Boundary Element Methods for Soil-Structure Interaction* (2003).

SIEMENS Gamesa
RENEWABLE ENERGY

TU Delft